Using Electrostatic Nonlinearities to Enhance the Performance of Ring-based Coriolis Vibratory Gyroscopes

Davin Arifin

Supervised by Dr. Stewart McWilliam &

Prof. Atanas A. Popov

Thesis submitted to the University of Nottingham

for the degree of Doctor of Philosophy

March 2023

ABSTRACT

This research investigates electrostatic nonlinearities in capacitively operated ring-based Coriolis vibrating gyroscopes (CVG's). Large amplitude vibrations of the ring amplify the Coriolis force and are beneficial to achieving high-precision rate sensing. However, due to the miniature sizes of these devices and the narrow capacitive gaps, electrostatic nonlinearities manifest at relatively small ring displacements, thus resulting in the sensor output differing from what is expected of a standard linear device. As such, the current theory of operation commonly perceives electrostatic nonlinearities as an obstacle towards the development of high performance sensors.

Electrostatic nonlinearities is the dominant source of nonlinearity in ring-based CVG's. This work develops a mathematical model to analyse the influence of electrostatic nonlinearities on device performance. When the device operates using a basic electrostatic configuration incorporating only bias and drive voltages, it is found that the bias voltage induces single and mode-coupled cubic restoring forces, which are the main mechanisms through which electrostatic nonlinearities affect the ring dynamics and sensor output. These nonlinear restoring forces result in the amplitude-dependency of the drive and sense mode frequencies, and the presence of self-induced parametric excitation. These effects, in conjunction with the structural imperfections of the ring, degrade rate sensing performance by reducing the rate sensitivity and introducing bias rates and quadrature errors at larger drive amplitudes. A detailed theoretical analysis of the sense dynamics concludes that, depending on the interaction between the imperfections and the electrostatic nonlinearities, there are specific cases where the self-induced parametric excitation can enhance the rate sensitivity of the device. However, this enhancement cannot be achieved while retaining a trimmed sense response to keep the bias rate and quadrature error nullified. An analysis of the sense response and the modal forces shows that the imperfection-induced linear elastic coupling force and the nonlinear frequency imbalance are specifically responsible for the sensor output degradation. These nonlinear behaviours have also been validated against finite element results.

The research also investigates the strategic use of electrostatic forces to counteract the effects of nonlinearity and enhance device performance. It is shown that through careful selection of the voltages applied to the electrodes, the form of the resulting electrostatic forces can be tailored to manipulate the sense mode dynamics for device performance enhancement. The presented work develops a general framework to achieve this direct electrostatic force manipulation by considering the variations of the capacitance, voltage and electrostatic potential energy from electrode to electrode, which then enables direct control of the form of the total electrostatic potential energy. Through the use of the framework, this research shows

that the electrostatic nonlinearities can be manipulated to replicate the sensor outputs of a linear, trimmed device at larger drive amplitudes, or achieving parametric amplification of the sense response to enhance rate sensitivity without inducing bias rates and quadrature errors.

The proposed general framework is used to determine the electrostatic configurations capable of negating self-induced parametric excitation by generating a separate parametric excitation in antiphase with the self-induced parametric excitation. The proposed implementation has potential to reduce sensor output nonlinearity and is most effective in devices where the drive amplitude dependencies of the drive and sense modes are equal, thus resulting in amplitude-insensitive frequency detuning in a manner similar to linear devices. This implementation can also be used in conjunction with a balancing voltage component to eliminate quadrature errors present in the sensor output caused by linear elastic coupling and nonlinear frequency imbalance. The combination of using parametric pumping and balancing voltage components trims the sensor output and have potential to suppress the sensor output nonlinearity further. The effectiveness of the chosen electrostatic configuration is validated against results from transient finite element studies.

Rate measuring performance is enhanced further by parametrically exciting the sensor output to increase the quality factor of the device. To achieve enhanced performance the parametric excitation must be phase-tuneable and the proposed general framework is used to select electrostatic configurations capable of providing the required parametric excitation. Two approaches to develop the required parametric excitation are investigated. The first approach exploits linear electrostatic forces whilst the second approach uses quadratic electrostatic forces. Both approaches are shown to have potential to improve rate sensitivity through Q factor enhancing effects. However, the parametric excitation from the quadratic electrostatic forces is generally weaker unless compensated using larger parametric pumping voltages. On the other hand, it is found that the quadratic electrostatic forces promote nonlinear frequency balancing and so this approach is considered advantageous for achieving trimmed sensor output.

ACKNOWLEDGEMENT

I would like to express my deepest gratitude to my supervisors, Dr. Stewart McWilliam and Prof. Atanas A. Popov for all the support during the past four years. Dr. McWilliam, thank you very much for your constant guidance and supervision. This whole experience has been truly inspirational, and is one I will never forget.

To my wonderful friends here in Nottingham, thank you very much for being a family for me. I truly appreciate your support all this time and your friendship will always have a special place in my heart.

To my parents and my sister, thank you for always believing in me, and for the constant support and love.

CONTENTS

NOMENCLATURE

u, v	m	Radial and tangential displacements at the ring mid-surface
r	m	Radial position
θ	rad	Angular position
t	s	Elapsed time
X, Y	m	Drive and sense mode displacements
$\dot{}$, $\ddot{}$		Derivatives with respect to time, $\dot{} = d(\ )/dt$, $\ddot{} = d^2(\ )/dt^2$
x^*, y^*	m	Complex drive and sense amplitudes
x, y	m	Drive and sense amplitudes
$\phi_x, \phi_y, \phi_{yx}$	rad	Drive and sense phases, and relative phase $\phi_{yx} = \phi_y - \phi_x$
$\bar{\boldsymbol{y}}$	m	Sense amplitude components vector
T^*		Complex transmissibility amplitude
T		Transmissibility amplitude
ϕ_T		Transmissibility phase
n		Circumferential wave number
R	m	Radius of ring mid-surface
B	m	Out-of-plane height of ring
h	m	Radial thickness of ring
Ω	rad/s	Angular velocity
ρ	kg/m^3	Mean ring material density

$\delta\rho$		Magnitude of $2n\theta$ variation of density, normalised with the mean density ρ
Θ_ρ	rad	Orientation of density $2n\theta$ variation relative to the drive axis
m	kg	Ring mass
E	Pa	Mean elastic modulus of ring material
δE		Magnitude of $2n\theta$ variation of elastic modulus, normalised with the mean elastic modulus E
Θ_E	rad	Orientation of elastic modulus $2n\theta$ variation relative to the drive axis
I	m^4	Second moment of area of ring cross section
$F(\theta,t)$	kgs^{-2}	External radial force per unit arc length
W	kgm^2s^{-2}	Total work done by the external radial force
E_k	kgm^2s^{-2}	Ring kinetic energy
$E_{b,R}, E_{b,K}$	kgm^2s^{-2}	Bending potential energy of ring and support beams
U	kgm^2s^{-2}	Total electrostatic potential energy
$\overline{U}, U_{AC}$	kgm^2s^{-2}	Bias and drive components of electrostatic potential energy
D	kgm^2s^{-3}	Dissipation function
g_0	m	Capacitive gap between electrode and undeflected ring
δ	rad	Electrode span
j		Number of evenly distributed electrodes in the outer/inner electrode sets

ε_0	F/m	Permittivity of free space
V_0	V	Bias voltage
V_{AC}	V	Drive voltage amplitude
V_λ	V	Parametric pumping voltage amplitude
V_Δ	V	Balancing voltage amplitude
i_Δ		Balancing voltage phase index
V_4	V	Drive alignment voltage
Q_0		Nominal quality factor
Γ	rad/s	Linear modal damping coefficient
G_Ω		Non-dimensional gyroscopic coupling coefficient
$\omega_0, \omega_\lambda, \omega_\Delta$	rad/s	Linear resonant frequency with electrostatic contributions from the bias, parametric pumping and balancing voltage components
$\gamma_0, \gamma_\lambda, \gamma_\Delta$	$rad^{\frac{1}{2}}/s^{\frac{1}{2}}$	Modal-mass-normalised cubic single-mode stiffness coefficient contributions from the bias, parametric pumping and balancing voltage components
$\kappa_0, \kappa_\lambda, \kappa_\Delta$	$rad^{\frac{1}{2}}/s^{\frac{1}{2}}$	Modal-mass-normalised cubic coupled-mode stiffness coefficient contributions from the bias, parametric pumping and balancing voltage components
χ	N/kg	Modal-mass-normalised amplitude of harmonic drive force
ω	rad/s	Harmonic drive force frequency
Θ_χ	rad	Drive axis orientation

χ_Δ	ms^{-2}	Modal-mass-normalised amplitude of direct sense force due to balancing voltage
Δ_ω		Structural imperfection magnitude
Θ_ω	rad	Structural imperfection orientation relative to drive axis, i.e. the location of the frequency principal axes
Δ_b		Damping imperfection magnitude
Θ_b	rad	Damping imperfection orientation relative to drive axis, i.e. the location of the damping principal axes
η		Dimensionless back coupling parameter
Ω_{crit}	rad/s	Critical angular rate
f_Ω	N/kg	Modal-mass-normalised Coriolis force
f_Δ	N/kg	Modal-mass-normalised linear elastic coupling force
S	$m/(rad/s)$	Angular rate sensitivity
Ω_z	rad/s	Bias rate
S^V	$V^2/(rad/s)$	Closed-loop rate sensitivity using balancing voltage
Ω_z^V	rad/s	Closed-loop bias rate using balancing voltage
$\bar{\boldsymbol{q}}_1, \bar{\boldsymbol{q}}_2, \bar{\boldsymbol{q}}_3$	m, m^2, m^3	Linear, quadratic and cubic modal coordinates vector
$\bar{\bar{\boldsymbol{\eta}}}_1, \bar{\bar{\boldsymbol{\eta}}}_3$	rad^2/s^2	Coefficient matrices of linear and cubic modal coordinates
$\bar{\bar{\boldsymbol{\eta}}}_\chi$		Quadratic correction factor matrix of direct modal forces
ω_X, ω_Y	rad/s	Drive and sense frequencies
$\bar{\omega}^2$	rad^2/s^2	Frequency detuning

λ_1, λ_2	rad^2/s^2	Parametric excitation components at twice the drive phase and at $\pm\pi/2$ phase shift relative to the drive phase. λ_1 contains the self-induced parametric excitation
$\lambda_{1,r}, \lambda_{2,r}$	rad^2/s^2	λ_1, λ_2 when the drive phase is $\phi_x = -\pi/2$
$\lambda_{1,0}, \lambda_{1,\lambda}, \lambda_{1,\Delta}$	rad^2/s^2	Components of $\lambda_{1,r}$ stemming from the bias voltage (self-induced), parametric pumping voltage and balancing voltage
θ_0	rad	Mean angular position of electrode
V^+, V^-	V	Voltages applied to each outer and inner electrode
c^+, c^-	F	Capacitance of each outer and inner electrode
U^+, U^-	kgm^2s^{-2}	Electrostatic potential energy of each outer and inner electrode
q		Polynomial order of electrostatic potential energy in the modal coordinates X, Y
$\alpha^{\pm}_{q,4p_c}, \beta^{\pm}_{q,4p_c}$, $\alpha^{\pm}_{q,2(2p_c+1)}$, $\beta^{\pm}_{q,2(2p_c+1)}$	F	Capacitance distribution coefficients
m_V		Order of voltage squared variation components from electrode to electrode
$\xi^{\pm}_{m_V}, \zeta^{\pm}_{m_V}$	V^2	Voltage squared distribution components
$f_{m,X}, f_{m,Y}$	N/kg	Modal-mass-normalised mechanical forces on the drive and sense modes
$f_{U,X}, f_{U,Y}$	N/kg	Modal-mass-normalised electrostatic forces on the drive and sense modes

$f_{\lambda 2}$	N/kg	Modal-mass-normalised balancing force amplitude
f_0^l	N/kg	$f_{\lambda 2}$ when parametric excitation component $\lambda_{2,r} = 0$

Other symbols are defined as they appear in the text.

1. RESEARCH BACKGROUND AND SCOPE

1.1. Introduction to CVG's

Gyroscopes are a class of instruments used for measuring angular rates. They were originally devised and named by Léon Foucault in his experiment to measure rotation of the earth [1] and are now used in a wide range of aplications such as millitary and aerospace applications [2]. Traditional gyroscopes are mechanical devices composed of a spinning wheel or disc mounted in gimbal rings. As the disc spins, the precession of the spin axis is used to measure the rotation of the body to which the gyroscope it is attached [3]. The successful operation of these gyroscopes relies heavily on the disc and its rotation. The disc must be balanced to ensure a stable axis and high spin speeds are required to persist for a sufficiently long period.

The reliance on spinning structures presents several challenges. High precision bearings are required to support the high spin speeds. These devices are also susceptible to bearing friction and wear. In addition, they are relatively large and expensive, thus limiting their range of applications [2, 4]. High performance, smaller gyroscopes are in high demand in military applications such as guided missiles and weapons navigation, along with many other emerging applications such as driverless vehicles. The predominant engineering problem lies in the lack of feasible fabrication methods to produce light, miniaturised versions of gimballed wheel gyroscopes without compromising performance. This is because the performances of these devices generally improve with larger angular momentums, thus necessitating larger and heavier spinning structures [4].

These challenges motivated the search for alternatives towards rate sensing. Microfabrication technologies enable the manufacture of rate measuring devices which do not rely on spinning structures to exploit gyroscopic effects for rate sensing, at a miniature scale. The leading mechanical devices used for this purpose are Coriolis vibrating gyroscopes (CVG's). As the name suggests, these devices rely on vibrating elements instead of spinning structures and the Coriolis effect is the core operating principle. The main advantage of this class of gyroscopes lies in its compatibility with state-of-the-art microfabrication techniques, which allow batch production of these devices as Microelectromechanical Systems (MEMS) [2]. In this implementation, the core vibrating element is built on a silicon chip, along with electrical and mechanical components integral for the gyroscope function in a manner similar to integrated circuits. The main functions of the electronic components include driving and regulating the vibration of the element and sensing the vibrational response. CVG's are manufactured from silicon which has good material linearity as is perfectly brittle [2, 5], experiencing no plastic deformation. This leads to excellent mechanical stability and minimal hysteretic losses and

vibrational energy dissipation Also, the compatibility of silicon with batch microfabrication technology allows significant reductions in unit cost, size and weight.

Due to the reduced cost, size and weight of CVG's, these devices feature in a wide range of consumer electronics applications such as image stabilisation in cameras and virtual reality products. The applications of CVG's also include inertial navigation systems (INS) for the aerospace, military and automotive industries [2]. State-of-the-art INS are known to be accurate for short duration usages, but accumulate errors over time [4]. The most accurate systems are typically only found in applications involving long navigation durations, such as submarines and long-range military aircraft. As such, to date, there is still a need to improve the performance of existing commercial CVG's.

CVG's use a wide range of vibrating elements within the core of their constructions. Examples include axisymmetric structures [6-10] such as hemispheres, disks, cylinders, rings and bells, suspended proof masses [2], vibrating strings [4], single vibrating prismatic beams [10, 11] and tuning forks [12, 13]. The present work focuses on the class of gyroscopes of the former type, specifically using rings as the vibrating elements. Ring-based CVG's are mainly classified as capacitive [10], piezoelectric [14] or inductive [15] depending on the operating principle of the device. This research focuses on capacitive CVG's and an example of this device is shown in Figure 1.1, along with the main accompanying elements manufactured on the same chip.

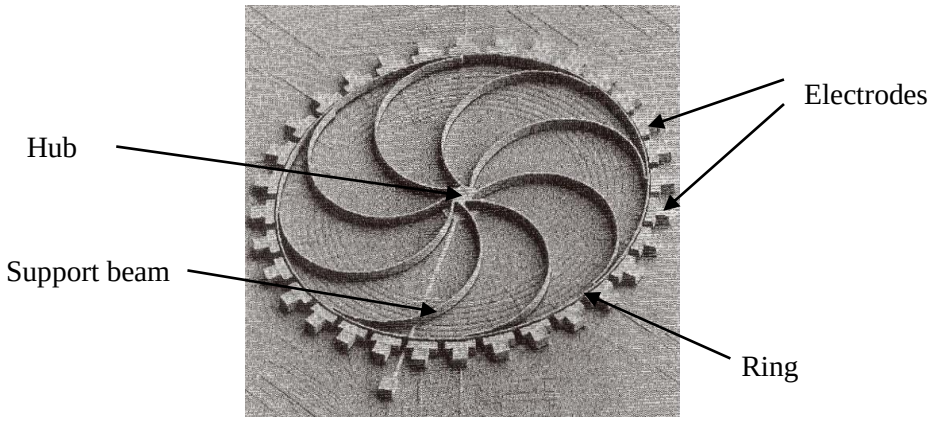

Figure 1.1: Capacitive ring-based CVG [16]

The device consists of a ring supported by 8 semi-circular support beams. The hub anchors the vibrating ring to the device substrate through the support beams, which are also known to provide additional stiffening towards the ring vibration [17]. Evenly spaced electrodes surround the ring, with narrow gaps between the ring and electrodes. Figure 1.1 shows a device implementing 32 evenly-spaced electrodes. However, the use of 8 or 16 electrodes are also

typical [6, 18]. This research mainly focuses on the case of 8 uniformly spaced electrodes. The implementation of 16 or 32 uniformly spaced electrodes is only investigated in specific cases.

The electrodes surrounding the ring are an integral part of the operation of these devices. Within capacitive CVG's, each electrode forms a capacitive pair with the ring, effectively storing charges similar to parallel-plate capacitors. The narrow gaps within each electrode-ring pair are within the order of $0.1 - 10\mu m$. In practice, voltages are applied to the electrodes depending on the function of each electrode. The electrodes are primarily used for biasing, driving the ring into vibration, and sensing the vibration [10, 19], where narrow capacitive gaps are desirable for higher ring vibration sensitivity [2]. The use of capacitive driving and sensing mechanisms has significant advantages over other types of CVG's, primarily due to its compatibility with most microfabrication processes [2]. Other reported advantages include good DC and noise responses, high sensitivity and low temperature sensitivity [20]. These advantages complement the advantages of using axisymmetric structures within CVG's.

Devices using axisymmetric structures like rings report improved robustness against environmental vibrations [17] and temperature insensitivities [9] as the vibration modes used in operation are equally affected. These advantages stem from the 'balanced' state of these structures during vibration owing to the non-moving mass centre. Specifically for rings, the planar construction is well suited to on-chip manufacturing [21]. The operation of ring-based CVG's can be understood by considering the interaction between the ring vibration and the imposed rotation, which is the core operation principle of these devices, and is discussed next.

1.2. Operation principle of CVG's

CVG's fundamentally rely on the Coriolis effect for rate sensing. The Coriolis effect manifests as a fictitious force acting on a moving body within a non-inertial rotating reference frame. An apparent force is generated as a result of the interaction between the body motion (velocity) and the rotation of the frame if the velocity is non-parallel to the frame rotation axis. This force is known as the Coriolis force and is proportional to the in-frame velocity and angular velocity [22]. This is illustrated in Figure 1.2 below, where a mass m moves with a velocity of $\dot{X}$ within a rotating reference frame at angular velocity Ω, generating the Coriolis force F_Ω.

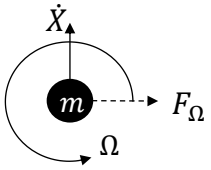

Figure 1.2: Relationship between the angular velocity, in-frame velocity and Coriolis force

The Coriolis force is given by:

$$F_{\Omega} = -2m\Omega\dot{X} \tag{1.1}$$

and acts in a direction perpendicular to the in-frame velocity $\dot{X}$, thus generating motion in this orthogonal direction. The coupling effect of the Coriolis force on mutually orthogonal velocities is an integral feature exploited for rate sensing in CVG's.

1.2.1. Coriolis effect in suspended proof mass CVG's

In CVG's, the Coriolis force serves to couple otherwise orthogonal modes of vibration. The applicability of the Coriolis force in CVG's can be understood by considering a simple CVG that uses a suspended proof mass as the vibrating element. The devices is mounted on a rotating body rotating with angular velocity Ω, and the mass element vibrates in two orthogonal directions within the plane of rotation.

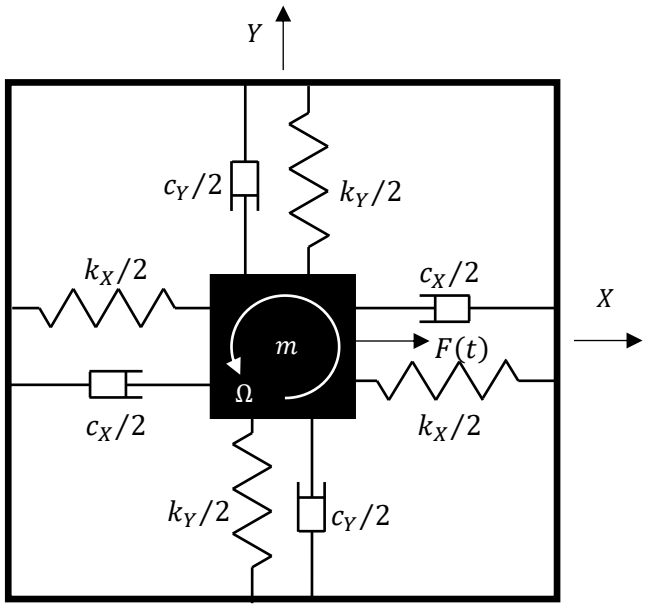

Figure 1.3: Schematic diagram of a CVG implementing a suspended proof mass vibrating element

Figure 1.3 shows a schematic representation of the basic construction of these devices, where the flexible support beams are represented by springs having stiffnesses k_X, k_Y. The support structures provide restoring forces and allow the mass element m to oscillate along the X and Y directions. Viscous dashpots have are included to account for energy dissipation mechanisms within the devices and have damping coefficients c_X, c_Y. For an ideal device, it is advantageous to have $k_X = k_Y$ and $c_X = c_Y$. This is to ensure the Coriolis coupling is maximised and occurs naturally for axisymmetric structures, provided the material and geometry is uniform. However, in practice the presence of manufacturing defects and material

imperfections generally results in $k_X \neq k_Y$ and $c_X \neq c_Y$. The influence of imperfections on the performance of CVG's will be discussed later.

An external harmonic force $F(t)$ is applied to initiate vibration along the X direction. In practice the excitation is chosen so the frequency causes resonance in the X direction. Resonant operation is exploited to yield large amplitude drive vibration. In the presence of angular rate Ω, the resonant drive response generates a Coriolis force in the Y direction, which generates vibration along Y. Throughout this work, X is referred to as the drive mode while Y is referred to as the sense mode, where the modal displacements are detected and used as a measure of the angular rate. In an ideal CVG the Coriolis effect is the only form of coupling between the drive and sense modes which are otherwise mutually orthogonal.

1.2.2. Coriolis effect in ring-based CVG's

In rings, the drive and sense modes are a pair of planar flexural modes [10, 17], distinguished by the order of spatial periodicity or the circumferential wavenumber, which is defined by the number of radial nodes/antinodes n. These modes exhibit sinusoidally varying radial and tangential displacements around the circumference of the ring [23, 24]. Figure 1.4 shows the mode shapes of the 5 lowest order mode pairs ($n = 2,3,4,5,6$).

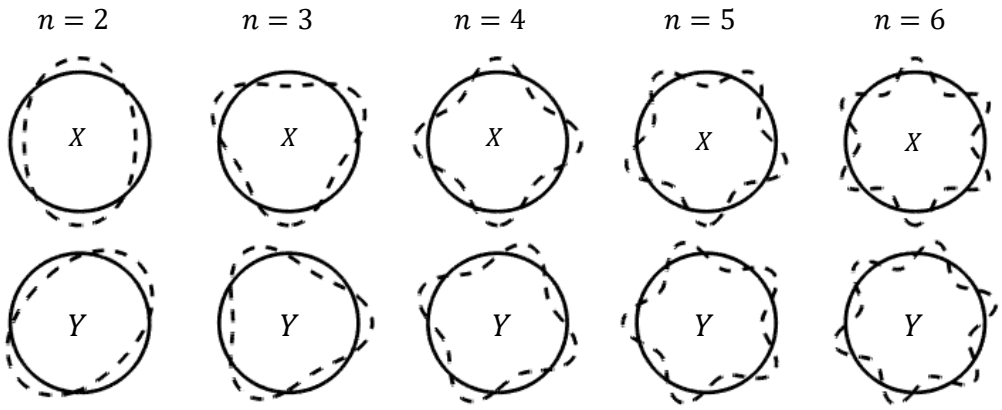

Figure 1.4: Flexural mode shapes for $n = 2, 3, 4, 5, 6$

The modes within each pair are similar. The modes have identical mode shapes and natural frequencies, meaning that the modes are degenerate. For a perfectly axisymmetric shell, the orientation of the mode shapes is indeterminate, that is, there is no preference for the angular positions of the nodes/antinodes. However, an angular separation of $\pi/2n$ defines the mutual orthogonality of the modes within each pair. In practice, the $n = 2$ modes are typically used as the drive and sense modes as this mode pair yields the strongest gyroscopic coupling.

The Coriolis effect in rings can be understood from an observation made by Bryan on the relationship between rotation and vibration of axisymmetric shells [25]. In this experiment, a hemispherical wine glass was struck to vibrate in one of the $n = 2$ flexural modes (the drive mode). When the wine glass is rotated while vibrating, the nodes of the vibrating wine glass do not rotate in unison with the glass. Instead, the 4 nodes lag behind the rotation. The lag of the nodes relative to the rotation of the mass is a direct consequence of the Coriolis force, which causes the participation of the other $n = 2$ mode (the sense mode) in the presence of rotation. The resulting vibration pattern is a superposition of the two $n = 2$ flexural modes, giving rise to the observed lag. To illustrate this, Figure 1.5(a) shows the velocity vectors at the radial antinodes of the drive mode without rotation at the instant when the displacement is maximum. At this instant, the wine glass lip is returning to the undeformed state. Figure 1.5(b) shows the resulting Coriolis force vectors in the presence of rotation and Figure 1.5(c) shows the net velocity vectors.

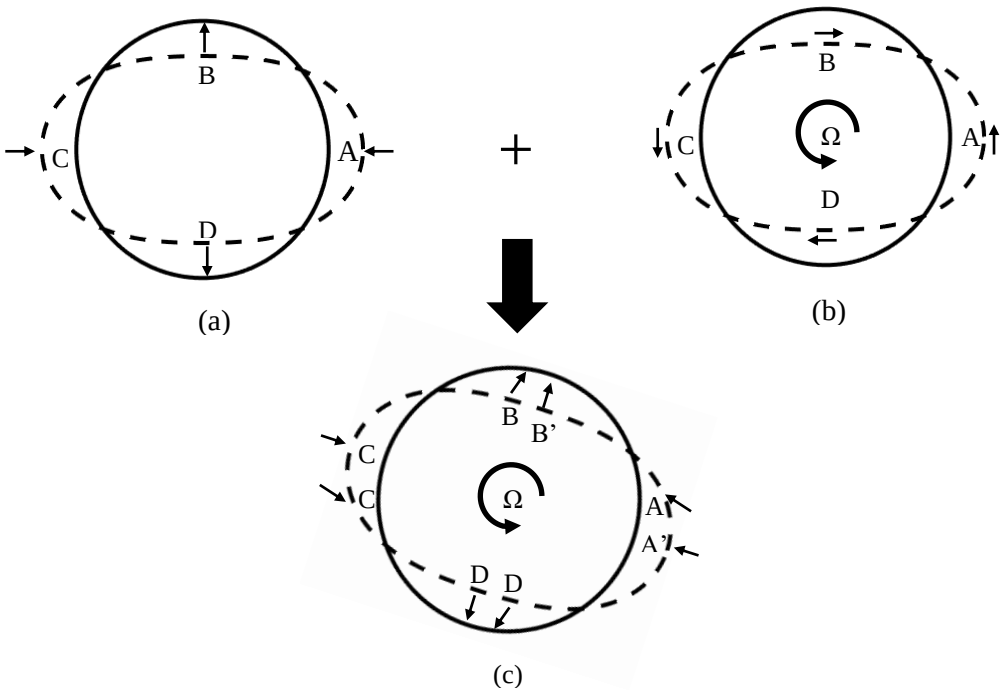

Figure 1.5: Deflection pattern of the wine glass lip at its drive mode (dashed line) showing the direction of the (a) antinodal velocity vectors due to the vibration, (b) rotation-and-vibration induced acceleration vectors, (c) net velocity vectors

In Figure 1.5(a), the radial antinodes A and C move towards the centre, reducing the radial eccentricity. Due to the conservation of angular momentum, this increases the angular velocity at these points, thus inducing a tangential acceleration in the direction of the angular velocity Ω, as shown in Figure 1.5(b). The opposite occurs at B and D. The tangential acceleration in Figure 1.5(b) results in a change in the direction of the velocity vectors, and Figure 1.5(c) shows that the velocities at the antinodes A, B, C, D are no longer completely radial as in

Figure 1.5(a). Radial velocities now occur at points A', B', C', D', which are the new antinode positions, causing the observed vibration pattern lag.

In ring-based CVG's, the drive mode in Figure 1.5(a) is conventionally initiated by applying forces with a 'push-pull' distribution as shown in Figure 1.6.

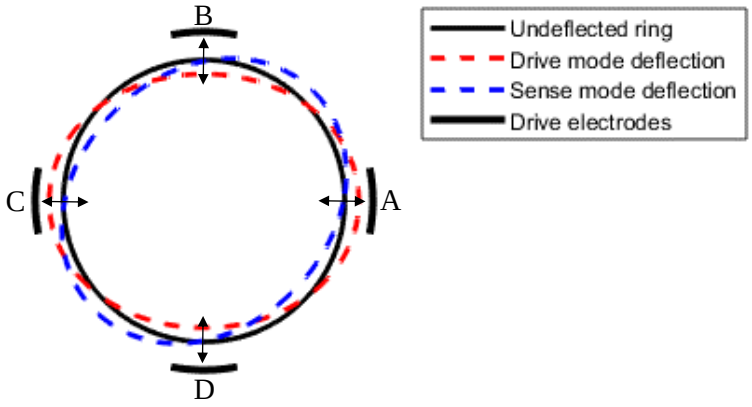

Figure 1.6: 'Push-pull' force distribution from drive electrodes

In practice, harmonic voltages are applied to the drive electrodes and the voltages at electrodes A, C are in antiphase relative to those at B, D. This ensures that electrodes A, C and B, D generate opposite repulsive/attractive forces on the ring during each drive mode oscillation cycle. The drive mode is then regulated at resonance using the phase-locked-loop control [26], ensuring a phase of $-90°$ relative to the voltages. When an angular rate is present, the sense mode responds, and owing to the degeneracy of these modes, both the drive and sense modes can be operated at resonance, in which case it can be shown that the sense mode amplitude y is [10]:

$$y = \frac{G_\Omega \mathrm{Q} x}{\omega} \Omega \tag{1.2}$$

where x is the resonant drive mode amplitude, ω is the resonant frequency, Q is the quality factor, and ω/Q is the modal bandwidth. G_Ω is a gyroscopic coupling constant dictating the portion of the mass m responding to the Coriolis force, and is determined by the geometry of the mass element. G_Ω is given by:

$$G_\Omega = \frac{4n}{n^2 + 1} \tag{1.3}$$

The $n = 2$ flexural modes yield the highest G_Ω compared to the other flexural modes, resulting in a stronger gyroscopic coupling between the mode pair.

From (1.2), the sense mode amplitude is proportional to the angular rate Ω, providing a direct rate measurement. The direct measurement of the mechanical sense response to determine the angular rate measurement is known as open-loop sensing [10]. An alternative approach is to use closed-loop rate sensing, or force-to-rebalance (FTR) [10, 26], whereby an external force is directly applied to the sense mode to nullify the sense response. This force acts to 'rebalance' the sense mode by opposing the Coriolis force and the force amplitude required to achieve this is proportional to the angular rate, and so can be used to measure angular rate. Throughout this dissertation open-loop sensing is the focus and the potential to achieve closed-loop sensing is only investigated in specific cases.

The ratio y/Ω defines the rate sensitivity, also known as the scale factor [27]. A high scale factor is generally desirable for high performance rate sensing, robustness against noise and the ability to detect small angular rates. From (1.2) it can be deduced that the conventional approaches to enhance rate sensitivity are to:

- Increase the drive amplitude
- Increase the Q factor (minimise the damping)

The challenges associated with enhancing rate sensitivity in commercial devices are discussed next.

1.3. Challenges in MEMS CVG's

MEMS CVG's used in inertial sensors are classified based on performance level: inertial-grade, tactical-grade and rate-grade devices [20]. Inertial-grade devices offer the highest performance level while rate-grade devices offer the lowest. With the current technological state, most micromachined vibrating structure gyroscopes, including ring-based CVG's fall short of inertial grade performance [20]. The main reason for this is the small mass of the vibrating element in these micro-scale devices, resulting in small Coriolis forces, as well as the relatively low structural precision of these devices relative to their macro-scale counterparts [28]. This section discusses the main challenges to developing inertial-grade CVG's and focus on damping and imperfections.

1.3.1. Damping

Damping defines the several mechanisms in which energy dissipates from the vibrating element. Linear damping is inversely proportional to the Q factor, which as shown in (1.1) is an important factor dictating the rate sensitivity. A high Q factor also eliminates the need for continuous power consumption of the device due to the suppressed energy dissipation rate [4].

However, the attainable Q factor in CVG's is often limited by a combination of several sources. The dominant sources of damping are structural and viscous damping [2].

Viscous damping stems from ambient pressure. When the ring vibrates in a non-vacuum, the ring surface moves against the surrounding molecules of the vacuum, effectively transferring kinetic energy to the surrounding. This is particularly significant in miniaturised CVG's due to the larger surface-to-volume ratio [29]. The viscous damping in capacitive CVG's is of the squeeze-film type [30], which occurs when the fluid in the gap between the electrodes and the ring is compressed as the ring vibrates. In practice, vacuum packaging is often implemented to minimise viscous damping by suppressing leak rates [2], in conjunction with getters to counteract outgassing from within the device [31]. The implementation of getters prevents the degradation of vacuum over time through constant chemical sorption of active gases. As the pressure within the device is lowered to near vacuum-conditions, the Q factor generally increases until it asymptotically converges to a limiting value. A typical variation of the Q factor with pressure is shown in Figure 1.7.

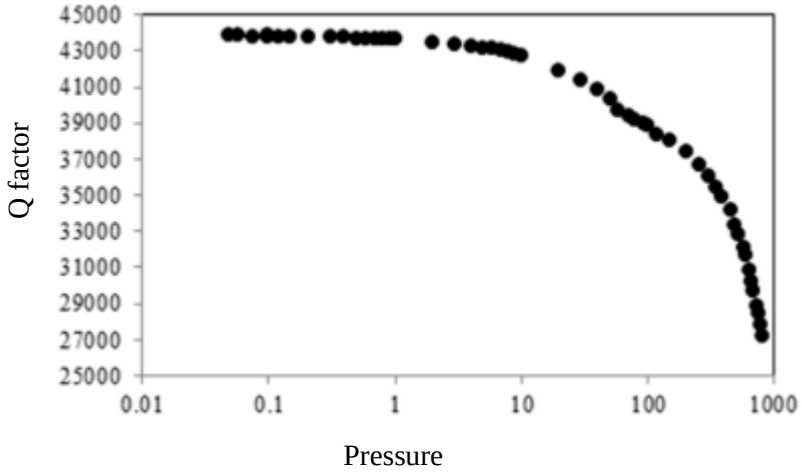

Figure 1.7: Q factor vs pressure plot for MEMS CVG's [29]

The limiting Q factor is determined by other damping mechanisms, mainly thermoelastic damping. It is desirable to evacuate the device sufficiently such that the Q factor of the device is operated within the flat region on the curve shown in Figure 1.7. This stabilises the response of the device by desensitising it to pressure fluctuations [2, 29].

The dominant form of structural damping in low viscous damping operations is thermoelastic damping which is an internal damping mechanism that occurs as a result of energy losses due to elastic deflections. It is in a sense, a form of internal friction that occurs when material particles move relative to each other to create alternating tensile and compressive strains [32, 33]. Areas in tension experience decreased temperature while the opposite occurs for areas in

compression, generating a temperature gradient. This temperature gradient is relaxed through irreversible heat flow from the higher to lower temperature regions. Thermoelastic damping depends on the material and geometry of the structure, and has been reported to limit the Q factor of CVG's to the order of 10^5 [2]. This form of damping is unavoidable as it is a natural result accompanying the flexural vibration of the drive and sense modes of the ring. Also, it has been shown in literature that when thin rings are used, typical of those implemented in MEMS CVG's, thermoelastic damping is suppressed only at larger diameters [34]. As such, the default geometry of the rings typically used in highly miniaturised MEMS CVG's is particularly susceptible to thermoelastic damping.

Thermoelastic damping is minimised in practice through the use of high quality factor materials such as silicon, germanium or quartz [35] in the vibrating structures. The introduction of hollow slots into the cross-section of the vibrating structure has also shown potential to increase the Q factor by disrupting the heat flow [34]. This approach is most effective for lower Q factor systems.

1.3.2. Imperfect rotational symmetry

In perfectly axisymmetric rings, the modes are degenerate. This enables resonant operation to be achieved simultaneously by both the drive and sense modes, and ensures the sense amplitude is given by (1.1). However, in practice manufacturing and materials imperfections can break the rotational symmetry of the ring and significantly modify the drive and sense mode dynamics. These imperfections arise from surface irregularities, inhomogenous materials, geometric variations, material anisotropy, and manufacturing processes [36]. These effects result in inhomogeneous mass, damping and stiffness distributions.

The mass and stiffness distributions around the ring directly affect the flexural mode pairs in two ways. Firstly, the modes in each pair are no longer degenerate, meaning the drive and sense mode natural frequencies are unequal and split [36-41]. Secondly, the orientation of the modes is no longer indeterminate [42]. Instead, the modes have 'preferred' orientations depending on the mass and stiffness distributions [40]. The angular orientation of the modes is known as the mode angle or the frequency principal axes, and the fixing of the mode angle generally results in misalignment between the antinodes of the modes and the drive axis [38, 43]. Figure 1.8 shows the drive and sense modes for an imperfect resonator. For the perfect resonator the drive mode can be considered as being aligned with the drive electrode axis because the modes are degenerate. However, for the imperfect case the drive and sense modes are fixed because they are determined by the mass and stiffness distribution asymmetries. The + and – symbols on the figure indicate the locations around the ring circumference, spaced $\pi/4$ apart, corresponding to axes of maximum and minimum stiffness-to-mass ratios

respectively. The antinodes of mode X' align at the angular positions marked with the + symbols while those of mode Y' align at the angular positions marked with the – symbols.

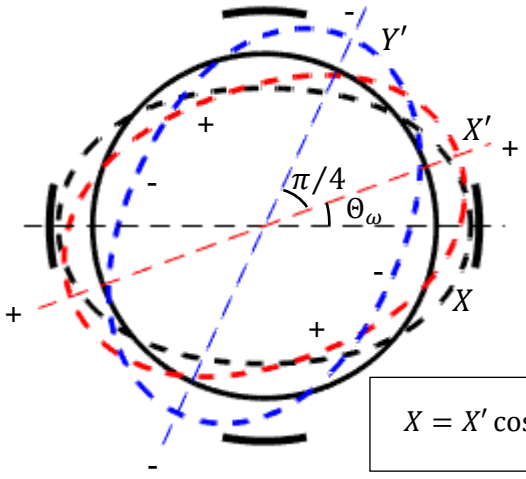

Figure 1.8: Orientation of the $n = 2$ modes (X',Y') relative to the driven deflected shape X in an imperfect ring

In Figure 1.8, due to the ring modes being fixed the modes are generally misaligned from the drive deflection shape X, where Θ_ω defines the misalignment angle. In this case, $X = X' \cos 2\Theta_\omega - Y' \sin 2\Theta_\omega$ so the driven deflection includes contributions from both ring modes. This gives rise to an undesirable elastic coupling that interferes with the Coriolis force coupling. In ideal rings, the ring exhibits equal tendency to vibrate in all orientations, thus ensuring that this elastic coupling does not occur. The combined effects of the frequency split and drive misalignment are known to degrade rate sensing performance in three ways [26]. Firstly, the scale factor is reduced. Secondly, the sense amplitude does not nullify when angular rate is absent, but responds with a systematic offset known as bias or zero-rate error. Thirdly, the phase of the sense mode shifts giving rise to a quadrature error.

A wide variety of techniques have been reported in the literature to compensate for these effects, and these mainly rely on the introduction of artificial imperfections to negate existing physical imperfections. One such method is electrostatic tuning of the modes, which takes advantage of the negative spring stiffness effect of an electrode [44, 45]. In these studies, appropriate activation of electrodes has been investigated to nullify the linear elastic coupling and generate unequal electrostatic restoring forces on the drive and sense modes, aimed at reducing or eliminating the frequency split. The electrostatic method is advantageous as it can be implemented post-fabrication, as it requires no structural modifications. Alternatively, mechanical trimming procedures have also been reported [46, 47] and involves using selectively-positioned mass removal on the neutral axis to increase one of the modal

frequencies. To achieve trimming, mass removal is targeted at an antinode of the low frequency mode.

Damping asymmetry is another form of imperfection and is attributed to uneven energy dissipation around the ring, colloquially known as anisodamping. Viscous damping can contribute to anisodamping through hydrodynamic lift effects, also known as the surfboard effect [12]. The surfboard effect occurs when sliding motion along one direction over a viscous medium generates a hydrodynamic lift force in the orthogonal direction. In this way, the velocity of the drive mode exerts a force on the sense mode and vice versa. Damping asymmetries are known to interfere with angular rate measurements by generating forces in phase/antiphase with the Coriolis force [26]. As such, the contributions from the Coriolis effect and damping asymmetry cannot be distinguished. Trimming techniques to reduce or eliminate damping asymmetry have been reported in the literature. Reference [14] uses piezoelectric elements to trim the damping. Piezoelectric elements of different lengths are placed at multiple angular positions around the ring and used to modify the Q factors of the drive and sense modes unequally to nullify any Q factor difference between the drive and sense modes.

Devices with high Q factors are known to be more susceptible to the performance degrading effects of imperfections [2] and for this reason it is essential to reduce the effects of imperfection as devices are developed with increasingly large Q factors.

1.4. Electrostatic nonlinearities

Nonlinear dynamics in ring-based CVG's occur as a result of large amplitude oscillations of the ring [48, 49]. As such, conventional operation of these devices often involve sufficiently small, linear displacements about the equilibrium to avoid the potential effects of such nonlinearities on the system response. To enhance rate sensitivity, (1.1) indicates a large drive mode amplitude is advantageous, and so it is imperative to take nonlinearities into account when analysing sensing performance as drive amplitude increases.

The sources of nonlinearities in CVG's are vast, some of which are reported in [15]. Of these sources electrostatic nonlinearities are well known as being dominant [49] and for this reason electrostatic nonlinearity is the central focus of the present research. Electrostatic nonlinearities arise due to the nonlinear relationship between force and displacement in capacitive electrodes [2, 21]. The strength of electrostatic nonlinearities in ring-based CVG's depends on the proximity of the ring to the electrode and increases significantly as the capacitive gaps reduce due to the increased capacitance. Since capacitive CVG's are micro-scale devices with very narrow capacitive gaps, electrostatic nonlinearities typically arise at

much lower amplitudes of vibration than other forms of nonlinearity. The presence of electrostatic nonlinearities provides a clear explanation of the deviation of the ring dynamics from linear behaviour even at relatively low amplitudes of flexural vibration, well below the ring radial thickness [15]. In one theoretical study on a practical device, the electrostatic nonlinearities have been shown to dominate the mechanical nonlinearities by an order of 10^4 [49]. The electrostatic nonlinearity also strengthens when larger voltages are applied across the electrodes.

Electrostatic nonlinearities introduces nonlinear coupling between the drive and sense modes, thus resulting in the drive mode affecting the sense response through other means asides from the Coriolis force even in perfect devices [49]. The dominant effect of the electrostatic-induced nonlinear coupling is the ability of the ring to self-energise through self-induced parametric excitation [48-50]. This differs from external excitation as it does not arise from direct forcing of the mass. Instead, it appears as a time variation of one or more of the system parameters, typically the stiffness, at twice the drive frequency. Self-induced parametric excitation occurs when the drive mode is forced into sufficiently large vibrations, resulting in a nonlinear elastic coupling between the drive and sense modes. This form of parametric excitation is self-induced and passively relies on the drive mode displacement to modulate the sense mode stiffness. The presence of self-induced parametric excitation modifies the modal response to the Coriolis force, such that the scale factor does not increase linearly with the drive amplitude [48], unlike a linear device as shown in (1.1).

Parametric amplification is the specific use of parametric excitation to amplify the mechanical response, hence the scale factor. The electrostatic forces in capacitive CVG's can be used for this purpose [51, 52], achieved through the deliberate introduction of harmonic parametric pumping voltages to modulate the modal stiffness. In rings, parametric amplification is applied on the drive and sense modes to complement the harmonic drive force and Coriolis force respectively [28]. Parametric amplification has been reported as a Q factor enhancing method independent of bandwidth as it can suppress energy dissipation [53], thus offering rate sensitivity enhancement potential regardless of damping. The effect of parametric amplification is most significant when parametric instability is approached, where the damping-induced energy dissipation is near completely negated by the parametric excitation. Unstable vibrations are not the focus of this thesis so this is not discussed further. However, the instability threshold is of particular interest for maximising parametric amplification. Parametric amplification is known to be phase-sensitive and the application of parametric amplification in disk resonator gyroscopes [54] showed that phase conditions exist where parametric excitation can either amplify or attenuate the sense response. The phase is used to amplify the Coriolis force while attenuating the quadrature error. Another study on rings

achieved scale factor amplification by imposing a double-frequency voltage component on the sense electrodes [52]. In these studies and the majority of other studies investigating the deliberate use of parametric excitation for response amplification [18], the sense mode is generally treated as a linear system. Nonlinearities have been avoided by keeping oscillation amplitudes relatively small, with the main aim of using parametric amplification to reduce the drive voltage required to attain a particular amplitude. This limits the attainable linear amplification of the Coriolis force from large drive amplitude operations.

Past studies involving investigating parametric amplification in the presence of nonlinearities mainly focus on restricted forms of nonlinearities, typically the Duffing nonlinearity. The study in [55] implements parametric amplification in a 2-DOF microgyroscope in the presence of Duffing nonlinearities to amplify mechanical displacements at non-resonant operations, thus improving the bandwidth. A study on a simple lumped-mass model [56] shows that the Duffing nonlinearity diminishes the attainable gain from parametric excitation compared to the case where the parametric excitation is applied to a linear system. Due to the limited scope of the nonlinearities investigated, there is still a need to address the effects of the general form of nonlinearities on parametric amplification and the potential for leveraging such nonlinearities for this purpose. The combination of parametric amplification of the sense response and linear amplification of the Coriolis force due to large, nonlinear amplitude vibrations is appealing for significant scale factor enhancement.

Electrostatic nonlinearities are commonly perceived as a hindrance towards enhanced scale factor at larger vibration amplitudes for CVGs [15]. However in contrast to this the present research focuses on using electrostatic nonlinearities as a way to enhance rate sensing performance.

1.5. Aims and objectives

The research is motivated by the challenge to develop miniaturised high performance ring-based CVG's As devices are miniaturised, electrostatic nonlinearities becomes increasingly important and to enhance rate sensitivity there is a need to re-consider the notion of avoiding electrostatic nonlinearities at larger amplitude vibrations of the ring. The present research aims to provide useful insight into the potential exploitation of electrostatic nonlinearities to improve open-loop rate sensing performance of devices, thus addressing the common perception of treating electrostatic nonlinearities as an undesirable feature. The main investigation steps to achieve this aim are:

- Develop a linear mathematical model describing the dynamics of a ring with mass, stiffness and damping imperfections. The analysis of the dynamics serves to introduce

the main concepts and is used to develop methods to identify ring imperfection parameters such as the mode angles. The effects of these identified imperfections on rate sensing performance in terms of the quadrature error, bias rate and rate sensitivity are of principal interest.

- Extend the linear mathematical model to include nonlinear electrostatic effects. It is necessary for the model to encapsulate the capacitive forcing generated by the electrodes on the ring and the nonlinear relationship between the electrostatic forces and the ring displacement must be modelled accurately. It is essential that this is first modelled so as to understand the basic operation of these devices.
- Determine the key features of electrostatic nonlinearity that affect rate sensing performance under basic operation and make comparisons against the expected behaviour of a corresponding linear, ideal device. To achieve this, a clear link must be established between the nonlinear electrostatic forces, the resulting fundamental effects such as self-induced parametric excitation, and the sense mode response. The nonlinear modifications on the rate sensitivity, bias rate and quadrature error will be of particular interest.
- Address the key nonlinear electrostatic effects and investigate the strategic use of the voltages and electrodes to improve device performance in the areas of trimming, linearisation and parametric amplification. To achieve this, it is necessary to consider the specific interaction between the mechanical forces, especially the Coriolis force, and the linear and nonlinear electrostatic forces, and appropriate modifications of the electrostatic force to replicate the state of a standard linear and ideal device. Similarly, it is also of interest to replicate the force state of a high quality factor device.
- Provide a general framework for goal-based selections of voltages and electrodes and make practical recommendations for the implementation of the electrostatics during device operation.

Finite element (FE) results will also be used to validate key findings predicted by the mathematical models.

1.6. Thesis outline

The proceeding parts of this dissertation are organised into chapters as described below:

- Chapter 2 provides an introduction to modelling the linear dynamics of ring-based CVG's. A model is developed to analyse and predict the flexural vibration of a ring resonator in the presence of rotation and structural and damping imperfections. Linear equations of motion are developed for a harmonically forced, imperfect, rotating ring, which are used to investigate the linear modal dynamics. The linear dynamics without

rotation are first considered to investigate practical measurement methods for identifying the imperfection parameters. The effects of rotation are then included to quantify the rate sensing performance in terms of the rate sensitivity, bias rate and quadrature error. The effects of imperfections and back coupling on device operation and rate sensing performance are investigated and conditions where back coupling effects are negligible are identified.

- Chapter 3 extends the linear model developed in chapter 2 to account for electrostatic nonlinearities. A basic electrostatic configuration involving 8 evenly spaced electrodes with bias and drive voltage components is considered. The electrostatic potential energy is derived to identify the resulting electrostatic forces contributing to the equations of motion. The effects of the electrostatic nonlinearities, such as self-induced parametric excitation, on the rate sensitivity, bias rate and quadrature error are then identified for the cases of perfect and imperfect rings. The conditions where the electrostatic nonlinearities trim the sensor output or enhance the rate sensitivity are investigated.
- Chapter 4 deals with the linearisation and trimming of the device output. This chapter is organised into two parts. The first part deals with negating the self-induced parametric excitation identified in Chapter 3. A modification of the voltage distribution between the electrodes is considered to counteract the self-induced parametric excitation. The equations of motion are developed for the updated electrostatic configuration. The resulting sense dynamics are analysed to identify the voltage conditions for negating the self-induced parametric excitation. The effects of negating the self-induced parametric excitation and the conditions for potential frequency matching of the drive and sense modes are then investigated. The second part of the chapter deals with restoring the output of a device which is both linear and trimmed in the presence of electrostatic nonlinearities. The electrostatic force arising from each electrode is generalised to provide a framework for the strategic selection of voltages and electrode number to tailor the electrostatic forces for specific aims, such as sensor output linearisation and trimming for this chapter. The balance of the forces on the sense mode is considered to identify the required form of the electrostatic forces to nullify the quadrature output and linearise and trim the rate output, based on which the proposed framework is used to identify a suitable electrostatic configuration. The effectiveness of the implementation of the updated electrostatic configuration to linearise and trim the sense response is assessed through comparisons with the case of without addressing the balance of the sense mode forces. The potential of using the chosen electrostatic configuration for closed-loop rate sensing is also investigated.

- Chapter 5 focuses on using electrostatic forces to yield parametric amplification effects on the rate output, while maintaining trimmed bias rates and quadrature errors. Approaches involving the use of linear and quadratic order electrostatic forces are considered for this purpose. Similar to Chapter 4, the balance of the forces on the sense mode is considered to identify suitable forms of the required electrostatic forces to achieve trimmed parametric amplification. Based on the identified form of the electrostatic forces required, the framework proposed in Chapter 4 is used to identify suitable voltage distributions and arrangement of electrodes to generate the required parametric excitation using linear or quadratic electrostatic forces. For both approaches, the equations of motion are developed to analyse the sense dynamics, based on which the conditions required to achieve rate output trimming and parametric amplification are identified. The use of linear and quadratic electrostatic forces are then compared and comments are made on the advantages and disadvantages of these approaches.
- Chapter 6 summarises the present research, drawing on the main conclusions essential for enhancement of device performance. Based on the outcome of this research, remaining open research questions are used for future work suggestions.

2. LINEAR DYNAMICS OF RING-BASED RESONATORS IN CVG'S: CHARACTERISING MECHANICAL IMPERFECTIONS

2.1. Introduction

This chapter develops a basic linear model to describe the dynamic behaviour of an imperfect, unsupported rotating ring resonator used in CVG's. The model incorporates the presence of general structural and damping imperfections in the ring and is used to develop expressions for the drive and sense responses when the ring is subjected to harmonic excitation. The model is used as a basis for identifying and characterising the magnitude and spatial distribution of structural and damping imperfections, and quantifying the effects of these imperfections on angular rate sensing performance.

The chapter is organised as follows: Section 2.2 describes the linear modelling approach used to describe the rotating ring dynamics and determines the equations of motions characterising the drive and sense responses when operated as a CVG. The mechanical energy expressions are derived for planar flexural vibrations of the ring, which are then used in Lagrange's equations to develop the linear equations of motion. In the model structural and damping imperfections are included by considering inhomogeneities of the density, elastic modulus and damping distribution. In Section 2.3, the equations of motion developed in Section 2.2 are used to determine the ring response under harmonic excitation and develop practical methods for identifying and characterising imperfections, which are unknown in practice. The magnitudes and principal orientations of the structural and damping imperfections are identified using measurements of the modal frequency, bandwidth, amplitude and phase by considering variations of the harmonic excitation orientation. In Section 2.4, the effects of angular rate are analysed to quantify the effects of imperfection and back coupling in the context of angular rate measurements. These effects are investigated by assessing the rate sensing performance in terms of the rate sensitivity and bias rate, and compared between the cases of with and without back coupling. Section 2.5 provides a summary of the main contributions from the chapter.

2.2. Linear mathematical model of the ring modal dynamics

In this section, a simplified mathematical model is developed to describe and determine the equations of motion describing the flexural vibration response of an imperfect, unsupported rotating ring resonator. The model accounts for structural and damping imperfections by considering circumferential variations of the density, elastic modulus and damping

distributions. Based on this, mechanical energy expressions are developed for the ring to be incorporated into Lagrange's equations to develop the linear equations of motion.

2.2.1. Ring description and modes

Figure 2.1 shows the displacement field (u, v, w) characterising the kinematics of a ring having radius R, radial thickness H and axial length B. u, v and w are the displacement components of the ring within the $Oe_1e_2e_3$ coordinate system, parallel to the Oe_1, Oe_2 and Oe_3 axes respectively. The $Oe_1e_2e_3$ coordinate system is a non-inertial frame that rotating with the ring at angular velocity Ω. The ring rotates with angular velocity Ω about the out-of-plane polar axis Oe_3 is the polar axis of the ring. In the plane of the ring, (r, θ) is a pair of polar coordinates in the radial and circumferential directions, where $\theta = 0$ is fixed to a reference position aligned with the ring drive axis.

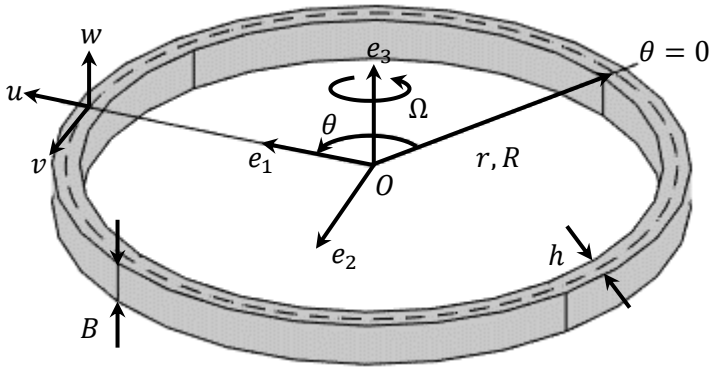

Figure 2.1: Dimensions and coordinate system of a ring rotating at angular velocity Ω

The vibration of the ring is expressed in terms of displacements u, v and w, and for a typical single axis CVG the in-plane vibration response ($w = 0$) used to measure angular velocity Ω is expressed in terms of the radial and tangential displacements u and v respectively.

Due to the spatial periodicity of the ring, the radial and tangential displacements of the ring must satisfy the boundary condition $u|_{\theta=0} = u|_{\theta=2\pi}$ and $v|_{\theta=0} = v|_{\theta=2\pi}$. It can be shown that the radial and tangential displacements for a ring vibrating in its $n\theta$ modes can be expressed as [24]:

$$u(\theta, t) = X(t)\cos n\theta + Y(t)\sin n\theta \tag{2.1}$$

$$v(\theta, t) = \frac{Y(t)}{n}\cos n\theta - \frac{X(t)}{n}\sin n\theta \tag{2.2}$$

For a perfectly axisymmetric ring, the (X, Y) pair describe degenerate modes possessing the same natural frequencies and indeterminate mode shapes separated by $\pi/2n$. For practical CVG's the $n = 2$ pair of modes is commonly employed but the notation n will be maintained throughout this chapter, as such X describes the radial displacement of the $n\theta$ drive mode and Y describes the radial displacement of the $n\theta$ sense mode.

The linear relationship between the displacement field (u, v) and modal displacements (X, Y) is based on the assumption that the ring displacement is small. The ring is also radially thin such that the radial and tangential displacements only vary circumferentially. The radial and tangential displacements are related such that $u = -\partial v/\partial\theta$ as the ring mid-surface is regarded to be inextensional. Shear deformation and tangential inertia are also neglected.

2.2.2. Mechanical energy expressions

An energy-based approach is employed to derive the equations of motion of the vibrating ring. In this section, expressions for the kinetic and potential energies of the ring are derived, together with expressions for the dissipation function and external work done. The expressions developed include the effects of structural and damping imperfections which are included by modelling the material properties as being inhomogeneous. The resulting expressions are used in Lagrange's equation [57] to obtain the equations of motion.

Kinetic energy of imperfect rotating ring

The kinetic energy of an imperfect rotating ring is given by:

$$E_K = \frac{1}{2} Bh \int_0^{2\pi} \rho(\theta) \left| \frac{d\underline{\boldsymbol{r}}}{dt} \right|^2 R d\theta \tag{2.3}$$

where $\rho(\theta)$ and $d\underline{\boldsymbol{r}}/dt$ are the material density and absolute velocity vector at location θ respectively.

The absolute velocity includes contributions from the rigid body rotation and vibration of the ring. Noting from Figure 2.1 that the position vector of a point on the ring in the non-inertial frame $Oe_1e_2e_3$ is $\underline{\boldsymbol{r}} = (r + u, v, 0)$ where r is a coordinate defining the radial position, and the ring and frame rotate with angular velocity vector $\underline{\boldsymbol{\Omega}} = (0, 0, \Omega)$, the components of the absolute velocity can be expressed in vector notation as:

$$\frac{d\underline{\boldsymbol{r}}}{dt} = \frac{\partial \underline{\boldsymbol{r}}}{\partial t} + \underline{\boldsymbol{\Omega}} \times \underline{\boldsymbol{r}} = \begin{pmatrix} \dot{u} - v\Omega \\ \dot{v} + (r + u)\Omega \\ 0 \end{pmatrix} \tag{2.4}$$

where the single overdot $\dot{(\ )}$ represents differentiation with respect to time. Using (2.1) and (2.2), the absolute velocity components can be expressed in terms of the modal displacements and velocities. The absolute velocity can then be expressed as the resultant of these components.

The material density around the ring circumference is expressed as a Fourier series expansion:

$$\rho(\theta) = \rho\left[1 + \sum_{\sigma=1}^{\infty} \delta\rho_\sigma \cos\sigma\left(\theta - \Theta_{\rho,\sigma}\right)\right] \tag{2.5}$$

where $\delta\rho_\sigma$ and $\Theta_{\rho,\sigma}$ define the magnitude and orientation (relative to the drive axis) of the σ'th Fourier component. In the absence of imperfections, the density is invariant around the circumference and $\delta\rho_\sigma = 0$.

Using (2.4) and (2.5) in (2.3) it can be shown that the ring kinetic energy E_k can be expressed as:

$$E_k = \int_0^{2\pi} \Delta E_k = E_{k1} + E_{k2} + E_{k3} \tag{2.6}$$

$$E_{k1} = \frac{m}{2}\left(\frac{n^2+1}{2n^2}\right)\left[\left(1 + \frac{n^2-1}{2n^2+2}\delta\rho\cos 2n\Theta_\rho\right)\dot{X}^2 + \left(1 - \frac{n^2-1}{2n^2+2}\delta\rho\cos 2n\Theta_\rho\right)\dot{Y}^2 + \frac{n^2-1}{n^2+1}\delta\rho\sin 2n\Theta_\rho\,\dot{X}\dot{Y}\right] \tag{2.7a}$$

$$E_{k2} = \frac{m\Omega}{n}\left(X\dot{Y} - \dot{X}Y + \delta\rho_n\cos n\Theta_{\rho,n}\frac{R\dot{Y}}{2} - \delta\rho_n\sin n\Theta_{\rho,n}\frac{R\dot{X}}{2}\right) \tag{2.7b}$$

$$E_{k3} = \frac{m\Omega^2}{2}\left\{R\left(R + \delta\rho_n\cos n\Theta_{\rho,n}X + \delta\rho_n\sin n\Theta_{\rho,n}Y\right) + \frac{n^2+1}{2n^2}\left[\left(1 + \frac{n^2-1}{2n^2+2}\delta\rho\cos 2n\Theta_\rho\right)X^2 + \left(1 - \frac{n^2-1}{2n^2+2}\delta\rho\cos 2n\Theta_\rho\right)Y^2 + \frac{n^2-1}{n^2+1}\delta\rho\sin 2n\Theta_\rho\,XY\right]\right\} \tag{2.7c}$$

In these equations $m = 2\rho\pi RhB$ is the mass of the ring, and $\delta\rho = \delta\rho_{2n}$ and $\Theta_\rho = \Theta_{\rho,2n}$ are the magnitude and orientation angle of the $2n\theta$ circumferential variation of the density in (2.5). As will be shown, the $2n\theta$ variation component is the dominant term in (2.5) contributing to the equations of motion.

E_{k1} represents the portion of the kinetic energy independent of angular rate. When the mass is homogeneous, the coefficients associated with $\dot{X}^2$ and $\dot{Y}^2$ are equal and the coefficient associated with $\dot{X}\dot{Y}$ vanishes.

E_{k2} represents the portion of the kinetic energy contributing to the Coriolis force which is proportional to Ω. The magnitude of this term is inversely proportional to mode order n indicates that selecting a small n value (e.g. $n = 2$) maximises the Coriolis force.

E_{k3} represents the portion of the kinetic energy contributing to the centripetal force which is proportional to Ω^2. In practice, the angular rate to be measured is orders of magnitude lower than the natural frequency of the mode pair (a ratio of 10^{-4} is typical) and for this reason this contribution is often neglected. This simplification is used in the remainder of this study.

It is clear from a physical perspective that circumferential density variations break the cyclic symmetry of the ring mass distribution for a perfect ring, and the equations indicate the dominant symmetry breaking effect is associated with the $2n$'th component of density variation. This cyclic symmetry breaking is studied in detail in Appendix A. It is also interesting to note that the n'th component of density variation also contributes to the total kinetic energy through terms proportional to $\delta\rho_n \cos n\Theta_{\rho,n}$ and $\delta\rho_n \sin n\Theta_{\rho,n}$, appearing in (2.7b) and (2.7c). However, it is shown in Appendix A that this component makes negligible contribution to the resulting equations of motion.

Ring bending potential energy

The bending potential energy of the ring is given by [24]:

$$E_{b,R} = \frac{I}{2}\int_0^{2\pi} E(\theta)\left(\frac{\partial^2 u}{R^2\partial\theta^2} + \frac{u}{R^2}\right)^2 Rd\theta \tag{2.8}$$

where $E(\theta)$ is the elastic modulus at location θ. Similar to the density variations considered earlier the elastic modulus around the ring circumference is expressed as a Fourier series expansion:

$$E(\theta) = E\left[1 + \sum_{\sigma=1}^{\infty} \delta E_\sigma \cos\sigma(\theta - \Theta_{E.\sigma})\right] \tag{2.9}$$

where E is the mean elastic modulus, and δE_σ and $\Theta_{E,\sigma}$ define magnitude and orientation (relative to the drive axis) of the σ'th Fourier component. In the absence of imperfections, the elastic modules is invariant around the circumference and $\delta E_\sigma = 0$.

Using equations (2.1) and (2.9) in equation (2.8) it can be shown that the ring bending strain energy $E_{b,R}$ can be expressed as:

$$E_{b,R} = \frac{EI\pi(n^2-1)^2}{2R^3}\left[\left(1+\frac{\delta E}{2}\cos 2n\Theta_E\right)X^2 + \left(1-\frac{\delta E}{2}\cos 2n\Theta_E\right)Y^2 + \delta E \sin 2n\Theta_E\, XY\right] \tag{2.10}$$

where $I = Bh^3/12$ is the second moment of area with respect to a principal axis parallel to the polar axis of the ring, and $\delta E = \delta E_{2n}$ and $\Theta_E = \Theta_{E,2n}$ are the magnitude and orientation angle of the $2n\theta$'th circumferential variation of the elastic modulus in (2.9). Similar to the kinetic energy result earlier only the $2n\theta$ variation participates in the bending potential energy.

Ring dissipation function

The ring dissipation function is based on viscous frictional forces summed over all particles of the system [57] and is expressed as follows:

$$D = \int_0^{2\pi} \left(\frac{1}{2}c(\theta)\dot{u}^2 + \frac{1}{2}c(\theta)\dot{v}^2\right)Rd\theta \tag{2.11}$$

where $c(\theta)$ is an arc-length-normalised damping coefficient applied in the radial and tangential directions. It is used to define damping variations around the ring circumference, and similar to density and elastic modulus variations earlier, the damping coefficient is expressed as a Fourier series expansion, such that:

$$c(\theta) = c\left[1 + \sum_{\sigma=1}^{\infty} \delta c_\sigma \cos\sigma\left(\theta - \Theta_{c,\sigma}\right)\right] \tag{2.12}$$

where δc_σ and $\Theta_{c,\sigma}$ define magnitude and orientation (relative to the drive axis) of the σ'th Fourier component. In the absence of imperfections, the damping coefficient is invariant around the circumference and $\delta c_\sigma = 0$.

Using equations (2.1), (2.2) and (2.12) in equation (2.11) it can be shown that the ring dissipation function can be expressed as:

$$D = \frac{c\pi R}{2n^2}(n^2+1)\left[\left(1+\frac{\delta c}{2}\cos 2n\Theta_c\right)\dot{X}^2 + \delta c \sin 2n\Theta_c\, \dot{X}\dot{Y} + \left(1-\frac{\delta c}{2}\cos 2n\Theta_c\right)\dot{Y}^2\right] \tag{2.13}$$

where $\frac{c\pi R}{n^2}(n^2+1)$ is the mean damping coefficient, and $\delta c = \delta c_{2n}$ and $\Theta_c = \Theta_{c,2n}$ are the magnitude and orientation of the $2n\theta$ circumferential variation of the damping in (2.12). Similar to the kinetic and ring bending potential energy results earlier only the $2n\theta$ variation participates in the dissipation function.

Work done due to external excitation

To model the external drive force applied to the ring a distributed radial force (per unit arc length) is applied which has the same circumferential variation as the drive mode. i.e.

$$F(\theta, t) = f(t)\cos n\theta$$

The work done by this radial force is given by:

$$W = \int_0^{2\pi} F(\theta, t) u R d\theta = f(t)\pi R X \tag{2.14}$$

In practice, $f(t)$ is harmonic with a frequency regulated in the vicinity of the natural frequencies of the drive and sense mode pair to achieve resonant operation.

2.2.3. Equations of motion

Having determined the expressions for the kinetic energy from (2.6) – (2.7c), bending potential energy from (2.10), Rayleigh's dissipation function from (2.13) and the work done by the electrostatic drive force from (2.14), the equations of motion describing the drive and sense mode dynamics are obtained using Lagrange's equation.

Lagrange's equations for the drive and sense modes are given by:

$$\frac{\partial}{\partial t}\left(\frac{\partial E_k}{\partial \dot{X}}\right) - \frac{\partial E_k}{\partial X} + \frac{\partial E_{b,R}}{\partial X} = \frac{\partial W}{\partial X} - \frac{\partial D}{\partial \dot{X}} \tag{2.15a}$$

$$\frac{\partial}{\partial t}\left(\frac{\partial E_k}{\partial \dot{Y}}\right) - \frac{\partial E_k}{\partial Y} + \frac{\partial E_{b,R}}{\partial Y} = \frac{\partial W}{\partial Y} - \frac{\partial D}{\partial \dot{Y}} \tag{2.15b}$$

Substituting (2.6) – (2.7c), (2.10), (2.13) and (2.14) into (2.15a) and (2.15b) and neglecting centripetal effects from the kinetic energy yields the following:

$$M\begin{bmatrix} 1+\Delta_{m1} & \Delta_{m2} \\ \Delta_{m2} & 1-\Delta_{m1} \end{bmatrix}\begin{bmatrix} \ddot{X} \\ \ddot{Y} \end{bmatrix} + \left(C\begin{bmatrix} 1+\Delta_{c1} & \Delta_{c2} \\ \Delta_{c2} & 1-\Delta_{c1} \end{bmatrix} + M_\Omega \Omega \begin{bmatrix} 0 & -1 \\ 1 & 0 \end{bmatrix}\right)\begin{bmatrix} \dot{X} \\ \dot{Y} \end{bmatrix} + K\begin{bmatrix} 1+\Delta_{k1} & \Delta_{k2} \\ \Delta_{k2} & 1-\Delta_{k1} \end{bmatrix}\begin{bmatrix} X \\ Y \end{bmatrix} = \begin{bmatrix} f(t)\pi R \\ 0 \end{bmatrix} \tag{2.16}$$

where M, C, K are the modal mass, damping and stiffness respectively while M_Ω is the modal Coriolis mass, given by:

$$M = m\left(\frac{n^2+1}{2n^2}\right)$$

$$C = \frac{c\pi R}{n^2}(n^2+1)$$

$$K = \frac{EI\pi(n^2-1)^2}{R^3}$$

$$M_\Omega = \frac{2m}{n}$$

and

$$\Delta_{m1} = \frac{n^2-1}{2n^2+2}\delta\rho\cos 2n\Theta_\rho$$

$$\Delta_{m2} = \frac{n^2-1}{2n^2+2}\delta\rho\sin 2n\Theta_\rho$$

$$\Delta_{c1} = \frac{\delta c}{2}\cos 2n\Theta_c$$

$$\Delta_{c2} = \frac{\delta c}{2}\sin 2n\Theta_c$$

$$\Delta_{k1} = \frac{\delta E}{2}\cos 2n\Theta_E$$

$$\Delta_{k2} = \frac{\delta E}{2}\sin 2n\Theta_E$$

Pre-multiplying these equations by the inverse mass matrix and retaining only first order terms involving the small imperfection coefficients gives:

$$\begin{bmatrix}\ddot{X}\\ \ddot{Y}\end{bmatrix} + \left(\frac{\omega_0}{Q_0}\begin{bmatrix}1+\Delta_{b1} & \Delta_{b2}\\ \Delta_{b2} & 1-\Delta_{b1}\end{bmatrix} + G_\Omega\Omega\begin{bmatrix}-\Delta_{\Omega2} & -(1-\Delta_{\Omega1})\\ 1+\Delta_{\Omega1} & \Delta_{\Omega2}\end{bmatrix}\right)\begin{bmatrix}\dot{X}\\ \dot{Y}\end{bmatrix} \qquad (2.17)$$
$$+ {\omega_0}^2\begin{bmatrix}1+\Delta_{\omega1} & \Delta_{\omega2}\\ \Delta_{\omega2} & 1-\Delta_{\omega1}\end{bmatrix}\begin{bmatrix}X\\ Y\end{bmatrix} = \begin{bmatrix}\chi_X\\ \chi_Y\end{bmatrix}$$

where

$$\Delta_{b1} = \Delta_b\cos 2n\Theta_b = \Delta_{c1} - \Delta_{m1}$$

$$\Delta_{b2} = \Delta_b\sin 2n\Theta_b = \Delta_{c2} - \Delta_{m2}$$

$$\Delta_{\omega 1} = \Delta_{\omega} \cos 2n\Theta_{\omega} = \Delta_{k1} - \Delta_{m1}$$

$$\Delta_{\omega 2} = \Delta_{\omega} \sin 2n\Theta_{\omega} = \Delta_{k2} - \Delta_{m2}$$

$$\Delta_{\Omega 1} = \Delta_{m1}$$

$$\Delta_{\Omega 2} = \Delta_{m2}$$

ω_0 and Q_0 are the natural frequency and Q factor for the n^{th} flexural mode pair of the perfectly axisymmetric ring without rotation. The natural frequency is given by:

$$\omega_0{}^2 = \frac{n^2(n^2-1)^2}{n^2+1}\left(\frac{Eh^2}{12\rho R^4}\right)$$

and the quantity ω_0/Q_0 defines the modal half-power bandwidth. In practice, high Q factors are often desirable to amplify the sensitivity of the angular rate measurement.

In (2.17) G_{Ω} is associated with the gyroscopic coupling matrix, which governs the operation of CVG's in the absence of other coupling terms, and dictates the portion of the modal mass participating in the Coriolis forcing of the drive and sense modes. G_{Ω} was given in (1.3):

$$G_{\Omega} = \frac{4n}{n^2+1}$$

Similar to the Q factor, a high G_{Ω} maximises angular rate sensitivity and it is clear that the lowest order flexural mode pair ($n = 2$) results in the highest G_{Ω}.

χ_X and χ_Y are the modal-mass-normalised drive force components applied on the drive and sense modes respectively, and are given by:

$$\chi_X = \frac{f(t)}{\rho B h}\left(\frac{n^2}{n^2+1}\right)(1-\Delta_{m1})$$

$$\chi_Y = -\frac{f(t)}{\rho B h}\left(\frac{n^2}{n^2+1}\right)\Delta_{m2}$$

In the absence of density variations the drive force only excites the drive mode X. However, if $\sin 2n\Theta_{\rho} \neq 0$ the drive force directly excites the sense mode. This sense force is undesirable as it can be orders of magnitude larger than the Coriolis force and 'leakage' of even a small portion of this force into the sense mode can significantly mask the useful Coriolis force arising from the angular rate, thus contaminating the CVG output.

$\Delta_{b1,2}$, $\Delta_{\omega 1,2}$ and $\Delta_{\Omega 1,2}$ are small imperfection parameters (values $<<$ 1) relating to the bandwidth, natural frequency and Coriolis coupling. These terms arise from $2n\theta$ circumferential variations in the density, elastic modulus and damping coefficients, and they

can have a significant impact on the dynamics of the resonator, particularly when imperfection generates coupling between the drive and sense modes, leading to zero-rate outputs in the sensor. $\Delta_{b1,2}$ and $\Delta_{\omega 1,2}$ define the damping and structural imperfections respectively.

Δ_{b1} and Δ_{b2} depend on damping and density variations and result in splitting of the bandwidth (causing the Q factors for the drive and sense modes to differ) and velocity coupling between the drive and sense modes.

$\Delta_{\omega 1}$ and $\Delta_{\omega 2}$ depend on the density and elastic modulus variations and result in frequency splitting and elastic coupling between the drive and sense modes.

$\Delta_{\Omega 1}$ and $\Delta_{\Omega 2}$ depend on the density variations and contribute to the gyroscopic matrix. In the absence of density variations the gyroscopic matrix couples the drive and sense modes. The inertial force coupling results in the gyroscopic forces partially self-exciting the drive and sense modes in a manner similar to conventional damping, as shown by the nonzero terms $\pm\Delta_{\Omega 2}$ on the principal diagonal of the gyroscopic matrix, giving rise to terms proportional to the corresponding modal velocities. This gyroscopic self-excitation can be treated similarly to the 'damping minus mass' variation involving $\pm\Delta_{\mathrm{b1}}$ on the principal diagonal of the coefficient matrix of ω_0/Q_0, contributing to the splitting of the effective modal bandwidth. On the other hand, $\Delta_{\Omega 1}$ causes an asymmetric gyroscopic coupling strength between the drive and sense modes.

In the following work and throughout the thesis the effects of $\Delta_{\Omega 1}$ and $\Delta_{\Omega 2}$ are neglected. This assumption serves to simply the analysis and makes the theoretical results more tractable. This assumption ensures that $\Delta_{\Omega 1} = \Delta_{\Omega 2} = 0$ and $\chi_Y = 0$ but maintains non-zero values for Δ_{b1}, Δ_{b2}, $\Delta_{\omega 1}$, $\Delta_{\omega 2}$, thus only focusing on the damping and structural imperfections.

In the following section, the above assumptions are used in the derived equations of motion (2.17) and the resulting equations are used to determine the drive and sense mode dynamics when a harmonic excitation is applied and characterise the damping and structural imperfection from frequency response measurements.

2.3. Characterising damping and structural imperfection parameters from frequency response measurements

It is well understood that the presence of imperfections negatively affects sensor output in CVG's [2, 26]. Having knowledge of the nature of these imperfections is generally of practical interest, especially for trimming procedures. However, the nature of these imperfections is generally unknown. This section investigates methods to explicitly identify the structural and damping imperfection parameters based on frequency response measurements.

In the following investigation, the linear equations of motion developed in Section 2.2.3 are solved for the case of a variable-orientation harmonic drive force. The modal frequency response in the absence of rotation is then considered to determine the variation of the resonant frequency, phase and bandwidth with the drive force orientation. This variation is used to identify specific conditions of the resonant frequency, phase and bandwidth associated with the orientations of the structural and damping imperfections. Based on these results, measurement procedures using specific drive force orientations are proposed to identify the magnitudes and orientations of the structural and damping imperfections. Approaches using the resonant frequency and bandwidth, or the amplitude and phase are investigated.

2.3.1. Linear, forced-response of drive and sense modes

(2.17) describes the equations governing the linear dynamics of the drive and sense modes of a ring resonator. A harmonic forced response analysis can be performed by applying a harmonic force to excite the ring into vibration and determining the resulting response. In what follows, the imperfection coefficients $\Delta_{b1,2}$ and $\Delta_{\omega 1,2}$ refer directly to damping and structural imperfections respectively. A commonly used assumption [2, 26, 58] is investigated whereby the back coupling from the sense mode to the drive mode can be neglected. The validity of this assumption is normally based on the fact that the angular rates measured in practice are relatively low such that the sense mode oscillates with much smaller amplitude than the drive mode. This assumption is advantageous because it allows the drive mode to be treated as a single-degree-of-freedom system and the resulting drive mode displacements and velocities are treated as net forces acting on the sense mode. However, the proposed analysis is amendable to the investigation of the general case involving mutual coupling between the drive and sense modes. This allows the investigation on the effects of sense-to-drive modal back coupling.

Using the assumptions outlined previously, the governing equations of motion (2.17) can be simplified to:

$$\begin{bmatrix}\ddot{X}\\ \ddot{Y}\end{bmatrix}+\left(\frac{\omega_0}{Q_0}\begin{bmatrix}1+\Delta_{b1} & \eta\Delta_{b2}\\ \Delta_{b2} & 1-\Delta_{b1}\end{bmatrix}+\begin{bmatrix}0 & -\eta G_\Omega\Omega\\ G_\Omega\Omega & 0\end{bmatrix}\right)\begin{bmatrix}\dot{X}\\ \dot{Y}\end{bmatrix} \qquad (2.18)$$
$$+\omega_0{}^2\begin{bmatrix}1+\Delta_{\omega 1} & \eta\Delta_{\omega 2}\\ \Delta_{\omega 2} & 1-\Delta_{\omega 1}\end{bmatrix}\begin{bmatrix}X\\ Y\end{bmatrix}=\begin{bmatrix}\chi(t)\\ 0\end{bmatrix}$$

The dimensionless parameter η has been introduced in the above equation to identify the forces governing the drive mode dynamics arising from back coupling from the sense mode. In practice $\eta = 1$, but setting $\eta = 0$ in later analysis enables results to be obtained for the case when the back coupling is neglected.

To analyse the harmonic forced responses it is necessary to set $\chi(t) = \chi e^{i\omega t}$ and $X = x^* e^{i\omega t}$, $Y = y^* e^{i\omega t}$, where χ is a real quantity defining the magnitude of the drive force (modal-mass-normalised drive force) and x^* and y^* are the resulting complex amplitudes of the drive and sense mode response. Substituting these expressions into equation (2.18) yields:

$$\left\{-\omega^2 + i\omega\left(\frac{\omega_0}{Q_0}\begin{bmatrix}1+\Delta_{b1} & \eta\Delta_{b2}\\ \Delta_{b2} & 1-\Delta_{b1}\end{bmatrix} + \begin{bmatrix}0 & -\eta G_\Omega \Omega\\ G_\Omega\Omega & 0\end{bmatrix}\right) + {\omega_0}^2\begin{bmatrix}1+\Delta_{\omega1} & \eta\Delta_{\omega2}\\ \Delta_{\omega2} & 1-\Delta_{\omega1}\end{bmatrix}\right\}\begin{bmatrix}x^*\\ y^*\end{bmatrix} = \begin{bmatrix}\chi\\ 0\end{bmatrix} \tag{2.19}$$

and solving these equations it can be shown that x^* and y^* are given by:

$$x^* = xe^{i\phi_x} = \chi\frac{-\omega^2 + {\omega_0}^2(1-\Delta_{\omega1}) + i\omega\frac{\omega_0}{Q_0}(1-\Delta_{b1})}{Z^*} \tag{2.20a}$$

$$y^* = ye^{i\phi_y} = \chi\frac{-{\omega_0}^2\Delta_{\omega2} - i\omega\left(\frac{\omega_0}{Q_0}\Delta_{b2} + G_\Omega\Omega\right)}{Z^*} \tag{2.20b}$$

where

$$Z^* = \left[-\omega^2 + {\omega_0}^2(1-\Delta_{\omega1}) + i\omega\frac{\omega_0}{Q_0}(1-\Delta_{b1})\right]\left[-\omega^2 + {\omega_0}^2(1+\Delta_{\omega1}) + i\omega\frac{\omega_0}{Q_0}(1+\Delta_{b1})\right] - \eta\left({\omega_0}^2\Delta_{\omega2} + i\omega\frac{\omega_0}{Q_0}\Delta_{b2}\right)^2 - \eta\omega^2{G_\Omega}^2\Omega^2 \tag{2.21}$$

x^* and y^* are the frequency response functions (FRF) governing the drive and sense mode harmonic responses. The real parts of x^* and y^* represent components of the drive and sense responses in phase/antiphase with the driving force, while the imaginary parts represent the amplitudes of the drive and sense response components in quadrature with the driving force. Using the real and imaginary parts of x^* and y^*, the frequency response of the amplitudes x, y and phases ϕ_x, ϕ_y can be determined by converting the expressions in (2.20a) and (2.20b) to polar form. The expressions for x, y and ϕ_x, ϕ_y are lengthy due to the presence of the imperfections, so the FRF as expressed in (2.20a) and (2.20b) will be used for the following analysis.

The impact of the imperfection parameters $\Delta_{b1}, \Delta_{b2}, \Delta_{\omega1}, \Delta_{\omega2}$ on the frequency response function is clear in (2.20a) and (2.20b). Expanding Z^* shows that the imperfection parameters appear only as second-order terms. As such, the dominant effects of the imperfection are described by the numerators in (2.20a) and (2.20b).

The FRF in (2.20a) and (2.20b) will be used in what follows to determine the resonant frequency, phase and bandwidth, and are used to identify the orientations of the structural and damping imperfections, also known as the principal axes. For this purpose, the half-power method is implemented, which involves identifying the frequencies yielding peak amplitudes x, y and identifying the frequencies at half-power relative to the peak amplitude to calculate the bandwidth, which can then be used to identify the Q factor. However, in the presence of imperfections, it is important to note that the FRF generally exhibits two distinct, but close amplitude peaks, resulting in difficulties to identify the resonant frequencies and Q factors. As such, approximate techniques or simplification of (2.20a) and (2.20b) are required. This is discussed next.

2.3.2. Circumferential variation of frequency response functions

To aid identification and characterisation of the structural and damping imperfection parameters, the following extends the FRF in (2.20a) and (2.20b) to consider the more general case when the drive and sense axes are rotated relative to the ring. The variation of this FRF with the orientation of these axes can then be used to describe how the phase and modal parameters such as the bandwidth and resonant frequency vary in this case. The complex amplitudes x^* and y^* are first treated individually to represent single point measurements at either the drive or sense points on the ring. This is then followed by analysing the ratio of these complex amplitudes $y^*(\omega)/x^*(\omega)$, where measurements at the drive and sense points are simultaneously considered.

To investigate the impact of moving the drive and sense axes relative to the ring it is necessary to redefine the imperfection parameters in terms of the new drive axis, such that:

$$\Delta_{b1} = \Delta_b \cos 2n\left(\Theta_b - \Theta_\chi\right), \Delta_{b2} = \Delta_b \sin 2n\left(\Theta_b - \Theta_\chi\right),$$

$$\Delta_{\omega 1} = \Delta_\omega \cos 2n\left(\Theta_\omega - \Theta_\chi\right), \Delta_{\omega 2} = \Delta_\omega \sin 2n\left(\Theta_\omega - \Theta_\chi\right)$$

where Θ_χ defines the orientation of the drive axis as well as the drive mode relative to the above case when $\Theta_\chi = 0$. As the drive and sense modes are separated by $\pi/2n$, $\Theta_\chi + \pi/2n$ defines the orientation of the sense axis as well as the sense mode. Figure 2.2 shows a diagrammatic representation of the drive and sense axes.

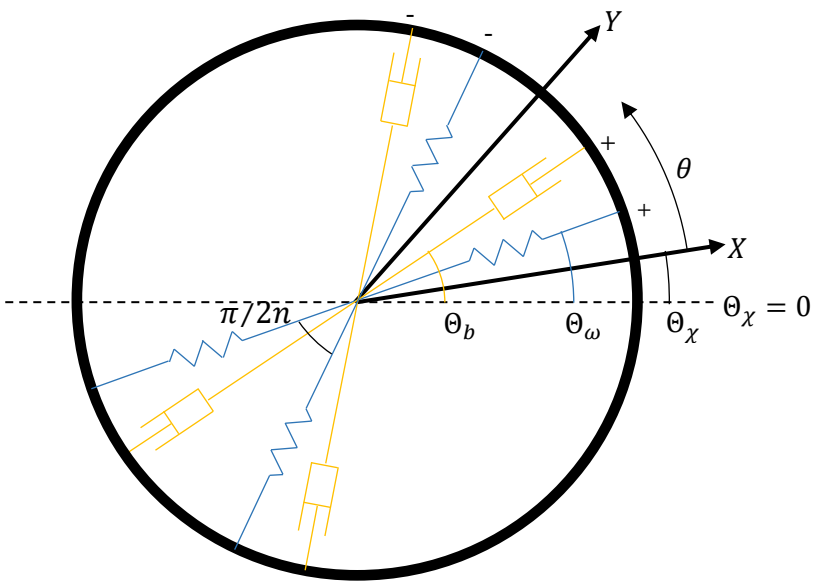

Figure 2.2: Schematic diagram of ring with superimposed structural and damping variations

The X-axis defines the drive axis and the orientation of the drive force relative to $\Theta_\chi = 0$. Rotating the drive force relative to the body of the ring (effectively varying Θ_χ) results in imperfection variations $\Delta_{b1}, \Delta_{b2}, \Delta_{\omega 1}, \Delta_{\omega 2}$ having a cyclic period of π/n. In practice, it is worth noting that the drive and sense axes can be rotated by using a stepped rotation stage [14, 43]. A direct consequence of this is that the drive and sense mode frequency response functions repeats every π/n and as such, the examples presented for the case studies considered later in this section will only display results for $0 < \Theta_\chi < \pi/n$.

In Figure 2.2, the damping and structural imperfections are represented as dashpots and springs attached at specific angular locations of the ring, acting to modify the damping and stiffness at these angular locations. The '+' symbols represent angular locations $\Theta_\chi = \Theta_\omega$ and $\Theta_\chi = \Theta_b$ associated with maximum positive perturbations of the $2n\theta$ 'stiffness minus mass' and 'damping minus mass'. The opposite interpretation applies for the '-' symbols. The angular orientations at these positions define the structural and damping principal axes. In this manner, Figure 2.2 shows how the 'damping minus mass' and 'stiffness minus mass' vary from maximum to minimum values within a drive force rotation of $\pi/2n$, returning to the maximum with a further rotation angle of $\pi/2n$. This cyclic variation of the modal properties is a fundamental effect of non-uniformities in the ring due to imperfections and as such, can be used to identify the principal axes. Focusing only on these imperfections, in what follows, the FRF in (2.20a) and (2.20b) are considered without the angular rate ($\Omega = 0$).

2.3.2.1. Single point measurements

To distinguish the resulting complex drive and sense mode amplitudes from those with rate applied, the notations $x_{\Omega 0}{}^{*} \coloneqq x^{*}|_{\Omega=0}$ and $y_{\Omega 0}{}^{*} \coloneqq y^{*}|_{\Omega=0}$ are used. In principle the derived results can be used to determine expressions for the phase, bandwidth and resonant frequencies. However, as noted previously, the complexity of the drive and sense mode amplitude frequency responses associated with the imperfection-induced peak splitting [2] make this intractable, and for this reason it is necessary to simplify the frequency response functions expressions. This is achieved by using the approximations $|\Delta_{\omega}|Q_0 \ll 1$ and $|\Delta_b| \ll 1$ which are conditions associated with small structural and damping imperfections of the ring respectively. These allow approximations of Z^{*} to be made, as it has been noted previously that the imperfection parameters only appear as second-order terms in (2.21). The scaling of $|\Delta_{\omega}|$ with the Q factor in this approximation serves to match the orders of magnitude of the forces arising from the structural and damping imperfections. This can be deduced from (2.18) by comparing the structural imperfection forces $\omega_0{}^2\Delta_{\omega 1,2}X$, $\omega_0{}^2\Delta_{\omega 1,2}Y$ against the damping imperfection forces $(\omega_0/Q_0)\Delta_{b1,2}\dot{X}$, $(\omega_0/Q_0)\Delta_{b1,2}\dot{Y}$.

Using this simplification in (2.20a), the (zero-rate) complex drive amplitude response can be approximated as:

$$x_{a,\Omega 0}{}^{*} = \left|x_{a,\Omega 0}{}^{*}\right| e^{i\phi_{x,a,\Omega 0}} = \frac{\chi}{-\omega^2 + \omega_0{}^2(1+\Delta_{\omega 1}) + i\omega\frac{\omega_0}{Q_0}(1+\Delta_{b1})} \tag{2.22}$$

The condition $|\Delta_{\omega}|Q_0 \ll 1$ is equivalent to requiring the frequency split to be much smaller than the mean bandwidth, so the accuracy of (2.22) is limited to very small amounts of imperfection particularly when the Q factor is large. It can be shown easily that approximation (2.22) is equivalent to setting $\eta = 0$ in (2.20a) and so is equivalent to neglecting the back coupling from the sense to the drive response. This approximation may not be well suited to very high Q factor resonators required for high performance CVG's. Provided the levels of imperfection are sufficiently small, the advantage of analysing the drive response using (2.22) is that the drive mode amplitude frequency response always exhibits a single peak, unlike the more general case, ensuring that the resonant peak and half-power bandwidth can be measured from frequency response measurements. This behaviour can be confirmed by identifying the excitation frequency ω at the stationary point of the drive response magnitude, i.e. by setting $\partial\left|x_{a,\Omega 0}{}^{*}\right|/\partial\omega = 0$. When peak splitting occurs, this condition yields 3 possible frequencies: 2 corresponding to amplitude maxima and 1 to a minimum.

Converting (2.22) to polar form, the following can be deduced for the approximated drive amplitude and phase and frequency responses:

$$\left|{x_{a,\Omega 0}}^*\right| = \frac{\chi}{\sqrt{[-\omega^2 + {\omega_0}^2(1+\Delta_{\omega 1})]^2 + \left[\omega\frac{\omega_0}{Q_0}(1+\Delta_{b1})\right]^2}} \tag{2.23a}$$

$$\phi_{x,a,\Omega 0} = \tan^{-1}\left[\frac{-\omega\frac{\omega_0}{Q_0}(1+\Delta_{b1})}{-\omega^2 + {\omega_0}^2(1+\Delta_{\omega 1})}\right] \tag{2.23b}$$

The resonant frequency ω_X is such that $Re\left({x_{a,\Omega 0}}^*\right) = 0$, which approximates the peak of the drive amplitude $\left|{x_{a,\Omega 0}}^*\right|$. The drive bandwidth b_X is the frequency range where the drive amplitude $\left|{x_{a,\Omega 0}}^*\right|$ is at least $1/\sqrt{2}$ of its maximum, obtained using the half-power method. The peak drive amplitude is obtained by identifying the excitation frequency ω at the stationary point of the drive amplitude, i.e. by setting $\partial\left|{x_{a,\Omega 0}}^*\right|/\partial\omega = 0$, then substituting this frequency into (2.23a). These give the following results:

- The drive response has an undamped frequency of ${\omega_X}^2 = {\omega_0}^2(1+\Delta_{\omega 1})$, yielding a drive phase of $\phi_{x,a,\Omega 0} = -\pi/2$.
- The half-power bandwidth is given by $b_X = \omega_0/Q_0\,(1+\Delta_{b1})$.

Due to the dependence of the measured drive response frequency ω_X and bandwidth b_X on $\Delta_{\omega 1}$, Δ_{b1}, it is clear that ω_X and b_X depend on the circumferential distribution of the structural and damping imperfections relative to the drive force distribution. Using frequency response measurements, by measuring the variation of ω_X and b_X with the drive angle Θ_χ, the corresponding maxima and minima can be used to identify the structural and damping principal axes, Θ_ω and Θ_b.

For the same magnitudes of imperfections as those for the drive mode, when $|\Delta_\omega|Q_0 \ll 1$ and $|\Delta_b| \ll 1$, the complex amplitude of the sense mode can be approximated by neglecting all terms involving the imperfection parameters Δ_{b1}, Δ_{b2}, $\Delta_{\omega 1}$, $\Delta_{\omega 2}$ in Z^*, since all of these coefficients appear only as second-order terms. The approximated complex sense mode amplitude is given by:

$${y_{a,\Omega 0}}^* = \left|{y_{a,\Omega 0}}^*\right|e^{i\phi_{y,a,\Omega 0}} = \chi\frac{-{\omega_0}^2\Delta_{\omega 2} - i\omega\frac{\omega_0}{Q_0}\Delta_{b2}}{\left(-\omega^2 + {\omega_0}^2 + i\omega\frac{\omega_0}{Q_0}\right)^2} \tag{2.24}$$

Similar to the approximated drive response described by (2.22), the terms involving η do not appear in the approximated complex sense mode amplitude. Setting $\partial\left|{y_{a,\Omega 0}}^*\right|/\partial\omega = 0$ also shows that there is a single amplitude peak at $\omega \approx \omega_0$. As such, the resonant peak can be similarly measured using frequency response measurements of the sense mode and the bandwidth can be similarly obtained using the half-power method. These give:

- The sense response has an undamped frequency at $\omega_Y = \omega_0$.
- The half-power bandwidth is invariant with the drive angle Θ_χ, given by $b_Y = \omega_0/Q_0\left(\sqrt{2}-1\right)^{1/2}$, which is significantly smaller than the nominal bandwidth ω_0/Q_0.

where ω_Y and b_Y are independent of the imperfection parameters due to the absence of the imperfection parameters in the denominator of (2.24). As such, for small imperfections, measuring the resonant peak and the half-power bandwidth of the sense mode does not provide any insight into the circumferential distribution of the structural and damping imperfections. The approximated complex sense amplitude only exhibits circumferential variations with the drive force distribution through the terms in the numerator of (2.24). As such, for this purpose, the phase frequency response is used to identify specific phase conditions which apply when the drive force distribution aligns with the maximum or minimum principal axes of the structural and damping imperfections. When the sense mode is at resonance, i.e. $\omega = \omega_0$, these phase conditions are given by:

- When $\Theta_\chi = \Theta_\omega + i\pi/2n$ (i is an integer), $\Delta_{\omega 2} = 0$ and ${y_{a,\Omega 0}}^*$ is imaginary, yielding $\phi_{y,a,\Omega 0} = \pi/2$ when $\Delta_{b2} > 0$ and $\phi_{y,a,\Omega 0} = -\pi/2$ when $\Delta_{b2} < 0$
- When $\Theta_\chi = \Theta_b + i\pi/2n$ (i is an integer), $\Delta_{b2} = 0$ and ${y_{a,\Omega 0}}^*$ is real, yielding $\phi_{y,a,\Omega 0} = 0$ when $\Delta_{\omega 2} > 0$ and $\phi_{y,a,\Omega 0} = \pm\pi$ when $\Delta_{\omega 2} < 0$

These phase conditions are then used to locate the orientations of the principal axes.

Numerical examples for resonant frequency and phase and bandwidth measurements

In what follows, the effects of varying the drive location on the measured resonant frequency, phase and bandwidth are investigated for the drive and sense modes. A device with nominal $n = 2$ frequency of $\omega_0 = 11.29\ kHz$ and Q factor of $Q_0 = 2.2e4$ is considered as the default parameters for this purpose and for the remainder of this chapter. The damping and structural imperfection magnitudes and principal axes orientations are $\Delta_b = 0.11$, $\Delta_\omega = 1.8e-6$ and $\Theta_b = 30°$, $\Theta_\omega = 22°$, resulting in a frequency split of $20\,mHz$ and bandwidth split of $115\,mHz$. The harmonic force amplitude is $\chi = 0.16\,m/s^2$. Figure 2.3(a) shows the variations of the amplitude frequency response of the drive mode as the drive location is

changed. Drive locations over the range $\Theta_\chi = 0°$ to $90°$ are considered, noting the spatially periodic nature of the $2n\theta$ imperfection variation components. In Figure 2.3(b), the top pane shows the variation of the drive resonant frequency with drive location, obtained by identifying the frequency ω yielding peak drive amplitude in Figure 2.3(a) for each drive location considered. The middle pane shows the corresponding drive phase when ω is set at the drive frequencies in the top pane. The bottom pane shows the drive bandwidth variation, obtained using the half-power method. For all the results in Figure 2.3(b), the accuracy of the approximated results given by ${x_{a,\Omega 0}}^*$ in (2.22) is shown through comparison with the corresponding results from the exact complex amplitudes ${x_{\Omega 0}}^*$. The exact results for the drive frequency using ${x_{\Omega 0}}^*$ in the top pane of Figure 2.3(b) are obtained by tracking the peak drive amplitudes as indicated by the light tones in Figure 2.3(a), and identifying the excitation frequency ω yielding the peak amplitude for each Θ_χ. The exact results for the bandwidth in the bottom pane are calculated using the half-power method based on the peak-amplitude frequencies identified in the top pane. Figure 2.4(a) and (b) show the same results, but for the sense mode.

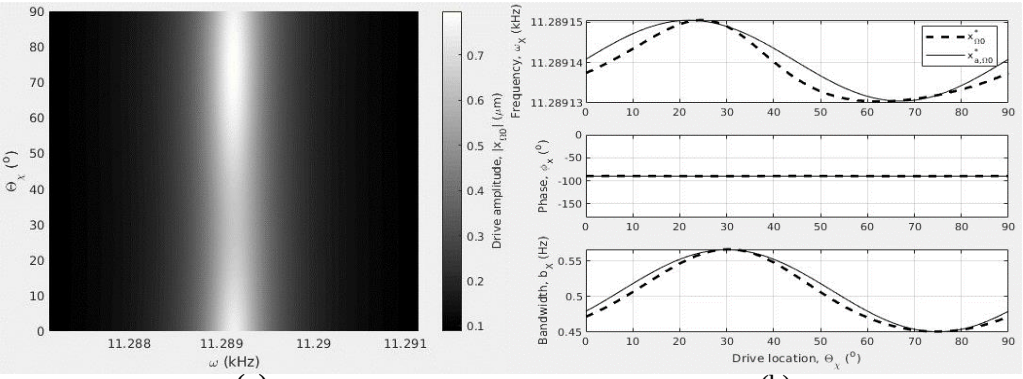

(a) (b)

Figure 2.3: (a) Amplitude-frequency response of the drive mode and (b) peak-amplitude frequency, phase and half-power bandwidth for a frequency split of $20\ mHz$ and bandwidth split of $115\ mHz$

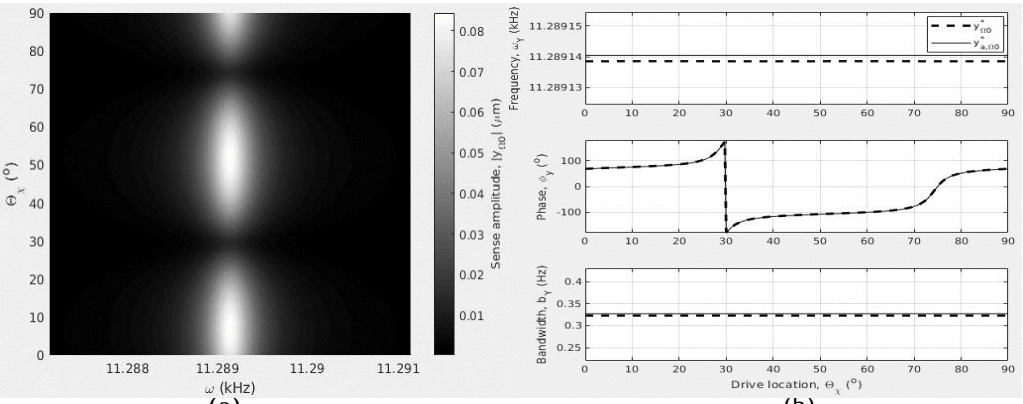

(a) (b)

Figure 2.4: (a) Amplitude-frequency response of the sense mode and (b) peak-amplitude frequency, phase and half-power bandwidth for a frequency split of $20\ mHz$ and bandwidth split of $115\ mHz$

The results in Figure 2.3(a) show that the peak drive amplitude attained is relatively invariant with respect to the drive location. On the other hand, the peak sense amplitude in Figure 2.4(a) diminishes to small values near the damping principal axes at $\Theta_\chi = 30°$ and $75°$. This is because, unlike the drive mode, the sense mode is not directly forced by the harmonic excitation, and only responds due to the imperfection-induced damping and elastic coupling forces. As such, when the damping coupling vanishes at the damping principal axes, the sense response diminishes accordingly. These results also indicate that the structural imperfection magnitudes considered are significantly smaller than those of the damping imperfections, as the peak sense amplitude remains relatively unaffected when the elastic coupling is eliminated at the structural imperfection principal axes at $\Theta_\chi = 22°$ and $67°$.

In Figure 2.3(b), the phase results show excellent agreement between the approximated and exact FRF's. This agreement is also shown for the sense phase in Figure 2.4(b). When the sense mode is driven into resonance, the phase conditions $\phi_y = \pm 90°$ and $\phi_y = 0, \pm\pi$ occur at the structural and damping principal axes respectively, as was noted previously. This confirms the potential to use the sense phase to locate the principal axes orientations.

Discussion

In both Figure 2.3(b) and Figure 2.4(b), the results for the frequency and bandwidth exhibit discrepancies between the approximated and exact FRF's. For the sense response, these discrepancies are relatively constant with drive location. For the drive mode, the discrepancies in the results for the frequency and bandwidth are negligible for drive locations near the structural and damping principal axes respectively, but are maximised at the midpoint of the corresponding principal axes. Generally, these discrepancies arise due to the assumptions associated with the approximated results, and the accuracy of the approximated result depends on how well the conditions $|\Delta_\omega| Q_0 \ll 1$ and $|\Delta_b| \ll 1$ are satisfied. Since $\Delta_b = 0.11$, the condition $|\Delta_b| \ll 1$ is only marginally satisfied, thus predominantly contributing to the observed discrepancy compared to the condition $|\Delta_\omega| Q_0 \ll 1$. For the drive mode, the approximated result is equivalent to the assumption that back coupling has been neglected. As such, the effects of linear elastic and damping coupling forces are not accounted for, so the maximum discrepancy is observed in the measured bandwidth at drive locations where Δ_{b2} is maximised, i.e. $\Theta_\chi = 52.5°$ which is precisely midway between the principal axes of damping maximum and minimum. Similarly, the maximum discrepancy for the frequency results is observed at drive locations where $\Delta_{\omega 2}$. Despite these discrepancies, good accuracy is observed at the principal axes. As such, the principal axes of structural and damping imperfections can still be identified from the drive locations of maximum and minimum drive frequency and bandwidth respectively. The magnitudes of the structural and damping imperfections can be

calculated from the differences between the extreme and mean values of the frequency and bandwidth of the drive mode in Figure 2.3(b).

The practicality of using the half-power method to obtain the results in Figure 2.3(b) and Figure 2.4(b) relies on the single-peak nature of the amplitude frequency response, which is achieved for the imperfections considered, as can be observed from the singular light tones in Figure 2.3(a) and Figure 2.4(a) at each drive location. However it is important to note that, as previously discussed, complexity arises when using the half-power method for systems with larger imperfections where the conditions $|\Delta_\omega|Q_0 \ll 1$ and $|\Delta_b| \ll 1$ are less satisfied.

Effects of larger structural imperfections on amplitude frequency response

In the following, the amplitude frequency responses of the drive and sense modes for larger structural imperfection magnitudes are investigated, focusing on the possibility of amplitude peak bifurcation in the amplitude frequency responses which is typical of imperfect systems. From the complex drive and sense amplitudes in (2.20a) and (2.20b), by setting the gradients of the amplitude frequency responses $\partial|x_{\Omega 0}{}^*|/\partial\omega^2 = 0$ and $\partial|y_{\Omega 0}{}^*|/\partial\omega^2 = 0$ in the absence of angular rate and solving for the excitation frequencies ω, three solutions can be obtained. For small structural imperfection magnitudes such as the system considered for the results in Figure 2.3(a) and Figure 2.4(a), two of these frequencies are complex, consequently yielding amplitude frequency responses with single peaks. As Δ_ω increases, there is a threshold Δ_ω where these frequencies become real-valued, thus leading to peak splitting. In Figure 2.5(a) and (b) below, the system considered for the results in Figure 2.3(a) and Figure 2.4(a) is used, but with a larger Δ_ω. The threshold Δ_ω is first calculated for the parameters used in the results in Figure 2.3(a) and Figure 2.4(a), and Δ_ω is selected such that it exceeds the peak-splitting threshold calculated. For this purpose, Δ_ω is increased to 8.9e-5, corresponding to a frequency split of 1 Hz.

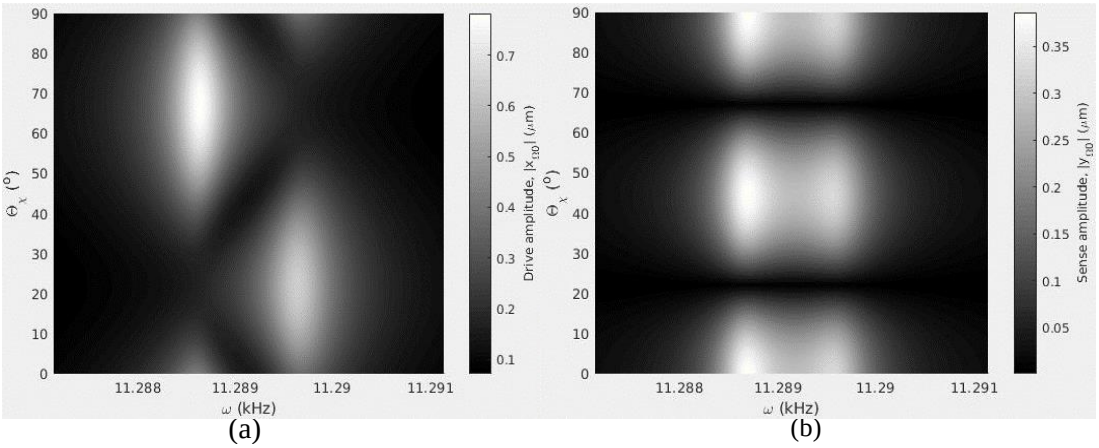

(a) (b)

Figure 2.5: Amplitude frequency response plots of the (a) drive and (b) sense modes with a frequency split of 1 Hz and a bandwidth split of 115 mHz

In Figure 2.5(a) and Figure 2.5(b), the peak splitting is characterised by a low-frequency amplitude peak at $\omega = 11288.7\,Hz$ and a high-frequency amplitude peak at $\omega = 11289.7\,Hz$, and the mean of these frequencies is the nominal frequency ω_0. The amplitude frequency response of the sense mode in Figure 2.5(b) exhibits near-symmetric behaviour about $\omega = \omega_0$. This is because the sense mode only arises due the damping and elastic coupling forces, shown in the terms $(\omega_0/Q_0)\Delta_{b2}\dot{X}$ and ${\omega_0}^2\Delta_{\omega 2}X$ in (2.18), whose amplitudes are minimally affected by the excitation frequency ω. On the other hand, for the drive mode, one of the amplitude peaks vanishes when the drive force aligns with one of the structural imperfection principal axes, as shown in Figure 2.5(a) when $\Theta_\chi = 22°$ or $67°$.

Due to the peak bifurcation, the half-power method can result in erroneous interpretations of the bandwidth. For example, when examining the frequency range defining the half-power bandwidth of the sense mode in Figure 2.5(b), the half-power bandwidth of the two peaks overlap, where the overlapping frequencies of the two bandwidths range from $\omega = 11288.5\,Hz$ corresponding to the low-frequency amplitude peak, to $\omega = 11289.7\,Hz$ corresponding to the high-frequency amplitude peak. This bandwidth overlap poses difficulties for measuring the drive and sense bandwidths separately.

In practice, typical untrimmed CVG's can exhibit frequency splits in the order of $10^1 - 10^2\,Hz$ [44, 45, 59]. Depending on the Q factor of the device, frequency splits of such orders of magnitude can exhibit peak-bifurcated amplitude frequency responses, in which case the numerical half-power approach outlined here is incompatible for the aim of identifying the magnitude and principal axes of structural and damping imperfections. Having defined the limitations for using the individual drive and sense point response measurements to identify the structural and damping imperfections, in what follows, this challenge is addressed using an alternative approach.

2.3.2.2. Dual point measurements

In this section, the drive and sense point measurements are simultaneously considered to identify the structural and damping imperfection parameters. Noting that the complex drive and sense amplitudes in (2.20a) and (2.20b) share a common denominator Z^*, the effects of Z^* can be avoided by evaluating the ratio of these complex amplitudes. For this purpose, the complex transmissibility amplitude is introduced, defined as $T^* = y^*/x^*$, giving:

$$T^* = \frac{-{\omega_0}^2\Delta_{\omega 2} - i\omega\left(\frac{\omega_0}{Q_0}\Delta_{b2} + G_\Omega\Omega\right)}{-\omega^2 + {\omega_0}^2(1-\Delta_{\omega 1}) + i\omega\frac{\omega_0}{Q_0}(1-\Delta_{b1})} \tag{2.25}$$

An advantage of using the complex transmissibility amplitude is that the result is exact, avoiding the approximations used to obtain the complex drive and sense amplitudes in (2.22) and (2.24). Secondly, setting $\partial|T^*|/\partial\omega^2 = 0$ and solving for ω shows that the amplitude frequency response of the transmissibility always exhibits a single peak, regardless of the imperfection magnitudes Δ_b and Δ_ω. This avoids the complications associated with applying the half-power method in the presence of larger structural imperfections.

Similar to single point measurements considered earlier, the transmissibility is investigated in the absence of angular rate, in which case the following conditions apply for the transmissibility frequency ω_T and bandwidth b_T:

- In the absence of damping ($Q_0 \to \infty$), the undamped frequency is $\omega_T = \omega_0\sqrt{1-\Delta_{\omega 1}}$.
- The half-power bandwidth is $b_T = \omega_0/Q_0\,(1-\Delta_{b1})$

Similar to the approximated drive FRF in (2.22), the drive locations of maximum and minimum frequency and bandwidth can be used to locate the principal axes of the structural and damping imperfections respectively.

When $\omega = \omega_T$, the phase angle is $\phi_T = \angle[-\Delta_{b2}(\omega_0/Q_0) + i\omega_0\Delta_{\omega 2}]$ when $|\Delta_\omega| \ll 1$, giving the following conditions for the transmissibility phase:

- When $\Theta_\chi = \Theta_\omega + i\pi/2n$ (i is an integer), $\Delta_{\omega 2} = 0$ and T^* is real, yielding $\phi_T = \pm\pi$ when $\Delta_{b2} > 0$ and $\phi_T = 0$ when $\Delta_{b2} < 0$
- When $\Theta_\chi = \Theta_b + i\pi/2n$ (i is an integer), $\Delta_{b2} = 0$ and T^* is imaginary, yielding $\phi_T = \pi/2$ when $\Delta_{\omega 2} > 0$ and $\phi_T = -\pi/2$ when $\Delta_{\omega 2} < 0$

Numerical example

In the following, the effects of varying the drive location on the transmissibility frequency, phase and bandwidth is investigated. The system considered for this investigation is identical to that used for the results in Figure 2.5(a) and Figure 2.5(b), thus serving to show the applicability of the results in the presence of larger structural imperfection magnitudes. In Figure 2.6(a), the undamped frequency of the transmissibility is approximated by identifying the excitation frequency ω yielding peak transmissibility amplitude. In Figure 2.6(b), the resulting phase of the transmissibility is shown for the case when ω is fixed at the frequencies calculated in Figure 2.6(a). In Figure 2.6(c), the drive location dependency of the transmissibility bandwidth is shown, obtained using the half-power method implemented on the transmissibility amplitude frequency bandwidth.

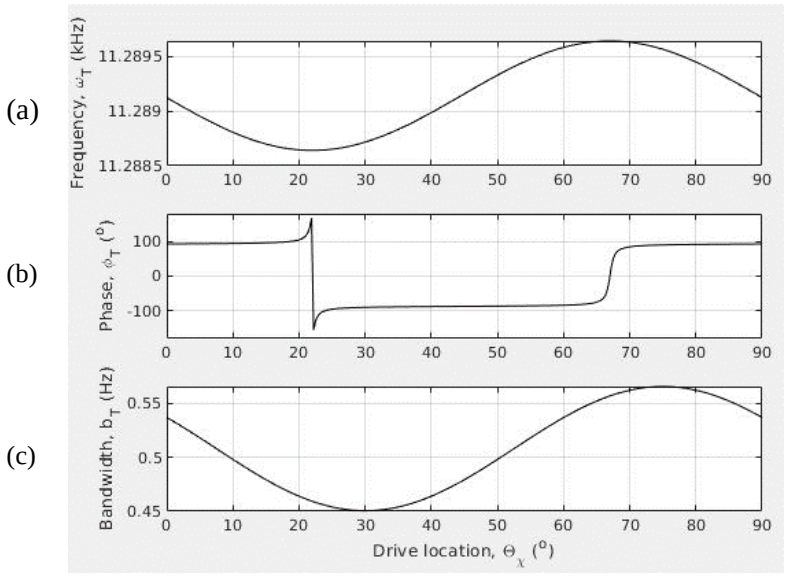

Figure 2.6: Transmissibility response for the (a) frequency and (b) phase at amplitude peak and (c) the half-power bandwidth

In Figure 2.6(a) and (c), the variations of the transmissibility frequency and bandwidth with the drive location can be used to identify the principal axes and the magnitudes of the structural and damping imperfections in a manner similar to the drive point measurements shown earlier in Figure 2.3(b). The drive locations of extreme values of the frequency and bandwidth are used to locate the principal axes while the differences between the mean and extreme values are used to calculate the imperfection magnitudes. In Figure 2.6(b), the phase can also be used to identify the principal axes, as $\phi_T = 0, \pm\pi$ and $\phi_T = \pm\pi/2$ at the principal axes of structural and damping imperfections respectively, as was previously noted.

The exact nature of the results shown in Figure 2.6(a) – (c) indicates that using the drive and sense point measurements simultaneously provides a more accurate method for identifying the imperfection magnitudes and principal axes compared to using the drive and sense FRF's individually. However, additional displacement measurement mechanisms are required to measure the FRF's of both the drive and sense modes.

2.3.3. Measurement procedures with finite driving points

In Section 2.3.2, the drive location dependency of the bandwidth, frequency and phase are used to identify the structural and damping imperfection parameters. However, the approach investigated necessitates FRF measurements at many drive locations to obtain an accurate description of such variations, i.e. sufficiently fine resolution of Θ_χ. In this section, practical measurement procedures are proposed to identify the structural and damping imperfection parameters based on the response of the ring when excited at only a few driving locations. The following measurement procedures are based on the transmissibility response due to the exact nature of these results. In what follows, identification of the imperfection parameters using

the transmissibility frequency and bandwidth, and amplitude and phase measurement procedures are proposed.

Identifying imperfection parameters with frequency and bandwidth measurements

Recalling from Section 2.3.2, the transmissibility frequency and half-power bandwidth are:

$$\omega_T(\Theta_\chi) = \omega_0\sqrt{1 - \Delta_\omega \cos 2n(\Theta_\omega - \Theta_\chi)} \tag{2.26}$$

$$b_T(\Theta_\chi) = \frac{\omega_0}{Q_0}[1 - \Delta_b \cos 2n(\Theta_b - \Theta_\chi)] \tag{2.27}$$

where ω_T and b_T have been expressed as functions of the driving orientation Θ_χ.

Considering transmissibility FRF measurements at drive locations $\Theta_\chi = \Theta_{\chi 0}$ and $\Theta_\chi = \Theta_{\chi 0} + \pi/2n$, where $\Theta_{\chi 0}$ is arbitrary, the nominal frequency ω_0 and bandwidth ω_0/Q_0 can be calculated from the measured transmissibility frequency and bandwidth in (2.26) and (2.27) at these drive locations. These are given by:

$$\omega_0 = \sqrt{\frac{{\omega_T}^2(\Theta_{\chi 0}) + {\omega_T}^2\left(\Theta_{\chi 0} + \frac{\pi}{2n}\right)}{2}} \tag{2.28}$$

$$\frac{\omega_0}{Q_0} = \frac{b_T(\Theta_{\chi 0}) + b_T\left(\Theta_{\chi 0} + \frac{\pi}{2n}\right)}{2} \tag{2.29}$$

These results are equivalent to calculating the mean of the measured transmissibility frequency and bandwidth. Using the results in Figure 2.6(a) and (c) as examples, the mean of the measured frequency and bandwidth at any two drive locations spaced $45°$ apart are used to calculate the nominal frequency and bandwidth. If $\Theta_{\chi 0}$ coincides with either principal axes of the structural or damping imperfection, the maximum and minimum values of the transmissibility frequency and bandwidth are used.

After calculating the nominal frequency and bandwidth, the imperfection magnitudes Δ_ω, Δ_b and principal axes orientations Θ_ω, Θ_b can be determined by considering the measured frequency and bandwidth at two additional drive locations, $\Theta_\chi = \Theta_{\chi 0} + \pi/4n$ and $\Theta_\chi = \Theta_{\chi 0} + 3\pi/4n$. It can then be shown that the imperfection magnitudes and principal axes orientations can be identified using the following relationships:

$$\Delta_\omega = \frac{\sqrt{\left[{\omega_T}^2\left(\Theta_{\chi 0}+\frac{\pi}{2n}\right)-{\omega_T}^2\left(\Theta_{\chi 0}\right)\right]^2+\left[{\omega_T}^2\left(\Theta_{\chi 0}+\frac{3\pi}{4n}\right)-{\omega_T}^2\left(\Theta_{\chi 0}+\frac{\pi}{4n}\right)\right]^2}}{2{\omega_0}^2} \tag{2.30}$$

$$\Theta_\omega = \frac{\tan^{-1}\left[\frac{{\omega_T}^2\left(\Theta_{\chi 0}+\frac{3\pi}{4n}\right)-{\omega_T}^2\left(\Theta_{\chi 0}+\frac{\pi}{4n}\right)}{{\omega_T}^2\left(\Theta_{\chi 0}+\frac{\pi}{2n}\right)-{\omega_T}^2\left(\Theta_{\chi 0}\right)}\right]}{2n}+\Theta_{\chi 0} \tag{2.31}$$

$$\Delta_b = \frac{\sqrt{\left[b_T\left(\Theta_{\chi 0}+\frac{\pi}{2n}\right)-b_T\left(\Theta_{\chi 0}\right)\right]^2+\left[b_T\left(\Theta_{\chi 0}+\frac{3\pi}{4n}\right)-b_T\left(\Theta_{\chi 0}+\frac{\pi}{4n}\right)\right]^2}}{2\left(\frac{\omega_0}{Q_0}\right)} \tag{2.32}$$

$$\Theta_b = \frac{\tan^{-1}\left[\frac{b_T\left(\Theta_{\chi 0}+\frac{3\pi}{4n}\right)-b_T\left(\Theta_{\chi 0}+\frac{\pi}{4n}\right)}{b_T\left(\Theta_{\chi 0}+\frac{\pi}{2n}\right)-b_T\left(\Theta_{\chi 0}\right)}\right]}{2n}+\Theta_{\chi 0} \tag{2.33}$$

The relationships in (2.30) - (2.33) show that the structural and damping imperfection parameters can be identified using the measured transmissibility frequency and bandwidth at only 4 arbitrary drive locations, spaced $\pi/4n$. This avoids the need to obtain results such as those in Figure 2.6(a) and (c) where measurements at more drive locations are involved.

Identifying imperfection parameters with amplitude and phase measurements

From the complex transmissibility amplitude in (2.25), when $\omega = \omega_T$ in the absence of angular rate, the transmissibility phase ϕ_T and amplitude T are given by:

$$\phi_T\left(\Theta_\chi\right) = \angle\left[-\frac{\omega_0}{Q_0}\Delta_b \sin 2n\left(\Theta_b-\Theta_\chi\right)+i\omega_0\Delta_\omega \sin 2n\left(\Theta_\omega-\Theta_\chi\right)\right] \tag{2.34}$$

$$T\left(\Theta_\chi\right) = \frac{\sqrt{\left[\omega_0\Delta_\omega \sin 2n\left(\Theta_\omega-\Theta_\chi\right)\right]^2+\left[\frac{\omega_0}{Q_0}\Delta_b \sin 2n\left(\Theta_b-\Theta_\chi\right)\right]^2\left(1-\Delta_{\omega 1}\right)}}{\frac{\omega_0}{Q_0}\left[1-\Delta_b \cos 2n\left(\Theta_b-\Theta_\chi\right)\right]\sqrt{1-\Delta_{\omega 1}}} \tag{2.35}$$

where the transmissibility phase and amplitude have been expressed as functions of the driving orientation in a manner similar to the frequency and bandwidth in (2.26) and (2.27).

The phase result in (2.34) shows that when the driving force aligns with either principal axes of the structural or damping imperfections such that $\Delta_{\omega 2} = 0$ or $\Delta_{b2} = 0$, the elastic or damping coupling nullifies such that the phase is only characterised by either the damping or

structural imperfection parameters. This subsequently simplifies the measurements needed to identify the remaining imperfection parameters. Using this information, in the following approach, the structural imperfection magnitude and principal axis orientations are first identified using measurements at 4 driving orientations spaced $\pi/4n$ apart, $\Theta_\chi = \Theta_{\chi 0}$, $\Theta_{\chi 0} + \pi/4n$, $\Theta_{\chi 0} + \pi/2n$ and $\Theta_{\chi 0} + 3\pi/4n$, similar to the approach used previously using the frequency and bandwidth measurements.

The transmissibility phase measurements can be used to identify the structural imperfection magnitude and principal axis orientations using the following relationships:

$$\Delta_\omega = \sqrt{\sum_{i=0}^{1}\left[\frac{\tan^2\phi_T\left(\Theta_{\chi 0}+\frac{i\pi}{4n}\right)-\tan^2\phi_T\left(\Theta_{\chi 0}+\frac{(i+2)\pi}{4n}\right)}{\tan^2\phi_T\left(\Theta_{\chi 0}+\frac{i\pi}{4n}\right)+\tan^2\phi_T\left(\Theta_{\chi 0}+\frac{(i+2)\pi}{4n}\right)}\right]^2} \tag{2.36}$$

$$\Theta_\omega = \frac{\prod_{i=0}^{1}\left[\frac{\tan^2\phi_T\left(\Theta_{\chi 0}+\frac{i\pi}{4n}\right)+(-1)^i\tan^2\phi_T\left(\Theta_{\chi 0}+\frac{(i+2)\pi}{4n}\right)}{\tan^2\phi_T\left(\Theta_{\chi 0}+\frac{i\pi}{4n}\right)+(-1)^{i+1}\tan^2\phi_T\left(\Theta_{\chi 0}+\frac{(i+2)\pi}{4n}\right)}\right]}{2n}+\Theta_{\chi 0} \tag{2.37}$$

(2.36) and (2.37) show that using only the phase results is sufficient to identify the structural imperfection parameters.

After identifying the structural imperfection principal axes orientation Θ_ω, the transmissibility amplitude in (2.35) can be used to identify the damping imperfection magnitude and principal axes orientations by aligning the drive force at the structural imperfection principal axis and measuring the transmissibility amplitude at drive locations $\Theta_\chi = \Theta_\omega$, $\Theta_\omega + \pi/4n$, $\Theta_\omega + \pi/2n$ and $\Theta_\omega + 3\pi/4n$. (2.35) is first simplified by neglecting the terms involving $\Delta_{\omega 1}$, noting that $|\Delta_\omega| \ll 1$. The damping imperfection magnitude and principal axis orientations are then identified using the following relationships:

$$\Delta_b = \sqrt{\sum_{i=0}^{1}\left[\frac{T\left(\Theta_\omega+\frac{i\pi}{4n}\right)-T\left(\Theta_\omega+\frac{(i+2)\pi}{4n}\right)}{T\left(\Theta_\omega+\frac{i\pi}{4n}\right)+T\left(\Theta_\omega+\frac{(i+2)\pi}{4n}\right)}\right]^2} \tag{2.38}$$

$$\Theta_b = \frac{\tan^{-1}\left(\prod_{i=0}^{1}\left[\frac{\left|T\left(\Theta_\omega + \frac{i\pi}{4n}\right)\right| + (-1)^i\left|T\left(\Theta_\omega + \frac{(i+2)\pi}{4n}\right)\right|}{\left|T\left(\Theta_\omega + \frac{i\pi}{4n}\right)\right| + (-1)^{i+1}\left|T\left(\Theta_\omega + \frac{(i+2)\pi}{4n}\right)\right|}\right]\right)}{2n} + \Theta_\omega \tag{2.39}$$

Inspecting the relationships in (2.36) – (2.39), the transmissibility amplitude and phase measurements at 8 drive locations have been used to identify the structural and damping imperfection parameters, compared to using the frequency and bandwidth which only involves 4 drive locations. However, in practice, amplitude and phase measurements can be directly measured from the amplitude and phase frequency responses, without requiring the implementation of the half-power method as required for bandwidth measurements.

Having characterised the structural and damping imperfections, the next section includes the effects of angular rate to investigate the interaction between the angular rate and the imperfections identified using the analysis in this section.

2.4. Effects of imperfections and back coupling on device operation and rate sensing performance

In this section, the effects of angular rate on the drive and sense frequency responses are investigated to assess the rate sensing performance in the presence of structural and damping imperfections. The following study also investigates the effects of sense-to-drive back coupling which are often neglected in the literature in the analysis of linear dynamics in CVG's, and the validity of this assumption is investigated.

In what follows, the drive and sense frequency responses in (2.20a) and (2.20b) are considered for the cases where the structural or damping imperfections are present to determine the respective effects on the drive mode operation and rate sensing performance separately. For both cases, the effects of sense-to-drive back coupling are also included ($\eta = 1$ in (2.18)) and the resulting modal responses are compared with the case of neglected back coupling ($\eta = 0$). The sense response is then analysed to identify the dominant effects of each imperfection and back coupling on rate sensing performance in terms of rate sensitivity, bias rate and quadrature error.

2.4.1. Gyroscopic coupling with damping imperfections

Considering the drive and sense mode responses in the absence of structural imperfection ($\Delta_{\omega 1} = \Delta_{\omega 2} = 0$), the complex drive and sense amplitudes in (2.20a) and (2.20b) simplify to:

$$x_b{}^* = x_b e^{i\phi_{xb}} = \chi \frac{-\omega^2 + {\omega_0}^2 + i\omega \frac{\omega_0}{Q_0}(1 - \Delta_{b1})}{Z_b{}^*} \tag{2.40a}$$

$$y_b{}^* = y_b e^{i\phi_{yb}} = \chi \frac{-i\omega \left(\frac{\omega_0}{Q_0}\Delta_{b2} + G_\Omega \Omega\right)}{Z_b{}^*} \tag{2.40b}$$

where

$$Z_b{}^* = (-\omega^2 + {\omega_0}^2)^2 - \omega^2 \left(\frac{{\omega_0}^2}{{Q_0}^2} + \eta {G_\Omega}^2 \Omega^2\right) + \omega^2 \frac{{\omega_0}^2}{{Q_0}^2}\left({\Delta_{b1}}^2 + \eta {\Delta_{b2}}^2\right) + 2i\omega \frac{\omega_0}{Q_0}(-\omega^2 + {\omega_0}^2) \tag{2.41}$$

where x_b, y_b are the amplitudes and ϕ_{xb}, ϕ_{yb} are the phases of the drive and sense modes without the effects of structural imperfection. The back-coupling effects are explicitly identified as the terms in $Z_b{}^*$ involving η. The back coupling effects arise from gyroscopic and damping coupling forces. The 'b' within the subscripts indicates that only damping imperfections are present.

Effects of back coupling on drive mode operation

In CVG's, the PLL algorithms lock the device at resonance by ensuring the drive mode phase is fixed at $\phi_{xb} = -\pi/2$, which is also the phase result $\phi_{x,a,\Omega 0}$ for the approximated drive mode FRF in the absence of angular rate as shown in Figure 2.3(b). For this to occur in the presence of angular rate, the forcing frequency ω must be tracked and adjusted until the real part of $x_b{}^*$ in (2.40a) vanishes. This yields a cubic polynomial in ω^2 where the frequency ω is solved for, giving three solutions for ω. These frequencies are:

$$\omega = \begin{bmatrix} \omega_{X,b0} \\ \omega_{X,b\pm} \end{bmatrix} = \left[\frac{\omega_0}{\sqrt{{\omega_0}^2 + \left(\frac{\delta\omega_b}{2}\right)^2}} \pm \frac{\delta\omega_b}{2} \right] \tag{2.42}$$

where

$$\delta\omega_b = 2\sqrt{\eta\left(\frac{G_\Omega \Omega}{2}\right)^2 - \left(\frac{\omega_0}{2Q_0}\right)^2 \left[(1 - \Delta_{b1})^2 + \eta {\Delta_{b2}}^2\right]} \tag{2.43}$$

$\delta\omega_b$ is a rate-induced frequency split that increases with angular rate and dictates the difference between frequencies $\omega_{X,b+}$ and $\omega_{X,b-}$. $\delta\omega_b$ differs from the structural

imperfections-induced frequency split described in Section 2.3.2 because $\delta\omega_b$ is present even in ideal rings. When the angular rate is sufficiently low or there is sufficient damping in the system, i.e. low Q factors, $\delta\omega_b$ can be minimised and nullified.

When back coupling effects are neglected, i.e. $\eta = 0$, $\delta\omega_b$ is always imaginary, so the rate-induced frequency split is not accounted for and only one frequency ($\omega = \omega_0$) results in a drive phase of $\phi_{xb} = -\pi/2$, in which case the drive and sense mode amplitude frequency responses also exhibit single peaks. However, when back coupling effects are accounted for and for a given bandwidth, there is a critical angular rate Ω_{crit} where $\delta\omega_b$ becomes real-valued. When $\Omega > \Omega_{crit}$, $\omega_{X,b\pm}$ in (2.42) become real, resulting in three frequencies where the drive phase condition $\phi_{xb} = -\pi/2$ can be achieved. Ω_{crit} is obtained by setting $\delta\omega_b = 0$ and solving for Ω, giving:

$$|G_\Omega \Omega_{crit}| = \frac{\omega_0}{Q_0}\sqrt{(1-\Delta_{b1})^2 + {\Delta_{b2}}^2} \tag{2.44}$$

This result indicates that high Q factor devices have lower critical angular rates and as such, are more susceptible to rotation-induced frequency splitting. The damping imperfection parameters have a small influence on the critical angular rate. As a consequence of this frequency split, the multiplicity of the frequencies in (2.42) yielding a drive phase of $\phi_{xb} = -\pi/2$ can lead to the PLL fixing the driving frequency at $\omega_{X,b\pm}$ instead of ω_0, which can affect the sense response considerably, and hence the rate sensing performance. As such, this frequency split is of particular concern for high Q factor devices, especially if Ω_{crit} falls within the designated dynamic range of the device.

In the following, the effects of the angular rate on the drive mode phase in relation to the critical angular rate are investigated. The system considered for this investigation is subjected to the same damping imperfection parameters used for the results in Figure 2.5(a) and (b), but since the this section only includes the damping imperfections, the structural imperfection parameters are set to zero. The drive force is oriented at $\Theta_\chi = 0°$. Angular rates are imposed at 40%, 100%, 120% and 200% of the critical angular rate, which is $\Omega_{crit} = 121\,°/s$ for the present system. Figure 2.7 shows the phase frequency response of the drive mode ϕ_{xb} for the different angular rates considered. Markers have also been shown to show the multiple possible driving frequencies to fix the drive phase at $\phi_{xb} = -\pi/2$ for the angular rate cases $\Omega/\Omega_{crit} = 1.2$ and 2.

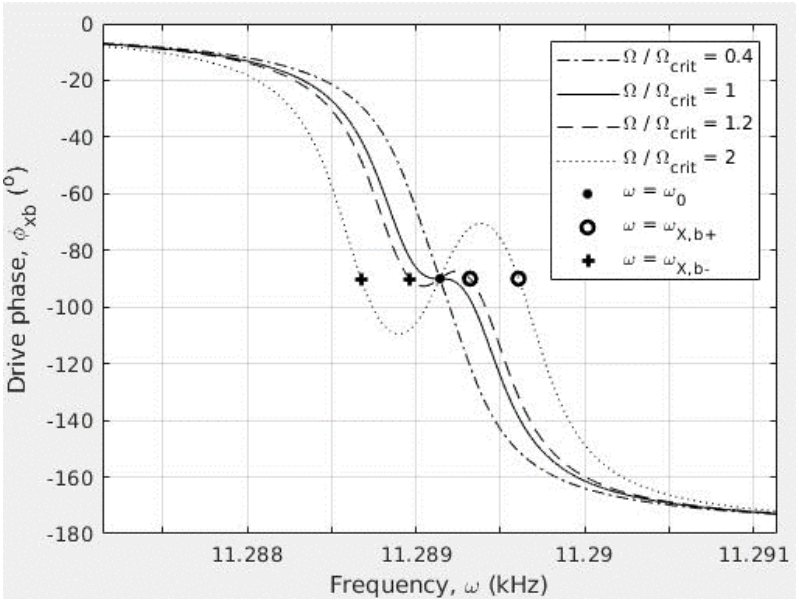

Figure 2.7: Phase frequency response of drive mode at various imposed angular rates

In Figure 2.7, when the angular rate is below the critical angular rate, the drive phase $\phi_{xb} = -\pi/2$ is only achieved at $\omega = \omega_0$, similar to the case with back coupling neglected, indicating that back coupling has negligible impact on the operation of the PLL. The slope of the phase frequency response $\partial\phi_{xb}/\partial\omega$ is monotonically negative. As the angular rate increases, the back coupling effects are increasingly significant. The phase slope $\partial\phi_{xb}/\partial\omega$ at $\omega = \omega_0$ increases, approaching zero as the critical angular rate Ω_{crit} is approached. Increasing the angular rate beyond Ω_{crit} reverses the polarity of the phase slope, thus introducing two additional frequencies at $\omega_{X,b\pm}$ where the drive phase condition $\phi_{xb} = -\pi/2$ is also achieved. To ensure the device continues responding in a manner similar to the case where back coupling is neglected at higher angular rates, it is important that the PLL fixes the driving frequency at $\omega = \omega_0$ at angular rates beyond Ω_{crit}, instead of deviating to $\omega = \omega_{X,b\pm}$.

When $\omega = \omega_0$, the complex drive amplitude in (2.40a) is:

$$x_b{}^*(\omega_0) = \chi \frac{i\omega_0 \frac{\omega_0}{Q_0}(1 - \Delta_{b1})}{-\omega_0{}^2\left[\frac{\omega_0{}^2}{Q_0{}^2}\left(1 - \Delta_{b1}{}^2 - \eta\Delta_{b2}{}^2\right) + \eta G_\Omega{}^2\Omega^2\right]} \tag{2.45}$$

$x_b{}^*(\omega_0)$ is purely imaginary and the imaginary part is negative, indicating a quadrature phase offset relative to the harmonic drive force as $\phi_{xb} = -\pi/2$.

When back coupling is neglected, setting $\eta = 0$ in (2.45) shows that standard CVG operation requires a constant drive amplitude which is unaffected by angular rate changes to ensure

steady sensor output. However, when back coupling is taken into account, the gyroscopic back coupling term $\eta {G_\Omega}^2 \Omega^2$ reduces the drive amplitude attained. The validity of the neglected back coupling assumption is thus confined to the case when $|G_\Omega \Omega| \ll \omega_0/Q_0$, indicating that high Q factor operations are susceptible to larger back coupling effects. To compensate for the back coupling effects, the automatic gain control (AGC) [26] must regulate the harmonic drive force amplitude χ such that it increases with the angular rate to ensure the net drive amplitude remains constant with angular rate changes.

In the following, the effects of the gyroscopic back coupling on the operational drive amplitude are investigated. Figure 2.8(a) and (b) show the drive amplitude frequency responses in the presence of angular rates at $\Omega/\Omega_{crit} = 0.4, 1$ and 2 for the cases of constant and rate-variable driving force amplitudes χ respectively, where the rate-variable χ serves to compensate for the gyroscopic back coupling effects. Markers are also shown to indicate the operating point at $\omega = \omega_0$. The results in Figure 2.8(b) are obtained by varying the drive force amplitude such that $\chi = 0.19, 0.34$ and $0.89\ N/kg$ for angular rates $\Omega/\Omega_{crit} = 0.4, 1$ and 2 respectively.

(a)

(b)

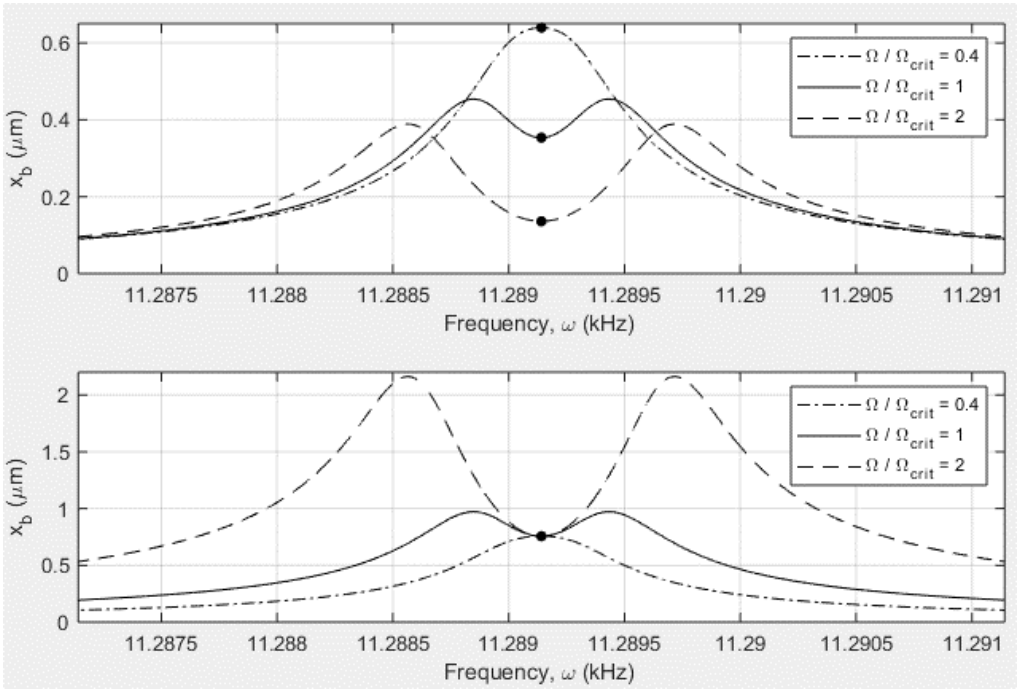

Figure 2.8: Drive mode amplitude frequency responses with (a) constant and (b) rate-variable drive force amplitudes

In Figure 2.8(a), without varying the drive force amplitude to compensate for the gyroscopic back coupling, the angular rate affects the drive amplitude frequency response most significantly for frequencies near $\omega = \omega_0$, while these effects are negligible for off-resonant frequencies. For the frequencies near $\omega = \omega_0$, the amplitudes reduce as the angular rate

increases and the amplitude attenuation is most significant at the chosen driving frequency $\omega = \omega_0$. This is due to the rate-induced frequency split, which results in a change from an amplitude peak at $\omega = \omega_0$ to a local minimum as the angular rate increases. The peak splitting for the results corresponding to $\Omega/\Omega_{crit} = 1$ also shows that the angular rate threshold for peak splitting is lower than Ω_{crit}. However, as this peak splitting threshold is approached, the peak is 'flattened' significantly, increasing the half-power bandwidth.

In Figure 2.8(b), as χ is increased with angular rate, the net drive amplitude at $\omega = \omega_0$ is invariant with the angular rate, as required for standard CVG operation. The increase in drive force amplitude also results in a general increase of the drive amplitude at off-resonant frequencies. However, higher angular rates result in greater drive amplitude fluctuations when ω deviates from ω_0, thus placing a greater necessity for the robustness of the phase-locked-loop (PLL) to keep the frequency constant to ensure steady sensor output.

Rate sensing performance

When $\omega = \omega_0$, the complex sense amplitude in (2.40b) used for rate measurement is given by:

$$y_b{}^*(\omega_0) = -x_b{}^*(\omega_0)\frac{\omega_0\left(\frac{\omega_0}{Q_0}\Delta_{b2} + G_\Omega\Omega\right)}{\omega_0\frac{\omega_0}{Q_0}(1-\Delta_{b1})} \tag{2.46}$$

where $y_b{}^*(\omega_0)$ is purely imaginary, similar to the complex drive amplitude in (2.45).In the absence of imperfections ($\Delta_{b1} = \Delta_{b2} = 0$), the following phase relationships apply:

- When $\Omega > 0$, the imaginary parts of $x_b{}^*(\omega_0)$ and $y_b{}^*(\omega_0)$ are of opposite signs, the sense mode oscillates in antiphase with the drive mode
- When $\Omega < 0$, the imaginary parts of $x_b{}^*(\omega_0)$ and $y_b{}^*(\omega_0)$ are of identical signs, the sense mode oscillates in phase with the drive mode

The presence of damping imperfection retains the in/antiphase relationship between the drive and sense mode oscillations, but the term involving Δ_{b2} in (2.46), which stems from the damping coupling force, results in a systematic offset of the sense amplitude. This offset is commonly known as the bias as the sensor output does not nullify in the absence of angular rate. Using (2.46) for rate sensing, (2.46) can be expressed as:

$$Im\left[y_b{}^*(\omega_0)|_{\chi(\Omega)}\right] = -S_b\left(\Omega + \Omega_{z,b}\right) \tag{2.47}$$

where

$$S_b = -x_b(\omega_0)\frac{G_\Omega}{\frac{\omega_0}{Q_0}(1-\Delta_{b1})} \tag{2.48}$$

$$\Omega_{z,b} = \frac{\frac{\omega_0}{Q_0}\Delta_{b2}}{G_\Omega} \tag{2.49}$$

S_b and $\Omega_{z,b}$ are the rate sensitivity and bias rate in the presence of damping imperfections. The rate sensitivity and bias rate are commonly known as the scale factor and zero-rate error, and are important parameters dictating rate sensing performance. In practice, a high rate sensitivity and nullified bias rate are desirable. From (2.49), the damping imperfections degrade rate sensing performance by introducing a bias rate, unless the drive force aligns with the damping principal axes such that $\Delta_{b2} = 0$. For the rate sensitivity, the damping imperfection effects are dependent on the drive force orientation. Rate sensitivity increases when $\Delta_{b1} > 0$, and vice versa. However, since $|\Delta_b| \ll 1$, such effects are small. The damping imperfections mainly affect the rate sensing performance through bias rate rather than rate sensitivity.

The following investigates the effects of angular rate on the sense amplitude in the presence of damping imperfections, as in the case for open-loop rate sensing. The systems considered are subjected to nominal Q factors of $Q_0 = 1.1e4, 2.2e4$ and $5.5e4$, resulting in critical angular rates of $\Omega_{crit} = 243, 121$ and $49\ °/s$ respectively. The system with $Q_0 = 2.2e4$ is identical to that used for the results in Figure 2.8(a) and (b). The driving frequency has been set at $\omega = \omega_0$ while the angular rate is varied. Based on these, Figure 2.9 below shows the variation of the sense amplitude $y_b(\omega_0)$ with the angular rate for the different nominal Q factors considered, with and without back coupling. Markers are also shown where the sense amplitude nullifies, indicating the bias rate.

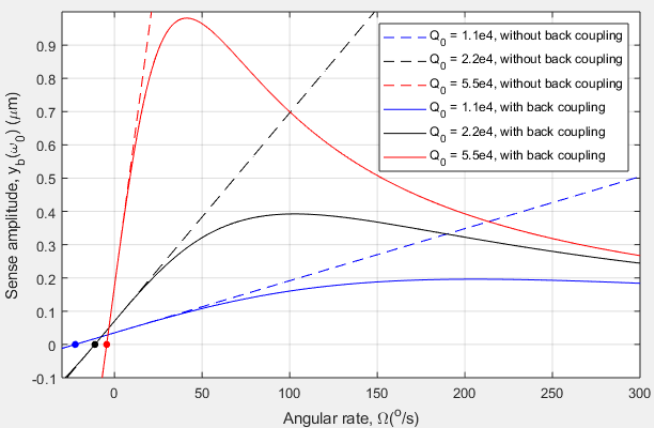

Figure 2.9: Effect of nominal Q factor on the variation of the sense mode amplitude at $\omega = \omega_0$ with the angular rate for the cases of with and without back coupling

When back coupling effects are taken into account ($\eta = 1$), the sense amplitude increases linearly with the angular rate for low angular rates. As the angular rate increases, this is followed by a nonlinear variation where the gradient of the sense amplitude reduces, until a turning point is reached, beyond which the sense amplitude decreases. This turning point occurs at the critical angular rate. The reduced sense amplitude gradient up to the critical angular rate results in a reduced rate sensitivity. This occurs because the angular rate has two competing effects on the net Coriolis force. Increasing the angular rate linearly amplifies the Coriolis force, which is responsible for the linear growth of the sense amplitude at low angular rates. Increasing the angular rate also amplifies the gyroscopic back coupling, thus reducing the drive amplitude in the manner shown in Figure 2.8(a), which then reduces the Coriolis force amplitude. Similar to the drive amplitude in Figure 2.8(b), the back coupling effects can be compensated by fixing the drive amplitude with angular rate changes using rate-variable drive force amplitudes, in which case the sense amplitude variation of the neglected back coupling case ($\eta = 0$) is reproduced.

The results in Figure 2.9 also show that the nonlinearity occurs at lower angular rates for higher Q factor operations due to the reduced critical angular rate. As such, as the Q factor is increased, the sense amplitude and rate sensitivity diminishes more significantly due to the gyroscopic back coupling. At higher angular rates where $|G_\Omega \Omega| \gg \omega_0/Q_0$, the sense amplitudes are desensitised to Q factor variations, unlike conventional CVG operations where Q factor enhancements generally amplify the sense amplitude. As such, the implementation of rate-varying drive force amplitudes is of greater importance for higher Q factor devices.

Figure 2.9 shows that higher Q factors suppress the bias rate. At higher Q_0, the increased rate sensitivity results in the sense amplitude nullifying at smaller angular rates. This is clear from Figure 2.9 as increasing Q_0 from 1.1e4 to 5.5e4 reduces the bias rate from $\Omega_{z,b} = 22.4\,°/s$ to $4.8\,°/s$. This highlights the two ways high Q factor operations are advantageous for standard linear device operation, as both the rate sensitivity and bias rate performance are improved.

In the following, the effects of the damping imperfection magnitude on the bias rate are investigated. Figure 2.10 below shows the variations of the bias rate with the drive force orientation for damping imperfection magnitudes of $\Delta_b = 0.0011, 0.022$ and $, 0.11$.

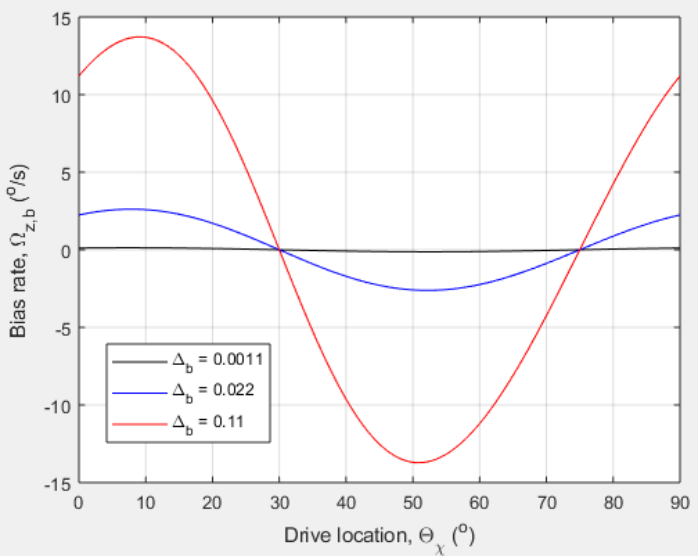

Figure 2.10: Bias rate variation with drive location Θ_χ with different damping imperfection magnitudes

In Figure 2.10, the bias rate nullifies at both damping principal axes, $\Theta_\chi = 30°$ and 75°. This is due to the elimination of the modal damping coupling force, i.e. $\Delta_{b2} = 0$. The alignment of the drive force with the principal axes is of increasing importance at larger damping imperfection magnitudes to minimise bias rate errors. On the other hand, for small damping imperfection magnitudes, the effect of the drive force orientation is insignificant as the bias rate is negligible in all cases.

In practice, due to the cyclic symmetry of the ring, larger magnitudes of damping imperfections are untypical unless significant material anisotropies are present. Δ_b values within the order of magnitude of 0.1 have been reported in literature for piezoelectric devices [14, 43], but these cases have not been widely reported for capacitive devices. As such, the effects of damping imperfections on rate sensing performance will not be considered for the remainder of this dissertation.

2.4.2. Gyroscopic coupling with structural imperfections

The complex drive and sense mode amplitudes in the absence of damping imperfections are obtained from (2.20a) and (2.20b) by setting $\Delta_{b1} = \Delta_{b2} = 0$, yielding:

$$x_\omega{}^* = x_\omega e^{i\phi_{x\omega}} = \frac{\chi\left[-\omega^2 + {\omega_0}^2(1-\Delta_{\omega 1}) + i\omega\frac{\omega_0}{Q_0}\right]}{{Z_\omega}^*} \tag{2.50a}$$

$$y_\omega{}^* = y_\omega e^{i\phi_{y\omega}} = \frac{\chi(-{\omega_0}^2\Delta_{\omega 2} - i\omega G_\Omega \Omega)}{{Z_\omega}^*} \tag{2.50b}$$

where

$$Z_\omega{}^* = (-\omega^2 + {\omega_0}^2)^2 - \omega^2\left(\frac{{\omega_0}^2}{{Q_0}^2} + \eta {G_\Omega}^2\Omega^2\right) - {\omega_0}^4\left({\Delta_{\omega 1}}^2 + \eta {\Delta_{\omega 2}}^2\right) + 2i\omega\frac{\omega_0}{Q_0}(-\omega^2 + {\omega_0}^2) \tag{2.51}$$

Here, the back coupling originates from the gyroscopic back coupling term $\eta {G_\Omega}^2\Omega^2$ and linear elastic back coupling term $\eta {\Delta_{\omega 2}}^2$. x_ω, y_ω are the amplitudes and $\phi_{x\omega}$, $\phi_{y\omega}$ are the phases of the drive and sense modes without damping imperfection. The 'ω' within the subscript indicates the present case where only structural imperfections are present.

Effects of back coupling on drive mode operation

As described in Section 2.4.1, the PLL sets the frequency ω to ensure drive mode resonance using the drive phase condition $\phi_{x\omega} = -\pi/2$, which eliminates the real part of the complex drive amplitude in (2.50a). This yields a cubic equation in ω^2 which must be solved to identify the driving frequency ω applied in operation. This is given by:

$$\mathrm{A}_\omega = [-\omega^2 + {\omega_0}^2(1 - \Delta_{\omega 1})]\left[(-\omega^2 + {\omega_0}^2)^2 - \omega^2\left(\frac{{\omega_0}^2}{{Q_0}^2} + \eta {G_\Omega}^2\Omega^2\right) - {\omega_0}^4\left({\Delta_{\omega 1}}^2 + \eta {\Delta_{\omega 2}}^2\right)\right] + 2\omega^2\frac{{\omega_0}^2}{{Q_0}^2}(-\omega^2 + {\omega_0}^2) = 0 \tag{2.52}$$

When back coupling effects are neglected ($\eta = 0$), the real-valued solution of (2.52) is $\omega = \omega_0\sqrt{1 + \Delta_{\omega 1}}$, which is the undamped frequency in the absence of rotation identified in Section 2.3.2.1. When back coupling effects are taken into account, exact solutions of (2.52) can be obtained using Cardano's method [60], which results in lengthy expressions for ω. As such, for this investigation, an approximate method will be implemented to solve (2.52).

When $\Delta_{\omega 1} = 0$, an exact real-valued solution of $\mathrm{A}_\omega = 0$ in (2.52) is $\omega = \omega_0$, similar to the case without structural imperfections investigated in Section 2.4.1. This is because $\Delta_{\omega 1} = 0$ represents the case where the drive force orientation aligns precisely between the principal axes of maximum and minimum stiffnesses, i.e. the drive force aligns at positions of mean stiffness of the ring. Similar to the case of damping imperfections, two other driving frequencies having drive mode phase $\phi_{x\omega} = -\pi/2$ are possible, and are given by:

$$\omega = \omega_{X,\omega\pm} = \sqrt{\frac{{\omega_0}^2}{2}\left(1 + \sqrt{1 - \eta {\Delta_{\omega 2}}^2}\right) + \eta\left(\frac{G_\Omega\Omega}{2}\right)^2 - \left(\frac{\omega_0}{2Q_0}\right)^2} \pm \frac{\delta\omega_\omega}{2} \tag{2.53}$$

where

$$\delta\omega_\omega = 2\sqrt{\frac{{\omega_0}^2}{2}\left(1-\sqrt{1-\eta{\Delta_{\omega 2}}^2}\right)+\eta\left(\frac{G_\Omega\Omega}{2}\right)^2-\left(\frac{\omega_0}{2Q_0}\right)^2} \tag{2.54}$$

which gives the critical angular rate:

$$|G_\Omega\Omega_{crit}| = \sqrt{\left(\frac{\omega_0}{Q_0}\right)^2-2{\omega_0}^2\left(1-\sqrt{1-{\Delta_{\omega 2}}^2}\right)} \tag{2.55}$$

Similar to the case without structural imperfections investigated in Section 2.4.1, the frequencies giving $\phi_{x\omega} = -\pi/2$ depend on the frequency split $\delta\omega_\omega$. When $\Omega > \Omega_{crit}$, $\delta\omega_\omega$ is real, giving rise to the frequency multiplicity at $\phi_{x\omega} = -\pi/2$. Comparing (2.55) against the critical angular rate without structural imperfections in (2.44), the structural imperfection lowers the critical angular rate through the elastic back coupling, and if $\Delta_{\omega 2}$ is sufficiently large, the frequency split can occur at zero angular rate, i.e. $\Omega_{crit} = 0$. This shows that the angular rate and structural imperfections interact constructively, contributing to the frequency split. Since the effects of the critical angular rate have been discussed in Section 2.4.1, such investigation will not be repeated in this section.

In what follows, (2.52) is solved using a perturbation method to obtain the driving frequency required for the drive phase condition $\phi_{x\omega} = -\pi/2$, unrestricted to the case where $\Delta_{\omega 1} = 0$. Using this method, the exact solution frequency $\omega = \omega_0$ when $\Delta_{\omega 1} = 0$ is used as the unperturbed solution and $\Delta_{\omega 1}$ is used as the perturbation variable. With this implementation, the driving frequency is expressed as $\omega^2 = {\omega_0}^2 + (\partial\omega^2/\partial\Delta_{\omega 1})\Delta_{\omega 1} + O\left({\Delta_{\omega 1}}^2\right)$, where the derivative $\partial\omega^2/\partial\Delta_{\omega 1}$ is to be determined. Higher order expansions require calculations of higher order derivatives of ω^2 with respective to $\Delta_{\omega 1}$. By differentiating (2.52) such that $\partial \mathrm{A}_\omega/\partial\Delta_{\omega 1} = 0$, the first derivative of the driving frequency $\partial\omega^2/\partial\Delta_{\omega 1}$ can be obtained, yielding the following result for the driving frequency up to first order in $\Delta_{\omega 1}$:

$$\omega^2 = {\omega_{X,\omega 0}}^2 = {\omega_0}^2\left[1+\left(\frac{\frac{{\omega_0}^2}{{Q_0}^2}+\eta{G_\Omega}^2\Omega^2+\eta{\omega_0}^2{\Delta_{\omega 2}}^2}{\frac{{\omega_0}^2}{{Q_0}^2}-\eta{G_\Omega}^2\Omega^2-\eta{\omega_0}^2{\Delta_{\omega 2}}^2}\right)\Delta_{\omega 1}\right]+O\left({\Delta_{\omega 1}}^2\right) \tag{2.56}$$

The accuracy of the first-order expansion result in (2.56) is limited to small $\Delta_{\omega 1}$, corresponding to the case where the structural imperfection magnitude is sufficiently small or larger structural imperfection magnitudes for drive locations near $\Theta_\chi = \Theta_\omega \pm \pi/4n$. As such, the following investigation is based on this assumption. The accuracy for cases involving

larger structural imperfection magnitudes or other drive locations can be improved by increasing the order of expansion in (2.56).

Compared to the drive frequency for the neglected back coupling case $\omega = \omega_0\sqrt{1+\Delta_{\omega 1}}$, the back coupling in (2.56) amplifies the deviation of the driving frequency from the nominal frequency ω_0. This effect is more significant as the critical angular rate is approached.

The complex drive amplitude when $\omega = \omega_{X,\omega 0}$ can similarly be obtained using a perturbation approach. (2.50a) is expanded as a Taylor series in $\Delta_{\omega 1}$, using ${x_\omega}^*(\omega_0)$ as the unperturbed, zero-order component such that:

$$
\begin{aligned}
{x_\omega}^*(\omega_{X,\omega 0}) &= {x_\omega}^*(\omega_0) + \Delta_{\omega 1}\left(\frac{\partial {x_\omega}^*}{\partial \Delta_{\omega 1}}\right)|_{\omega=\omega_0} + O\left({\Delta_{\omega 1}}^2\right) \\
&= \chi \frac{i\omega_0 \frac{\omega_0}{Q_0}}{-{\omega_0}^2\left(\frac{{\omega_0}^2}{{Q_0}^2} + \eta{\omega_0}^2{\Delta_{\omega 2}}^2 + \eta{G_\Omega}^2\Omega^2\right)}\left[1\right. \\
&\quad \left. - \frac{\frac{{\omega_0}^2}{{Q_0}^2} + \eta{G_\Omega}^2\Omega^2 - \eta{\omega_0}^2{\Delta_{\omega 2}}^2}{\frac{{\omega_0}^2}{{Q_0}^2} - \eta{G_\Omega}^2\Omega^2 - \eta{\omega_0}^2{\Delta_{\omega 2}}^2}\frac{\Delta_{\omega 1}}{2}\right] + O\left({\Delta_{\omega 1}}^2\right)
\end{aligned}
\tag{2.57}
$$

where

$$
{x_\omega}^*(\omega_0) = \chi \frac{i\omega_0 \frac{\omega_0}{Q_0}}{-{\omega_0}^2\left(\frac{{\omega_0}^2}{{Q_0}^2} + \eta{\omega_0}^2{\Delta_{\omega 2}}^2 + \eta{G_\Omega}^2\Omega^2\right)} \tag{2.58}
$$

$$
\begin{aligned}
&\left(\frac{\partial {x_\omega}^*}{\partial \Delta_{\omega 1}}\right)|_{\omega=\omega_0} \\
&= \chi \frac{i\omega_0 \frac{\omega_0}{Q_0}}{-2{\omega_0}^2\left(\frac{{\omega_0}^2}{{Q_0}^2} + \eta{\omega_0}^2{\Delta_{\omega 2}}^2 + \eta{G_\Omega}^2\Omega^2\right)}\left(\frac{\frac{{\omega_0}^2}{{Q_0}^2} + \eta{G_\Omega}^2\Omega^2 - \eta{\omega_0}^2{\Delta_{\omega 2}}^2}{\frac{{\omega_0}^2}{{Q_0}^2} - \eta{G_\Omega}^2\Omega^2 - \eta{\omega_0}^2{\Delta_{\omega 2}}^2}\right)
\end{aligned}
\tag{2.59}
$$

Compared to the complex drive amplitude without structural imperfections in (2.45), the unperturbed complex drive amplitude in (2.58) is subjected to a larger attenuation as both the elastic and gyroscopic back coupling reduce the drive amplitude. As such, to achieve any drive amplitude and keep it constant across angular rate changes, the drive force amplitude χ must be increased to larger values compared to the case without structural imperfections as this increase must compensate for both the gyroscopic and elastic back coupling effects. This also

shows that the presence of the structural imperfections-induced elastic back coupling reduces the accuracy of the neglected back coupling assumption, where the validity of this assumption is restricted to sufficiently low nominal Q factors such that $(\omega_0/Q_0)^2 \gg {\omega_0}^2{\Delta_{\omega 2}}^2 + {G_\Omega}^2\Omega^2$.

Rate sensing performance

The complex sense amplitude is given by:

$$y_\omega{}^*\left(\omega_{X,\omega 0}\right) = \frac{\left(f_\Omega\bar{\omega}^2 - f_\Delta\omega_{X,\omega 0}\frac{\omega_0}{Q_0}\right) + i\left(f_\Omega\omega_{X,\omega 0}\frac{\omega_0}{Q_0} + f_\Delta\bar{\omega}^2\right)}{(\bar{\omega}^2)^2 + {\omega_{X,\omega 0}}^2\frac{{\omega_0}^2}{{Q_0}^2}} \tag{2.60}$$

where

$$f_\Omega = G_\Omega\Omega\omega_{X,\omega 0}\left[x_\omega\left(\omega_{X,\omega 0}\right)\right] \tag{2.61}$$

$$f_\Delta = -{\omega_0}^2\Delta_{\omega 2}\left[x_\omega\left(\omega_{X,\omega 0}\right)\right] \tag{2.62}$$

$$\bar{\omega}^2 = {\omega_{X,\omega 0}}^2 - {\omega_0}^2(1-\Delta_{\omega 1}) = {\omega_0}^2\Delta_{\omega 1}\left(1 + \frac{\frac{{\omega_0}^2}{{Q_0}^2} + \eta{G_\Omega}^2\Omega^2 + \eta{\omega_0}^2{\Delta_{\omega 2}}^2}{\frac{{\omega_0}^2}{{Q_0}^2} - \eta{G_\Omega}^2\Omega^2 - \eta{\omega_0}^2{\Delta_{\omega 2}}^2}\right) \tag{2.63}$$

f_Ω and f_Δ are the amplitudes of the modal-mass-normalised Coriolis and linear elastic coupling forces respectively. Due to the proportionality of these forces to the drive amplitude $x_\omega\left(\omega_{X,\omega 0}\right)$, as shown in (2.57), the amplitudes of these forces are reduced due the gyroscopic and elastic back coupling effects. $\bar{\omega}^2$ is a frequency detuning parameter which, from (2.63), is amplified by the gyroscopic and elastic back coupling. Appearing in the denominator of (2.60), the frequency detuning diminishes both real and imaginary parts of the sense mode response. The gyroscopic back coupling results in the nonlinear rate dependence of the frequency detuning $\bar{\omega}^2$. This leads to a nonlinear relationship between the complex sense amplitude in (2.60) and the angular rate Ω, particularly at higher angular rates unless the condition $(\omega_0/Q_0)^2 \gg {\omega_0}^2{\Delta_{\omega 2}}^2 + {G_\Omega}^2\Omega^2$ is sufficiently satisfied or $\Delta_{\omega 1} = 0$.

The structural imperfection parameters $\Delta_{\omega 1}$ and $\Delta_{\omega 2}$ have distinct effects. From (2.63), $\Delta_{\omega 1}$ contributes to the frequency detuning and from (2.62), $\Delta_{\omega 2}$ contributes to the linear elastic coupling force. These are the main principles through which the structural imperfections deviate the sense response from that of the ideal case, hence the rate sensing performance. When $\Delta_{\omega 1} = 0$, the frequency detuning $\bar{\omega}^2$ nullifies. The real and imaginary parts of the complex sense amplitude in (2.60) are purely attributed to the linear elastic coupling and

Coriolis forces respectively, as the contributions of f_Ω and f_Δ decouple. On the other hand, $\Delta_{\omega 2} = 0$ eliminates the linear elastic coupling force due to the alignment of the drive force with the principal axes. Unless the ring is ideal or trimmed, the conditions $\Delta_{\omega 1} = 0$ and $\Delta_{\omega 2} = 0$ are mutually exclusive as they correspond to different driving force orientations.

The real and imaginary parts of the complex sense amplitude in (2.60) affect the sensor performance through distinct roles. For an ideal device or an imperfect device with only damping imperfections as discussed in Section 2.4.1, the complex sense amplitude is imaginary (see (2.46)), similar to the drive complex amplitude, as the sense mode oscillates in phase/antiphase with the drive mode. As such, the imaginary part in (2.60) is the useful rate output for measuring Ω. However, in the presence of structural imperfections, a nonzero real part appears in the complex sense amplitude. The real part is known as the quadrature output and is regarded as a measurement error, as the presence of the real part distorts the phase relationship between the drive and sense modes. As such, expressing the imaginary part as $Im\left[{y_\omega}^*\left(\omega_{X,\omega 0}\right)\right] = -S_\omega\left(\Omega + \Omega_{z,\omega}\right)$, the corresponding angular rate sensitivity and bias rate can be obtained, given by:

$$S_\omega(\Omega) = -x_\omega\left(\omega_{X,\omega 0}\right)\frac{G_\Omega {\omega_{X,\omega 0}}^2 \frac{\omega_0}{Q_0}}{(\bar{\omega}^2)^2 + {\omega_{X,\omega 0}}^2 \frac{{\omega_0}^2}{{Q_0}^2}} \tag{2.64}$$

$$\Omega_{z,\omega} = -\frac{{\omega_0}^2 \Delta_{\omega 2}(\bar{\omega}^2|_{\Omega=0})}{G_\Omega {\omega_{X,\omega 0}}^2 \frac{\omega_0}{Q_0}} \tag{2.65}$$

Recalling that $Im\left[{y_\omega}^*\left(\omega_{X,\omega 0}\right)\right]$ is nonlinear in Ω due to the rate-varying frequency detuning $\bar{\omega}^2$ in (2.63), the rate sensitivity is rate-dependent, decreasing at higher angular rates due to the gyroscopic and elastic back coupling. This shows that the back coupling has performance degrading effects on rate sensing. A larger structural imperfection magnitude also amplifies the frequency detuning, thus similarly degrading the rate sensitivity. The bias rate is also dependent on the frequency detuning. However, since the bias rate corresponds to the sense response without rotation, the frequency detuning when $\Omega = 0$ is used in (2.65).

In (2.64), the presence of structural imperfections limits the rate sensitivity gain through the enhancement of the nominal Q factor as the frequency detuning $\bar{\omega}^2$ in (2.64) is not nullified. The interaction between the frequency detuning and bandwidth terms in the denominator of (2.64) dictates the rate sensitivity, where the following interpretations apply:

i) When $|\bar{\omega}^2| \gg \omega_{X,\omega 0}(\omega_0/Q_0)$, the rate sensitivity is inversely proportional to Q_0, so increasing the nominal Q factor reduces the rate sensitivity. The rate sensitivity decreases with larger frequency detuning.

ii) When $\omega_{X,\omega 0}(\omega_0/Q_0) \gg |\bar{\omega}^2|$, the rate sensitivity is proportional to Q_0, so increasing the nominal Q factor increases the rate sensitivity. The rate sensitivity is insensitive to frequency detuning.

As such, systems with higher Q_0 (case i)) are generally more susceptible to rate sensitivity degradation effects of the frequency detuning, thus necessitating a higher manufacturing precision to ensure $\bar{\omega}^2 = 0$. High Q_0 also increases the magnitude of the bias rate, as (2.65) shows that $\Omega_{z,\omega} \propto Q_0$. This contrasts for the case with damping imperfections, $\Omega_{z,b}$ in (2.49) where $\Omega_{z,b} \propto {Q_0}^{-1}$.

Back coupling effects on rate dependency of rate output

In the following, the effects of back coupling on the rate output in the presence of structural imperfections is investigated. A system with a structural imperfection magnitude of $\Delta_\omega = 2.66e-5$ is considered, corresponding to a frequency split of $0.3\,Hz$ in the absence of rotation. The damping imperfection magnitude Δ_b is set at zero and the remaining parameters are identical to those used for the results in Figure 2.3(a), (b) and Figure 2.4(a), (b). Using the system described, Figure 2.11 below shows a comparison of the variations of the rate output with the angular rate for the cases of with and without back coupling. The angular rate is ranged up to the critical angular rate $\Omega_{crit} = 92\,°/s$ and the drive amplitude is fixed at $0.39\,\mu m$ across the angular rates considered by varying the drive force amplitude χ.

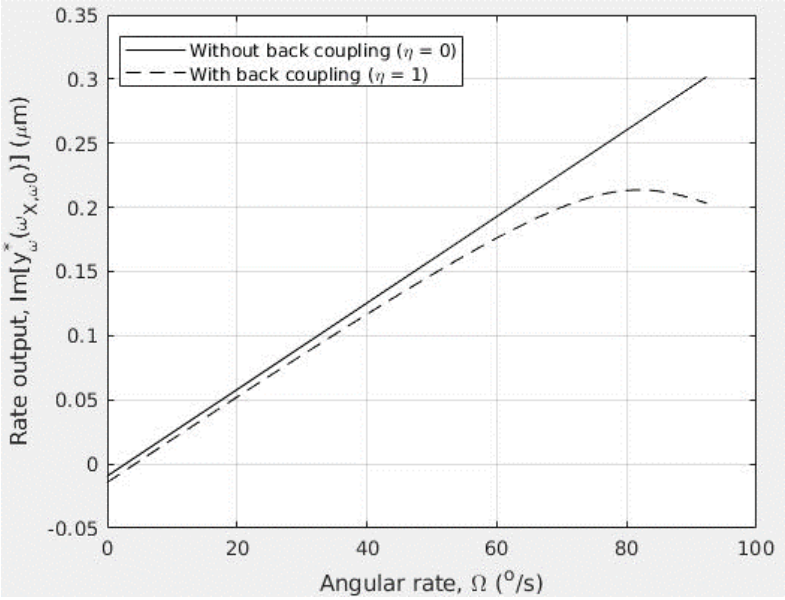

Figure 2.11: Variation of the imaginary part of the complex sense amplitude with the angular rate, with and without back coupling

In Figure 2.11, for angular rates much lower than the critical angular rate, the rate output is linear with respect to the angular rate for both $\eta = 0$ and $\eta = 1$, indicating that the back coupling effects are insignificant as the condition $(\omega_0/Q_0)^2 \gg {\omega_0}^2{\Delta_{\omega 2}}^2 + {G_\Omega}^2\Omega^2$ is well satisfied. The nonlinearity of the variation increases in significance at higher angular rates, decreasing the rate output beyond a threshold angular rate at $\Omega = 82\,°/s$. This reduction of the rate output can be interpreted erroneously as a lower measured angular rate. This nonlinear variation is not eliminated despite the implementation of the rate-variable drive force amplitude to fix the drive amplitude across the range of angular rates considered. This an important distinction from the case without structural imperfections shown in Figure 2.9, indicating the structural imperfections pose a limitation on the device dynamic range.

Effects of structural imperfection magnitude, back coupling and Q factor on rate sensing performance

In the following, the effects of the structural imperfection magnitude, back coupling and the nominal Q factor on the bias rate and rate sensitivity are investigated. The structural imperfection magnitudes in the system are varied from $\Delta_\omega = 0$ to $3.1e-5$, corresponding to rotation-free frequency splits up to $0.35\,Hz$. Nominal quality factors of $Q_0 = 1.1e4$ and $2.2e4$ are used. Figure 2.12(a) shows the variation of the bias rate with the rotation-free frequency split $\omega_0\Delta_\omega$ for both the Q_0 considered, with and without back coupling. Figure 2.12(b) shows the corresponding results for the rate sensitivity, normalised with respect to the rate sensitivity for the ideal/trimmed ring. These results are obtained by calculating the imaginary part of the complex sense amplitude for angular rates below the critical angular rate, i.e. $(\omega_0/Q_0)^2 > {\omega_0}^2{\Delta_{\omega 2}}^2 + {G_\Omega}^2\Omega^2$.

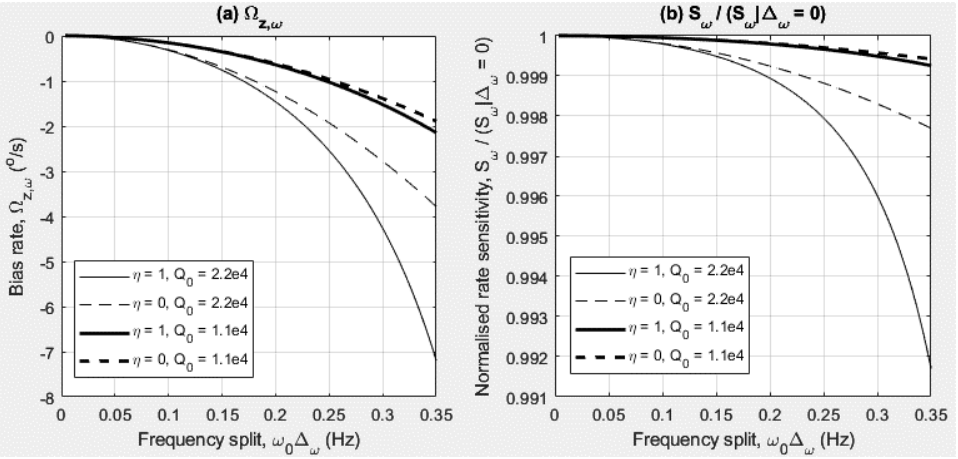

Figure 2.12: Effects of back coupling and Q factor on the (a) bias and (c) sensitivity variation with frequency split

In Figure 2.12(a), the back coupling clearly degrades rate sensing performance by amplifying the bias error. This effect is negligible for smaller structural imperfection magnitudes, but

amplifies significantly as the imperfection magnitude increases. For a rotation-free frequency split of $0.35\,Hz$, the back coupling doubles the bias rate for the case with $Q_0 = 2.2e4$. Reducing the Q factor significantly reduces the bias rate and suppresses the back coupling effects. This is because reducing the Q factor increases the bandwidth, which increases the critical angular rate. In Figure 2.12(b), the rate sensitivity degradation exhibits similar variations, where the back coupling significantly degrades the rate sensitivity more significantly for the case with $Q_0 = 2.2e4$ compared to $Q_0 = 1.1e4$.

The effects of back coupling and structural imperfection on the angular rate sensing performance have been investigated. Such effects negatively affect the rate sensitivity and bias rate of the device, and devices with higher quality factors are more susceptible to this performance degradation. These are significant considerations when sensor performance enhancement based on quality factor amplification is pursued.

2.5. Summary and conclusions

In this chapter, a linear mathematical model has been developed to describe the linear dynamics of the vibrating rings subjected to damping and structural imperfections. The damping and structural imperfections are modelled as non-uniform material properties such as the Young's modulus which varies with circumferential position on the ring, and measurement-based methods have been developed to identify the magnitudes and principal axis orientations of these imperfections. The effects of angular rate are also included in the mathematical model, based on which the effects of the sense-to-drive back coupling and imperfections on the rate sensing performance have been analysed in terms of the rate sensitivity, bias rate and quadrature error.

The structural and damping imperfection magnitudes and principal axes can be identified using frequency response measurements of the drive and sense modes in the absence of rotation. Using this approach, single point measurements with either the drive or sense mode response, and dual point measurements involving both the drive and sense responses have been considered. The drive force orientation is varied around the ring, varying the drive and sense amplitude frequency responses with the drive force orientation. The varying amplitude frequency responses are used to obtain the variations of the modal bandwidth and resonant frequency with the drive force orientation. It is found that for the drive mode these quantities exhibit maximum and minimum values at the principal axes, thus enabling the orientations of these principal axes to be located. The phase frequency response of the sense mode can also be used for this purpose, where it is found that specific phase conditions apply when the drive force aligns with the principal axes. The identified variations of these quantities with the drive

location are then used to develop practical measurement procedures to identify the imperfection parameters using measurements at only 4 or 8 drive force orientations.

When angular rate is imposed, the resulting sense response is analysed to represent open-loop rate measurements. The sense-to-drive back coupling, in conjunction with the structural and damping imperfections have different effects on the rate sensing performance. The back coupling is characterised by gyroscopic, elastic and damping back coupling. For the drive mode, the damping back coupling has small impact on achieving resonance. However, the gyroscopic and elastic back coupling result in the emergence of multiple frequencies achieving resonant drive phase condition when the angular rate exceeds a critical value, where this critical angular rate is dictated by the bandwidth (or Q factor). Systems with more damping, hence larger bandwidth, possess higher critical angular rates. The PLL must ensure the frequency remains fixed when the critical angular rate is exceeded to ensure proper device operation. The gyroscopic and elastic back coupling also reduce the drive amplitude at resonance, in which case the AGC must increase the drive force amplitude to compensate for these effects. The validity of the neglected back coupling assumption is restricted to the case where the angular rate is significantly below the critical angular rate, which requires a larger bandwidth relative to the gyroscopic and elastic back coupling.

When the drive amplitude is fixed, the sense response is then analysed to assess rate sensing performance in terms of the bias rate, rate sensitivity and quadrature error. It is found that the damping imperfections mainly result in the introduction of bias rates while minimally affecting the rate sensitivity. The bias rate due to damping imperfections can be eliminated by aligning the drive force orientation with the damping principal axes, which have been identified from the preceding analysis in this chapter. The structural imperfection effects are more significant, impacting the bias rate, rate sensitivity and quadrature error negatively. The structural imperfection results in a frequency detuning which is amplified by the gyroscopic and elastic back coupling. This frequency detuning introduces a bias rate and quadrature error, thus distorting the phase of the sense oscillation. This frequency detuning also degrades the rate sensitivity. It is found that higher Q factor systems are more susceptible to the performance degrading effects of the structural imperfections, gyroscopic and elastic back coupling.

The remainder of this thesis will focus on the nonlinear modelling of the ring and as such, detailed discussions of the imperfections will not be pursued further and it is assumed that the imperfection magnitudes and principal axes orientations have been identified. The following studies will also ensure that the neglected back coupling assumption is accurate by focusing on the cases where the critical angular rate is high.

3. ELECTROSTATIC NONLINEARITIES: GENERAL EFFECTS ON BASIC OPERATION

3.1. Introduction

In Chapter 2, the linear dynamics of a vibrating ring in the presence of angular rate was modelled and the sense response was investigated in the context of rate measurement. For a perfect, linear device the sense response is proportional to the applied angular rate and the rate sensitivity (scale factor) is proportional to the drive amplitude. Driving the resonator into large amplitude vibrations offers potential performance enhancements by amplifying the Coriolis force, which is small in MEMS vibrating gyroscopes due to the small mass [28]. However, in practice ring vibration is susceptible to nonlinearities at large ring displacements which cause the rate output to deviate compared to linear operation [48]. In capacitive CVG's, significant nonlinear electrostatic forces can occur at relatively low displacement levels due to the narrow gaps between the ring and electrodes [48, 49].

The purpose of this chapter is to extend the mathematical model developed in Chapter 2 to include electrostatic nonlinearity effects and investigate the effects of electrostatic nonlinearity on sensor performance. In this chapter and the remainder of this dissertation, the investigations on the electrostatic nonlinearities focus on the $n = 2$ flexural mode pair typically used in the operation of these devices. The origin of the nonlinear electrostatic effects is studied in detail, followed by a development of the nonlinear equations of motion to investigate the sense dynamics pertinent to rate sensing. The sensor performance is investigated in terms of the rate sensitivity, bias rate and quadrature error for the cases of perfect and imperfect rings, based on which comparisons are made against the expected sensor performance of the corresponding linear device. The effects of key device parameters are also identified. For both perfect and imperfect cases, numerical results are shown based on the theoretical analysis and compared against FE results to validate the presence of the nonlinear electrostatic effects.

Section 3.2 introduces the general arrangement of electrodes for capacitive ring-based CVG's and introduces the model used to determine the electrostatic potential energy for a capacitor formed between the ring and a single electrode. In Section 3.3 this model is extended to a ring resonator having 8 uniformly spaced electrodes and the basic electrostatic configuration is introduced using a fundamental form of voltage distribution implemented in practice. The non-linear equations of motion governing the drive and sense modes are then determined. In Section 3.5 averaged steady-state solutions are obtained for the drive and sense mode responses, and it is shown that the sense response involves self-induced parametric excitation.

Section 3.5.3 investigates the influence of electrostatic nonlinearity on the rate sensing performance of a CVG by considering the scale factor, zero-rate output and quadrature error. These are investigated for cases with and without the imperfections, and the effects of specific design parameters and operating conditions are identified. Comparisons are made against the rate sensitivity, bias rate and quadrature error for the corresponding linear device to identify conditions where the electrostatic nonlinearities can trim the sensor output or enhance rate sensitivity. FE results are also shown, serving to validate the theoretical results.

3.2. Fundamentals of capacitive elements

This section introduces the general arrangement of electrodes for capacitive ring-based CVG's and introduces the model used to determine the electrostatic potential energy for a capacitor formed between the ring and a single electrode.

3.2.1. Electrodes as capacitors

Figure 3.1 shows a typical arrangement for a capacitive ring-based CVG where the electrodes are evenly spaced around the circumference of the ring. Each ring-electrode pair has an identical radial gap and for the case shown electrodes are located on both the inner and outer sides of the ring. The main dimensions of the ring are indicated in the figure. δ is the electrode angular span, g_0 is the inner/outer capacitive gap for the undeflected ring and $B_{electrode}$ is the out-of-plane electrode thickness.

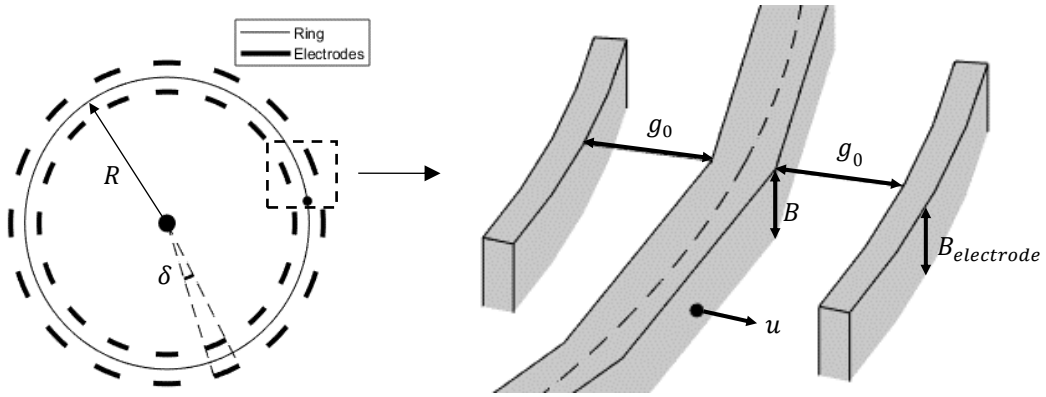

Figure 3.1: Electrode placement around the ring, with definition of dimensional variables

In practice capacitive gaps operate near vacuum and voltages are applied to the electrodes to elicit a potential difference between each electrode-ring pair. Due to this potential difference, there is a movement of electrons positively charging either the electrode or ring while negatively charging the other. In this manner, each electrode-ring pair holds a charge and acts as a capacitor.

The charge difference between the ring and electrode generates an electric field between the two conducting bodies, transferring electric flux from the positively charged conductor to the negatively charged conductor. If the conductors are sufficiently close, fringing effects from the electric field can be neglected and each electrode-ring pair approximates to a closed sector of a cylindrical capacitor. In this case, Gauss's law is applicable and the capacitance of each ring-electrode pair can be expressed as:

$$c^{\pm} = \varepsilon_0 B \int_{\theta_0 - \frac{\delta}{2}}^{\theta_0 + \frac{\delta}{2}} \frac{R}{g_1^{\pm}} d\theta \tag{3.1}$$

provided electrode thickness $B_{electrode}$ is greater than ring thickness B, where

$$g_1^{+} = R \ln\left(\frac{R + \frac{h}{2} + g_0}{R + \frac{h}{2} + u}\right) \tag{3.2a}$$

$$g_1^{-} = R \ln\left(\frac{R - \frac{h}{2} + u}{R - \frac{h}{2} - g_0}\right) \tag{3.2b}$$

In (3.1) c^{+} and c^{-} represent the capacitance for one of the electrodes, where '+' and '-' superscripts represent the outer and inner electrode sets respectively. g_1^{+} and g_1^{-} are the corresponding effective gaps. ε_0 is the permittivity of free space and θ_0 is the mean angular position of each electrode. It is important to note that the capacitance varies nonlinearly with radial displacement u.

3.2.2. Electrostatic potential energy

In practice, the ring is thin ($h \ll R$) and the nominal capacitive gap g_0 is small ($g_0 \ll R$) to maximise the capacitance effects. Since the radial displacements are confined within the capacitive gap (while avoiding pull-in [21, 61, 62]) $u \ll R$ as well. Under these conditions, expanding g_1^{+} and g_1^{-} as a Taylor series in g_0 and u about $g_0 = 0$ and $u = 0$ up to linear order in both terms gives:

$$g_1^{\pm} \approx g_0 \mp u + O({g_0}^2) + O(u^2) \tag{3.3}$$

Substituting (3.3) into (3.1) it can be shown that the capacitance of each electrode-ring pair approaches that of a parallel plate capacitor when $u, g_0 \ll R$, where effects of the radial position difference between the inner and outer electrode sets have been neglected. The

validity of this parallel plate approximation has been demonstrated in literature [10, 49, 63]. For the case considered, the ring can be considered to be a moveable plate while the electrode is the fixed plate, as shown in Figure 3.2. The potential difference imposed between the ring and electrode is ΔV, and $+Q_{c^+}$ and $-Q_{c^+}$ are the positive and negative charges accumulated in the outer electrode and ring due to the imbalance of electrons in the two conducting plates.

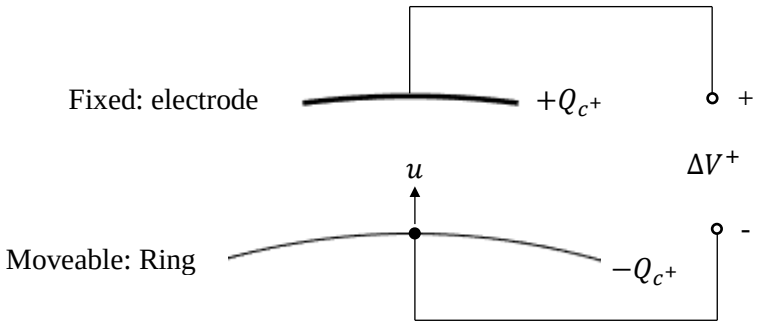

Figure 3.2: Parallel plate representation of the capacitor formed between the ring and one outer electrode

The positive and negative charges have a mutual attraction, but are separated by the non-conducting vacuum between the ring and electrode (the dielectric). This stores electrostatic potential energy in each electrode-ring pair. This electrostatic potential energy can be obtained from the work done when pulling the plates apart from zero gap to the effective gap $g_1^{\pm}$ [21]. The differential work corresponding to an infinitesimal overlapping area $dA(=BRd\theta)$ for one electrode is:

$$W^{\pm} = \int_{\theta_0-\frac{\delta}{2}}^{\theta_0+\frac{\delta}{2}} \frac{\varepsilon_0 dA}{2g_1^{\pm}} (\Delta V^{\pm})^2 \tag{3.4}$$

The total capacitive work $W^+ + W^-$ can be substituted for W on the right side of the Lagrange's equations in (2.15a) and (2.15b) to obtain the electrostatic modal forces. Alternatively, this term can be shifted to the left side of (2.15a) and (2.15b) giving:

$$\frac{\partial}{\partial t}\left(\frac{\partial E_k}{\partial \dot{X}}\right) - \frac{\partial E_k}{\partial X} + \frac{\partial E_b}{\partial X} + \frac{\partial U}{\partial X} = -\frac{\partial D}{\partial \dot{X}} \tag{3.5a}$$

$$\frac{\partial}{\partial t}\left(\frac{\partial E_k}{\partial \dot{Y}}\right) - \frac{\partial E_k}{\partial Y} + \frac{\partial E_b}{\partial Y} + \frac{\partial U}{\partial Y} = -\frac{\partial D}{\partial \dot{Y}} \tag{3.5b}$$

where $U = -W$ and $E_b = E_{b,R} + E_{b,K}$. E_b is the total mechanical bending potential energy and $E_{b,K}$ has been introduced here to account for the bending potential energy due to the support structures, which is known to have linear stiffening effects on the ring [63].

The support structures used in the following investigation are composed of 8 flexible semi-circular beams, attached at evenly distributed points around the ring (see Appendix B). These beams act as linear springs, providing radial and tangential restoring forces resulting in its bending potential energy contribution derived in (B-11):

$$E_{b,K} = \frac{4k_{uu} + k_{vv}}{2}(X^2 + Y^2)$$

where k_{uu} and k_{vv} are the radial and tangential stiffnesses of each support beam.

Comparing terms involving U and E_b in (3.5a) and (3.5b) shows that the electrostatic effects can be interpreted in the same manner as the total mechanical bending potential energy E_b, and the total potential energy is the sum of the electrostatic potential energy U and mechanical bending potential energy E_b. $\partial U/\partial X$, $\partial U/\partial Y$ describe the resulting electrostatic modal forces, and these forces are the core principle through which capacitive CVG's operate.

The notion of quantifying electrostatic effects as a potential energy is useful for analysing effective stiffness-modifying effects reported in capacitive CVG's [10]. Throughout the remainder of this dissertation, electrostatic potential energy is used to represent and discuss electrostatic effects.

3.3. Equations of motion for a capacitive CVG

In this section the model developed in Section 3.2 for a single capacitor formed between the ring and electrode is extended to include contributions from all electrodes for a ring resonator having 8 uniformly spaced electrodes, and determines the non-linear equations of motion governing the drive and sense modes.

3.3.1. Basic electrostatic configuration

As discussed in Chapter 2, ring-based CVG's typically operate using the $n = 2$ flexural mode pair possessing 2 nodal diameters as shown in Figure 1.4. Capacitive CVG's typically implement 8, 16 or 32 electrodes evenly spaced around the ring [6, 10, 18, 45, 64]. The electrostatic configuration in MEMS CVG's is dictated by two factors: i) the number of evenly spaced electrodes and ii) the distribution of voltage from electrode to electrode.

The fundamental operation of a device involves applying harmonic voltages to the electrodes to excite the drive mode into vibration together with a bias voltage to avoid frequency doubling

of the drive force [6]. The analysis presented in this section is based on the 8 electrode design shown in Figure 3.3. V_0 is the constant bias voltage applied to all electrodes while V_{AC} is the harmonic drive voltage at drive frequency ω. In Figure 3.3 the deflections shown for the drive and sense modes, X and Y, are exaggerated.

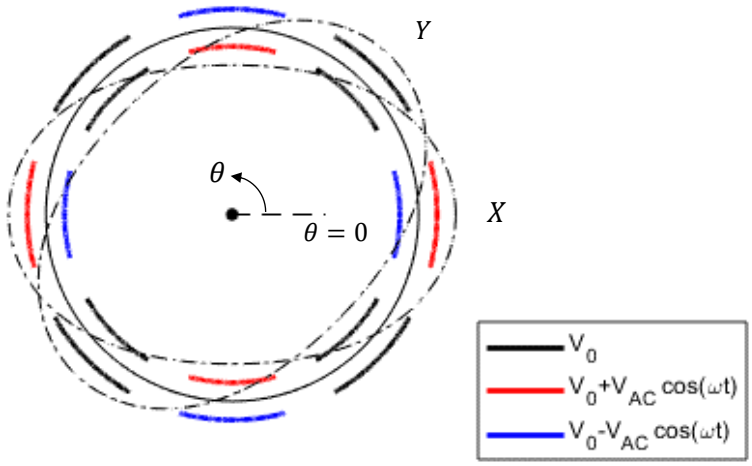

Figure 3.3: Basic electrostatic configuration incorporating bias and drive mechanisms

In Figure 3.3, the electrodes with drive voltage $V_{AC}\cos\omega t$ are referred to as the drive electrodes. The drive electrodes are positioned at the antinodes of the drive mode and the main purpose of the drive electrodes is to generate a 'push-pull' force to excite the drive mode into resonance. To generate the 'push-pull' force, the voltages applied to the drive electrodes with angular positions centred at $\theta = 0, \pi$ are in antiphase with those applied to the drive electrodes at positions $\theta = \pi/2\,, 3\pi/2$. When the ring vibrates, the ring displaces towards one of the inner or outer drive electrodes while displacing by the same amount away from the other. The antiphase relationship between the inner and outer drive electrodes ensures a constructive interaction between the electrostatic potential energy generated by the inner and outer drive electrodes.

The electrostatic configuration in Figure 3.3 can be described by voltages represented as a discrete Fourier series in the central angular position of the i^{th} inner/outer electrode, $\theta_0(i)$:

$$V^{\pm}[\theta_0(i)] = V_0 \pm V_{AC}\cos\omega t\cos 2\theta_0(i) \tag{3.6}$$

where $i = 1, \cdots, 8$ is an integer identifying the ith drive electrode of each of the inner and outer electrode sets. $V^{\pm}[\theta_0(i)]$ describes the voltage applied to the i^{th} inner/outer electrode. Due to the even distribution of the electrodes, the central angular position θ_0 of the i^{th} electrode is given by:

$$\theta_0(i) = \frac{2i\pi}{j}$$

where $j = 8$ is the total number of inner or outer electrodes.

When the ring is grounded, the potential difference $\Delta V^{\pm}$ in (3.4) is equal to the voltages applied to the electrodes. Using (3.6) for $\Delta V^{\pm}[\theta_0(i)]$ in (3.4) and noting that $U = -W$ gives the electrostatic potential energy arising from the i^{th} inner and outer electrodes. Summing this expression over i gives the total electrostatic potential energy for this electrostatic configuration.

$$U = \bar{U} + U_{AC} \tag{3.7}$$

where

$$\bar{U} = -\frac{1}{2}\sum_{i=1}^{j} {V_0}^2 c^{++-}[\theta_0(i)] \tag{3.8}$$

$$U_{AC} = -\frac{1}{2}\sum_{i=1}^{j} 2V_0 V_{AC} \cos\omega t \cos 2\theta_0(i)\, c^{+--}[\theta_0(i)] \tag{3.9}$$

$c^{++-}[\theta_0(i)]$ and $c^{+--}[\theta_0(i)]$ are the summation and subtraction of the capacitance between the i th inner and outer electrodes, such that $c^{++-}[\theta_0(i)] \coloneqq c^{+}[\theta_0(i)] + c^{-}[\theta_0(i)]$ and $c^{+--}[\theta_0(i)] \coloneqq c^{+}[\theta_0(i)] - c^{-}[\theta_0(i)]$ respectively.

$\bar{U}$ and U_{AC} are the contributions of the bias and drive voltages to the total electrostatic potential energy respectively and terms proportional to ${V_{AC}}^2$ have been discarded as the drive voltage is small in practice, $V_{AC} \ll V_0$. $\bar{U}$ and U_{AC} have been expressed as a summation of the result of the product of the capacitance and voltage squared for each electrode-ring pair. $c^{++-}[\theta_0(i)]$ and $c^{+--}[\theta_0(i)]$ are given by:

$$c^{++-}[\theta_0(i)] = \varepsilon_0 BR \int_{\theta_0(i)-\frac{\delta}{2}}^{\theta_0(i)+\frac{\delta}{2}} \left(\frac{1}{g_0 - u} + \frac{1}{g_0 + u}\right) d\theta \tag{3.10a}$$

$$\approx \frac{2\varepsilon_0 BR}{g_0} \int_{\theta_0(i)-\frac{\delta}{2}}^{\theta_0(i)+\frac{\delta}{2}} \left[1 + \frac{u^2}{{g_0}^2} + \frac{u^4}{{g_0}^4} + O\left(\frac{u^6}{{g_0}^6}\right)\right] d\theta$$

$$c^{+--}[\theta_0(i)] = \varepsilon_0 BR \int_{\theta_0(i)-\frac{\delta}{2}}^{\theta_0(i)+\frac{\delta}{2}} \left(\frac{1}{g_0 - u} - \frac{1}{g_0 + u}\right) d\theta \tag{3.10b}$$

$$\approx \frac{2\varepsilon_0 BR}{g_0} \int_{\theta_0(i)-\frac{\delta}{2}}^{\theta_0(i)+\frac{\delta}{2}} \left[\frac{u}{g_0} + \frac{u^3}{{g_0}^5} + O\left(\frac{u^5}{{g_0}^5}\right)\right] d\theta$$

The interaction between the voltage squared and capacitance is important as it directly dictates the result of the summations in (3.8) and (3.9), enabling the net effects of the bias and drive voltages to be explicitly identified. $c^{++-}[\theta_0(i)]$ directly interacts with components of the square of the voltage distribution in (3.6) which are of the same polarity between the inner and outer electrode sets, which is the case for the bias voltage V_0 since it is identically applied to the inner and outer electrodes. On the other hand, $c^{+--}[\theta_0(i)]$ interacts with components of the square of (3.6) which are of opposite polarities between the inner and outer electrode sets. This is the case for the drive voltage since it has an antiphase relationship between the inner and outer electrode sets, as shown in Figure 3.3.

In (3.10a) and (3.10b), the terms in the bracket have been expanded as a Taylor series in radial displacement up to the 4th order. To model the linear dynamics of the system, a 2nd order expansion is sufficient. However, noting that larger amplitude vibrations are generally desirable for performance enhancement of these devices, the analysis presented in this chapter takes 3rd and 4th order terms into account. These terms are responsible for yielding the lowest-order nonlinear effects on the system, deviating the vibrational response from what would be expected from the corresponding linear system.

$c^{++-}[\theta_0(i)]$ and $c^{+--}[\theta_0(i)]$ contribute to even and odd-ordered terms in the total electrostatic potential energy respectively. As will be shown, even and odd-ordered terms in the electrostatic potential energy have distinct effects on the drive and sense modes.

In Chapter 2 the radial ring displacement u was expressed as:

$$u = X \cos n\theta + Y \sin n\theta \tag{2.1}$$

Substituting (2.1) into (3.10a) and (3.10b) it can be shown that the capacitance can be approximated as a discrete Fourier series in terms of electrode central angular position $\theta_0(i)$, similar to the voltage distribution in (3.6). Substituting this result into (3.8) and (3.9) and summing across the electrodes from i = 1 to 8 gives:

$$\bar{U} = -j\frac{\varepsilon_0 BR}{2g_0}{V_0}^2\left[2\delta + \delta\frac{X^2+Y^2}{{g_0}^2} + \left(\frac{3}{4}\delta + \frac{\sin 4\delta}{16}\right)\frac{X^4+Y^4}{{g_0}^4} + \frac{3}{4}\left(\delta - \frac{\sin 4\delta}{4}\right)\frac{2X^2Y^2}{{g_0}^4}\right] \tag{3.11}$$

$$U_{AC} = -\frac{j}{2}\frac{\varepsilon_0 BR\sin\delta}{g_0}(2V_0V_{AC}\cos\omega t)\left[\frac{X}{g_0} + \left(\frac{5+\cos 2\delta}{6}\right)\frac{X^3}{{g_0}^3} + \sin^2\delta\frac{XY^2}{{g_0}^3}\right] \tag{3.12}$$

$\bar{U}$ and U_{AC} depend on the voltage distribution (3.6) and dictate the resulting form of the electrostatic forces affecting the modal dynamics. As such, the chosen voltage distribution provides direct control of the device output and is a key feature in later chapters.

$\bar{U}$ is composed of even-ordered terms, similar to the ring bending potential energy $E_{b,R}$ in (2.10) and contribute to the modal elastic properties. However, unlike $E_{b,R}$, $\bar{U}$ exhibits modal symmetry as $\bar{U}$ is unchanged when the drive and sense displacements are exchanged, i.e. X to Y and vice versa. As such, the drive and sense modes are equally affected by the bias voltage V_0 and the elastic asymmetry between the drive and sense modes arises purely due to the mechanical imperfection.

U_{AC} is composed of only odd-ordered terms and is modal asymmetric, thus contributing unequally to the drive and sense modes. The linear term in (3.12) is proportional to X, ensuring only the drive mode is directly forced.

3.3.2. Equations of motion with basic electrostatic configuration

The linear and nonlinear electrostatic forces generated for the aforementioned basic electrostatic configuration can be obtained by substituting (3.11) and (3.12) into (3.7), and then substituting the resulting total electrostatic potential energy expression into Lagrange's equations (3.5a) and (3.5b). As previously discussed, $\bar{U}$ and U_{AC} contribute to the equations of motion in a manner similar to the bending potential energy E_b and the direct work done on the drive mode, W in Lagrange's equations (eq (2.15a) and (2.15b)). However, the presence of 3rd and 4th order terms in the electrostatic potential energy give rise to additional nonlinear terms compared to the linear equations of motion in (2.18). Substituting the resulting expression for U in conjunction with expressions for E_k in (2.6) – (2.7c), $E_{b,R}$ in (2.10), $E_{b,K}$ in (B-11) and D in (2.13) with $n = 2$ into the pair of Lagrange's equations (3.5a) and (3.5b) gives the following nonlinear equations of motion for the drive and sense modes.

$$M\begin{bmatrix}1+\Delta_{m1} & \Delta_{m2}\\ \Delta_{m2} & 1-\Delta_{m1}\end{bmatrix}\bar{\ddot{\boldsymbol{q}}}_{\boldsymbol{1}}+\left(C\begin{bmatrix}1+\Delta_{c1} & \Delta_{c2}\\ \Delta_{c2} & 1-\Delta_{c1}\end{bmatrix}+M_{\Omega}\Omega\begin{bmatrix}0 & -1\\ 1 & 0\end{bmatrix}\right)\bar{\dot{\boldsymbol{q}}}_{\boldsymbol{1}} \tag{3.13}$$
$$+K\begin{bmatrix}1+\Delta_{k1} & \Delta_{k2}\\ \Delta_{k2} & 1-\Delta_{k1}\end{bmatrix}\bar{\boldsymbol{q}}_{\boldsymbol{1}}+M\bar{\bar{\boldsymbol{\eta}}}_{\boldsymbol{3}}\frac{\bar{\boldsymbol{q}}_{\boldsymbol{3}}}{{g_0}^2}$$
$$=M\chi\cos\omega t\left(\begin{bmatrix}1\\0\end{bmatrix}+\bar{\bar{\boldsymbol{\eta}}}_{\boldsymbol{\chi}}\frac{\bar{\boldsymbol{q}}_{\boldsymbol{2}}}{{g_0}^2}\right)$$

Modal-mass-normalising the resulting equations of motion in a manner similar to the procedure from (2.16) to (2.17) gives the following:

$$\bar{\ddot{\boldsymbol{q}}}_{\boldsymbol{1}}+2\Gamma\bar{\dot{\boldsymbol{q}}}_{\boldsymbol{1}}+{\omega_0}^2\bar{\bar{\Delta}}\bar{\boldsymbol{q}}_{\boldsymbol{1}}+\bar{\bar{\boldsymbol{\eta}}}_{\boldsymbol{3}}\frac{\bar{\boldsymbol{q}}_{\boldsymbol{3}}}{{g_0}^2}=\Omega\bar{\bar{\boldsymbol{G}}}_{\boldsymbol{\Omega}}\bar{\dot{\boldsymbol{q}}}_{\boldsymbol{1}}+\chi\cos\omega t\left(\begin{bmatrix}1\\0\end{bmatrix}+\bar{\bar{\boldsymbol{\eta}}}_{\boldsymbol{\chi}}\frac{\bar{\boldsymbol{q}}_{\boldsymbol{2}}}{{g_0}^2}\right) \tag{3.14}$$

where the condition $\Delta_{c1}-\Delta_{m1}=\Delta_{c2}-\Delta_{m2}=0$ has been imposed so only structural imperfections will be considered in the following investigation.

Quantities with single and double overbars, $\bar{\ }$ and $\bar{\bar{\ }}$ represent vector and matrix quantities respectively. Vectors $\bar{\boldsymbol{q}}_{\boldsymbol{1}}$, $\bar{\boldsymbol{q}}_{\boldsymbol{2}}$ and $\bar{\boldsymbol{q}}_{\boldsymbol{3}}$ contain the linear, quadratic and cubic order modal coordinates respectively and are given by

$$\bar{\boldsymbol{q}}_{\boldsymbol{1}}=\begin{bmatrix}X\\Y\end{bmatrix} \tag{3.15}$$

$$\bar{\boldsymbol{q}}_{\boldsymbol{2}}=\begin{bmatrix}X^2\\XY\\Y^2\end{bmatrix} \tag{3.16}$$

$$\bar{\boldsymbol{q}}_{\boldsymbol{3}}=\begin{bmatrix}X^3\\X^2Y\\XY^2\\Y^3\end{bmatrix} \tag{3.17}$$

Terms proportional to $\bar{\boldsymbol{q}}_{\boldsymbol{1}}$ and $\bar{\boldsymbol{q}}_{\boldsymbol{3}}$ give rise to linear and cubic-order restoring forces acting on the drive and sense modes respectively. In this manner, the effective elastic properties of the drive and sense modes depend on the linear resonant frequency ω_0, but are subjected to nonlinear corrections from the cubic-order forces.

The linear natural frequency ω_0 is given by:

$${\omega_0}^2=\frac{1}{5\rho}\left(\frac{3Eh^2}{R^4}+\frac{4K}{h\pi BR}-j\frac{4\varepsilon_0{V_0}^2}{h\pi{g_0}^3}\delta\right) \tag{3.18}$$

where K is the effective total modal stiffness of the support beams, defined as $K = 4k_{uu} + k_{vv}$.

ω_0 depends on the linear modal stiffnesses, which has mechanical and electrostatic origins. Mechanical contributions to the linear modal stiffnesses arise from the flexural stiffness of the ring, as well as the support structure (see Appendix B for details). The mechanical bending potential energy components $E_{b,R}$ and $E_{b,K}$ contribute to the first and second terms defining ${\omega_0}^2$ in (3.18) respectively. The mechanical bending potential energy has stiffening effects on the ring and as such, the first two terms in (3.18) are positive, increasing the linear resonant frequency of the drive and sense modes. The electrostatic contribution corresponds to the last term defining ${\omega_0}^2$ in (3.18), and is only affected by the bias voltage. This term is always negative, showing that the bias voltage results in modal softening.

The drive voltage contributes to the equation of motion through the harmonic force $\chi \cos \omega t$ directly applied to the drive mode. The force amplitude χ is given by:

$$\chi = j\frac{4\varepsilon_0 V_0 V_{AC} \sin\delta}{5\rho h \pi {g_0}^2} \tag{3.19}$$

χ is proportional to the drive voltage amplitude V_{AC}, and in practice the drive voltage is regulated to maintain a constant drive amplitude to ensure a steady sensor output.

$\bar{\bar{\boldsymbol{\eta}}}_{\boldsymbol{\chi}}$ and $\bar{\bar{\boldsymbol{\eta}}}_{\boldsymbol{3}}$ define the nonlinear electrostatic effects and are given by:

$$\bar{\bar{\boldsymbol{\eta}}}_{\boldsymbol{\chi}} = \begin{bmatrix} \frac{5+\cos 2\delta}{2} & 0 & \frac{1-\cos 2\delta}{2} \\ 0 & 1-\cos 2\delta & 0 \end{bmatrix} \tag{3.20}$$

$$\bar{\bar{\boldsymbol{\eta}}}_{\boldsymbol{3}} = \begin{bmatrix} \gamma_0 & 0 & \kappa_0 & 0 \\ 0 & \kappa_0 & 0 & \gamma_0 \end{bmatrix} \tag{3.21}$$

where

$$\gamma_0 = -j\frac{6\varepsilon_0 {V_0}^2}{5\rho h \pi {g_0}^3}\left(\delta + \frac{\sin 4\delta}{12}\right) \tag{3.22}$$

$$\kappa_0 = -j\frac{6\varepsilon_0 {V_0}^2}{5\rho h \pi {g_0}^3}\left(\delta - \frac{\sin 4\delta}{4}\right) \tag{3.23}$$

$\bar{\bar{\boldsymbol{\eta}}}_{\boldsymbol{\chi}}$ is a nonlinear correction matrix to the harmonic drive force $\chi \cos \omega t$. The elements of the first row modify the effective drive force amplitude slightly, while the element of the second row gives rise to a form of indirect excitation on the sense mode by the drive voltage. As will

be shown, this gives rise to a small parametric excitation of the sense mode. However, since $V_{AC} \ll V_0$ in practice, the nonlinear effects arising from the quadratic-order electrostatic forces associated with $\overline{\overline{\boldsymbol{\eta}}}_{\boldsymbol{\chi}}$ are negligible.

$\overline{\overline{\boldsymbol{\eta}}}_{\boldsymbol{3}}$ contains the cubic-order modal stiffnesses, which are responsible for the main electrostatic nonlinear effects arising from the implementation of the basic electrostatic configuration. γ_0 is the single-mode stiffness (modal-mass-normalised). It appears exclusively in the first and last columns of $\overline{\overline{\boldsymbol{\eta}}}_{\boldsymbol{3}}$. The modal electrostatic forces in the equations of motion associated with γ_0 are proportional to X^3 and Y^3 for the drive and sense modes respectively. As such, γ_0 is the modal Duffing coefficient. κ_0 is the coupled-mode stiffness. It gives rise to a form of nonlinear elastic coupling between the drive and sense modes, which is responsible for causing self-induced parametric excitation [48, 49]. This coupling is negligible for small electrode spans δ because $\kappa_0 \approx 0$, causing the electrostatic nonlinearities between the drive and sense modes to approach uncoupled behaviour. Due to the electrostatic origin of both γ_0 and κ_0, these nonlinear stiffnesses are negative. Also, for this basic electrostatic configuration, $|\kappa_0| \leq |\gamma_0|$, where the equality is only for the case when $\delta = \pi/4$, i.e. the 8 electrodes form a continuous electrode. As will be shown, the relationship between γ_0 and κ_0 has an important effect on the resulting nonlinearities affecting the rate output of the device.

Γ describes the linear damping coefficient and for the conventional, linear system, $2\Gamma = \omega_0/Q_0$.

The imperfection and gyroscopic matrices $\overline{\overline{\Delta}}$ and $\overline{\overline{\boldsymbol{G}}}_{\boldsymbol{\Omega}}$ are defined via a direct comparison of (3.14) and (2.18). In (3.14), the structural imperfection parameters are described within $\overline{\overline{\Delta}}$.

3.4. Drive and sense mode responses

In this section, the nonlinear equations of motion (3.14) are solved to derive the modal responses needed to determine the rate output. Conditions relevant to practical operation are considered to obtain a clear comparison of the nonlinear response against the corresponding linear device.

Due to the nonlinearities, exact, closed-form solutions of (3.14) are analytically unobtainable. Also, unlike the linear system, the steady-state nonlinear response is only approximately harmonic depending on the strength of the nonlinearities. As such, the method implemented in Section 2.3.1 is not applicable, and alternative, approximate methods are needed to obtain the response, as discussed next.

3.4.1. Drive mode response

In CVG's, the drive mode oscillation generates a Coriolis force proportional to the drive mode amplitude and larger drive amplitudes are desirable to enhance rate sensitivity. The nonlinear electrostatic forces acting to excite the ring are important and the drive mode can be regarded as a nonlinear oscillator having a much larger amplitudes than the sense mode, i.e. $y/x \ll 1$. In the absence of rotation and neglecting the back coupling effects from the sense mode due to drive misalignment and the nonlinear coupled-mode stiffness, the drive mode equation of motion approaches that of a forced Duffing equation:

$$\ddot{X} + 2\Gamma\dot{X} + {\omega_0}^2(1 + \Delta_\omega \cos 4\Theta_\omega)X + \gamma_0 \frac{X^3}{{g_0}^2} = \chi \cos \omega t \left[1 + c_{XX} \frac{X^2}{{g_0}^2}\right] \tag{3.24}$$

where $c_{XX} = (5 + \cos 2\delta)/2$.

An approximate solution to (3.24) can be obtained using the averaging method [65, 66]. Using this method, the drive response remains periodic at the excitation frequency ω but exhibits slowly varying amplitude and phase, provided that the Duffing stiffness γ_0 is sufficiently small. This condition is applicable for capacitive devices since the feasible bias voltage V_0 is restricted to avoid pull-in, thus limiting γ_0. Here, the drive response is defined as $X = x(t) \cos[\omega t + \phi_x(t)]$. Substituting this definition into (3.24) and assuming that the amplitude and phase exhibit negligible variation within each oscillation cycle, this gives:

$$\begin{aligned}[-\omega^2 + {\omega_0}^2(1 + \Delta_\omega \cos 4\Theta_\omega)]x + \frac{3}{4}\gamma_0 \frac{x^3}{{g_0}^2} - 2x\omega\dot{\phi}_x \\ = \chi \cos \phi_x \left[1 + \frac{3}{4} c_{XX} \frac{x^2}{{g_0}^2}\right]\end{aligned} \tag{3.25}$$

$$-2(x\Gamma + \dot{x})\omega = \chi \sin \phi_x \left[1 + \frac{1}{4} c_{XX} \frac{x^2}{{g_0}^2}\right] \tag{3.26}$$

(3.25) and (3.26) can be used to assess the stability of the drive mode oscillatory response, but for the present purpose, only the steady-state response is of interest. At steady-state, the amplitude and phase rates, $\dot{x}$ and $\dot{\phi}_x$ approach zero and (3.25) and (3.26) reduce to phase-decomposed force balancing equations for forces acting in quadrature and in phase relative to damping respectively. Solving these equations simultaneously yields the following result for the phase-decomposed drive amplitudes:

$$\begin{bmatrix} x\cos\phi_x \\ x\sin\phi_x \end{bmatrix} = -\frac{\begin{bmatrix} \omega^2 - {\omega_X}^2 & 2\Gamma\omega \\ 2\Gamma\omega & -\omega^2 + {\omega_X}^2 \end{bmatrix} \bar{\boldsymbol{f}}_{\chi}}{(2\Gamma\omega)^2 + (-\omega^2 + {\omega_X}^2)^2} \tag{3.27}$$

where

$$\bar{\boldsymbol{f}}_{\chi} = \begin{bmatrix} \chi\left[1 + c_{XX}\frac{x^2}{4{g_0}^2}(2 + \cos 2\phi_x)\right] \\ -\chi c_{XX}\frac{x^2}{4{g_0}^2}\sin 2\phi_x \end{bmatrix} \tag{3.28}$$

$${\omega_X}^2 = {\omega_0}^2(1 + \Delta_\omega \cos 4\Theta_\omega) + \frac{3}{4}\gamma_0\frac{x^2}{{g_0}^2} \tag{3.29}$$

$\bar{\boldsymbol{f}}_{\chi}$ contains the effective phase-decomposed components of the drive force amplitude. The quadratic-order nonlinearity results in a small dependence of these drive force amplitude components on the drive mode vibration amplitude and phase. As such, the effective phase of the drive force depends on the drive response. This is in contrast to the corresponding linear system where this dependence is not present ($c_{XX} = 0$), causing the second row of $\bar{\boldsymbol{f}}_{\chi}$ to be nullified and fixing the effective phase of the drive force. This phase fixation of the drive force can be reproduced in the presence of the quadratic nonlinearities if the drive mode is locked at resonance, i.e. $\phi_x = -\pi/2$ which similarly nullifies the second row of $\bar{\boldsymbol{f}}_{\chi}$. However, in this case, the effective drive force amplitude is increased as the drive mode oscillates at larger amplitudes.

ω_X is the effective resonant frequency of the drive mode, resulting in $\phi_x = -\pi/2$. When $\gamma_0 = 0$, this frequency eliminates the real part of the complex drive amplitude ${x_{a,\Omega 0}}^*$ in (2.22) and ensures resonance when angular rate is not present. ω_X is composed of an amplitude-independent component described by the first two terms in (3.29) and a nonlinear, amplitude-dependent component due to the modal Duffing coefficient γ_0. The amplitude-independent component of this frequency depends on the drive misalignment angle Θ_ω, which dictates if this component is higher or lower than the ideal case, ω_0. As will be shown, this has important implications on the ability to trim the device response. When the drive response is harmonic at steady-state, i.e. $X = x\cos(\omega t + \phi_x)$, the linear and cubic drive displacements, X and X^3 share the same sign, and the linear restoring force reach maximum/minimum values at the same time as the cubic restoring force. This allows the cubic restoring force to act in unison with the linear restoring force to dictate the effective stiffness of the drive mode. Since $\gamma_0 < 0$, ω_X decreases as the drive amplitude increases, confirming the nonlinear softening role of

the electrostatics on the drive mode. From (3.22) $|\gamma_0|$ increases with bias voltage and electrode angle, and the electrostatic nonlinearity strengthens, serving to increase the softening rate of the drive mode.

From (3.27), it can be shown that when $\omega = \omega_X$, the resulting resonant drive amplitude is:

$$x_r = -\frac{{\chi_r}'}{2\Gamma\omega_X} \tag{3.30}$$

where ${\chi_r}'$ is the effective resonant drive force amplitude given by:

$${\chi_r}' = \chi\left(1 + \frac{1}{4}c_{xx}\frac{{x_r}^2}{{g_0}^2}\right) \tag{3.31}$$

When resonance is achieved, the harmonic drive force amplitude χ can be tuned to fix the drive amplitude. When χ remains unchanged, the electrostatic nonlinearity acts to increase the resonant drive amplitude in two ways. First, the effective drive force amplitude ${\chi_r}'$ increases due to the quadratic-ordered electrostatic forces. This is shown in the amplitude-dependency of ${\chi_r}'$. Secondly, the drive frequency ω_X decreases due to the nonlinear softening of the drive mode. The electrostatic nonlinearity leads to the implicit nature of the expression for x_r in (3.30). As such, unlike a linear drive oscillator, the drive force amplitude χ does not admit a linearly proportional relationship with the resonant amplitude x_r. For the remainder of this chapter, the presented study is strictly based on resonant operation.

3.4.2. Sense mode response

Considering the angular rate within the typical dynamic range of CVG's, the maximum measurable angular rates are such that Ω/ω_0 is typically in the order of 10^{-4}. As a result, the responding sense mode is in practice much smaller than the drive mode, and quadratic and cubic terms in Y can be neglected from sense equation of motion (3.14). This approximation has been used and validated in previous studies [49], and gives:

$$\ddot{Y} + 2\Gamma\dot{Y} + \left[{\omega_0}^2(1 - \Delta_\omega\cos 4\Theta_\omega) + \kappa_0\frac{X^2}{{g_0}^2} - \frac{\chi c_{XY}}{g_0}\cos\omega t\frac{X}{g_0}\right]Y = -G_\Omega\Omega\dot{X} - {\omega_0}^2\Delta_\omega\sin 4\Theta_\omega X \tag{3.32}$$

where $c_{XY} = 1 - \cos 2\delta$.

The sense mode approximates a linear forced oscillator, with the drive mode directly forcing the sense mode through the two terms on the right side of (3.32). The first term is the rate-

sensitive Coriolis force, while the second term is an undesirable, imperfection-induced linear elastic coupling force due to the drive misalignment. The Coriolis and linear elastic coupling forces are proportional to the drive velocity and displacement respectively, and are in quadrature. In an ideal device, only the Coriolis force is present, so the phase of the sense mode forcing is fixed to be $\pm\pi/2$ relative to the phase-regulated drive response. However, depending on the level of imperfection and misalignment, the linear elastic coupling force can be significant compared to the Coriolis force, acting to phase-shift the effective force acting on the sense mode. The phase-shift of the direct force has a significant impact on the nature of the sense response relevant to the rate-measuring performance of these devices.

The sense mode is also subjected to parametric excitation due to the modulation of its elastic properties. This is shown in the coefficient of the sense displacement Y in (3.32). Noting that the steady-state sense response is harmonic, the quadratic and cubic electrostatic forces give rise to a double-frequency variation of the sense mode stiffness through terms involving the drive force amplitude χ and the nonlinear coupled-mode stiffness κ_0 respectively. This form of parametric excitation is self-induced as it naturally arises from sufficiently large-amplitude drive mode displacements, without requiring the implementation of time-varying pump voltages for this purpose, as in the approach implemented in [28, 52]. As will be shown, the parametric excitation affects how the sense mode responds to the direct Coriolis and linear elastic coupling forces.

The steady-state sense response can be obtained using the method of averaging in a manner similar to the drive mode, provided that $|\kappa_0|$ is sufficiently small. Comparing (3.22) and (3.23), it is clear that $|\kappa_0| \leq |\gamma_0|$ so the applicability of the averaging method is also well-justified in this case. Using this method, since the direct forces acting on the sense mode stem from the drive response, it is convenient to define the sense response phase as an offset relative to the drive phase ϕ_x. For this purpose, the steady-state sense response is defined as $Y = y\cos(\omega t + \phi_x + \phi_{yx})$, where y is the sense amplitude and ϕ_{yx} is the sense displacement phase relative to the drive displacement. Substituting this expression into (3.32) and performing the averaging procedure yields the following phase-decomposed components of the sense amplitude:

$$\begin{bmatrix} y\cos\phi_{yx} \\ y\sin\phi_{yx} \end{bmatrix} = -\frac{\bar{\bar{\mathbf{A}}}\bar{\boldsymbol{f}}_{\boldsymbol{Y}}}{{P_1}^2 - P_2^+ P_2^-} \tag{3.33}$$

where

$$\bar{\bar{\mathbf{A}}} = \begin{bmatrix} \omega^2 - {\omega_Y}^2 + \lambda_1 & 2\Gamma\omega + \lambda_2 \\ 2\Gamma\omega - \lambda_2 & -\omega^2 + {\omega_Y}^2 + \lambda_1 \end{bmatrix} \tag{3.34}$$

$$\bar{\boldsymbol{f}}_{\boldsymbol{Y}} = \begin{bmatrix} f_\Delta \\ f_\Omega \end{bmatrix} = \begin{bmatrix} -x{\omega_0}^2 \Delta_\omega \sin 4\Theta_\omega \\ G_\Omega \Omega x \omega \end{bmatrix} \tag{3.35}$$

$$P_1 = 2\Gamma\omega \tag{3.36}$$

$$P_2^{\pm} = \left({\lambda_1}^2 + {\lambda_2}^2\right)^{\frac{1}{2}} \pm (-\omega^2 + {\omega_Y}^2) \tag{3.37}$$

and in $\bar{\bar{\mathbf{A}}}$:

$${\omega_Y}^2 = {\omega_0}^2(1 - \Delta_\omega \cos 4\Theta_\omega) + \kappa_0 \frac{x^2}{2{g_0}^2} - \frac{\chi}{2g_0} c_{XY} \frac{x}{g_0} \cos\phi_x \tag{3.38}$$

$$\lambda_1 = \kappa_0 \frac{x^2}{4{g_0}^2} - \frac{\chi}{4g_0} c_{XY} \frac{x}{g_0} \cos\phi_x \tag{3.39}$$

$$\lambda_2 = -\frac{\chi}{4g_0} c_{XY} \frac{x}{g_0} \sin\phi_x \tag{3.40}$$

$\bar{\boldsymbol{f}}_{\boldsymbol{Y}}$ contains the effective amplitudes of the direct force components acting on the sense mode. f_Δ and f_Ω are the modal-mass-normalised amplitudes of the linear elastic coupling and Coriolis forces respectively. For the basic electrostatic configuration considered, these force amplitudes scale proportionally with drive amplitude. As such, for the Coriolis force, a large drive amplitude provides a rate-independent amplification even at low angular rates. This rate-independent amplification of the Coriolis force is desirable for scale factor improvement. However, this also amplifies the linear elastic coupling force unless the ring is perfect ($\Delta_\omega = 0$) or there is no drive misalignment ($\sin 4\Theta_\omega = 0$).

$\bar{\bar{\mathbf{A}}}$ distinguishes the contributions from the linear elastic coupling and Coriolis forces to the sense amplitude components $y\cos\phi_{yx}$ and $y\sin\phi_{yx}$. The first and second columns of $\bar{\bar{\mathbf{A}}}$ represent the 'weights' dictating the relative contributions of the linear elastic coupling and Coriolis forces respectively. As such, for an ideal or trimmed device, elements of the first column of $\bar{\bar{\mathbf{A}}}$ are insignificant and the drive frequency ω can be selected to adjust the element $\bar{\bar{\mathbf{A}}}_{\mathbf{22}}$ for phase tuning of the sense mode.

ω_Y is the effective sense frequency, where ${\omega_Y}^2$ is proportional to the mean stiffness of the sense mode. As such, ${\omega_Y}^2$ is the coefficient of the sense displacement in (3.32), neglecting the

double-frequency variation. Similar to the drive frequency ω_X, ω_Y is composed of an amplitude-independent and a nonlinear, amplitude-dependent component. The amplitude dependency is composed of linear and quadratic-ordered variations, arising from quadratic and cubic electrostatic forces respectively. These represent the last two terms in (3.38). The linear amplitude dependence, associated with the drive force amplitude χ is the result of the drive voltage V_{AC}, while the quadratic-ordered amplitude dependence stems from the nonlinear elastic coupling between the drive and sense modes due to the coupled-mode stiffness κ_0, which depends on the bias voltage V_0. Since $V_{AC} \ll V_0$, the linear amplitude dependence is negligible, and the nonlinear softening of the sense mode is predominantly dictated by the strength of the nonlinear elastic coupling between the drive and sense modes.

λ_1 and λ_2 dictate the phase-decomposed amplitudes of the self-induced parametric excitation. The definitions for λ_1 and λ_2 in (3.39) and (3.40) are derived from the amplitude of the 2ω variation in the coefficient of Y in (3.32). Since $V_{AC} \ll V_0$, λ_2 is negligible so the amplitude of the self-induced parametric excitation is predominantly dictated by λ_1. Comparing (3.38) and (3.39) shows that the nonlinear amplitude-dependence of the sense frequency ${\omega_Y}^2$ is identical to $2\lambda_1$. As such, λ_1 is similarly dictated by the nonlinear elastic coupling between the drive and sense modes. A direct consequence of this is that increasing the strength of the self-induced parametric excitation will also result in an increased softening rate of the sense frequency. Due to the amplitude dependence of λ_1 and λ_2, the self-induced parametric excitation is a purely nonlinear effect. The self-induced parametric excitation amplitude depends on both the bias voltage and chosen drive amplitude, which can be tuned to manipulate the sense response. However, as previously noted, $|\lambda_2/\lambda_1| \ll 1$ so the effects of λ_2 will be neglected in the proceeding analysis associated with the basic electrostatic configuration.

The denominator ${P_1}^2 - P_2^+ P_2^-$ in (3.33) quantifies the energy dissipation rate of the sense mode vibration for the corresponding free vibration case, i.e. when $f_\Delta = f_\Omega = 0$. From a free vibration analysis of (3.32), it can be shown that the effective time constant is given by $2\omega/\left(P_1 - \sqrt{P_2^+ P_2^-}\right)$, where $\sqrt{P_2^+ P_2^-} < P_1$. P_1 is associated with the damping, so $P_1 > 0$ in all cases, indicating a positive contribution towards the energy dissipation rate. On the other hand, the product $P_2^+ P_2^-$ can be positive or negative depending on the opposing effects of the parametric excitation amplitude and the splitting between the drive and sense frequencies. The following cases apply.

i. If $\left|{\lambda_1}^2 + {\lambda_2}^2\right| > |-\omega^2 + {\omega_Y}^2|$ then $P_2^+ P_2^- > 0$ so $\sqrt{P_2^+ P_2^-}$ is real. Q factor is increased by the parametric excitation.

ii. If $\left|{\lambda_1}^2 + {\lambda_2}^2\right| < |-\omega^2 + {\omega_Y}^2|$ then $P_2^+ P_2^- < 0$ so $\sqrt{P_2^+ P_2^-}$ is imaginary. Parametric excitation does not increase Q factor.

For the linear system, self-induced parametric excitation is not present so $\lambda_1 = \lambda_2 = 0$ and case ii always applies. The denominator of (3.33) increases due to the linear frequency split, thus attenuating the sense amplitude. When electrostatic nonlinearities are accounted for, $P_2^+ P_2^- > 0$ when the parametric excitation amplitude is sufficiently large (case i). In this case, the parametric excitation acts to reduce the energy dissipation rate, lengthening the time constant. When $P_2^+ P_2^-$ approaches ${P_1}^2$, the time constant approaches infinite and the denominator of (3.33) approaches zero, significantly amplifying the sense response. This is highly desirable for scale factor enhancement of the device. However, the case where ${P_1}^2 = P_2^+ P_2^-$ results in parametric resonance, which elicits an unstable sense response where the vibration amplitude grows without bound. As will be shown, the product $P_2^+ P_2^-$ has important effects when considering nonlinear electrostatic effects.

3.5. Effects of electrostatic nonlinearity on rate sensing performance

This section investigates the influence of electrostatic nonlinearity on rate sensing performance and compares the resulting rate sense performance to the linear and ideal device case considered in Chapter 2. The effects of the electrostatic nonlinearities are considered for both trimmed and untrimmed devices. The rate sensing performance is quantified in terms of the rate sensitivity, bias rate and quadrature error for those cases based on the sense response investigated in Section 3.4.2. The theoretical results of the investigation are then validated against FE results.

For a conventionally-operated, linear and ideal device, the sense amplitude is proportional to angular rate (see (1.11)), and a fixed phase relationship also exists between the drive and sense modes. Results for this case can be obtained from (3.33) by neglecting all amplitude-dependent terms in $\overline{\overline{\mathbf{A}}}$, P_1, $P_2^{\pm}$ and setting $\omega = \omega_Y$ and $f_\Delta = 0$ due to the absence of imperfections. This gives the following standard sense response used as the rate output:

$$\begin{bmatrix} y_0^l \cos \phi_{yx,0}^l \\ y_0^l \sin \phi_{yx,0}^l \end{bmatrix} = \begin{bmatrix} S_0^l \Omega \\ 0 \end{bmatrix} \tag{3.41}$$

where the '0' notation in the subscript represents the ideal/trimmed case ($\Delta_\omega = 0$) while the 'l' superscript represents the linear case. S_0^l is the rate sensitivity, given by $S_0^l = -G_\Omega x/(2\Gamma)$. Based on this standard sense response, the in/antiphase sense amplitude component

$y\cos\phi_{yx,0}^{l}$ is conventionally used as the rate output, while the quadrature sense amplitude component $y_0^l \sin\phi_{yx,0}^{l}$ is regarded as the quadrature output dictating the quadrature error. It is clear that rate sensitivity (scale factor) is conventionally enhanced by minimising the damping Γ or operating at large amplitude drive responses. However, in practice devices are imperfect and operating at large drive amplitudes introduces electrostatic nonlinearities.

In what follows, studies are performed to investigate the impact of imperfection and nonlinearity on rate measuring performance of devices. This is achieved by investigating rate measuring performance for: i) an imperfect ring device operating at small drive amplitude; ii) a perfect ring device operating at large drive amplitude; and iii) an imperfect ring device operating at large drive amplitude. In each case results are obtained for the rate sensitivity, bias rate and quadrature error and comparisons are made with the linear, ideal sense response in (3.41).

3.5.1. Imperfect ring, small drive amplitude operation

Small drive amplitudes relative to the gap guarantee near linear sense response, thus retaining the conditions relating to the standard sense response in (3.41) but with $\Delta_\omega \neq 0$ when imperfection effects are considered. In this case, the linear drive and sense frequencies approximate the case when the drive amplitude ratio x/g_0 approaches zero, and are given by:

$$\begin{bmatrix}{\omega_X^l}^2\\ {\omega_Y^l}^2\end{bmatrix} = \lim_{x\to 0}\begin{bmatrix}{\omega_X}^2\\ {\omega_Y}^2\end{bmatrix} = \begin{bmatrix}{\omega_0}^2(1+\Delta_\omega\cos 4\Theta_\omega)\\ {\omega_0}^2(1-\Delta_\omega\cos 4\Theta_\omega)\end{bmatrix} \tag{3.42}$$

The imperfection results in splitting of the drive and sense frequencies about the ideal, linear resonant frequency ω_0 depending on the alignment of the modes. The frequency split is only nullified in the specific case when $\Theta_\omega = (2i-1)\pi/8$, where i is an integer. This applies when the drive and sense modes align at circumferential positions of mean stiffness on the ring, causing the modal stiffnesses to coincide. Fixing the excitation frequency at the drive frequency such that $\omega = \omega_X^l$, substituting ω_Y for ω_Y^l and setting $\lambda_1 = \lambda_2 = 0$ in (3.34) - (3.37), and substituting the resulting expressions for $\bar{\bar{\mathbf{A}}}$, $\bar{\boldsymbol{f}}_{\boldsymbol{Y}}$, P_1, P_2 in (3.33) gives the following sense amplitude components for the linear, imperfect case:

$$\begin{bmatrix}y^l\cos\phi_{yx}^l\\ y^l\sin\phi_{yx}^l\end{bmatrix} = -\frac{\bar{\bar{\mathbf{A}}}^{\boldsymbol{l}}\begin{bmatrix}f_\Delta\\ f_\Omega\end{bmatrix}}{4\Gamma^2{\omega_X^l}^2 + \left(\bar{\omega}^{l^2}\right)^2} \tag{3.43}$$

where

$$\overline{\overline{\mathbf{A}}}^{\boldsymbol{l}} = \begin{bmatrix} \bar{\omega}^{l\,2} & 2\Gamma\omega_X^l \\ 2\Gamma\omega_X^l & -\bar{\omega}^{l\,2} \end{bmatrix} \tag{3.44}$$

$$\bar{\omega}^{l\,2} = 2{\omega_0}^2\Delta_\omega \cos 4\Theta_\omega \tag{3.45}$$

$\bar{\omega}^{l\,2} = {\omega_X^l}^2 - {\omega_Y^l}^2$ is a linear frequency detuning parameter, describing the imperfection-induced linear frequency split between the drive and sense modes. $\bar{\omega}^{l\,2}$ is identical to the frequency detuning without back coupling ($\eta = 0$) in (2.63). The diagonal elements in $\overline{\overline{\mathbf{A}}}^{\boldsymbol{l}}$ are not nullified in the presence of linear frequency detuning, resulting in a cross-contribution of the Coriolis and linear elastic coupling forces to both sense amplitude components. As such, unlike $y_0^l \cos \phi_{yx,0}^l$ for the ideal case, the sense amplitude component $y^l \cos \phi_{yx}^l$ is not solely dictated by the Coriolis force, thus persisting when angular rate is absent due to the linear elastic coupling force amplitude f_Δ. Also, the orthogonal sense amplitude component $y^l \sin \phi_{yx}^l$ does not nullify, thus deviating the relative phase ϕ_{yx}^l away from 0 or $\pm\pi$. These effects deviate the sense response from what is expected of a linear, ideal device, thus significantly impacting the resulting rate sensing performance of the device. In this manner, the rate output $y^l \cos \phi_{yx}^l$ is no longer proportional to the angular rate and a quadrature output $y^l \sin \phi_{yx}^l$ is introduced.

3.5.1.1. Rate sensitivity (scale factor) and bias rate

To demonstrate rate-sensing, it is convenient to express the in/antiphase sense amplitude component as a linear relationship with angular rate, yielding:

$$y^l \cos \phi_{yx}^l = S^l\left(\Omega + \Omega_z^l\right) \tag{3.46}$$

where

$$\left|S^l\right| = \frac{G_\Omega x {\omega_X^l}^2 (2\Gamma)}{4\Gamma^2 {\omega_X^l}^2 + \left(\bar{\omega}^{l\,2}\right)^2} \tag{3.47}$$

$$\Omega_z^l = -\frac{\bar{\omega}^{l\,2}{\omega_0}^2\Delta_\omega \sin 4\Theta_\omega}{G_\Omega {\omega_X^l}^2 (2\Gamma)} \tag{3.48}$$

S^l and Ω_z^l are the rate sensitivity and the bias rate (zero-rate error) respectively. The zero-rate error results in a systematic offset of the rate output, causing the device to respond in the absence of an applied angular rate, i.e. when $\Omega = 0$. From (3.48), the zero-rate error only

manifests when both a linear frequency detuning and a drive misalignment are present. As for the sensitivity, the linear frequency detuning always acts to reduce $|S^l|$ compared to the linear, ideal form $|S_0^l|$, indicating an off-resonant operation of the sense mode. As shown from the denominator of (3.47), the presence of the linear frequency detuning $\bar{\omega}^l$ also limits the attainable amplification of the sense response when practical attempts at minimising the damping Γ are pursued.

3.5.1.2. Quadrature error

The quadrature error can be expressed in terms of the relative phase to quantify the phase error due to the presence of the imperfection-induced quadrature sense amplitude component $y^l \sin \phi_{yx}^l$. The relative phase for this linear case is directly derived from (3.43), giving:

$$\phi_{yx}^l = \tan^{-1} \frac{(2\Gamma\omega_X^l) f_\Delta - \left(\bar{\omega}^{l^2}\right) f_\Omega}{\left(\bar{\omega}^{l^2}\right) f_\Delta + (2\Gamma\omega_X^l) f_\Omega} \tag{3.49}$$

The relative phase quantifies the ratio of the quadrature sense amplitude component to the in/antiphase sense amplitude component. It is highly sensitive to the imperfection parameter Δ_ω. When the imperfection is small such that $\left|\bar{\omega}^{l^2}/(2\Gamma\omega_X^l)\right| \ll 1$, the relative phase approximates the ratio between the linear elastic coupling and Coriolis forces such that $\phi_{yx}^l \approx f_\Delta/f_\Omega$. For example, for a lightly damped system such that $\omega_X^l/\Gamma = 240$, a small frequency split of 400 mHz ($\Delta_\omega = 4e-5$) within an ideal resonant frequency of $\omega_0 = 10\ kHz$ results in a force amplitude ratio of $f_\Delta/f_\Omega = -0.6$ when the drive force is slightly misaligned ($\Theta_\omega = 1°$) and an angular rate of $\Omega = 10°/s$ is applied. This force amplitude ratio amplifies further for larger misalignments, showing that even minimal imperfections can potentially elicit a linear elastic coupling force greater than the useful Coriolis force, thus generating significant phase errors.

Since high rate-measuring performance of CVG's depends on device outputs which are very sensitive to the applied angular rate with minimal zero-rate and quadrature errors, the aforementioned effects clearly degrade the performance of these devices in all cases.

3.5.2. Perfect ring, large drive amplitude operation

At larger drive amplitude operations, nonlinear electrostatic forces are dominant. As discussed in Section 3.4, the dominant effects of the electrostatic nonlinearities are the amplitude dependence of the drive and sense frequencies, as well as the presence of self-induced parametric excitation.

When electrostatic nonlinearities are considered in the absence of imperfections, the nonlinear sense response (3.33) with $\Delta_\omega = 0$ yields:

$$\begin{bmatrix} y_0 \cos\phi_{yx,0} \\ y_0 \sin\phi_{yx,0} \end{bmatrix} = -\frac{\begin{bmatrix} 2\Gamma\omega_{X,0} \\ -\bar{\omega}_0{}^2 + \lambda_{1,r} \end{bmatrix} f_\Omega}{P_{1,r,0}{}^2 - P^+_{2,r,0}P^-_{2,r,0}} \tag{3.50}$$

where

$$\omega_{X,0}{}^2 = \omega_0{}^2 + \frac{3}{4}\gamma_0 \frac{x^2}{g_0{}^2} \tag{3.51}$$

$$\bar{\omega}_0{}^2 = \frac{1}{4}(3\gamma_0 - 2\kappa_0)\frac{x^2}{g_0{}^2} \tag{3.52}$$

$$\lambda_{1,r} = \kappa_0 \frac{x^2}{4g_0{}^2} \tag{3.53}$$

and $P_{1,r,0}$, $P^+_{2,r,0}$ and $P^-_{2,r,0}$ in the denominator are given by:

$$P_{1,r,0} = 2\Gamma\omega_{X,0} \tag{3.54}$$

$$P^\pm_{2,r,0} = \lambda_{1,r} \mp \bar{\omega}_0{}^2 = [\kappa_0 \pm (2\kappa_0 - 3\gamma_0)]\frac{x^2}{4g_0{}^2} \tag{3.55}$$

The linear elastic coupling force is absent, i.e. $f_\Delta = 0$ causing both the in/antiphase and quadrature sense amplitude components to amplify linearly with Coriolis force amplitude f_Ω. As such, both sense amplitude components nullify in the absence of angular rate and energy transfer from the drive to the sense mode.

$\omega_{X,0}$ is the effective drive frequency for the perfect, nonlinear case, while $\bar{\omega}_0{}^2$ is the nonlinear frequency detuning. In contrast to $\bar{\omega}^{l\,2}$ for the linear, imperfect case, $\bar{\omega}_0{}^2$ is amplitude-dependent because the drive and sense frequencies soften at different rates. Comparing (3.22) and (3.23) shows that $|\kappa_0| \leq |\gamma_0|$ at all amplitudes, indicating that the drive mode softens more significantly than the sense mode and $\bar{\omega}_0{}^2 < 0$.

From the general nonlinear sense response in (3.33) to the perfect case in (3.50), the parametric excitation amplitude λ_2 has been discarded as it has been noted to be negligible. $\lambda_{1,r}$ dictates the self-induced parametric excitation amplitude when the drive mode is operated at resonance, i.e. $\lambda_{1,r} = \lambda_1$ when $\phi_x = -\pi/2$. The self-induced parametric excitation amplitude can be

adjusted by varying the chosen drive amplitude. However, since λ_2 is negligible, the phase of the self-induced parametric excitation is fixed relative to the drive vibration phase when the basic electrostatic configuration is implemented.

$P_{2,r,0}^{+}$ and $P_{2,r,0}^{-}$ are the dominant parameters describing the effects of the electrostatic nonlinearities on both sense amplitude components. The frequency detuning ${\bar{\omega}_0}^2$ interacts with the self-induced parametric excitation $\lambda_{1,r}$ and significantly modifies the resulting sense response. Substituting (3.52) and (3.53) into (3.55) shows that the presence of $P_{2,r,0}^{+}$ and $P_{2,r,0}^{-}$ is a purely nonlinear effect, as these are amplitude-dependent parameters stemming from the unequal softening rates of the drive and sense frequencies, and the presence of the self-induced parametric excitation, determined by γ_0 and κ_0. The product $P_{2,r,0}^{+}P_{2,r,0}^{-}$ depends on the relationship between γ_0 and κ_0. On the other hand, $P_{1,r,0}$ is directly associated to the linear damping coefficient Γ. The interaction between $P_{1,r,0}$, $P_{2,r,0}^{+}$ and $P_{2,r,0}^{-}$ dictates the resulting sense response amplitude components.

In what follows, the effects of the linear damping (affecting $P_{1,r,0}$), drive amplitude and the relationship between γ_0 and κ_0 (affecting $P_{2,r,0}^{+}$ and $P_{2,r,0}^{-}$) will be investigated to understand how they influence the quadrature response and the rate sensitivity.

3.5.2.1. Rate sensitivity (scale factor)

The influence of electrostatic nonlinearity on rate sensitivity is considered in this section. In a manner similar to the imperfect, linear case in Section 3.5.1, it is convenient to express the rate output in (3.50) as being proportional to the angular rate as follows:

$$y_0 \cos\phi_{yx,0} = S_0\Omega \tag{3.56}$$

where the magnitude of the rate sensitivity S_0 is given by:

$$|S_0| = \frac{G_\Omega x\omega_{X,0}\left(P_{1,0}\right)}{{P_{1,r,0}}^2 - P_{2,r,0}^{+}P_{2,r,0}^{-}} \tag{3.57}$$

Rate sensitivity (3.57) is enhanced by self-induced parametric excitation when $P_{2,r,0}^{+}P_{2,r,0}^{-} > 0$ and Q factor enhancement and parametric resonance potentially occur as ${P_{1,r,0}}^2 - P_{2,r,0}^{+}P_{2,r,0}^{-}$ approaches zero. To understand (3.57) it necessary to investigate the values that product $P_{2,r,0}^{+}P_{2,r,0}^{-}$ can take. Noting that $\kappa_0, \gamma_0 < 0$ and $|\kappa_0| \leq |\gamma_0|$ it can be shown quite easily using (3.55) that $P_{2,r,0}^{-} < 0$ and $P_{2,r,0}^{+} \geq 0$. The condition $P_{2,r,0}^{+} = 0$ applies when the electrode is continuous around the ring such that $\kappa_0 = \gamma_0$. This results in the coincidence of the frequency detuning and the self-induced parametric excitation amplitude, i.e. $\lambda_{1,r} = {\bar{\omega}_0}^2$ and can be

regarded as a nonlinear frequency balancing condition, requiring balancing the inertial force amplitude against those of the restoring and parametric excitation forces on the sense mode. Comparing S_0 against S_0^l in (3.41), $S_0 = S_0^l$ when $P_{2,r,0}^{+} = 0$. This condition is key to retaining a trimmed sense response at larger drive amplitudes where electrostatic nonlinearities are dominant. For all other cases $P_{2,r,0}^{+} > 0$ and $P_{2,r,0}^{+} P_{2,r,0}^{-} < 0$, reducing the rate sensitivity. Using these results in (3.57) it can be concluded that in general self-induced parametric excitation does not result in parametric resonance and rate sensing performance is degraded unless $\kappa_0 = \gamma_0$ and nonlinear frequency balancing occurs.

Electrode continuity/discontinuity

In the following, the effects of the implementation of continuous and discontinuous electrode configurations on the linearity of the rate sensitivity are compared. This demonstrates the importance of the nonlinear frequency balancing condition, dictated by the conditions $\gamma_0 = \kappa_0$ or $\gamma_0 \neq \kappa_0$. In Figure 3.4, the rate sensitivity is plotted against the gap-normalised drive amplitude for electrode spans of $\delta = 30°$ and $\delta = 45°$, corresponding to $\kappa_0/\gamma_0 = 0.52$ and $\kappa_0/\gamma_0 = 1$ (nonlinear frequency balanced) respectively. The bias voltages V_0 for the continuous and discontinuous electrode cases are $2V$ and $2.3V$ respectively, so that γ_0 remains constant. This avoids the electrostatic nonlinearity from weakening when the electrode span is reduced. Fixing γ_0 retains the softening rate of the drive mode. The drive amplitude is increased by increasing the drive voltage V_{AC}. The linear damping coefficient Γ for these results is $48Hz$, corresponding to a nominal Q factor of 120 and a critical angular rate of $\Omega_{crit} = 2.16e4\ °/s$. The device considered for these results and the remainder of this dissertation has default properties as listed in Table C.1. FE results are also shown, serving to validate the theoretical results. The FE results are obtained from a transient analysis of the ring radial displacement at steady-state. Details of the procedures taken to obtain the FE results are given in Appendix C.

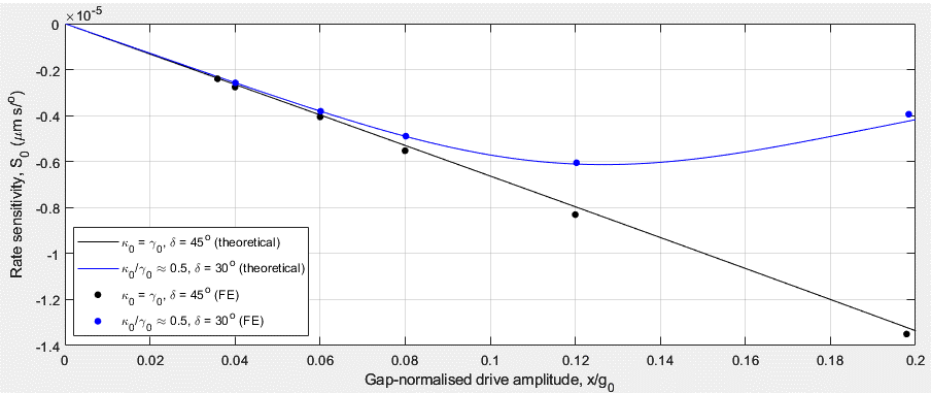

Figure 3.4: Rate sensitivity variation with gap-normalised drive amplitude for the cases of continuous ($\gamma_0 = \kappa_0$) and discontinuous electrodes ($\gamma_0 \neq \kappa_0$)

The theoretical results are in good agreement with the FE results and validate the theoretical model. It is clear from Figure 3.4 that the continuous electrode case results in nonlinear frequency balancing, ensuring that rate sensitivity scales linearly with drive amplitude, similar to a linear, ideal device. The discontinuous electrode case does not satisfy nonlinear frequency balance and in this case the rate sensitivity deteriorates as the drive amplitude increases. This is because of a competing effect between the Coriolis force and the electrostatic nonlinearities. While increasing the drive amplitude amplifies the Coriolis force, the electrostatic nonlinearities acts in a manner similar to a frequency split to detune the sense response, resulting in an off-resonant operation. This potential degradation of the scale factor in an ideal device accentuates the importance of satisfying the $\kappa_0 = \gamma_0$ nonlinear frequency balance condition.

Linear damping

The merits of varying the linear damping coefficient Γ for rate sensitivity enhancement can be investigated using the derivative $\partial|S_0|/\partial P_{1,r,0}$, given by:

$$\frac{\partial|S_0|}{\partial P_{1,r,0}} = -G_\Omega x \omega_{X,0} \frac{{P_{1,r,0}}^2 + P^+_{2,r,0}P^-_{2,r,0}}{\left({P_{1,r,0}}^2 - P^+_{2,r,0}P^-_{2,r,0}\right)^2} \tag{3.58}$$

Recalling that $P^+_{2,r,0}P^-_{2,r,0} \leq 0$, the rate sensitivity gain as the linear damping is reduced is clearly maximised for the case of nonlinear frequency balance where $P^+_{2,r,0}P^-_{2,r,0} = 0$. In this case, $\partial|S_0|/\partial P_{1,r,0} < 0$ and the rate sensitivity gain is such that $|S_0|$ amplifies to infinite as the linear damping approaches zero in a manner similar to that of the corresponding linear, ideal/trimmed case $|S_0^l|$.

Without nonlinear frequency balance, the rate sensitivity reduces compared to the corresponding standard ideal, linear operation, but $\partial|S_0|/\partial P_{1,r,0} < 0$ is no longer strictly the case. As such, linear damping reduction does not generally guarantee rate sensitivity enhancement. In principle, the rate sensitivity variation with the linear damping can be distinguished into three stages:

- For higher levels of damping such that $\left|P^+_{2,r,0}P^-_{2,r,0}\right| < {P_{1,r,0}}^2$, $\partial|S_0|/\partial P_{1,r,0} < 0$ so rate sensitivity increases as damping is reduced
- For a critical level of damping such that $\left|P^+_{2,r,0}P^-_{2,r,0}\right| = {P_{1,r,0}}^2$, $\partial|S_0|/\partial P_{1,r,0} = 0$ so rate sensitivity is insensitive to damping variations
- For low damping levels such that $\left|P^+_{2,r,0}P^-_{2,r,0}\right| > {P_{1,r,0}}^2$, $\partial|S_0|/\partial P_{1,r,0} > 0$ so rate sensitivity degrades when damping is reduced

The effect of linear damping reduction on rate sensitivity and its viability for rate sensitivity enhancement is shown in Figure 3.5 for electrode spans of $10°, 30°$ and $45°$, corresponding to κ_0/γ_0 ratios of 0.06, 0.52 and 1 respectively. Similar to Figure 3.4, γ_0 is kept constant by varying the bias voltage between the different electrode span cases considered. The drive voltage is fixed to maintain a drive amplitude of $x/g_0 = 0.13$. The critical linear damping thresholds are also shown for the electrode span cases of 10° and 30°, which are $\Gamma = 43.5Hz$ and $29.4Hz$ respectively, corresponding to Q factors of 136 and 197 in the absence of parametric excitation.

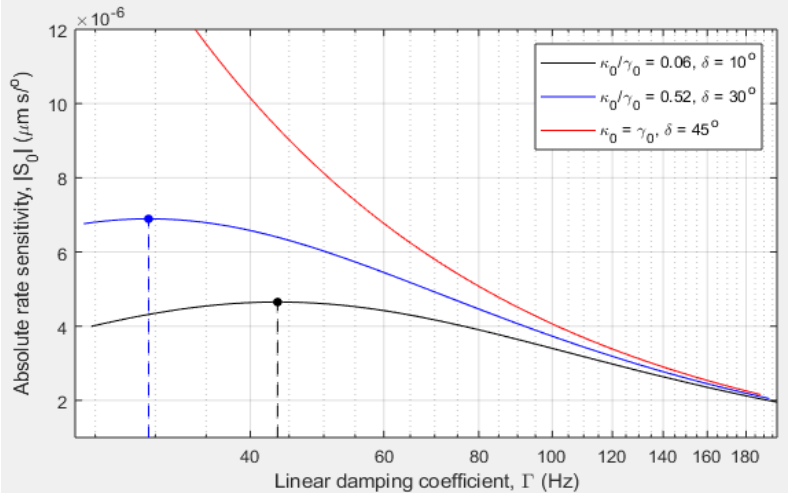

Figure 3.5: Effect of linear damping on the rate sensitivity for varying electrode spans

In Figure 3.5, unless the electrodes are continuous and nonlinear frequency balancing applies, the rate sensitivity exhibits the aforementioned variation stages with linear damping reduction. For large damping values, the nonlinearities are negligible compared to the damping, i.e. $\left|P_{2,r,0}^{+}P_{2,r,0}^{-}\right| \ll {P_{1,r,0}}^2$, so the mismatch between γ_0 and κ_0 has negligible effects on the rate sensitivity. However, when the linear damping reduces below the thresholds shown, the rate sensitivity degrades, in contrast with what is expected of a standard linear, trimmed device. This linear damping threshold increases while the maximum rate sensitivity attained decreases as the electrode span decreases, indicating the increased susceptibility of a smaller electrode span configurations to rate sensitivity degradation in an ideal device.

3.5.2.2. Quadrature error

From (3.50), similar to the rate sensitivity discussed previously, the relationship between κ_0 and γ_0 dictates the quadrature sense amplitude component $y_0 \sin \phi_{yx,0}$, hence the quadrature error. Substituting (3.52) and (3.53) into (3.50) shows that $y_0 \sin \phi_{yx,0}$ is proportional to $\gamma_0 - \kappa_0$, indicating that quadrature response is nullified only when κ_0 and γ_0 are coincident. In other cases, the presence of the amplitude-dependent frequency detuning and the self-induced

parametric excitation generally results in the quadrature sense response component gaining a portion of the vibrational energy, in a manner similar to the effects of an imperfection-induced frequency split described in Section 3.5.1.

Electrode continuity/discontinuity

In what follows, the effects of the relationship between κ_0 and γ_0 on the quadrature error are investigated by manipulating the electrode span. Figure 3.6(a)-(c) shows the effects of cubic stiffness ratio κ_0/γ_0 on the variation of the relative sense phase with the gap-normalised drive amplitude. Figure 3.6(a) plots the relative phase of the sense (which dictates the quadrature error) against both the drive amplitude (gap-normalised) and the ratio between κ_0 and γ_0. Ratio κ_0/γ_0 is varied from 0.015 to 1 by varying the electrode span and bias voltage. A larger electrode span yields a higher κ_0/γ_0 ratio, with the minimum value of 0.015 corresponding to an electrode span of $\delta = 5°$ while the maximum value of 1 corresponding to a continuous electrode arrangement ($\delta = 45°$). γ_0 is kept constant by increasing the bias voltage V_0 from $2V$ to $5.2V$ as the electrode span decreases from 45° to 5°. Figure 3.6(b) and (c) represent specific sections of the result shown in Figure 3.6(a). Figure 3.6(b) shows the variation of the sense relative phase with the drive amplitude for the cases of a continuous electrode (δ = 45°) and a discontinuous ($\delta = 30°$) electrode distributions, and are based on the same systems used for the results in Figure 3.4. Figure 3.6(c) plots the relative sense phase against the electrode span when the drive amplitude is fixed at 8%, 12% and 20% of the electrode gap g_0.

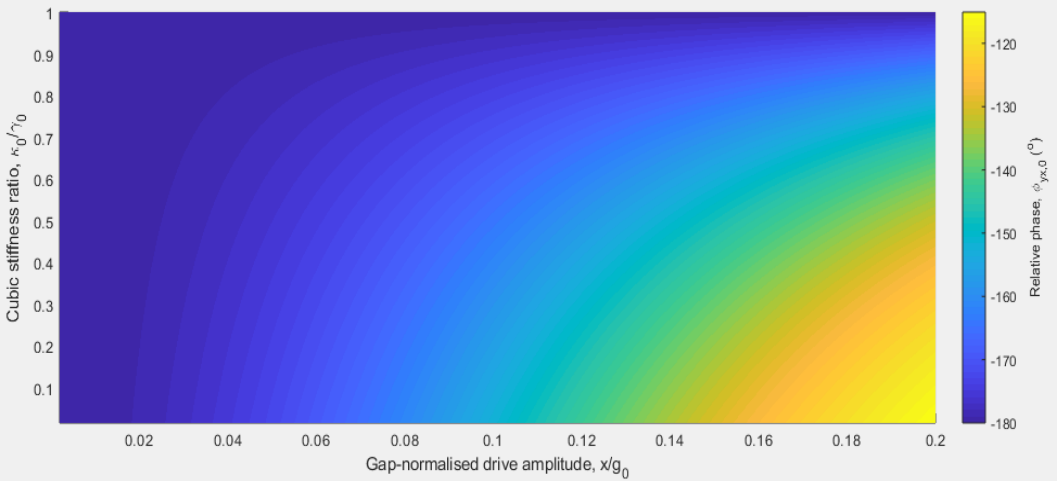

(a)

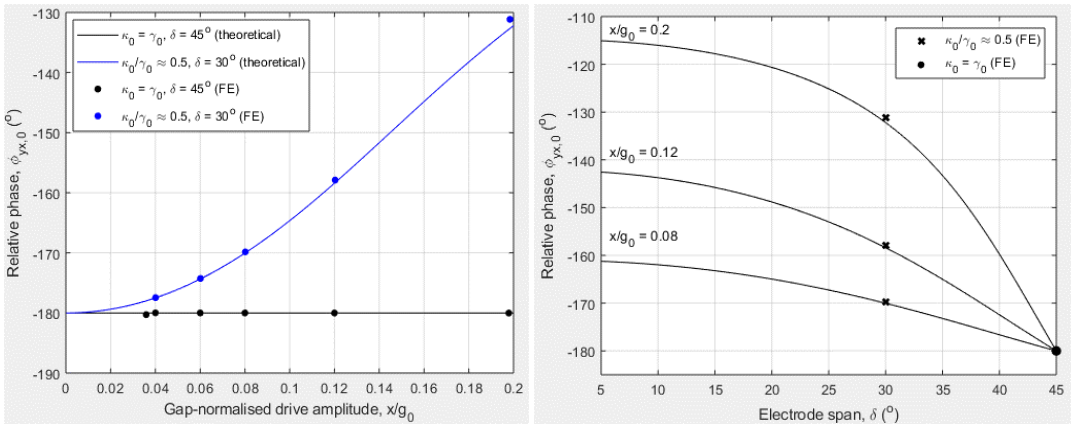

(b) (c)

Figure 3.6: (a) Relative sense phase variation with gap-normalised drive amplitude and cubic stiffness ratio, with (b) showing the drive amplitude effects for electrode spans of 30° and 45° and (c) showing the electrode span effects for drive amplitude ratios of 8%, 12% and 20%

The result in Figure 3.6(a) show that the relative phase deviates significantly from $-180°$ at large drive amplitudes and smaller cubic ratios, thus increasing the quadrature error. The effect of increasing the drive amplitude is similar to that of reducing the electrode span to increase the difference $|\gamma_0 - \kappa_0|$, as both lead to an increase in the effective modal detuning.

In Figure 3.6(b), the relative phase deviates at an increasing rate from $-180°$ with drive amplitude for the discontinuous electrode case and remains relatively constant for the continuous electrode case. In both cases theoretical results are in good agreement with the FE results, serving to validate the mathematical model. For the discontinuous case, the relative phase variation is approximately quadratic, attributed to the quadratic-ordered amplitude dependence of the nonlinear frequency imbalance $P_{2,r,0}^{\pm}$ in (3.55). The magnitude of this nonlinear frequency imbalance increases monotonically with the drive amplitude because of the constructive interaction between the nonlinear frequency detuning $\bar{\omega}_0{}^2$ and the parametric excitation $\lambda_{1,r}$. These results show the increasing importance of the nonlinear frequency balancing condition at larger drive amplitude operations.

In Figure 3.6(c), the relative phase exhibits greater changes between the constant-amplitude results for smaller electrode spans. For example, as the drive amplitude increases from 8% to 20% of the gap, the relative phase deviates by $46°$ for an electrode spans of 5°, while deviating by only $17°$ for an electrode span of $40°$. This shows that using a larger electrode span desensitises the relative phase deviations to drive amplitude variations, corresponding to a reduced gradient of the relative phase variation in Figure 3.6(b). This is due to the suppressed amplitude dependence of the nonlinear frequency imbalance at larger electrode spans.

Linear damping

From (3.50), the in/antiphase and quadrature sense response are differently affected by the linear damping. The following investigates the linear damping effects on the relative sense phase. Figure 3.7 shows how changing the linear damping parameter affects the relative phase variation with the drive amplitude. The results shown are for the discontinuous electrode configuration considered in Figure 3.6(b) with linear damping parameters $\Gamma = 96$, 48 and $24\ Hz$. In the absence of parametric excitation these values yield energy dissipation rates equivalent to Q factors of 60, 120 and 240 respectively. The case corresponding to $\Gamma = 48Hz$ is identical to the discontinuous electrode case in Figure 3.6(b) and the data points at $\delta = 30°$ in Figure 3.6(c).

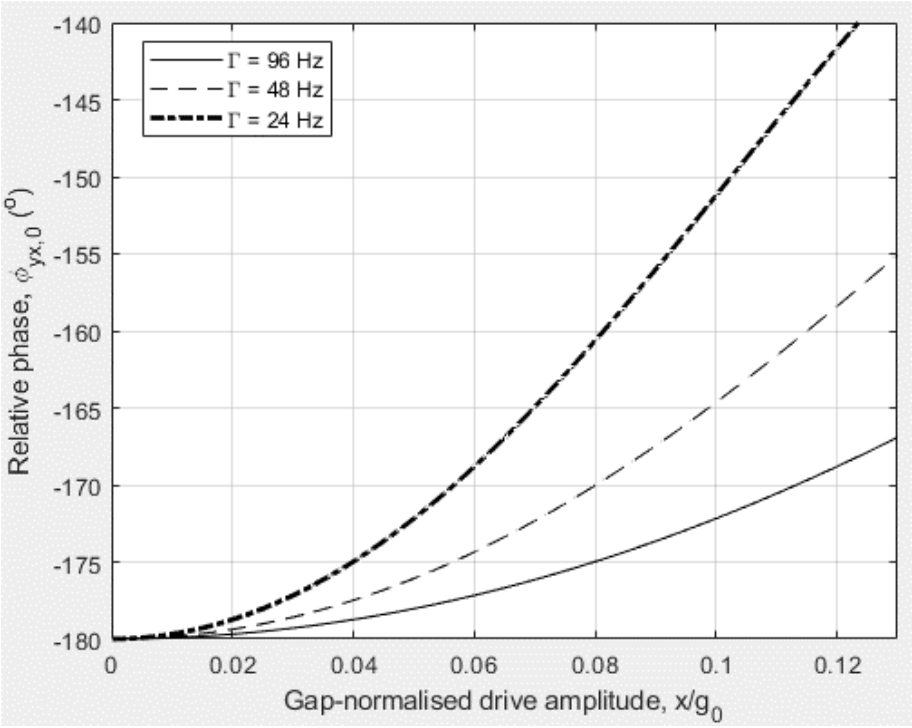

Figure 3.7: Effects of linear damping on the relative sense phase variation with gap-normalised drive amplitude for an electrode span of $\delta = 30°$

Figure 3.7 shows that the relative sense phase deviates more significantly from $-180°$ as the linear damping is reduced. This phase variation depends on the in/antiphase and quadrature sense response components, which are affected by linear damping in different ways. This behaviour is illustrated in Figure 3.8 when $\Omega = 250°/s$, which shows how the normalised sense amplitude components vary with linear damping for the case when the drive amplitude $x/g_0 = 0.13$. The in/antiphase sense amplitude component in Figure 3.8 gives the rate sensitivity result in Figure 3.5 for $\delta = 30°$.

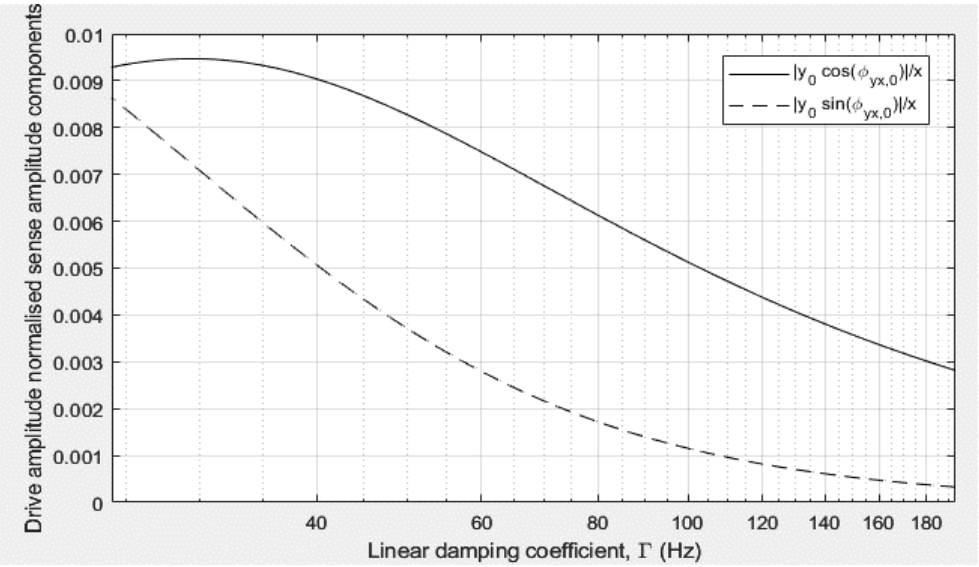

Figure 3.8: Effect of linear damping on the absolute values of the sense amplitude components (drive amplitude normalised)

For large linear damping parameter values the quad component is much smaller than the in/antiphase component, but as the linear damping reduces it can be seen that both the in/antiphase and quadrature sense amplitude components increase, with the quadrature sense amplitude amplifying more significantly than the in/antiphase sense amplitude. At lower damping parameter values the in/antiphase and quadrature sense components have similar magnitudes which give rise to increased relative phase values.

It is clear from Figure 3.8 that damping reduction techniques used in conventional linear devices can promote the growth of quadrature errors in an ideal or trimmed device operating at large, nonlinear drive amplitude operations. The reason for this is that at lower damping levels, the case where $\left|P_{2,r,0}^{+}P_{2,r,0}^{-}\right| \gg {P_{1,r,0}}^{2}$ applies. In this case, the nonlinear frequency imbalance arising from the mismatch between γ_0 and κ_0 limits the attainable amplification of both sense amplitude components, but only the in/antiphase sense amplitude component exhibits attenuation when the linear damping is reduced beyond a threshold, as shown from the growth of the in/antiphase component in Figure 3.8, which exhibits a turning point.

3.5.2.3. Effect of number of electrodes on nonlinear frequency balancing condition for perfect rings

This section has highlighted the importance of achieving nonlinear frequency balancing to avoid the rate output degradation and the introduction of quadrature output at large drive amplitudes where electrostatic nonlinearities are dominant. For the perfect ring case, the $\gamma_0 = \kappa_0$ continuous electrodes case guarantees that nonlinear frequency balancing is achieved regardless of drive and sense mode softening, maintaining sensor performance. As discussions so far have focused on the basic electrostatic configuration having 8 biasing electrodes, it is

of practical interest to identify conditions where nonlinear frequency balance is achieved when the distribution of electrodes is discontinuous. To identify such cases, the biasing electrostatic potential energy in (3.11) is revisited:

$$\bar{U} = -j\frac{\varepsilon_0 BR}{2g_0}{V_0}^2\left[2\delta + \delta\frac{X^2+Y^2}{{g_0}^2} + \left(\frac{3}{4}\delta + \frac{\sin 4\delta}{16}\right)\frac{X^4+Y^4}{{g_0}^4} + \frac{3}{4}\left(\delta - \frac{\sin 4\delta}{4}\right)\frac{2X^2Y^2}{{g_0}^4}\right] \tag{3.11}$$

$\bar{U}$ is the total biasing component of the electrostatic potential energy from all 8 electrodes and the 4th order terms govern the relationship between κ_0 and γ_0. Equality condition $\gamma_0 = \kappa_0$ requires the 4th order terms to be proportional to $(X^2+Y^2)^2$, which requires $\sin 4\delta = 0$ and is achieved when $\delta = \pi/4$. Conditions also exist to ensure $\gamma_0 = \kappa_0$ regardless of electrode span and these are discussed in Appendix D. It is shown in Appendix D that the condition $\gamma_0 = \kappa_0$ is guaranteed if 16 or 32 electrodes are used, so for basic electrode configurations using 16 and 32 electrodes nonlinear frequency balancing is satisfied, the rate sensitivity scales linearly with drive amplitude and the quadrature response remains dormant in a manner similar to the linear, ideal device regardless of the electrode span.

3.5.2.4. Summary

In the absence of imperfections, the electrostatic nonlinearities generally do not offer rate sensing performance enhancement. Compared to a linear, ideal/trimmed device, the electrostatic nonlinearities either retain or degrade rate sensing performance, depending on the electrode span. This is because, in an ideal/trimmed device, the electrode span is the dominant factor dictating the nonlinear frequency balance.

Using continuous electrodes guarantees nonlinear frequency balance, enabling the device to replicate linear, trimmed output in the presence of electrostatic nonlinearities. Electrode discontinuities, on the other hand, introduce quadrature errors and rate sensitivity degradation. The extents of these undesirable effects generally amplify as the electrode span reduces. When linear damping is minimised in an attempt to improve the performance of discontinuous-electrode devices, the rate sensitivity can degrade, which is the opposite of what is expected of a linear device.

3.5.3. Effects of electrostatic nonlinearity including imperfection

This section deals with the rate sensing performance when mechanical imperfections and electrostatic nonlinearities are simultaneously considered. Similar to the previously discussed cases, the rate sensing performance is investigated in terms of the rate sensitivity, zero-rate

error and quadrature error. The conditions required for rate sensitivity, zero-rate error and quadrature error trimming and potential rate sensitivity enhancement are identified.

3.5.3.1. Rate sensitivity (scale factor)

Similar to the rate sensitivity considered in Sections 3.5.1 and 3.5.2, the in/antiphase sense amplitude component in (3.33) is expressed as:

$$y\cos\phi_{yx} = S(\Omega + \Omega_z) \tag{3.59}$$

where the magnitude of rate sensitivity S is given by:

$$|S| = \frac{G_\Omega x \omega_X (2\Gamma\omega_X)}{{P_{1,r}}^2 - P_{2,r}^+ P_{2,r}^-} \tag{3.60}$$

The amplitude-dependent drive frequency ω_X is given in (3.29). $\bar{\omega}^2$, $P_{1,r}$, $P_{2,r}^+$ and $P_{2,r}^-$ are given by:

$$\bar{\omega}^2 = {\omega_X}^2 - {\omega_Y}^2 = {\bar{\omega}^l}^2 + {\bar{\omega}_0}^2 \tag{3.61}$$

$$P_{1,r} = 2\Gamma\omega_X \tag{3.62}$$

$$P_{2,r}^{\pm} = \lambda_{1,r} \mp \bar{\omega}^2 = \kappa_0 \frac{x^2}{4{g_0}^2} \mp \left[2{\omega_0}^2 \Delta_\omega \cos 4\Theta_\omega + \frac{1}{4}(3\gamma_0 - 2\kappa_0)\frac{x^2}{{g_0}^2}\right] \tag{3.63}$$

The total frequency detuning $\bar{\omega}^2$ is a summation of the contributions from the mechanical imperfections and electrostatic nonlinear terms, represented by ${\bar{\omega}^l}^2$ and ${\bar{\omega}_0}^2$ respectively – see (3.45) and (3.52). As discussed in Section 3.5.2, for the imperfection-free case ${\bar{\omega}_0}^2 < 0$. This is because the drive mode softens at a higher rate than the sense mode as the drive amplitude, and since the drive and sense frequencies are equal at small amplitude the drive frequency is always less than the sense frequency. When mechanical imperfection is present this behaviour is not guaranteed because the mechanical imperfection can cause the drive frequency to be greater than the sense frequency, depending on the location of the imperfection, even though the drive mode softens at a higher rate than the sense mode.

It is clear from (3.60) that $P_{2,r}^+$ and $P_{2,r}^-$ modify the rate sensitivity and zero rate error and the sign of product $P_{2,r}^+ P_{2,r}^-$ in (3.60) is key to understanding the effect, as summarised in Table 3.1.

Table 3.1: Effect of the product $P_{2,r}^{+}P_{2,r}^{-}$ on the nonlinear rate sensitivity relative to the corresponding linear, ideal/trimmed form

Case	**Effect**
$P_{2,r}^{+}P_{2,r}^{-} < 0$	Effective detuning is introduced, rate sensitivity decreases. $\lvert S\rvert < \lvert S_0^l\rvert$.
$P_{2,r}^{+}P_{2,r}^{-} = 0$	Rate sensitivity approaches linear, ideal/trimmed state. $\lvert S\rvert = \lvert S_0^l\rvert$.
$P_{2,r}^{+}P_{2,r}^{-} > 0$	Q factor is increased, rate sensitivity is enhanced. $\lvert S\rvert > \lvert S_0^l\rvert$.

For $P_{2,r}^{+}P_{2,r}^{-} < 0$, the electrostatic nonlinearities act in a manner similar to a linear frequency split or a nonlinear frequency imbalance. The rate sensitivity decreases compared to the linear, trimmed case and the attainable rate sensitivity enhancement through conventional linear damping reduction methods is limited.

For $P_{2,r}^{+}P_{2,r}^{-} = 0$, either $P_{2,r}^{-} = 0$ applies or nonlinear frequency balancing $\left(P_{2,r}^{+} = 0\right)$ is achieved. The rate sensitivity of a linear, trimmed device is reproduced at larger drive amplitudes despite the presence of electrostatic nonlinearities and mechanical imperfections.

For $P_{2,r}^{+}P_{2,r}^{-} > 0$ the energy dissipation rate is reduced by the parametric excitation, increasing the effective Q factor and enhancing the rate sensitivity. This enhancement was not possible for the perfect ring case because the drive frequency is always lower than the sense frequency. $P_{2,r}^{+}P_{2,r}^{-} > 0$ is satisfied when $P_{2,r,0}^{+} < {\bar{\omega}^{l}}^2 < -P_{2,r,0}^{-}$, where ${\bar{\omega}^{l}}^2$ is the imperfection-induced component of the frequency detuning. The rate sensitivity is maximised when $P_{2,r}^{+}P_{2,r}^{-}$ is maximised and this occurs when the total frequency detuning $\bar{\omega}^2 = 0$, i.e. $\omega_X = \omega_Y$. As such, despite the presence of imperfections, matching the drive and sense frequencies results in an increased rate sensitivity beyond the corresponding linear, ideal/trimmed case. To match the drive and sense frequencies the different softening rates of the drive and sense modes can be used to ensure $\omega_X = \omega_Y$ at a particular drive amplitude. Comparing (3.29) and (3.38) the linear stiffening effects for the drive and sense modes differ due to the imperfection-induced frequency split, such that:

- If $\cos 4\Theta_\omega < 0$ the drive frequency is less than the sense frequency $\left({\omega_X^l}^2 < {\omega_Y^l}^2\right)$
- If $\cos 4\Theta_\omega > 0$ the drive frequency is greater than the sense frequency $\left({\omega_X^l}^2 > {\omega_Y^l}^2\right)$

Noting that the drive mode always softens at a higher rate than the sense mode $(|\kappa_0| \leq |\gamma_0|)$ the drive and sense frequencies cannot be matched when $\cos 4\Theta_\omega < 0$. However, it is possible to use drive amplitude to match the frequencies when $\cos 4\Theta_\omega > 0$.

Enhanced rate sensitivity can be obtained from the condition $P_{2,r,0}^{+} < \bar{\omega}^{l^2} < -P_{2,r,0}^{-}$ and it can be shown that the range of drive amplitudes with enhanced rate sensitivity is given by:

$$\sqrt{\frac{8{\omega_0}^2\Delta_\omega \cos 4\Theta_\omega}{\kappa_0 - 3\gamma_0}} < \frac{x}{g_0} < \sqrt{\frac{8{\omega_0}^2\Delta_\omega \cos 4\Theta_\omega}{3(\kappa_0 - \gamma_0)}} \tag{3.64}$$

where the lower and upper bounds of this drive amplitude range correspond to the conditions $P_{2,r}^{-} = 0$ and $P_{2,r}^{+} = 0$ (nonlinear frequency balancing) respectively, resulting in rate sensitivity trimming. When the drive amplitude does not lie within the amplification range the rate sensitivity is reduced compared to the linear, ideal/trimmed state.

Within this amplification range, the nonlinear amplification of the rate sensitivity peaks when $P_{2,r}^{+}P_{2,r}^{-}$ is maximum. The maximum value of $P_{2,r}^{+}P_{2,r}^{-}$ is:

$$P_{2,r}^{+}P_{2,r}^{-}|_{max} = (2{\omega_0}^2\Delta_\omega \cos 4\Theta_\omega)^2 \frac{{\kappa_0}^2}{(\kappa_0 - 3\gamma_0)(3\kappa_0 - 3\gamma_0)} \tag{3.65}$$

The nonlinear amplification of the rate sensitivity is greatest for large electrode spans where $\kappa_0 \approx \gamma_0$. When the electrodes are continuous, $P_{2,r}^{+}P_{2,r}^{-}|_{max}$ approaches large values, along with the upper bound of the drive amplitude range in (3.64). $P_{2,r}^{+}P_{2,r}^{-}|_{max}$ can also be amplified when the magnitude of the coupled-mode stiffness κ_0 increases.

On the other hand, when rate sensitivity trimming is considered, small values of $P_{2,r}^{+}P_{2,r}^{-}|_{max}$ are desirable. When $P_{2,r}^{+}P_{2,r}^{-}|_{max} \approx 0$, $S \approx S_0^l$ across the whole drive amplitude range in (3.64), thus improving the robustness of the rate sensitivity trimming. This can be achieved if $\kappa_0 \approx 0$, in which case the lower and upper bounds in (3.64) approach each other.

Electrode continuity/discontinuity and bias voltage

From (3.64) and (3.65), the coupled-mode stiffness κ_0 is a key parameter dictating the amplification range and the maximum attainable nonlinear amplification of the rate sensitivity. From (3.23), the bias voltage and electrode span are important parameters dictating the magnitude of κ_0. In what follows, the effects of the bias voltage and electrode span on the conditions required for rate sensitivity trimming and enhancement are demonstrated.

Figures 3.9(a) and (b) show numerical results obtained for the rate sensitivity as the drive amplitude is increased. The rate sensitivity has been normalised with respect to the corresponding linear form, S^l and compared against the linear, ideal/trimmed form S_0^l. This normalisation eliminates the linear amplification effects of the drive amplitude on the rate

sensitivity, thus showing only the nonlinear variation of the rate sensitivity. The normalised rate sensitivity S/S^l describes the role of the electrostatic nonlinearities to either amplify or diminish the rate sensitivity, depending on whether $S/S^l > 1$ or $S/S^l < 1$. The range of drive amplitudes where the rate sensitivity S exceeds the corresponding linear, ideal/trimmed form is indicated by the shaded regions on these plots. Figure 3.9(a) presents results for the continuous electrode case, while Figure 3.9(b) presents the discontinuous electrode case with $\delta = 38°$ ($\kappa_0/\gamma_0 = 0.78$). Similar to Figure 3.6(a)-(c), the strength of the electrostatic nonlinearity is retained by keeping γ_0 constant between the cases shown in Figure 3.9(a) and (b). To achieve this, the bias voltages implemented in the examples shown in Figure 3.9(a) and (b) are $2V$ and $2.1V$ respectively. The imperfect ring considered in both cases possesses a 4θ circumferential variation component of the Young's modulus in (2.9) of magnitude $\delta E = \delta E_4 = 1.1e-3$ while the density does not contain a 4θ variation, i.e. $\delta\rho = \delta\rho_4 = 0$ in (2.5). This corresponds to $\Delta_\omega = 8e-4$ and a frequency split of 9 Hz. The linear elastic coupling force is generated by introducing a drive misalignment of $\Theta_\omega = 1°$. The imperfection results in a 3.6% decrease of the linear rate sensitivity. FE results are also shown in Figure 3.9(a) and (b), serving to validate the theoretical results.

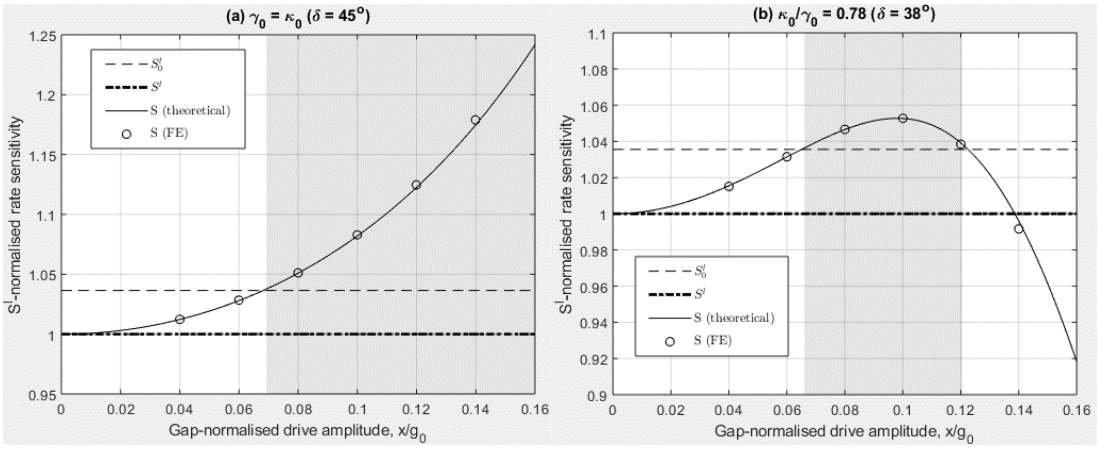

Figure 3.9: Variation of the rate sensitivity normalised to the corresponding linear form against the drive amplitude for the cases of (a) $\delta = 45°$ and (b) $\delta = 38°$

The FE results are in good agreement with the theoretical results, confirming the nonlinear dependence of the rate sensitivity on the drive amplitude and the possibility of rate sensitivity amplification in the imperfect ring.

In Figure 3.9(a), $S/S^l > 1$ for all drive amplitudes. This shows that the electrostatic nonlinearities always amplify the rate sensitivity beyond its linear form when a continuous electrode distribution is implemented. Also, the drive amplitude corresponding to the upper bound of the rate sensitivity amplification range is not present as the rate sensitivity exhibits a monotonically increasing trend as the drive amplitude increases. The required drive

amplitude for rate sensitivity trimming in this case is $x/g_0 = 6.9\%$, and when this is exceeded, the total frequency detuning and self-induced parametric excitation interact such that the Q factor is increasingly enhanced as the electrostatic nonlinearity gains significance. This result highlights how large drive amplitude operations amplifies rate sensitivity for the continuous electrode case, enabling the imperfect device to perform at significantly higher rate sensitivities than what is expected of a conventional linear, ideal/trimmed device. However, the rate sensitivity is increasingly sensitive to drive amplitude variations as the drive amplitude increases, as indicated by the increasing gradient of the nonlinear rate sensitivity in Figure 3.9(a). As such, in practical operation it would be important to keep the drive amplitude constant to ensure a steady rate output and scale factor. While the monotonically increasing trend of the rate sensitivity appears desirable, it is important to note that in practice, higher order electrostatic nonlinearities play an increasingly important role as the drive amplitude increases and the range of feasible drive amplitude in operation is limited to avoid pull-in.

Figure 3.9(b) shows that electrode discontinuity significantly reduces the drive amplitude range of rate sensitivity amplification. With an electrode span reduction of 16%, the range of drive amplitudes enabling rate sensitivity amplification diminishes compared to the continuous electrode case (Figure 3.9(a)) and amplification only occurs for drive amplitudes in the range 6.6-12% of the gap. Within this range, the rate sensitivity amplification is maximum when the drive amplitude is 9.7% of the gap. The maximum rate sensitivity amplification depends on the self-induced parametric excitation amplitude and is relatively insensitive to drive amplitude fluctuations, resulting in a more stable rate output and scale factor. This is based on the gradient of the normalised rate sensitivity variation at this peak point. This drive amplitude insensitivity of the normalised rate sensitivity is also evident at small drive amplitudes, which is directly indicative of a linear behaviour. When increasing the drive amplitude from this linear regime, the electrostatic nonlinearities act to reduce the effective frequency split, thus increasing the rate sensitivity beyond the corresponding linear, imperfect form until it is nullified and rate sensitivity trimming is achieved at $x/g_0 = 6.6\%$. Beyond $x/g_0 = 12\%$, the electrostatic nonlinearities increase the effective frequency split, thus reducing the normalised rate sensitivity up to a drive amplitude of $x/g_0 = 13.8\%$, at which point the effective frequency split is identical to the imperfection-induced frequency split. Increasing the drive amplitude beyond this point significantly degrades the rate sensitivity compared to the corresponding linear case. As such, in contrast with the continuous electrode case, large drive amplitudes are not generally desirable for rate sensitivity enhancement.

Figure 3.10(a) shows the effects of the bias voltage and the electrode span on the peak normalised rate sensitivity S/S^l. The bias voltage is used to manipulate the Duffing

coefficient γ_0. For each of the iso-γ_0 plots, the bias voltage is increased when the electrode span decreases to keep γ_0 constant, thus retaining the strength of the electrostatic nonlinearities and drive mode softening rate. On the other hand, κ_0 diminishes to small values at small electrode spans and approaches γ_0 at larger electrode spans. For the cases of $\gamma_0 = -132, -85$ and $-48\ kHz^2$, the corresponding bias voltage ranges are $2.5 - 6.5V, 2 - 5.2V$ and $1.5 - 3.9V$ respectively. The peak normalised rate sensitivity is obtained by calculating S/S^l across a range of drive amplitudes in a manner similar to the results in Figure 3.9(a) and (b), up to $x/g_0 = 0.2$ and identifying the stationary point within this range. The imperfections considered in all 3 cases are such that the drive misalignment angle Θ_ω and the elastic modulus variation magnitude δE are identical to the systems considered in Figure 3.9(a) and (b).

Figure 3.10(b) plots the normalised rate sensitivity against drive amplitude for the $\delta = 38°$ case. The bias voltages for the cases $\gamma_0 = -132, -85$ and $-48\ kHz^2$ are 2.6, 2.1 and 1.6 V respectively and the $\gamma_0 = -85\ kHz^2$ plot is the same as the example shown in Figure 3.9(b). The dot markers show the rate sensitivity trimming points and the shaded regions between these points indicate the range of drive amplitudes yielding enhanced rate sensitivity beyond the linear, ideal/trimmed form as $P_{2,r}^{+}P_{2,r}^{-} > 0$.

Figure 3.10(c) plots the normalised rate sensitivity against drive amplitude with electrode spans of $\delta = 10°, 38°$ and $40°$ corresponding to the plot for $\gamma_0 = -85\ kHz^2$ in Figure 3.10(a), as indicated by the markers along this plot. Similar to Figure 3.10(b), the dot markers and shaded region indicate the drive amplitude range where $S > S_0^l$.

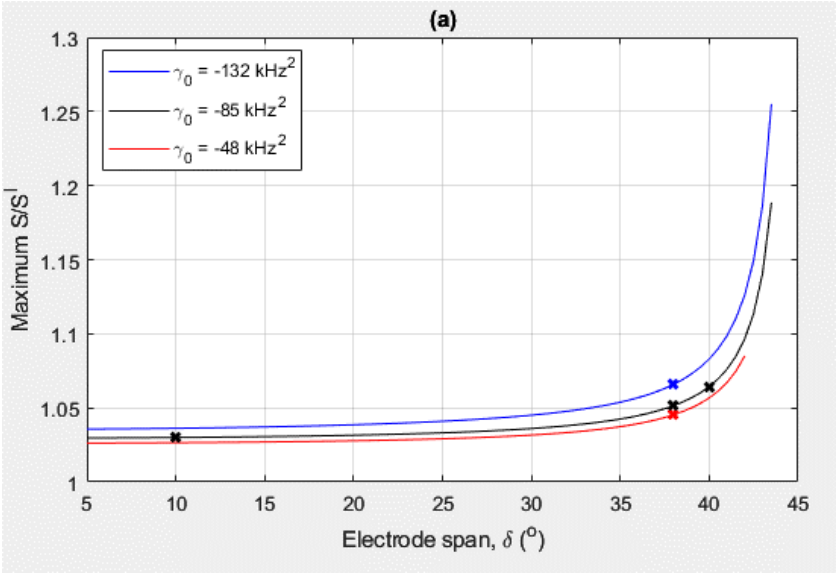

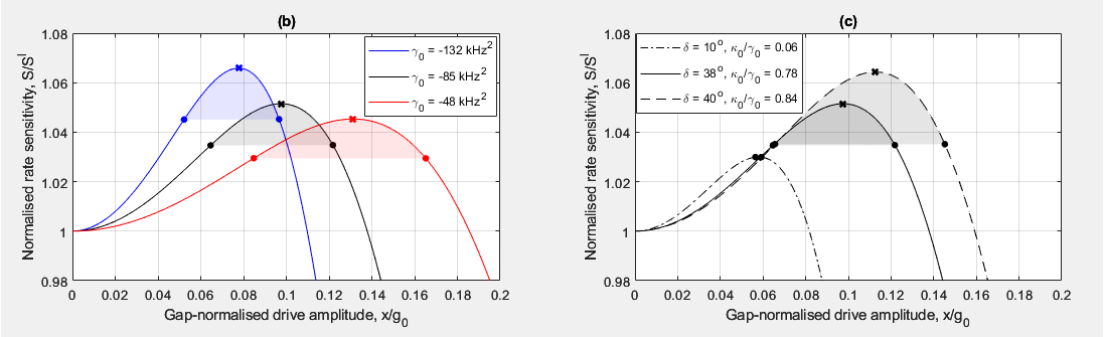

Figure 3.10: Effects of modal Duffing coefficient on (a) the variation of the maximum normalised rate sensitivity S/S^l with the electrode span and (b) the corresponding normalised rate sensitivity variation with the drive amplitude for $\delta = 38°$

In Figure 3.10(a), the maximum normalised rate sensitivity approaches large values when δ approaches 45°. This is because the upper bound of the drive amplitude range yielding rate sensitivity amplification diverges to large values when the electrodes approach continuity and the rate sensitivity increases monotonically with drive amplitude without exhibiting a turning point, as confirmed in Figure 3.9(a).

As the electrode span is reduced to small values such that $|\kappa_0/\gamma_0| \ll 1$, the maximum normalised rate sensitivity asymptotically approaches a fixed value. For the example in Figure 3.10(a), the maximum normalised rate sensitivities approach 1.036, 1.03 and 1.026 for cases $\gamma_0 = -132, -85$ and $-48\ kHz^2$ respectively, which are the calculated values of S_0^l/S^l. This indicates that the maximum normalised rate sensitivity approaches that of the linear, ideal/trimmed form. This is also shown in Figure 3.10(c), where S/S^l peaks at decreasing values as the electrode span decreases. The result for $\delta = 10°$ shows that S/S^l peaks at approximately S_0^l/S^l, offering negligible amplification beyond its linear, trimmed form. The two drive amplitudes at the amplification boundaries also approach each other, allowing the linear, trimmed rate sensitivity to be achieved across a range of drive amplitudes. This is the case when setting κ_0 at very small values in (3.64). The self-induced parametric excitation is responsible for the nonlinear amplification of the rate sensitivity within this amplification range, which is diminished at small electrode spans due to the negligible coupled-mode stiffness κ_0. Based on this result, smaller electrode spans provide rate sensitivity trimming of higher robustness due to the wider range of drive amplitudes yielding linear, trimmed rate sensitivities.

In Figure 3.10(b) the rate sensitivity trimming points indicated by the dot markers show that the same level of imperfection results in an increasing degradation of linear rate sensitivity as $|\gamma_0|$ increases due to the increased bias voltage. The linear rate sensitivity reductions are 4.6%, 3.5% and 3% for $\gamma_0 = -132, -85$ and $-48\ kHz^2$ respectively. This is because the drive frequency reduces when the bias voltage increases, thus decreasing the modal velocity and the

resulting damping force amplitude. This increases the susceptibility of the rate sensitivity to the degradation effects of the frequency split. When the bias voltage is increased to increase $|\gamma_0|$, the electrostatic nonlinearity strengthens, allowing trimming to be achieved at lower drive amplitudes. The decreasing drive amplitude at the S/S^l peaks and the increased bias voltage $|\kappa_0|$ have competing effects on the resulting self-induced parametric excitation amplitude dictating the maximum attainable S/S^l. However, the maximum normalised rate sensitivity exhibits a net increase as $|\gamma_0|$ increases, indicating that the increased coupled mode stiffness $|\kappa_0|$ has a more significant impact on the rate sensitivity amplification. This result indicates the desirability of a having a larger bias voltage for achieving amplification of the rate sensitivity. On the other hand, when $|\gamma_0|$ is reduced, the rate sensitivity amplification reduces and the drive amplitude range defining this amplification is wider, indicating that a smaller bias voltage is better suited for rate sensitivity trimming purposes.

3.5.3.2. Bias rate

In this section the zero-rate (bias) error arising from interactions between the nonlinear electrostatic forces and the linear elastic coupling force is investigated. Similar to the linear, imperfect case investigated in Section 3.5.1, the bias error is introduced as a rate-equivalent systematic offset of the sensor output, as described in (3.59), where Ω_z is the rate-equivalent bias given by:

$$\Omega_z = -\left(\frac{P_{2,r}^-}{2\Gamma\omega_X}\right)\frac{{\omega_0}^2\Delta_\omega \sin 4\Theta_\omega}{G_\Omega\omega_X} \tag{3.66}$$

Ω_z varies nonlinearly with drive amplitude due to term $P_{2,r}^-$, where the self-induced parametric excitation amplitude $\lambda_{1,r}$ interacts with the total detuning $\bar{\omega}^2$ to dictate the resulting bias output. This is in direct contrast with the corresponding linear form, Ω_z^l in (3.48), which is independent of drive amplitude.

$P_{2,r}^- = 0$ is the condition required for bias rate trimming, which is also one of the conditions for rate sensitivity trimming as indicated by the lower bound of the amplification range in (3.64). Inspection of (3.45), (3.55) and (3.63) shows that $P_{2,r}^-$ is related to its ideal/trimmed form $P_{2,r,0}^-$ by the relationship $P_{2,r}^- = {\bar{\omega}^l}^2 + P_{2,r,0}^-$. As such, the possibility for bias rate trimming is dictated by the drive misalignment. Noting from (3.55) that $P_{2,r,0}^- < 0$ because $|\kappa_0| < |3\gamma_0|$, the following interpretation apply:

- $\cos 4\Theta_\omega > 0, {\bar{\omega}^l}^2 > 0$: The electrostatic nonlinearities and linear detuning interact destructively.

- $\cos 4\Theta_\omega = 0, \bar{\omega}^{l^2} = 0$: The electrostatic nonlinearities introduce a bias rate independent of the linear frequency split.
- $\cos 4\Theta_\omega < 0, \bar{\omega}^{l^2} < 0$: The electrostatic nonlinearities and the linear detuning interact constructively.

The latter two cases are undesirable as these represent the cases where the electrostatic nonlinearities amplify the magnitude of the bias rate. Of these two cases, the case where $\cos 4\Theta_\omega = 0$ leads to larger bias rates because the drive misalignment is such that the linear elastic coupling force is maximised, i.e. $|\sin 4\Theta_\omega| = 1$. The first case represents the only possibility for nonlinear bias rate trimming.

Electrode continuity/discontinuity

The following investigates the effects of the electrode span on the bias rate nonlinearity, where this nonlinearity is a key feature for bias rate trimming. Figure 3.11 plots the nonlinear bias rate trimming for the systems considered in Figure 3.9(a) and (b). FE results are also shown for the corresponding cases.

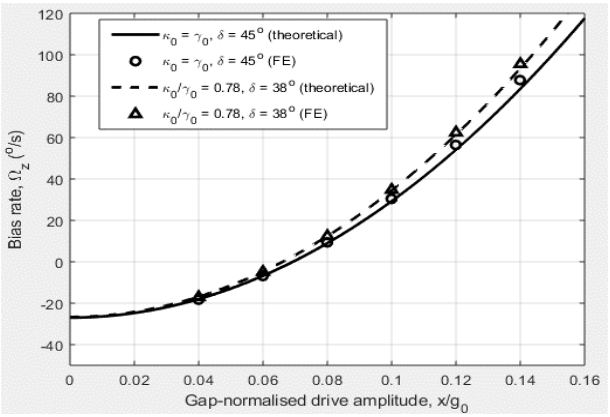

Figure 3.11: Effect of drive amplitude variation on bias rate for continuous and discontinuous electrodes

Figure 3.11 shows that with a drive misalignment of $\Theta_\omega = 1°$, nonlinear bias rate trimming is possible for both continuous and discontinuous electrode configurations. The FE results are in good agreement with the theoretical results across the range of drive amplitudes considered, particularly near the nonlinear bias rate trimming points. The bias rate trimming points are $x/g_0 = 6.9\%$ and 6.6% for the results corresponding to electrode spans of $\delta = 45°$ and $\delta = 38°$ respectively, which are also the lower boundaries of the rate sensitivity amplification range shown in Figure 3.9(a) and (b) for the corresponding electrode spans.

The electrostatic nonlinearities are negligible for lower drive amplitudes, so the nonlinear bias rate Ω_z approaches its linear, trimmed form $\Omega_z^l = -27°/s$, dictated predominantly by the imperfection-induced linear frequency split. As the drive amplitude increases, the electrostatic

nonlinearities counteract the linear frequency split, reducing the bias rate until the nonlinear bias rate trimming point. When the drive amplitude increases beyond this point, the electrostatic nonlinearities dominate, reversing the bias rate polarity. The bias rate variation is nonlinear, exhibiting in an increased amplitude sensitivity at higher drive amplitudes. As such, larger drive amplitude operations necessitate a stable drive amplitude to ensure a steady rate output.

The bias rate varies less nonlinearly when larger electrode spans are implemented. As such, the nonlinear bias rate trimming occurs at a larger drive amplitude for the results in Figure 3.11 corresponding to the continuous electrode configuration. This is desirable as achieving nonlinear bias rate trimming at a larger drive amplitude also results in a higher, trimmed rate sensitivity.

Bias voltage

The bias rate nonlinearity is also associated with the strength of the electrostatic nonlinearity, dictated by the bias voltage. The following investigates these nonlinear effects of the bias voltage. Figure 3.12 shows the effects of the bias voltage on bias rate variation with the drive amplitude. The plots correspond to the systems giving the rate sensitivity results in Figure 3.10(b). The result for the case of $V_0 = 2.1V$ is identical to the result for the electrode span of $\delta = 38°$ in Figure 3.11.

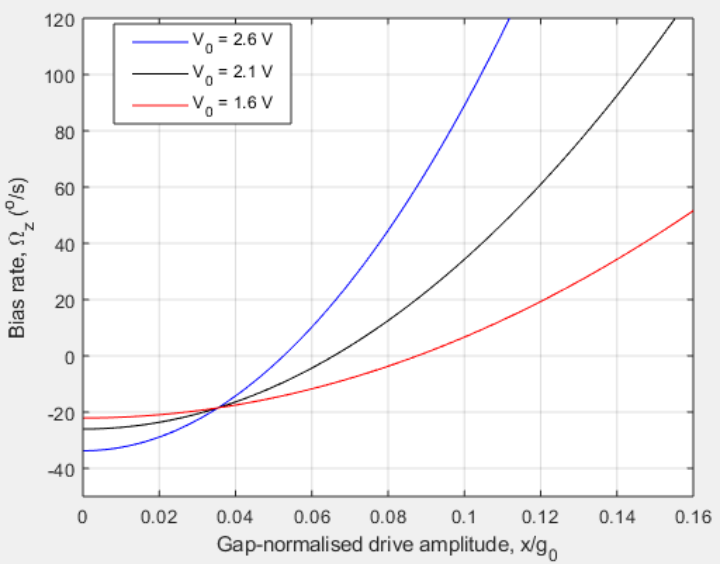

Figure 3.12: Effect of bias voltage on the nonlinear bias rate variation against the gap-normalised drive amplitude

In Figure 3.12, as observed for low drive amplitudes, the same level of imperfection results in increasing linear bias rate magnitudes when the bias voltage is increased. This is because a

larger bias voltage reduces the drive frequency ω_x, which reduces the modal velocity and Coriolis force. This can be confirmed from (3.66).

Increasing the bias voltage increases the magnitude of the Duffing coefficient γ_0, thus strengthening the electrostatic nonlinearity and the amplitude sensitivity of the bias rate. As such, similar to the rate sensitivity results in Figure 3.10(b), larger bias voltages are undesirable for nonlinear bias rate trimming due to the increased drive amplitude precision required to minimise bias rate.

3.5.3.3. Quadrature error

Similar to the perfect ring case in Section 3.5.2, the presence of a quadrature output is indicated by a deviation of the relative sense phase from $\phi_{yx} = \pm\pi$ ($\Omega > 0$) or $\phi_{yx} = 0$ ($\Omega < 0$). In the presence of imperfections, the relative sense phase is derived from (3.33), giving:

$$\phi_{yx} = \tan^{-1}\frac{P_{1,r}f_\Delta + P_{2,r}^{+}f_\Omega}{P_{2,r}^{-}f_\Delta + P_{1,r}f_\Omega} \tag{3.67}$$

Unlike the perfect ring case where the linear elastic coupling force f_Δ is absent, the nonlinear frequency balancing condition $\left(P_{2,r}^{+} = 0\right)$ does not generally guarantee a nullified quadrature error. In this case, nullifying the quadrature error imposes a condition for the linear elastic coupling force, $f_\Delta = f_{\Delta,\phi=n\pi}$ where $f_{\Delta,\phi=n\pi}$ is given by:

$$f_{\Delta,\phi=n\pi} = -\frac{P_{2,r}^{+}}{P_{1,r}}f_\Omega = -\left(\lambda_{1,r} - \bar{\omega}^2\right)\frac{G_\Omega \Omega x}{2\Gamma} \tag{3.68}$$

where the bracketed terms represent the nonlinear frequency imbalance $P_{2,r}^{+}$.

The condition in (3.68) can be satisfied in several ways:

- Ensuring nonlinear frequency balancing by nullifying the parametric excitation $\left(\lambda_{1,r} = 0\right)$ and matching the drive and sense frequencies ($\bar{\omega}^2 = 0$), while aligning the drive electrodes ($f_\Delta = 0$)
- Ensuring nonlinear frequency balancing such that $\lambda_{1,r} = \bar{\omega}^2$ without specifically $\lambda_{1,r} = 0$ and $\bar{\omega}^2 = 0$, while aligning the drive electrodes ($f_\Delta = 0$)
- $f_{\Delta,\phi=n\pi} \propto \Omega$ without nonlinear frequency balancing condition.

where the latter case requires the linear elastic coupling force amplitude to vary proportionally with the angular rate, which cannot be realised with the present basic electrostatic configuration.

In the absence of linear elastic coupling force (one of the former two cases), the effects of the nonlinear frequency imbalance on the relative phase is shown Figure 3.13(b), where the relative phase are plotted for drive amplitudes corresponding to the markers in the rate sensitivity plot in Figure 3.13(a). In a manner similar to Figure 3.10(b) and (c), the shaded region defines the amplification range where $S > S_0^l$. The results in Figure 3.13(a) and (b) correspond to the same system for the results in Figure 3.9(b), but without drive misalignment ($\Theta_\omega = 0°$).

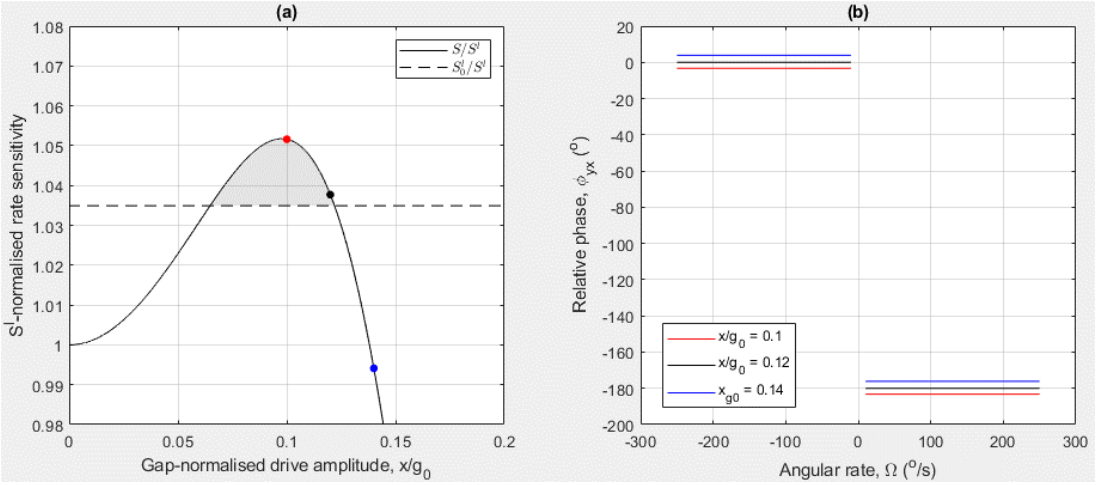

Figure 3.13: (a) Variation of the rate sensitivity normalised to the corresponding linear form against the drive amplitude and (b) the corresponding relative phase against the angular rate for $x/g_0 = 0.1, 0.12, 0.14$

In Figure 3.13(a), the dot markers are selected at various separations from the upper bound of the amplification range where nonlinear frequency balancing occurs. The magnitude of the nonlinear frequency imbalance is the smallest at $x/g_0 = 0.1$, yielding relative phase values at $\phi_{yx} \approx 0°$ for $\Omega < 0$ and $\phi_{yx} \approx -180°$ for $\Omega > 0$ in Figure 3.13(b). Larger deviations from the nonlinear frequency balancing point in Figure 3.13(a) increases the relative phase error due to the presence of the quadrature sense response. The drive amplitudes $x/g_0 = 10\%, 12\%$ and 14% yield nonlinear frequency imbalances of $P_{2,r}^{+} = -6.2e4, 5.3$ and $7.3e4\ Hz^2$ respectively, and the corresponding relative phase errors are $-3.3°, 2.8e-4°$ and $3.9°$ respectively.

From the results shown in Figure 3.13(b), nonlinear trimming can be simultaneously achieved for bias rate, rate sensitivity and quadrature error with the implementation of the basic electrostatic configuration at increased drive amplitudes, but only with drive alignment and nonlinear frequency balancing.

3.5.3.4. Summary

In the presence of imperfections, drive amplitude conditions exist where rate sensitivity trimming and enhancements can be achieved. However, these conditions are generally incompatible. The cubic coupled-mode stiffness dictated by the bias voltage and electrode span is a key parameter dictating the attainable rate sensitivity enhancement or the robustness of the trimming. Larger bias voltages and electrode spans promote rate sensitivity enhancement while smaller bias voltages and electrode spans are more desirable for robust rate sensitivity trimming.

Nonlinear trimming can be simultaneously achieved for the bias rate and rate sensitivity. However, this cannot be simultaneously achieved with quadrature error trimming unless there are no drive misalignments, in which case the nonlinear frequency balancing condition must be satisfied. This signifies the main limitation of the basic electrostatic configuration to replicate the output of a linear, ideal/trimmed device.

3.6. Summary and conclusions

A mathematical model has been developed to investigate the influence of electrostatic nonlinearity on the rate measuring performance of a capacitive ring based CVG having 8 evenly spaced electrodes inside and outside the ring resonator, where each electrode is subjected to bias and drive voltage components. The electrostatic nonlinearities stem from the nonlinear capacitance-displacement relationship for each electrode and it was found that the primary nonlinear effects arise from the bias voltage applied to all electrodes which generate cubic-ordered restoring forces. These forces are characterised by single and coupled-mode restoring forces and cause the drive and sense modes to exhibit the following non-linear behaviour as the drive amplitudes increases:

- amplitude-dependency of the drive and sense mode resonant frequencies
- the presence of self-induced parametric excitation

The influence of electrostatic nonlinearity on the rate measuring performance was investigated by investigating the rate sensitivity, bias rate and quadrature error as the drive amplitude increases and the main findings were:

- sense response does not scale linearly with drive amplitude.
- direct rate sensitivity cannot be enhanced without inducing quadrature and bias errors. The sense response deviates from its expected standard behaviour, with or without ring imperfections.

The nonlinear frequency balancing condition has been established as a nonlinear extension of the mode-matched condition in linear operation, involving a balance between drive frequency against the sense frequency and self-induced parametric excitation amplitude. The nonlinear frequency balancing condition, in conjunction with drive force alignment, are the key requirements to achieve nonlinear trimming of the sense response at increased drive amplitudes. When these conditions are not satisfied, the sense response cannot generally be simultaneously trimmed for the rate sensitivity, bias rate and quadrature error, which are important characteristics to replicate the expected rate output of a linear, trimmed device. Due to the drive amplitude dependency of the drive frequency, sense frequency and self-induced parametric excitation amplitude, specific conditions exist to achieve nonlinear trimming in the absence or presence of imperfections.

For the ideal/trimmed device, the absence of imperfections eliminates the possibility of drive misalignment so only the nonlinear frequency balancing condition is required to achieve trimmed sense response. It is found that implementing a continuous electrode distribution guarantees nonlinear frequency balancing. Smaller electrode spans introduce nonlinear frequency imbalances, which result in the introduction of quadrature errors and rate sensitivity reductions. Nonlinear frequency balancing can be achieved regardless of electrode discontinuities if 16 or 32 electrodes are implemented.

In the presence of imperfections, nonlinear frequency balancing is no longer guaranteed with electrode continuity, and is only achieved at specific drive amplitudes. When this is not achieved, it is found that the resulting nonlinear frequency imbalance in the presence of imperfections enables the possibility of rate sensitivity enhancement beyond that expected of the corresponding linear, ideal/trimmed device. This enhancement is more significant for larger electrode spans, but not without the introduction of quadrature errors and bias rates. On the other hand, minimising this enhancement improves the robustness of the trimming, in which case smaller electrode spans are desirable.

The restricted possibilities where nonlinear trimming can be achieved (with or without imperfections) necessitate strategic approaches to replicate linear, ideal/trimmed rate output. This is addressed in the next chapter.

4. LINEARISING AND TRIMMING SENSOR OUTPUT WITH ELECTROSTATIC NONLINEARITIES

4.1. Introduction

Chapter 3 details the effects of electrostatic nonlinearities on the rate sensing performance of CVG's as implemented under conventional operating conditions, where the electrostatic configuration is composed of biasing and driving mechanisms. It was shown that the rate output (dictating rate sensitivity and bias rate) and quadrature output (dictating quadrature error) deviate from what is expected of a standard, linear device as the drive amplitude increases. Under certain circumstances the rate sensitivity can be enhanced but this generally cannot be achieved without the introduction of zero rate bias and quadrature errors. These effects ultimately degrade device performance under large amplitude operation.

This chapter addresses the effects of these electrostatic nonlinearities, with the aim of developing practical methods to suppress these undesirable effects at increased drive amplitudes. The methods investigated are based on manipulating the electrostatic configuration by modifying the voltages applied to each electrode. This can be achieved in two stages:

1) Nullify the net parametric excitation.
2) Trim the device and nullify the quadrature output.

Section 4.2 re-considers the sense response from Chapter 3 and considers the dominant parameters responsible for sensor output nonlinearity. Section 4.3 investigates the potential to negate the self-induced parametric excitation by considering a modification of the basic electrostatic configuration. The advantage of negating the self-induced parametric excitation is demonstrated by comparing the bias rate, rate sensitivity and quadrature error for devices where the self-induced parametric excitation has been nullified against that corresponding to the basic electrostatic configuration. The conditions that lead to frequency matching are also considered as well as the effect of using different electrode spans. Section 4.4 investigates the potential to manipulate the net modal electrostatic force, and aims to develop a general framework to tailor the electrostatic force to nullify the self-induced parametric excitation and simultaneously trim the frequencies at a selected drive amplitude and eliminate the quadrature output[1]. In Section 4.5, the results in Section 4.3 are addressed to replicate the rate and

[1] This framework is also used in Chapter 5 for parametric amplification of the rate output.

quadrature outputs of a standard device which is both linear and trimmed when the net parametric excitation is nullified. For this purpose, the electrostatic configuration developed in Section 4.3 is modified further, using the framework proposed in Section 4.4. For the chosen electrostatic configuration, the equations of motions for the drive and sense modes are derived and used to determine the resulting sense mode dynamics. Conditions are then determined where the chosen voltage components can be used to nullify the net parametric excitation, linearise and trim the rate output, and nullify the quadrature output. To evaluate the effectiveness of the linearisation and trimming achieved, comparisons of the rate and quadrature outputs are made with those without addressing the force imbalances, as in the case investigated in Section 4.3. The potential of using the chosen electrostatic configuration for closed-loop rate sensing is also investigated, and conditions are identified where the closed-loop rate sensing performance are improved. The versatility of the implementation of the chosen electrostatic configuration to linearise and trim the sense response without negating the self-induced parametric excitation is also discussed by considering cases with and without nonlinear frequency balancing.

4.2. Sense response for the basic electrostatic configuration

In Section 3.4.2, the sense equation in (3.32) takes on the following general form:

$$\ddot{Y} + 2\Gamma\dot{Y} + \left[{\omega_Y}^2 + 2\lambda_{1,r}\cos 2(\omega t + \phi_x)\right]Y = f_\Omega \sin(\omega t + \phi_x) + f_\Delta \cos(\omega t + \phi_x) \tag{4.1}$$

where the averaged drive response is $X = x\cos(\omega t + \phi_x)$ and $\phi_x = -\pi/2$ so the drive mode is excited at resonance.

In this equation the coefficient associated with the sense displacement Y has been expressed to highlight the constant and double-frequency components. The constant component ${\omega_Y}^2$ characterises the amplitude-dependent effective sense frequency while the amplitude of the double-frequency component, $2\lambda_{1,r}$ is the self-induced parametric excitation amplitude characterising the stiffness modulation of the sense mode. This parametric excitation is phase-locked at twice the drive displacement phase. The rate output ($y\cos\phi_{yx}$) and quadrature output ($y\sin\phi_{yx}$) as described in (3.33) - (3.40) with λ_2 neglected are given by:

$$\begin{bmatrix} y\cos\phi_{yx} \\ y\sin\phi_{yx} \end{bmatrix} = -\frac{\bar{\bar{\mathbf{A}}}\bar{\boldsymbol{f}}_{\boldsymbol{Y}}}{{P_{1,r}}^2 - P_{2,r}^{+}P_{2,r}^{-}} = -\frac{\bar{\bar{\mathbf{A}}}\bar{\boldsymbol{f}}_{\boldsymbol{Y}}}{(2\Gamma\omega_X)^2 + (-{\omega_X}^2 + {\omega_Y}^2)^2 - {\lambda_{1,r}}^2} \tag{4.2}$$

where

$$\bar{\bar{\mathbf{A}}} = \begin{bmatrix} {\omega_X}^2 - {\omega_Y}^2 + \lambda_{1,r} & 2\Gamma\omega_X \\ 2\Gamma\omega_X & -{\omega_X}^2 + {\omega_Y}^2 + \lambda_{1,r} \end{bmatrix} \tag{4.3}$$

$$\bar{\boldsymbol{f}}_{\boldsymbol{Y}} = \begin{bmatrix} f_\Delta \\ f_\Omega \end{bmatrix} \tag{4.4}$$

In these equations ω_X, ω_Y and $\lambda_{1,r}$ are given in (3.29), (3.38) and (3.53) respectively, while the dissipation rate parameters $P_{1,r}$, $P_{2,r}^{\pm}$ are defined in (3.62) and (3.63) respectively.

For the linear, imperfect case, the rate output ($y^l \cos\phi_{yx}^l$) and quadrature output ($y^l \sin\phi_{yx}^l$) are (see (3.43)):

$$\begin{bmatrix} y^l \cos\phi_{yx}^l \\ y^l \sin\phi_{yx}^l \end{bmatrix} = -\frac{\begin{bmatrix} {\omega_X^l}^2 - {\omega_Y^l}^2 & 2\Gamma\omega_X^l \\ 2\Gamma\omega_X^l & -{\omega_X^l}^2 + {\omega_Y^l}^2 \end{bmatrix} \begin{bmatrix} f_\Delta \\ f_\Omega \end{bmatrix}}{4\Gamma^2 {\omega_X^l}^2 + \left({\omega_X^l}^2 - {\omega_Y^l}^2\right)^2} \tag{4.5}$$

(4.2) and (4.5) can be used to compare the sense response components for the nonlinear and linear cases. For large amplitude responses it can be shown that:

- If $\lambda_{1,r} = 0$, $\omega_X \neq \omega_Y$, $f_\Delta \neq 0$, the rate and quadrature outputs contain errors.
- If $\lambda_{1,r} = 0$, $\omega_X = \omega_Y$, $f_\Delta \neq 0$, the rate output is the same as a linear trimmed device, but the quadrature output is non-zero.
- If $\lambda_{1,r} = 0$, $\omega_X = \omega_Y$ and $f_\Delta = 0$, the rate output is the same as a linear trimmed device and the quadrature output is zero.

These conditions determine the different stages to achieve linearisation and trimming of the sense response, where $\lambda_{1,r} = 0$, $\omega_X = \omega_Y$ and $f_\Delta = 0$ ensures the nonlinear sense amplitude components in (4.2) approach $y_0^l \cos\phi_{yx,0}^l$ and $y_0^l \cos\phi_{yx,0}^l$ in (3.41). The different stages are: i) nullify the self-induced parametric excitation; ii) frequency match the drive and sense modes; iii) eliminate the drive/sense mode linear elastic coupling. The next section investigates how nullifying the net parametric excitation can be achieved, and the conditions for possible frequency matching.

4.3. Nullifying net parametric excitation

To nullify the net parametric excitation, the net electrostatic forces are changed by manipulating the voltages applied to the electrodes. Feasible modifications of the basic electrostatic configuration described in Section 3.3.1 are investigated to achieve this aim. The resulting equations of motion for the updated electrostatic configuration are developed, based

on which the drive and sense dynamics are similarly analysed to identify the voltage conditions where the self-induced parametric excitation is negated. The resulting rate output is then assessed in terms of the rate sensitivity and bias rate, and compared against that resulting from the basic electrostatic configuration. The conditions where the drive and sense frequencies are matched, thus trimming the rate output, are also investigated.

4.3.1. General description of voltage distribution

$V^{\pm}[\theta_0(i)]$ in (3.6) describes how the voltages are applied to each electrode for the basic electrostatic configuration. This electrostatic configuration can be modified by manipulating the voltages applied to each electrode. Before pursuing such modifications, it is useful to express the voltage squared distribution for the i'th electrode for the basic electrostatic configuration as:

$$V^{\pm}[\theta_0(i)]^2 = \xi_0^{\pm} + \xi_2^{\pm}\cos 2\theta_0(i) \tag{4.6}$$

The coefficient $\xi_0^{\pm}$ represents the component of voltage squared applied to all electrodes while $\xi_2^{\pm}$ represents the $\cos 2\theta_0(i)$ variation component of the voltage squared necessary to generate the 'push-pull' drive force to excite the drive mode into vibration. By comparing (4.6) against (D-1), $\xi_0^{\pm} = {V_0}^2$ and $\xi_2^{\pm} = \pm 2V_0V_{AC}\cos\omega t$, where terms involving ${V_{AC}}^2$ have been neglected because the drive voltage is small in practice. $\xi_0^{\pm}$ and $\xi_2^{\pm}$ contribute to the electrostatic potential energy components $\overline{U}$ and U_{AC} in (3.11) and (3.12) and contribute to the modal restoring force and the harmonic drive force respectively. Using (4.6) it can be shown that $\overline{U}$ and U_{AC} in (3.11) and (3.12) can be reformulated as:

$$\overline{U} = -j\frac{\varepsilon_0 BR}{4g_0}(\xi_0^{+} + \xi_0^{-})\left[2\delta + \delta\frac{X^2+Y^2}{{g_0}^2} + \left(\frac{3}{4}\delta + \frac{\sin 4\delta}{16}\right)\frac{X^4+Y^4}{{g_0}^4} + \frac{3}{4}\left(\delta - \frac{\sin 4\delta}{4}\right)\frac{2X^2Y^2}{{g_0}^4}\right] \tag{4.7}$$

$$U_{AC} = -\frac{j}{4}\frac{\varepsilon_0 BR\sin\delta}{g_0}(\xi_2^{+} - \xi_2^{-})\left[\frac{X}{g_0} + \left(\frac{5+\cos 2\delta}{6}\right)\frac{X^3}{{g_0}^3} + \sin^2\delta\frac{XY^2}{{g_0}^3}\right] \tag{4.8}$$

These equations indicate how $\xi_0^{\pm}$ and $\xi_2^{\pm}$ in (4.6) can be used to manipulate the form of $\overline{U}$ and U_{AC} and the resulting equations of motion when these electrostatic potential energy components are incorporated into Lagrange's equations.

In what follows, the forms for $\xi_0^{\pm}$ and $\xi_2^{\pm}$ are determined and used to select the voltage distribution $V^{\pm}[\theta_0(i)]$ necessary to negate the self-induced parametric excitation. This is

achieved by considering the elastic and drive components of the electrostatic potential energy, and then determining conditions to select the required voltage distribution.

Elastic component of electrostatic potential energy

The most direct approach to negate the self-induced parametric excitation is to apply a separate parametric excitation, acting in direct antiphase with the self-induced parametric excitation. For the basic electrostatic configuration presented in Section 3.3.1 where the existing parametric excitation is self-induced, the double-frequency variation of the stiffness term in (4.1) is the result of the harmonic drive displacement due to the cubic coupled-mode restoring force when the bias voltage V_0 is constant. This double-frequency stiffness variation can be achieved by directly modulating either the linear or cubic-order stiffnesses by manipulating the voltages. This is in contrast to self-induced parametric excitation where the double-frequency variation arises via the harmonic drive displacement instead of the voltages.

The electrostatic contributions to the linear and cubic stiffnesses contribute to the sense equation in (3.14) via the coefficients associated with the linear and cubic terms, i.e. ${\omega_0}^2, \gamma_0, \kappa_0$, which arise from the electrostatic potential energy component $\overline{U}$ in (3.11) or (4.7). For the basic electrostatic configuration (see Section 3.3.1), $\xi_0^{\pm} = {V_0}^2$ and $\xi_0^+ + \xi_0^-$ are time invariant and for this case, the linear modal stiffness is constant. However if the bias voltage V_0 is replaced by a harmonic voltage, coefficients $\xi_0^{\pm}$ can be modified so that $\xi_0^+ + \xi_0^-$ appearing in (4.7) includes a double-frequency variation and the desired stiffness variation can be achieved. In essence a separate parametric excitation is generated by varying the voltage, and the targeted form of $\xi_0^+ + \xi_0^-$ for this purpose is:

$$\xi_0^+ + \xi_0^- = \left(\xi_{0,0}^+ + \xi_{0,0}^-\right) + \left(\xi_{0,2}^+ + \xi_{0,2}^-\right)\cos 2(\omega t + \phi_x) \tag{4.9}$$

Coefficients $\xi_{0,0}^{\pm}$ and $\xi_{0,2}^{\pm}$ distinguish the constant and 2ω components, where the second subscript number determines the integral multiple of the frequency ω variation component. Provided that $\xi_{0,2}^+ + \xi_{0,2}^- \neq 0$, these coefficients generate the necessary 2ω variation of the linear stiffness, which must be designed to interact destructively with the self-induced parametric excitation. To ensure an antiphase relationship between the generated parametric excitation and the self-induced parametric excitation it is necessary to ensure $\xi_{0,2}^+ + \xi_{0,2}^- < 0$.

Driving component of electrostatic potential energy

To generate a harmonic drive force at frequency ω to excite the drive mode, it is necessary to apply squared voltages to the inner and outer electrodes such that $\xi_2^+ - \xi_2^-$ has the following targeted form:

$$\xi_2^+ - \xi_2^- = \left(\xi_{2,1}^+ - \xi_{2,1}^-\right)\cos\omega t \tag{4.10}$$

Noting that $\xi_2^\pm = \pm 2V_0V_{AC}\cos\omega t$ for the basic electrostatic configuration, the targeted form is achieved easily in this case. However, as will be shown, introducing a harmonic variation in $\xi_0^\pm$ to satisfy (4.9) can lead to other harmonic terms appearing in (4.10), leading to multi-frequency drive mode excitation. This outcome must be avoided to minimise any potential excitation of other modes of vibration. Also it is worth noting that if $\xi_2^+ = \xi_2^-$, the electrostatic drive forces arising from the inner and outer electrode sets cancel each other out, generating zero net drive force amplitude, and so should be avoided.

Voltage selection

The chosen voltage distribution must nullify the self-induced parametric excitation and excite the drive mode by satisfying both (4.9) and (4.10) respectively. The simplest approach to satisfy (4.9) and (4.10) is to use the same voltages described in (3.6), involving only spatially constant and $\cos 2\theta_0(i)$ variation components, but also vary the spatially constant component with time. For this purpose, the voltage applied to the *i*'th electrode is reformulated as:

$$V^\pm[\theta_0(i)] = a_{V,0}^\pm V_0 + a_{V,\lambda}^\pm V_\lambda \sin(\omega t + \phi_x) + a_{V,AC}^\pm V_{AC}\cos\omega t\cos 2\theta_0(i) \tag{4.11}$$

where $a_{V,0}^\pm$, $a_{V,\lambda}^\pm$, $a_{AC,0}^\pm$ are constants that dictate the relative magnitudes of the voltage components between the inner and outer electrode sets, and need to be determined.

In contrast to (3.6), an additional harmonic voltage $a_{V,\lambda}^\pm V_\lambda \sin(\omega t + \phi_x)$ is applied to all electrodes to generate the necessary double-frequency parametric excitation to satisfy (4.9). This is a parametric pumping voltage component applied in quadrature with the drive displacement. Squaring (4.11) and comparing with (4.6), it can be shown that coefficients $\xi_0^\pm$ and $\xi_2^\pm$ are given by:

$$\xi_0^\pm = {a_{V,0}^\pm}^2 {V_0}^2 + \frac{{a_{V,\lambda}^\pm}^2 {V_\lambda}^2}{2} + 2a_{V,0}^\pm a_{V,\lambda}^\pm V_0 V_\lambda \sin(\omega t + \phi_x) - \frac{{a_{V,\lambda}^\pm}^2 {V_\lambda}^2}{2}\cos 2(\omega t + \phi_x) \tag{4.12}$$

$$\xi_2^\pm = a_{V,AC}^\pm\left[a_{V,\lambda}^\pm V_\lambda V_{AC}\sin\phi_x + 2a_{V,0}^\pm V_0 V_{AC}\cos\omega t + a_{V,\lambda}^\pm V_\lambda V_{AC}\sin(2\omega t + \phi_x)\right] \tag{4.13}$$

where terms proportional to ${V_{AC}}^2$ have been discarded because they are assumed to be negligible.

Recalling from (4.7) that $\xi_0^{\pm}$ govern the linear and nonlinear modal elastic properties and $\xi_2^{\pm}$ contributes to the drive force it can be deduced that:

- $\xi_0^{\pm}$ has a constant component and harmonic components at frequencies ω and 2ω. The 2ω variation ensures the required parametric excitation is generated and contributes to $\xi_{0,2}^{+} + \xi_{0,2}^{-}$ in (4.9). However the ω variation leads to an undesirable isochronous parametric resonance which must be nullified when designing the electrode configuration.
- $\xi_2^{\pm}$ contains a constant component and harmonic components at frequencies ω and 2ω. The ω variation generates the desired drive force component but the 2ω component must be nullified to avoid undesirable excitation.

Using (4.12) and (4.13) and comparing with targeted forms (4.9) and (4.10), the conditions needed to obtain $a_{V,0}^{\pm}$, $a_{V,\lambda}^{\pm}$, $a_{AC,0}^{\pm}$ can be determined. Table 4.1 summarises the conditions to be satisfied.

Table 4.1: Description of the conditions for the constants $a_{V,0}^{\pm}$, $a_{V,\lambda}^{\pm}$, $a_{V,AC}^{\pm}$ in the voltage distribution in (4.11)

Condition	**Aim**
$a_{V,\lambda}^{+} a_{V,AC}^{+} = a_{V,\lambda}^{-} a_{V,AC}^{-}$	Eliminate constant and 2ω variation components in $\xi_2^{+} - \xi_2^{-}$
$a_{V,0}^{+} a_{V,AC}^{+} \neq a_{V,0}^{-} a_{V,AC}^{-}$	Ensure $\xi_2^{+} - \xi_2^{-}$ contains a harmonic component at frequency ω, i.e. $\xi_{2,1}^{+} - \xi_{2,1}^{-} \neq 0$ in (4.10)
$a_{V,0}^{+} a_{V,\lambda}^{+} = -a_{V,0}^{-} a_{V,\lambda}^{-}$	Eliminate ω variation component in $\xi_0^{+} + \xi_0^{-}$
$a_{V,\lambda}^{\pm} \neq 0$	Ensure $\xi_0^{+} + \xi_0^{-}$ contains a double-frequency component, i.e. $\xi_{0,2}^{+} + \xi_{0,2}^{-} \neq 0$ in (4.9)

Table 4.1 can be used to determine a suitable voltage distribution and hence voltages applied to the i'th electrode based on (4.11). These voltages can then be used to derive the electrostatic potential energy and equations of motion. This is considered in the next section.

4.3.2. Modal dynamics

In this section, equations of motion are developed based on applying a voltage distribution that satisfies the conditions in Table 4.1. The equations of motion are then used to investigate the sense mode dynamics when the self-induced parametric excitation has been negated.

Equations of motion

Based on the constraints outlined in the previous section, the equations of motion are developed using Lagrange's equation similar to that used for the basic electrostatic

configuration in (3.14), but with a modification to the electrostatic potential energy components $\overline{U}$ and U_{AC}. In what follows, the investigation is based on the specific voltage distribution with $a_{V,0}^{+} = a_{V,\lambda}^{+} = a_{V,AC}^{+} = a_{\overline{V},0}^{-} = 1$ and $a_{\overline{V},AC}^{-} = a_{\overline{V},\lambda}^{-} = -1$, which satisfy all conditions in Table 4.1. Substituting these coefficient values into (4.12) and (4.13) and then substituting the resulting expressions for $\xi_0^{\pm}$ and $\xi_2^{\pm}$ into (4.7) and (4.8) yields expressions for the electrostatic potential energy components $\overline{U}$ and U_{AC}. The total electrostatic potential energy $U = \overline{U} + U_{AC}$ is then substituted into Lagrange's equations in (3.5a) and (3.5b) to yield the resulting electrostatic modal forces represented by the derivatives $\partial U/\partial X$ and $\partial U/\partial Y$. The other elements of Lagrange's equations, i.e. the kinetic energy E_k, bending potential energy E_b and dissipation function D, have mechanical origins and are unaffected by the modification of the voltage distribution introduced. The resulting equations of motion are:

$$\overline{\overline{\boldsymbol{q}}}_{\boldsymbol{1}} + 2\Gamma\overline{\dot{\boldsymbol{q}}}_{\boldsymbol{1}} + \overline{\overline{\boldsymbol{\eta}}}_{\boldsymbol{1}}(t)\overline{\boldsymbol{q}}_{\boldsymbol{1}} + \overline{\overline{\boldsymbol{\eta}}}_{\boldsymbol{3}}(t)\frac{\overline{\boldsymbol{q}}_{\boldsymbol{3}}}{{g_0}^2} = \Omega\overline{\overline{\boldsymbol{G}}}_{\boldsymbol{\Omega}}\overline{\dot{\boldsymbol{q}}}_{\boldsymbol{1}} + \chi\cos\omega t\left(\begin{bmatrix}1\\0\end{bmatrix} + \overline{\overline{\boldsymbol{\eta}}}_{\boldsymbol{\chi}}\frac{\overline{\boldsymbol{q}}_{\boldsymbol{2}}}{{g_0}^2}\right) \tag{4.14}$$

Compared to (3.14), additional terms appear in (4.14) due to the parametric pumping voltage component $a_{V,\lambda}^{\pm}V_\lambda\sin(\omega t + \phi_x)$ applied to all electrodes. (4.14) is distinguishable from (3.14) through the time-varying linear and cubic stiffness matrices $\overline{\overline{\boldsymbol{\eta}}}_{\boldsymbol{1}}(t)$ and $\overline{\overline{\boldsymbol{\eta}}}_{\boldsymbol{3}}(t)$, which replace the constant stiffness matrices ${\omega_0}^2\overline{\overline{\Delta}}$ and $\overline{\overline{\boldsymbol{\eta}}}_{\boldsymbol{3}}$ in (3.14) respectively. $\overline{\overline{\boldsymbol{\eta}}}_{\boldsymbol{1}}(t)$ and $\overline{\overline{\boldsymbol{\eta}}}_{\boldsymbol{3}}(t)$ are given by:

$$\overline{\overline{\boldsymbol{\eta}}}_{\boldsymbol{1}}(t) = \begin{bmatrix}{\omega_{0,\lambda}}^2 & 0\\ 0 & {\omega_{0,\lambda}}^2\end{bmatrix} + {\omega_0}^2\overline{\overline{\Delta}}_\Delta + \begin{bmatrix}{\omega_\lambda}^2 & 0\\ 0 & {\omega_\lambda}^2\end{bmatrix}\cos 2(\omega t + \phi_x) \tag{4.15}$$

$$\overline{\overline{\boldsymbol{\eta}}}_{\boldsymbol{3}}(t) = \begin{bmatrix}\gamma_{0,\lambda} & 0 & \kappa_{0,\lambda} & 0\\ 0 & \kappa_{0,\lambda} & 0 & \gamma_{0,\lambda}\end{bmatrix} - \begin{bmatrix}\gamma_\lambda & 0 & \kappa_\lambda & 0\\ 0 & \kappa_\lambda & 0 & \gamma_\lambda\end{bmatrix}\cos 2(\omega t + \phi_x) \tag{4.16}$$

where

$${\omega_{0.\lambda}}^2 = {\omega_0}^2 - {\omega_\lambda}^2 \tag{4.17}$$

$$\gamma_{0,\lambda} = \gamma_0 + \gamma_\lambda \tag{4.18}$$

$$\kappa_{0,\lambda} = \kappa_0 + \kappa_\lambda \tag{4.19}$$

and the imperfection matrix $\overline{\overline{\Delta}}_\Delta$ is:

$$\bar{\bar{\Delta}}_{\Delta} = \bar{\bar{\boldsymbol{\Delta}}} - \bar{\bar{\mathbf{I}}} = \begin{bmatrix} \Delta_\omega \cos 4\Theta_\omega & \Delta_\omega \sin 4\Theta_\omega \\ \Delta_\omega \sin 4\Theta_\omega & -\Delta_\omega \cos 4\Theta_\omega \end{bmatrix} \tag{4.20}$$

${\omega_{0.\lambda}}^2$, $\gamma_{0,\lambda}$ and $\kappa_{0,\lambda}$ are the effective linear resonant frequency, single and coupled-mode cubic stiffnesses (modal mass normalised) respectively, arising from contributions associated with the bias and parametric pumping voltages. The definitions in (4.17) – (4.19) decompose the contributions of these voltages in terms of ${\omega_0}^2$, γ_0, κ_0 and ${\omega_\lambda}^2$, γ_λ and κ_λ. ${\omega_0}^2$, γ_0 and κ_0 are defined in (3.18), (3.22) and (3.23) and are associated with the bias voltage V_0 which is present in both the voltage distributions of the basic electrostatic configuration in (3.6) and the present scheme in (4.11). ${\omega_\lambda}^2$, γ_λ and κ_λ arise purely from the parametric pumping voltage amplitude V_λ in (4.11), resulting in constant and double frequency components in $\bar{\bar{\boldsymbol{\eta}}}_{\mathbf{1}}(t)$ and $\bar{\bar{\boldsymbol{\eta}}}_{\mathbf{3}}(t)$, as a result of squaring the second term in (4.11). The constant components contribute to ${\omega_{0.\lambda}}^2$, $\gamma_{0,\lambda}$ and $\kappa_{0,\lambda}$ in (4.17) – (4.19), while the double frequency components, as will be shown, can be used to negate the self-induced parametric excitation. ${\omega_\lambda}^2$, γ_λ and κ_λ are given by:

$${\omega_\lambda}^2 = j\frac{2\varepsilon_0 {V_\lambda}^2}{5\rho h\pi {g_0}^3}\delta \tag{4.21}$$

$$\gamma_\lambda = -j\frac{3\varepsilon_0 {V_\lambda}^2}{5\rho h\pi {g_0}^3}\left(\delta + \frac{\sin 4\delta}{12}\right) \tag{4.22}$$

$$\kappa_\lambda = -j\frac{3\varepsilon_0 {V_\lambda}^2}{5\rho h\pi {g_0}^3}\left(\delta - \frac{\sin 4\delta}{4}\right) \tag{4.23}$$

In the absence of any parametric pumping voltage, ${\omega_\lambda}^2 = \gamma_\lambda = \kappa_\lambda = 0$ and the linear and cubic stiffness matrices in (4.15) and (4.16) are constant, and the equations of motion in (4.14) revert to those of the basic electrostatic configuration in (3.14).

When nonlinear terms are neglected, i.e. setting $\bar{\boldsymbol{q}}_{\mathbf{2}} = \bar{\boldsymbol{q}}_{\mathbf{3}} = 0$ in (4.14), $\bar{\bar{\boldsymbol{\eta}}}_{\mathbf{1}}(t)$ retains its double frequency variation, modulating the linear modal stiffness due to the terms involving ${\omega_\lambda}^2$. This indicates that the additional parametric pumping voltage generates a linear parametric excitation independent of the drive amplitude, in direct opposition to the self-induced parametric excitation. This linear parametric excitation is the direct result of satisfying (4.9), which is used to counteract the self-induced parametric excitation.

When ${V_\lambda}^2$ in (4.21) – (4.23) is replaced by $2{V_0}^2$, (4.21) is identical to the last term defining ${\omega_0}^2$ in (3.18), while (4.22) and (4.23) are identical to the definitions of γ_0 and κ_0 in (3.22) and (3.23) respectively. This similarity is because, as shown in (4.11), the bias and parametric

pumping voltage components possess identical spatial variations. They are both identically applied across all electrodes. As such, γ_λ and κ_λ exhibit a similar relationship as γ_0 and κ_0, where γ_λ and κ_λ are only coincident if $\delta = 45°$. Also, $\gamma_\lambda, \kappa_\lambda < 0$ and $|\gamma_\lambda| \geq |\kappa_\lambda|$, indicating a stronger effect of the parametric pumping voltage V_λ on the single-mode cubic stiffness compared to its effect on the nonlinear modal elastic coupling. The discussion in Section 3.5.2 on the effect of the number of electrodes *j* also applies. If 16 or 32 electrodes are used, the terms involving $\sin 4\delta$ do not appear in (4.22) and (4.23) due to the nature of the electrostatic potential energy summation (see the detailed discussion in Appendix D), so $\gamma_\lambda = \kappa_\lambda$ regardless of electrode discontinuities in this case. The following investigation will highlight the significance of γ_λ and κ_λ, and the coincidence of these cubic stiffnesses.

The equations of motion developed in (4.14) are used to determine the resulting drive and sense mode dynamics and used to investigate rate sensing performance. In what follows, the assumptions, conditions and analysis implemented are similar to those applied in Sections 3.4.1 and 3.4.2.

Drive mode dynamics

Applying a similar single-degree-or-freedom approximation to the drive equation of motion in (4.14) as for (3.24) the drive equation of motion can be approximated as:

$$\ddot{X} + 2\Gamma\dot{X} + \left[{\omega_{0,\lambda}}^2 + {\omega_0}^2\Delta_\omega \cos 4\Theta_\omega + {\omega_\lambda}^2 \cos 2(\omega t + \phi_x)\right]X + \left[\gamma_{0,\lambda} - \gamma_\lambda \cos 2(\omega t + \phi_x)\right]\frac{X^3}{{g_0}^2} = \chi \cos \omega t \left[1 + c_{XX}\frac{X^2}{{g_0}^2}\right] \tag{4.24}$$

Similarly, applying the averaging procedure on (4.24), the effective drive frequency can be derived. The drive frequency is:

$${\omega_X}^2 = {\omega_X^l}^2 - {\omega_X^c}^2 - {\omega_{X,\lambda}^l}^2 - {\omega_{X,\lambda}^c}^2 \tag{4.25}$$

where

$$\begin{bmatrix} {\omega_X^c}^2 \\ {\omega_{X,\lambda}^l}^2 \\ {\omega_{X,\lambda}^c}^2 \end{bmatrix} = \begin{bmatrix} -\frac{3}{4}\gamma_0\frac{x^2}{{g_0}^2} \\ \frac{{\omega_\lambda}^2}{2} \\ -\gamma_\lambda\frac{x^2}{4{g_0}^2} \end{bmatrix} \tag{4.26}$$

and ${\omega_X^l}^2$ is defined in (3.42) in the analysis of the linear, imperfect ring.

In (4.25), the effective drive frequency depends on the drive amplitude and the contributing voltage components. The frequency components with the 'l' and 'c' superscripts stem from linear and cubic restoring forces respectively. As such the 'l' superscript frequency terms is amplitude-independent while the 'c' superscript frequency has quadratic-ordered amplitude dependence.

Comparing with the drive frequency for the basic electrostatic configuration in (3.29), the parametric pumping voltage only contributes to the drive frequency through the frequency terms ${\omega_{X,\lambda}^{l}}^2$ and ${\omega_{X,\lambda}^{c}}^2$ in (4.25). As such, the parametric pumping voltage affects both the effective linear and cubic drive stiffnesses. Noting that γ_0 and γ_λ are both negative, the parametric pumping voltage amplitude V_λ has an additional softening effect on the drive mode, acting in conjunction with the bias voltage to increase the softening rate of the drive mode.

Sense mode dynamics

Implementing a similar approximation to the sense equation of motion in (4.14) as for (3.32), the approximated sense equation of motion when $\omega = \omega_X$ is given by:

$$\ddot{Y} + 2\Gamma\dot{Y} + \left[{\omega_{0,\lambda}}^2 - {\omega_0}^2\Delta_\omega \cos 4\Theta_\omega + \left({\omega_\lambda}^2 - \kappa_\lambda \frac{X^2}{{g_0}^2}\right)\cos 2(\omega t + \phi_x) + \kappa_{0,\lambda}\frac{X^2}{{g_0}^2} - \frac{\chi c_{XY}}{g_0}\cos\omega t\frac{X}{g_0}\right] Y = -G_\Omega \Omega\dot{X} - {\omega_0}^2\Delta_\omega \sin 4\Theta_\omega X \tag{4.27}$$

The averaged sense amplitude components are:

$$\begin{bmatrix} y\cos\phi_{yx} \\ y\sin\phi_{yx} \end{bmatrix} = -\frac{\bar{\bar{\mathbf{A}}}\bar{\boldsymbol{f}}_{\boldsymbol{Y}}}{{P_{1,r}}^2 - P_{2,r}^{+}P_{2,r}^{-}} \tag{4.28}$$

where

$$\bar{\bar{\mathbf{A}}} = \begin{bmatrix} \bar{\omega}^2 + \lambda_{1,r} & 2\Gamma\omega_X \\ 2\Gamma\omega_X & -\bar{\omega}^2 + \lambda_{1,r} \end{bmatrix} \tag{4.29}$$

$$P_{1,r} = 2\Gamma\omega_X \tag{4.30}$$

$$P_{2,r}^{\pm} = \lambda_{1,r} \mp \bar{\omega}^2 \tag{4.31}$$

and the force vector $\bar{\boldsymbol{f}}_{\boldsymbol{Y}}$ is defined in (3.35). $\bar{\omega}^2$ and $\lambda_{1,r}$ describe the total frequency detuning and effective parametric excitation amplitude respectively and are given by:

$$\bar{\omega}^2 = {\omega_X}^2 - {\omega_Y}^2 = {\bar{\omega}^l}^2 - {\bar{\omega}^c}^2 + {\bar{\omega}_\lambda^l}^2 - \bar{\omega}_\lambda^{c\,2} \tag{4.32}$$

$$\lambda_{1,r} = \lambda_{1,0} + \lambda_{1,\lambda} \tag{4.33}$$

where the definitions of $\lambda_{1,r}$ and $\bar{\omega}^2$ have been modified from those of the basic electrostatic configuration in (3.53) and (3.61) due to the presence of the parametric pumping voltage.

ω_Y in (4.32) is the effective sense frequency given by:

$${\omega_Y}^2 = {\omega_Y^l}^2 - {\omega_Y^c}^2 - {\omega_{Y,\lambda}^l}^2 - {\omega_{Y,\lambda}^c}^2 \tag{4.34}$$

where the contributions from the resulting linear and cubic electrostatic forces arising from bias voltage V_0 and parametric pumping voltage amplitude V_λ have been decomposed in a manner similar to the drive frequency in (4.25). ω_Y^l is defined in (3.42), and the remaining contributions to the sense frequency in (4.34) are given by:

$$\begin{bmatrix} \omega_Y^{c\,2} \\ {\omega_{Y,\lambda}^l}^2 \\ {\omega_{Y,\lambda}^c}^2 \end{bmatrix} = \begin{bmatrix} -\kappa_0 \dfrac{x^2}{2{g_0}^2} \\ {\omega_\lambda}^2 \\ -\kappa_\lambda \dfrac{x^2}{4{g_0}^2} \end{bmatrix} \tag{4.35}$$

Using (4.26) and (4.35) the softening behaviour of the drive and sense modes can be obtained and compared. The linear electrostatic forces associated with the parametric pumping voltage are such that ${\omega_{Y,\lambda}^l}^2 = 2{\omega_{X,\lambda}^l}^2$. This shows that the linear electrostatic forces generate a greater softening effect on the sense mode than the drive mode. This is in contrast to the effects of the cubic electrostatic forces which always yield greater softening effects on the drive mode than the sense mode because $\omega_X^{c\,2} > \omega_Y^{c\,2}$, in the presence of self-induced parametric excitation.

$\bar{\omega}^2$ and $\lambda_{1,r}$ in (4.32) and (4.33) have been expressed in a manner to show the explicit contribution of the parametric pumping voltage, through the terms involving 'λ' subscripts in a manner similar to (4.15), (4.16), (4.25) and (4.34). The amplitude-independent, imperfection-induced frequency detuning ${\bar{\omega}^l}^2$ is defined in (3.45). The remaining terms defining $\bar{\omega}^2$ and $\lambda_{1,r}$ are given by:

$$\begin{bmatrix} \bar{\omega}^{c\,2} \\ \bar{\omega}_{\lambda}^{l\,2} \\ \bar{\omega}_{\lambda}^{c\,2} \end{bmatrix} = \begin{bmatrix} (2\kappa_0 - 3\gamma_0)\dfrac{x^2}{4{g_0}^2} \\ \dfrac{{\omega_\lambda}^2}{2} \\ (\kappa_\lambda - \gamma_\lambda)\dfrac{x^2}{4{g_0}^2} \end{bmatrix} \tag{4.36}$$

$$\begin{bmatrix} \lambda_{1,0} \\ \lambda_{1,\lambda} \end{bmatrix} = \begin{bmatrix} \kappa_0 \dfrac{x^2}{4{g_0}^2} \\ \dfrac{{\omega_\lambda}^2}{2} \end{bmatrix} \tag{4.37}$$

As can be deduced from (4.32), in all cases, the drive mode exhibits a higher nonlinear softening rate than the sense mode because $\bar{\omega}^{c\,2}$ and $\bar{\omega}_{\lambda}^{c\,2}$ lower the total frequency detuning. In general the cubic restoring force associated with the parametric pumping voltage increases the softening rate difference between the drive and sense modes compared to that of the basic electrostatic configuration case, i.e. when $\bar{\omega}_{\lambda}^{c\,2} = 0$. However, an exception to this is when a continuous electrode distribution is implemented or the number of electrodes is increased to 16 or 32 such that $\kappa_\lambda = \gamma_\lambda$. In this case $\bar{\omega}_{\lambda}^{c\,2} = 0$ regardless of the presence of the parametric pumping voltage, so the relative nonlinear softening rate between the drive and sense modes is unaffected by the parametric pumping voltage. However, when considering the contribution of the parametric pumping voltage to the linear restoring force, $\bar{\omega}_{\lambda}^{l\,2}$ in (4.32) reduces the softening difference between the drive and sense modes due to the aforementioned relationship ${\omega_{Y,\lambda}^{l}}^2 = 2{\omega_{X,\lambda}^{l}}^2$. The opposing effects of the linear and cubic electrostatic forces on the effective frequency detuning is important and will be exploited for frequency matching purposes later in this chapter.

The sense amplitude components in (4.28) differ from those of the basic electrostatic configuration case in (3.33) due to the slightly reduced drive frequency (compare (4.25) against (3.29)) and the presence of the additional terms in the sense equation (4.27) due to the parametric pumping voltage. The slight reduction of the drive frequency ω_X slightly lowers the amplitudes of the Coriolis and damping forces, thus decreasing $P_{1,r}$ and f_Ω. However, the dominant effects of the parametric pumping voltage are on the total frequency detuning and effective parametric excitation amplitude described in (4.32) and (4.33). As discussed previously, the total frequency detuning and effective parametric excitation amplitude are generally amplitude-dependent and as such, they are important parameters dictating the strength of the nonlinearity of the rate and quadrature outputs.

4.3.3. Conditions for nullifying net parametric excitation

In the following, the sense dynamics in Section 4.3.2 are investigated to understand the impact of eliminating the net parametric excitation. The results are then assessed by comparing the rate output to that of a linear device, trimmed or untrimmed.

The effective parametric amplification amplitude described by $\lambda_{1,r}$ in (4.33) is the result of the interaction between the linear parametric excitation and the amplitude-dependent self-induced parametric excitation, represented by the terms $\lambda_{1,\lambda}$ and $\lambda_{1,0}$ respectively, where $\lambda_{1,\lambda} > 0$ and $\lambda_{1,0} < 0$ and the opposite signs are due to the antiphase relationship between the self-induced parametric excitation and the linear parametric excitation. As such, these parametric excitation components interact destructively, allowing the net parametric excitation amplitude to be nullified. Setting $\lambda_{1,r} = 0$ an expression for the required parametric pumping voltage amplitude V_λ to nullify the net parametric excitation can be obtained. Using (4.33) and (4.37) the linear resonant frequency contribution ${\omega_\lambda}^2$ after nullification is given by:

$$ {\omega_\lambda}^2|_{\lambda_{1,r}=0} = -\kappa_0 \frac{x^2}{2{g_0}^2} \tag{4.38} $$

Recalling from (4.21) and (3.23) that ${\omega_\lambda}^2 \propto {V_\lambda}^2$ and $\kappa_0 \propto {V_0}^2$, the condition for nullifying the net parametric excitation in (4.38) imposes a proportional relationship between the parametric pumping voltage amplitude V_λ, and the bias voltage and drive amplitude.

In the following, condition (4.38) is used to illustrate the effects of bias voltage and drive amplitude on the parametric pumping voltage V_λ required to negate the self-induced parametric excitation for a particular device having 8 evenly-spaced electrodes (inner and outer) with electrode span $\delta = 38°$, subjected to a linear damping of $\Gamma = 56.5\ Hz$. Figure 4.1(a) shows a plot of the required parametric pumping voltage amplitude against the bias voltage and drive amplitude. The drive voltage amplitude V_{AC} is tuned to yield varying drive amplitudes up to $x/g_0 = 0.2$. Figure 4.1(b) shows the corresponding variation of the parametric pumping voltage amplitude with the drive amplitude for the constant bias voltage planes $V_0 = 1, 2.1$ and $3\ V$ in Figure 4.1(a).

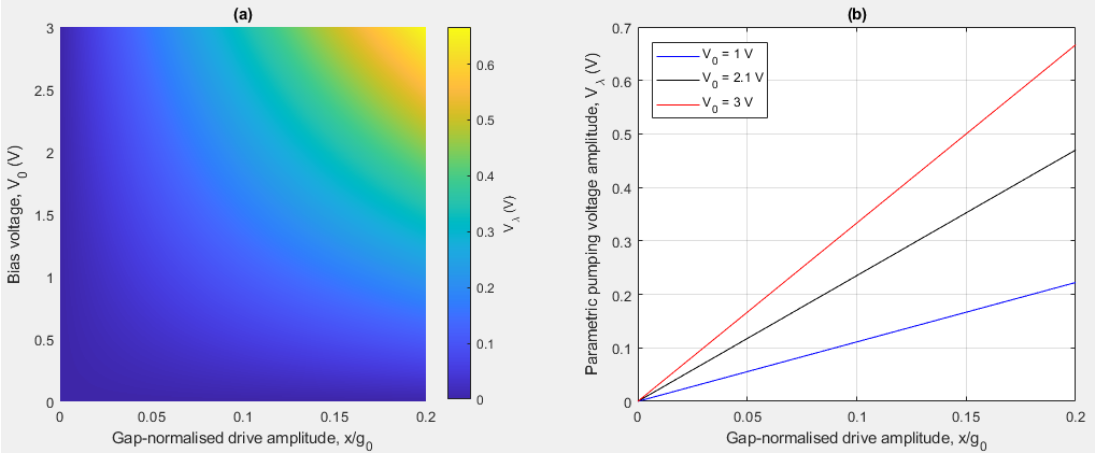

Figure 4.1: (a) Effects of drive amplitude and bias voltage on the required parametric pumping voltage to negate the self-induced parametric excitation and (b) the corresponding variation of this parametric pumping voltage with drive amplitude for bias voltages $V_0 = 1, 2.1, 3$ V

Figure 4.1(a) shows that increasing the drive amplitude or the bias voltage necessitates a larger parametric pumping voltage to nullify the net parametric excitation amplitude. This is because, as previously noted, the self-induced parametric excitation is amplitude-dependant. Increasing the bias voltage strengthens the electrostatic nonlinearity, hence the nonlinear elastic coupling, which has a similar effect of increasing the self-induced parametric excitation amplitude. The increase in the self-induced parametric excitation amplitude must be compensated for by increasing the linear parametric excitation amplitude to yield a nullified net parametric excitation. As shown in Figure 4.1(b), the parametric pumping voltage amplitude required to nullify the net parametric excitation is proportional to the drive amplitude, where a larger bias voltage increases the amplitude-sensitivity of this voltage amplitude.

4.3.4. Rate measuring performance with nullified net parametric excitation

When the net parametric excitation is nullified, the sense mode reverts back to being a simple harmonic oscillator, driven only directly by the Coriolis and linear elastic coupling forces. To assess the resulting performance of the device, it is useful to consider the resulting rate sensitivity and bias rate based on the rate and quadrature outputs in (4.28).

Recalling the rate sensitivity and bias rate for a linear device in (3.47) and (3.48), the rate output for a device that is not necessarily trimmed is characterised by:

- a rate sensitivity which scales proportionally with drive amplitude
- a bias rate which is invariant with drive amplitude

For the specific case of a device which is both linear and trimmed, the rate sensitivity is proportional to the drive amplitude and the bias rate is zero regardless of drive amplitude.

The effects of the parametric pumping voltage on the rate sensitivity and bias rate are investigated to identify conditions where the aforementioned linear rate output characteristics can be replicated. For this purpose, the in/antiphase sense amplitude component in (4.28) is expressed in the form $y\cos\phi_{yx} = S(\Omega + \Omega_z)$. The rate sensitivity and bias rate when the net parametric excitation is nullified (i.e. (4.38) is satisfied) are given respectively by:

$$S|_{\lambda_{1,r}=0} = -x\frac{G_\Omega\omega_X(2\Gamma\omega_X)}{(2\Gamma\omega_X)^2 + \left(\bar{\omega}^2|_{\lambda_{1,r}=0}\right)^2} \tag{4.39}$$

$$\Omega_z|_{\lambda_{1,r}=0} = -\left(\frac{\bar{\omega}^2|_{\lambda_{1,r}=0}}{2\Gamma\omega_X}\right)\frac{{\omega_0}^2\Delta_\omega\sin 4\Theta_\omega}{G_\Omega\omega_X} \tag{4.40}$$

and the relative phase quantifying the quadrature error is:

$$\phi_{yx}|_{\lambda_{1,r}=0} = \tan^{-1}\left[\frac{-(2\Gamma\omega_X)f_\Delta + \left(\bar{\omega}^2|_{\lambda_{1,r}=0}\right)f_\Omega}{-\left(\bar{\omega}^2|_{\lambda_{1,r}=0}\right)f_\Delta - (2\Gamma\omega_X)f_\Omega}\right] \tag{4.41}$$

where $\bar{\omega}^2|_{\lambda_{1,r}=0}$ and $\omega_X = \omega_X|_{\lambda_{1,r}=0}$ are the total frequency detuning and drive frequency under the condition that the parametric pumping voltage amplitude V_λ has been tuned to nullify the net parametric excitation amplitude, i.e. satisfying (4.38). This condition fixes the amplitude of the linear electrostatic forces arising from the parametric pumping voltage, and so fixes the softening difference between the drive and sense modes. This can be shown by substituting (4.38) into ${\omega_{X,\lambda}^l}^2$ and ${\omega_{Y,\lambda}^l}^2$ in (4.26) and (4.35), followed by substituting the results into the expressions for the drive and sense frequencies in (4.25) and (4.34). Substituting (4.38) into the general frequency detuning $\bar{\omega}^2$ in (4.32) gives the following expression for the constrained frequency detuning $\bar{\omega}^2|_{\lambda_{1,r}=0}$ when the net parametric excitation is nullified:

$$\bar{\omega}^2|_{\lambda_{1,r}=0} = 2{\omega_0}^2\Delta_\omega\cos 4\Theta_\omega - 3(\kappa_0 - \gamma_0)\frac{x^2}{4{g_0}^2} - (\kappa_\lambda - \gamma_\lambda)\frac{x^2}{4{g_0}^2} \tag{4.42}$$

The amplitude of the linear parametric excitation arising from the parametric pumping voltage has been matched to the self-induced parametric excitation amplitude, so ${\omega_\lambda}^2$ has been replaced with the nonlinear term representing the self-induced parametric excitation using (4.38). As such, the only amplitude-independent term in (4.42) arises from ring imperfection.

(4.39) and (4.40) are similar to the corresponding linear, imperfect forms of S^l and Ω_z^l in (3.47) and (3.48), but with amplitude-dependent frequency detuning and drive frequency, $\bar{\omega}^2|_{\lambda_{1,r}=0}$

and $\omega_X|_{\lambda_{1,r}=0}$ respectively. As such, if the frequency detuning $\bar{\omega}^2|_{\lambda_{1,r}=0}$ is independent of the drive amplitude in a manner similar to $\bar{\omega}^{l^2}$, $S|_{\lambda_{1,r}=0}$ is approximately proportional to the drive amplitude and $\Omega_z|_{\lambda_{1,r}=0}$ is desensitised to drive amplitude variations, thus yielding the rate output of a linear, imperfect device. In this case, the quadrature output is also linearised. Due to the linearity of both the rate and quadrature outputs, the relative phase in (4.41) is insensitive to drive amplitude variations as $f_\Omega \propto x$ and $f_\Delta \propto x$.

When the frequency detuning is both amplitude-insensitive and nullified, i.e. frequency matched, the device reproduces the rate output of a device which is both linear and trimmed, in which case the rate sensitivity $S|_{\lambda_{1,r}=0}$ is identical to S_0^l in (3.41) while the bias rate $\Omega_z|_{\lambda_{1,r}=0}$ nullifies. However, the quadrature output does not generally nullify as the relative phase in (4.41) reduces to $\phi_{yx}|_{\lambda_{1,r}=0} = \tan^{-1}(f_\Delta/f_\Omega)$ in this case. As such, in addition to frequency matching, nullification of the linear elastic coupling force ($f_\Delta = 0$) is also required to eliminate the quadrature error.

Frequency matching can be achieved when the amplitude-dependent component in (4.42) interacts destructively with the contribution of the imperfection, enabling the frequency detuning to be nullified at a specific drive amplitude. $\bar{\omega}^2|_{\lambda_{1,r}=0} = 0$ for a general drive amplitude only if the drive misalignment is such that $\cos 4\Theta_\omega = 0$, and $\kappa_0 = \gamma_0$ and $\kappa_\lambda = \gamma_\lambda$. This condition is discussed next.

The frequency detuning dictates the linearity of the rate and quadrature outputs as the drive amplitude increases. As shown in (4.42), $\bar{\omega}^2|_{\lambda_{1,r}=0}$ has a quadratic-ordered drive amplitude dependence, so linear rate and quadrature outputs are not generally guaranteed when the net parametric excitation is nullified. An exception to this is when a continuous electrode distribution is implemented, or the number of electrodes is increased to 16 or 32, in which case the conditions $\kappa_0 = \gamma_0$ and $\kappa_\lambda = \gamma_\lambda$ apply and the frequency detuning is amplitude independent. Thus for larger electrode spans the coupled and single-mode stiffnesses approximate each other, and nullifying the net parametric excitation leads to amplitude independent frequency detuning and linear rate and quadrature outputs.

Effects of electrode continuity/discontinuity on rate sensitivity, bias rate and quadrature error with negated self-induced parametric excitation

The following investigates the influence of electrode span on the rate sensitivity, bias rate and quadrature error for a device in which the net parametric excitation is nullified, and compares against the case when the self-induced parametric excitation is present. In this investigation and throughout the remainder of this chapter, two defaults systems are used as the controls to

represent continuous and discontinuous electrode distributions, with parameters listed in Table 4.2, in addition to the parameters listed Table C.1.

Table 4.2: Parameters of control sets of systems

	System 1	System 2
Parameters	Values	
j	8	8
$V_0\ (V)$	2.1	2
$\delta\ (°)$	38	45
$\Gamma\ (Hz)$	56.5	56.5
δE	0.0011	0.0011
$\Theta_\omega\ (°)$	1	1

In Table 4.2, the bias voltage is increased as the electrode span reduces to keep the modal Duffing coefficient γ_0 constant, thus fixing the strength of the electrostatic nonlinearity. In this investigation, an additional system is also considered, with electrode span $\delta = 15°$, bias voltage $V_0 = 3.1V$ and identical remaining parameters to those listed in Table 4.2. The electrode span cases of $\delta = 15°$, 38° and 45° correspond to cubic stiffness ratios of $\kappa_0/\gamma_0 = \kappa_\lambda/\gamma_\lambda$ of 0.14, 0.78 and 1 respectively.

The rate sensitivity and bias rate variations with drive amplitude for these systems are shown in Figure 4.2(a) and (b) respectively, and are compared against the corresponding rate sensitivity and bias rate when self-induced parametric excitation is present. The solid plots represent the results where self-induced parametric excitation is negated by the parametric pumping voltage where the amplitude V_λ is set at the values calculated using (4.38) for the drive amplitude range considered, and the dashed plots represent the results where the parametric pumping voltage is absent ($V_\lambda = 0$). In Figure 4.2(a), the imperfection considered results in a linear rate sensitivity reduction of 2.5% from S_0^l to S^l. In Figure 4.2(b), the linear bias rate is $\Omega_z^l = -23°/s$. FE results are also shown for the set of results corresponding to system 1 in Table 4.2. Figure 4.3 shows the corresponding relative phase for the same systems in Figure 4.2(a) and Figure 4.2(b) for one angular rate case at $\Omega = 250\,°/s$.

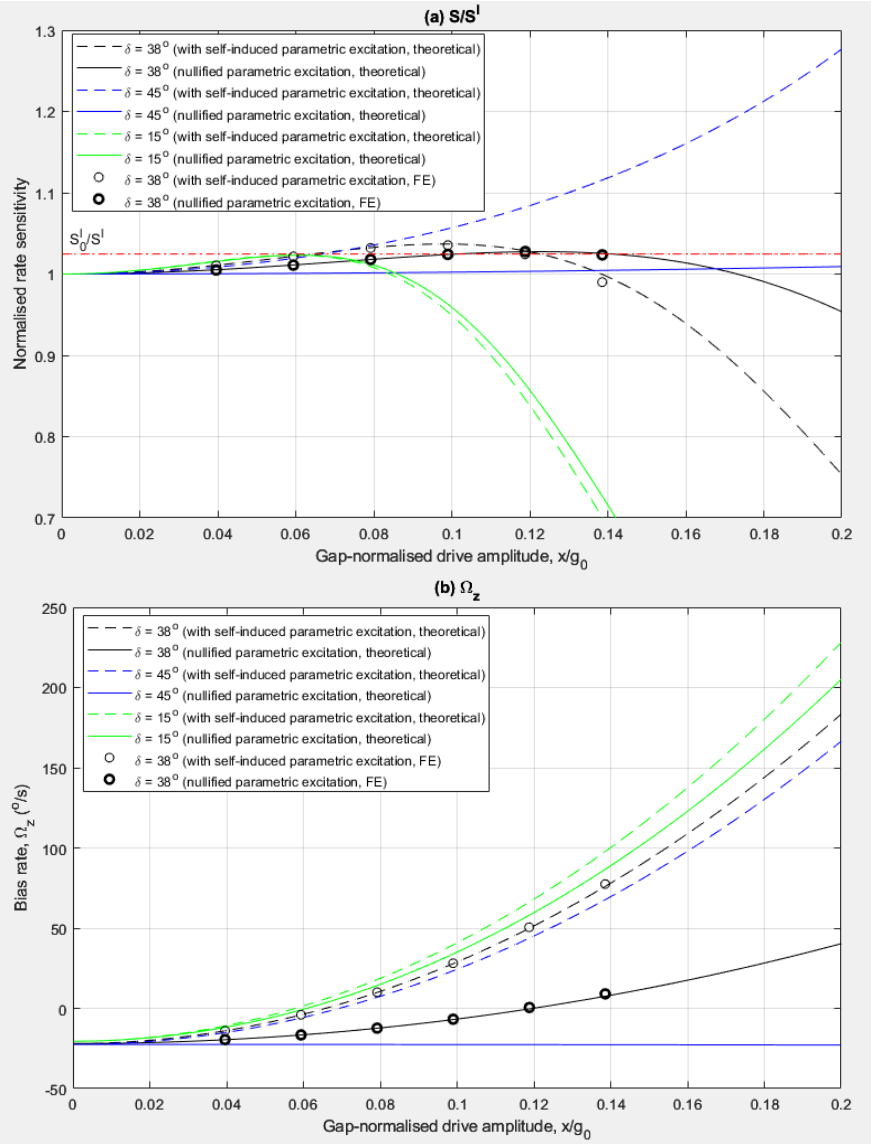

Figure 4.2: Effect of drive amplitude variation on the (a) normalised rate sensitivity and (b) bias rate with and without the parametric pumping voltage for various electrode spans

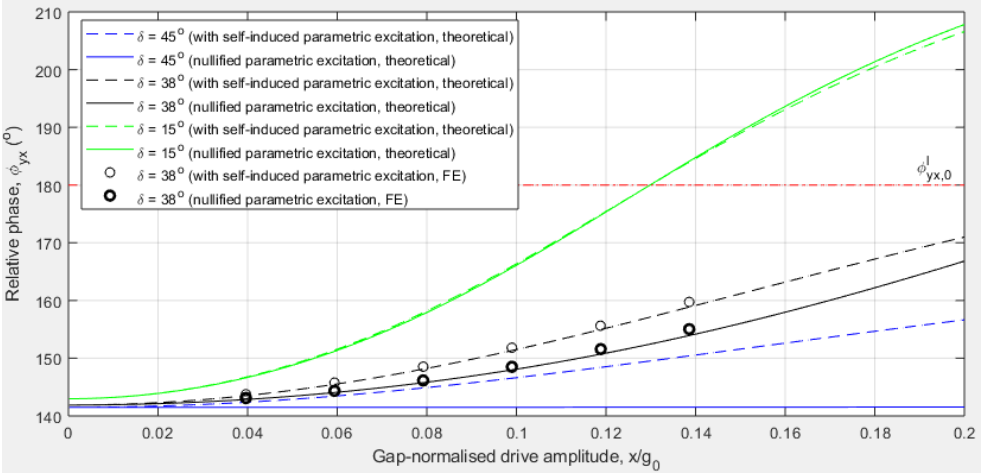

Figure 4.3: Drive amplitude dependency of relative phase for the cases of with and without the parametric pumping voltage for various electrode spans

In Figure 4.2(a), the rate sensitivity exhibits improved linearity when the net parametric excitation is nullified. Comparing the dashed and solid lines in Figure 4.2(a) for all the electrode span cases, it is clear that negating the self-induced parametric excitation suppresses the nonlinear behaviour, with the maximum effectiveness achieved when the electrodes are continuous. This is because, when the parametric pumping voltage is set to counteract the self-induced parametric excitation, the required amplitude V_λ also reduces the softening rate difference between the drive and sense modes. Consequently, the drive amplitude dependency of the frequency detuning is suppressed. For the discontinuous electrode cases, this nonlinear suppression is advantageous as the rate sensitivity degradation at larger drive amplitudes is reduced.

In Figure 4.2(a), nullifying the net parametric excitation also eliminates the possibility of the nonlinear rate sensitivity $S|_{\lambda_{1,r}=0}$ increasing beyond S_0^l. This is because, as discussed in Section 3.5.3, the special case of rate sensitivity amplification beyond what is expected of a linear, trimmed device is only achievable through the Q factor increasing the effects of parametric excitation. However, for the discontinuous electrode configuration with $\delta = 38°$, $S|_{\lambda_{1,r}=0}$ is slightly higher than S_0^l when x/g_0 is between 10.2% and 14.1%, indicating that the aforementioned amplification is still present. This indicates that the net parametric excitation is not completely nullified. The present scheme is only targeted at negating the self-induced parametric excitation stemming predominantly from the nonlinear elastic coupling due to the bias voltage, so the residual parametric excitation stems from the drive voltage as discussed in Section 3.4.2, which has been neglected in the present analysis. Despite this, the peak of $S|_{\lambda_{1,r}=0}/S^l$ is much lower than that in the presence of the self-induced parametric excitation and the amplification of $S|_{\lambda_{1,r}=0}$ beyond S_0^l is insignificant, thus confirming the dominance of the bias voltage for the self-induced parametric excitation.

In Figure 4.2(b), the bias rate nonlinearity is also reduced when the self-induced parametric excitation is negated. The bias rate approaches the corresponding linear case, unaffected by drive amplitude variations when the parametric pumping voltage is applied with a continuous electrode distribution. The reduced amplitude sensitivity of the bias rate in the presence of the parametric pumping voltage is the result of both the nullified net parametric excitation and the reduced relative softening rate between the drive and sense modes.

In Figure 4.3, the effects of nullifying the net parametric excitation on the relative phase are similar to those for the rate sensitivity and bias rate in Figure 4.2(a) and Figure 4.2(b). Nullifying the net parametric excitation ensures that the quadrature output amplifies linearly with the drive amplitude in a manner similar to the rate output, resulting in an amplitude-insensitive relative phase. The effects of the negation of the self-induced parametric excitation

are less significant for smaller electrode spans. The nonlinear variation of the relative phase for the discontinuous electrode cases enables nullification of the quadrature error at specific drive amplitudes. However, it is important to note that this is not a general case of quadrature error nullification as in the case for linear, perfect devices. This is because the result in Figure 4.3 only corresponds to a specific angular rate.

The results in Figure 4.2(a) and (b) and Figure 4.3 conclude that nullifying the net parametric excitation can suppress the nonlinear drive amplitude dependence of the rate sensitivity, bias rate and quadrature error, and linearity is achieved for continuous electrode distributions. However, trimming of the rate and quadrature outputs at an arbitrarily chosen drive amplitude is not guaranteed.

Effects of number of discontinuous electrodes on rate sensitivity and bias rate with negated self-induced parametric excitation

The results for the rate sensitivity $S|_{\lambda_{1,r}=0}$, bias rate $\Omega_z|_{\lambda_{1,r}=0}$ and relative phase $\phi_{yx}|_{\lambda_{1,r}=0}$ conclude that nullifying the net parametric excitation improves the linearity of the rate output, and is most effective when a continuous electrode distribution is implemented, thus signifying the importance of ensuring $\gamma_0 = \kappa_0$ and $\gamma_\lambda = \kappa_\lambda$ conditions. As noted previously, these conditions can also be met with discontinuous electrode configurations if the number of electrodes is increased to $j = 16$ or 32.

The following investigates the effectiveness of nullifying the parametric excitation for rate output linearisation in devices implementing a different number of discontinuous electrodes j. Devices implementing $j = 8$ and 16 discontinuous electrodes with electrode span $\delta = 15°$ are considered for this investigation, with bias voltages of $V_0 = 3.1\ V$ and $2.4\ V$ respectively. Figure 4.4(a) and (b) compare the drive amplitude dependencies of the normalised rate sensitivity S/S^l and bias rate Ω_z with and without the net parametric excitation being nullified. The system corresponding to the results for $j = 8$ is identical to that of the results in Figure 4.2(a) and (b) corresponding to the $\delta = 15°$ case.

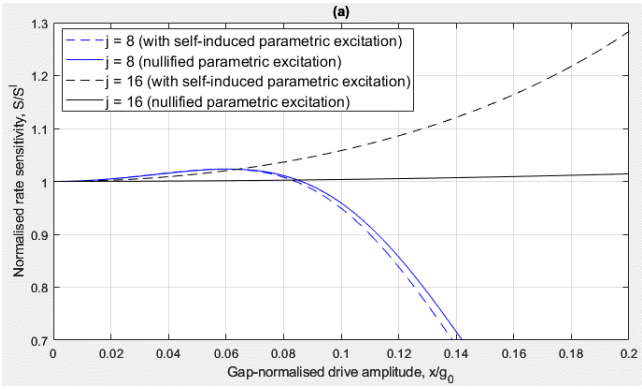

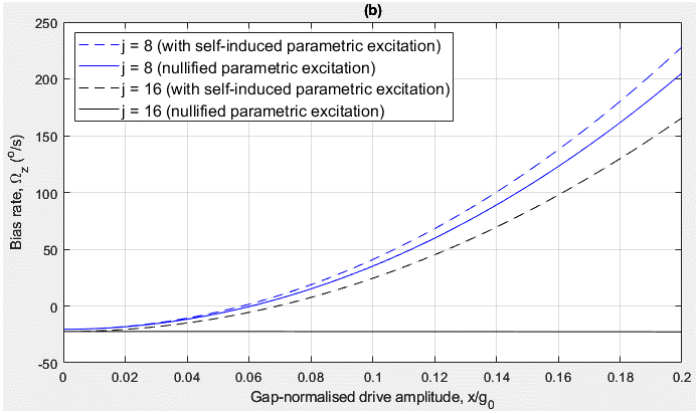

Figure 4.4: Variation of (a) normalised rate sensitivity S/S^I and (b) bias rate with the gap-normalised drive amplitude for electrode distributions with 8 and 16 electrodes within the inner and outer sets

In Figure 4.4(a) it can be seen that nullifying the net parametric excitation is significantly more effective for linearising the rate sensitivity when 16 electrodes are implemented, compared to the minimal linearisation effects on the rate sensitivity with 8 electrodes. Comparing Figure 4.2(a) and Figure 4.4(a), the rate sensitivity of the discontinuous electrode system with $j = 16$ electrodes is similar to that of a continuous electrode system with $j = 8$, for both cases of with and without nullifying the net parametric excitation.

In Figure 4.4(b), the bias rate variation similarly exhibits improved linearisation when the electrode number is increased from 8 to 16. Comparing Figure 4.2(b) and Figure 4.4(b), similar to the rate sensitivity, the bias rate variations with and without nullifying the net parametric excitation are similar between the results corresponding to 16 discontinuous electrodes and 8 continuous electrodes.

The results in Figure 4.4(a) and (b) show that the rate output of a continuous electrode distribution with 8 electrodes can be replicated in devices implementing discontinuous electrode distributions when the number of electrodes is increased to 16. Since the results in Figure 4.2(a) and (b) show diminished linearisation effectiveness as the electrode span reduces, it is advantageous to use 16 electrodes for devices implementing smaller electrode spans. Due to the similarity between the rate outputs for devices with 8 continuous electrodes and 16 discontinuous electrodes, the proceeding investigations will only focus on the 8 electrode design.

4.3.5. Frequency matching

In Section 4.2, it was shown that a combination of a nullified net parametric excitation amplitude and the coincidence of the effective drive and sense frequencies reproduces a linear and trimmed rate output, and the quadrature output is similarly linearised, but not generally nullified. When total frequency detuning is nullified such that $\bar{\omega}^2|_{\lambda_{1,r}=0} = 0$, the rate

sensitivity and bias rate in (4.39) and (4.40) are such that $\Omega_z|_{\lambda_{1,r}=0} = 0$ and $S|_{\lambda_{1,r}=0} = S_0^l$ while the relative phase $\phi_{yx}|_{\lambda_{1,r}=0}$ is insensitive to drive amplitude variations. If $\bar{\omega}^2|_{\lambda_{1,r}=0} = 0$ and there is no linear elastic coupling force ($f_\Delta = 0$), the quadrature output nullifies and $\phi_{yx}|_{\lambda_{1,r}=0} = \phi_{yx,0}^l$.

Frequency matching generally requires the condition $\bar{\omega}^2 = 0$ in (4.32). The parametric pumping voltage amplitude can be generally tuned to adjust the corresponding linear frequency detuning component ${\bar{\omega}_\lambda^l}^2$ such that the drive and sense frequencies are matched. However, the parametric pumping voltage amplitude is constrained to nullify the net parametric excitation condition by satisfying (4.38). In this case, the general frequency detuning $\bar{\omega}^2$ approaches its constrained form, $\bar{\omega}^2|_{\lambda_{1,r}=0}$ in (4.42). To investigate the possibility of simultaneously nullifying net parametric excitation and achieving frequency matching, frequency detuning expression (4.42) is revisited:

$$\bar{\omega}^2|_{\lambda_{1,r}=0} = 2{\omega_0}^2\Delta_\omega \cos 4\Theta_\omega - 3(\kappa_0 - \gamma_0)\frac{x^2}{4{g_0}^2} - (\kappa_\lambda - \gamma_\lambda)\frac{x^2}{4{g_0}^2} \tag{4.42}$$

To ensure frequency matching, condition $\bar{\omega}^2|_{\lambda_{1,r}=0} = 0$ imposes a condition on the chosen drive amplitude. For this purpose, the drive amplitude must be such that the imperfection-induced frequency split is negated by the nonlinear softening rate difference between the drive and sense modes. The softening rates of the drive and sense modes must differ for this purpose.

For a continuous electrode distribution, $\kappa_0 = \gamma_0$ and $\kappa_\lambda = \gamma_\lambda$ and the drive and sense modes exhibit equal softening rates, negating the nonlinear terms in (4.42). As such, in this case, the total frequency detuning $\bar{\omega}^2|_{\lambda_{1,r}=0}$ is only dependent on the imperfection-induced frequency split and frequency matching cannot be achieved unless the drive misalignment is such that $\Delta_\omega \cos 4\Theta_\omega = 0$. In this case frequency matching is achieved regardless of drive amplitude. However, it is important to note that nullifying the linear elastic coupling force f_Δ requires $\Delta_\omega \sin 4\Theta_\omega = 0$, which is incompatible with the drive misalignment condition $\Delta_\omega \cos 4\Theta_\omega = 0$ is imperfections are present ($\Delta_\omega \neq 0$). As such, an important consideration when using a continuous electrode distribution is that rate output trimming and quadrature output nullification cannot be simultaneously achieved unless there are no imperfections, i.e. $\Delta_\omega = 0$.

For a discontinuous electrode distribution, it can be deduced from (4.42) that frequency matching can only be achieved at specific drive amplitudes, under the following conditions:

- If $\Delta_\omega \cos 4\Theta_\omega > 0$, $3\gamma_0 + \gamma_\lambda < 3\kappa_0 + \kappa_\lambda$ must be satisfied

- If $\Delta_\omega \cos 4\Theta_\omega < 0$, $3\gamma_0 + \gamma_\lambda > 3\kappa_0 + \kappa_\lambda$ must be satisfied

Recalling that $\gamma_0, \kappa_0, \gamma_\lambda, \kappa_\lambda < 0$ and $|\gamma_\lambda| \geq |\kappa_\lambda|$, $|\gamma_0| \geq |\kappa_0|$, only the former case is achievable. In contrast to the case for the continuous electrode distribution, this drive misalignment condition is compatible with the nullification of the linear elastic coupling force with $\Delta_\omega \sin 4\Theta_\omega = 0$ in the presence of imperfections. As such, when there is no drive misalignment, i.e. $\Theta_\omega = 0$, rate output trimming and quadrature output nullification can be simultaneously achieved. To ensure $\Delta_\omega \cos 4\Theta_\omega > 0$, the linear drive frequency must be higher than the linear sense frequency. As the drive amplitude increases, the drive frequency decreases at a higher rate than the sense frequency, allowing frequency matching to be achieved at a particular drive amplitude. As the electrodes approximate continuity, this nonlinear softening rate inequality diminishes as $\gamma_0 \approx \kappa_0$ and $\gamma_\lambda \approx \kappa_\lambda$, so the drive amplitude required to achieve frequency matching increases without bound. The drive amplitude where frequency matching occurs also increases when the magnitude of the imperfection-induced component of the frequency detuning, i.e. the first term in (4.42) increases. As such, to ensure that frequency matching is achieved at a practical drive amplitude, the imperfection magnitude must be sufficiently small or the drive location must be sufficiently close to the midpoint of the frequency axes ($\cos 4\Theta_\omega \approx 0$), and the electrodes must be sufficiently discontinuous. These conditions are the main restrictions to achieving trimmed rate output through simultaneous frequency matching and negating the self-induced parametric excitation.

The restrictions for frequency matching are demonstrated in Figure 4.5, Figure 4.6, Figure 4.7(a), (b) and (c) for the case where the self-induced parametric excitation has been nullified. System 1 in Table 4.2 is considered in these plots. In these results, the drive and sense frequencies are plot against the gap-normalised drive amplitude to compare the softening rates of the drive and sense modes. Figure 4.5 shows the effects of varying the drive misalignment angle at $\Theta_\omega = 1°$ and $44°$ to represent the cases of $\cos 4\Theta_\omega > 0$ and $\cos 4\Theta_\omega < 0$ respectively. Figure 4.6 shows the effects of varying the stiffness modulus variation amplitude for the cases of $\delta E = 1.1e-3, 2.2e-3$ and $3.3e-3$, corresponding to linear frequency splits of $9, 18$ and $27\ Hz$ respectively. Figure 4.7(a), (b) and (c) show the effects of varying the electrode span for the cases of $\delta = 15°, 38°$ and $44°$ respectively, corresponding to cubic stiffness ratios of $\kappa_0/\gamma_0 = \kappa_\lambda/\gamma_\lambda = 0.14, 0.78$ and 0.97.

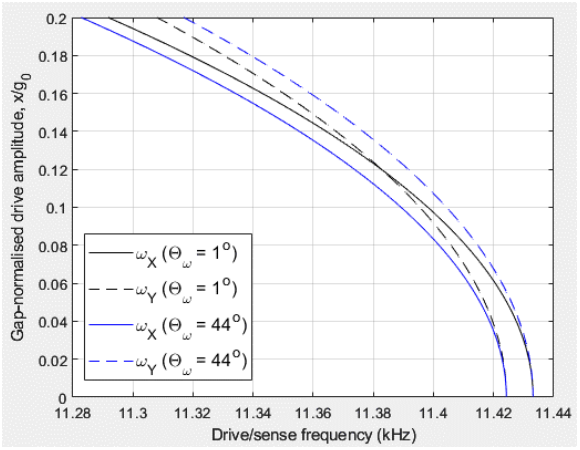

Figure 4.5: Effects of drive misalignment on the drive amplitude dependencies of the drive and sense frequencies with the net parametric excitation nullified

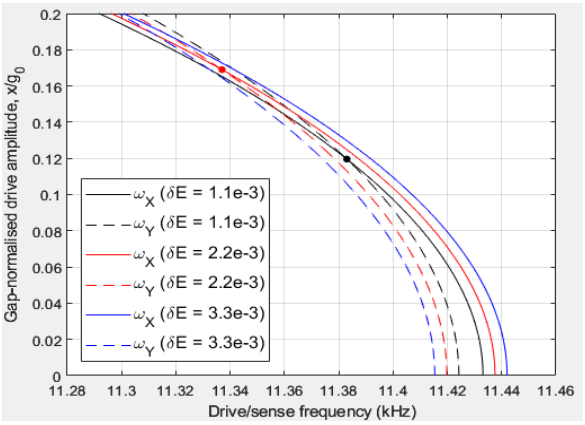

Figure 4.6: Effects of imperfection magnitude on the drive amplitude dependencies of the drive and sense frequencies with the net parametric excitation nullified

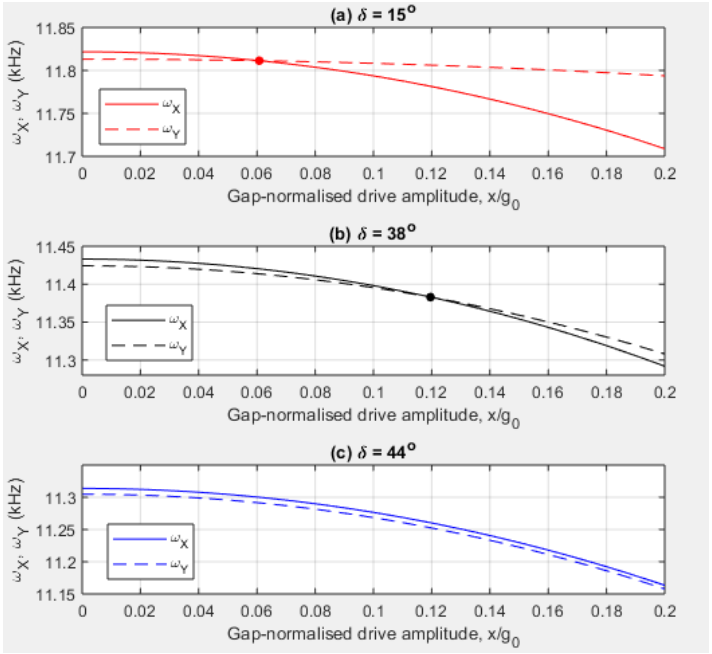

Figure 4.7: Drive amplitude dependencies of the drive and sense frequencies for various electrode spans

In Figure 4.5, noting that the absolute value of $\cos 4\Theta_\omega$ is identical for $\Theta_\omega = 1°$ and 44°, the linear drive and sense frequencies at low drive amplitudes are simply interchanged between these drive misalignment cases. However, the drive mode softens more significantly than the sense mode, so frequency matching can only be achieved when the linear drive frequency is higher than the linear sense frequency as for the case $\Theta_\omega = 1°$. For $\Theta_\omega = 44°$, since $\cos 4\Theta_\omega < 0$, the linear sense frequency is higher and the difference between the drive and sense frequencies increase as the drive amplitude increases, thus amplifying the frequency detuning.

In Figure 4.6, the softening rates of the drive and sense modes are relatively unaffected by the imperfection magnitude. Due to the unaltered softening rate difference between the drive and sense modes, it is clear that increasing the imperfection magnitude also increases the drive amplitude required to achieve frequency matching, where the systems with $\delta E = 1.1e-3$ and $2.2e-3$ achieve frequency matching at $x/g_0 = 12\%$ and 16.9% respectively, while the system with $\delta E = 3.3e-3$ achieves frequency matching at $x/g_0 > 20\%$.

In Figure 4.7(a), (b) and (c), unlike the effects of varying the imperfection magnitude in Figure 4.6, the electrode span varies the difference of the softening rates between the drive and sense modes, thus impacting the drive amplitude required for frequency matching. As shown in Figure 4.7(a), smaller electrode spans result in a larger difference between κ_0 and γ_0 (or κ_λ and γ_λ) which ensures a larger modal softening rate difference, thus enabling frequency matching to be achieved at a lower drive amplitude. On the other hand, when the electrodes approach continuity as for the case shown in Figure 4.7(c), the softening rate difference between the drive and sense modes is near negligible, thus increasing the drive amplitude required for frequency matching significantly.

Based on the preceding discussions and results, the relationship between frequency detuning and the conditions for frequency matching with the net parametric excitation nullified is summarised in Table 4.3 for the effects on linearisation and trimming of the rate output and nullifying the quadrature output. The shaded rows represent mutually exclusive cases.

Table 4.3: Conditions for frequency matching in conjunction with nullifying the net parametric excitation and effects on the rate output linearisation and trimming and quadrature output nullification

Rate output					
Electrode span	**Effective frequency detuning**	**Linearisation feasibility**	**Trimming feasibility**	**Drive amplitude condition**	**Other conditions**
$\delta = 45°$	Constant	✓	×	All	$\Delta_\omega \cos 4\Theta_\omega \neq 0$
		✓	✓	All	$\Delta_\omega \cos 4\Theta_\omega = 0$
$\delta < 45°$	Varies nonlinearly with drive amplitude	✓	×	Low amplitudes	$\Delta_\omega \cos 4\Theta_\omega \neq 0$
		✓	✓	Specific	$\Delta_\omega \cos 4\Theta_\omega > 0$, small Δ_ω, $\delta \not\approx 45°$
		×		All other drive amplitudes	None
Quadrature output					
Electrode span	**Effective frequency detuning**	**Linearisation feasibility**	**Nullification feasibility**	**Drive amplitude condition**	**Other conditions**
$\delta = 45°$	Constant	✓	×	All	$\Delta_\omega \neq 0$
		✓	✓	All	$\Delta_\omega = 0$
$\delta < 45°$	Varies nonlinearly with drive amplitude	✓	×	Low amplitudes	$\Delta_\omega \neq 0$
		✓	✓	Specific	$\Delta_\omega \cos 4\Theta_\omega > 0$, $\Delta_\omega \sin 4\Theta_\omega = 0$

		×	All other drive amplitudes	None

These results conclude that the nullification of the net parametric excitation does not reproduce the output of a device which is both linear and trimmed for a range of drive amplitudes unless the ring is perfect. In the presence of imperfections, linearisation and trimming of the rate output and nullification of the quadrature output can only be simultaneously achieved at specific drive amplitudes.

Effects of electrode continuity/discontinuity on frequency matching

In what follows, the effect of nullifying the net parametric excitation on frequency matching is investigated in systems with continuous and discontinuous electrode distributions. Systems 1 and 2 in Table 4.2 are considered for this investigation. Figure 4.8(a) and (b) show a comparison of the softening rates of the drive and sense modes for systems 2 and 1 respectively, with and without nullifying the net parametric excitation.

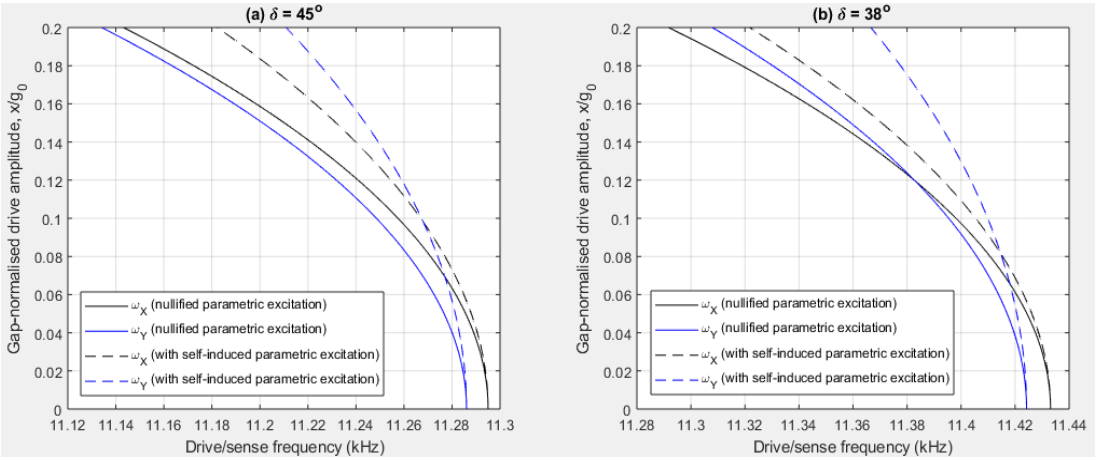

Figure 4.8: Drive and sense frequency variations with the gap-normalised drive amplitude with and without nullifying the net parametric excitation for electrode spans of (a) 45° and (b) 38°

Figure 4.8(a) and (b) show that in the absence of the parametric pumping voltage, the self-induced parametric excitation ensures that the sense mode softening rate is lower than that of the drive mode regardless of the electrode span. However, increasing the electrode span reduces the softening rate difference between the drive and sense modes, thus increasing the drive amplitude where the frequencies coincide from $x/g_0 = 8.2\%$ to 10% as the electrode span is increased from 38° to 45°.

When the parametric pumping voltage is introduced to negate the self-induced parametric excitation, the softening rates of both drive and sense modes increase. However, the softening

rate difference between the drive and sense modes is significantly reduced by the parametric pumping voltage. The parametric pumping voltage softens the sense mode more significantly than the drive mode, thus reducing the net softening rate difference between the drive and sense modes. The softening effect of the parametric pumping voltage on the sense mode is most significant when the electrodes are continuous, thus allowing the sense mode softening rate to match that of the drive mode, as shown in Figure 4.8(a), resulting in an amplitude-independent frequency detuning. As the parametric pumping voltage reduces the softening rate difference, the drive amplitude required to achieve frequency matching is increased compared to the case with self-induced parametric excitation and is not achievable for the continuous electrode case.

Effects of electrode span on drive amplitude for frequency matching

The following investigates the effects of the electrode span on the required drive amplitude to achieve frequency matching when the net parametric excitation is nullified. For this investigation, the electrode span cases in Figure 4.7(a), (b) and (c) are generalised to show the drive amplitude required to ensure $\omega_X|_{\lambda_{1,r}=0} = \omega_Y|_{\lambda_{1,r}=0}$ (hence trimming the rate output) at various electrode spans. Figure 4.9 shows the required drive amplitude for electrode spans ranging from $\delta = 1°$ to $43°$, which corresponds to cubic stiffness ratios $\kappa_0/\gamma_0 = \kappa_\lambda/\gamma_\lambda$ ranging from $6e-4$ to 0.97. A marker has also been shown to indicate the coincidence of $\omega_X|_{\lambda_{1,r}=0}$ and $\omega_Y|_{\lambda_{1,r}=0}$ for system 1, which corresponds to the frequency matching point for the nullified parametric excitation case in Figure 4.8(b). When varying the electrode span in Figure 4.9, the bias voltage V_0 is adjusted to keep the Duffing stiffness γ_0 constant, hence fixing the strength of the electrostatic nonlinearity as has been implemented for the results in Figure 4.2(a) and (b).

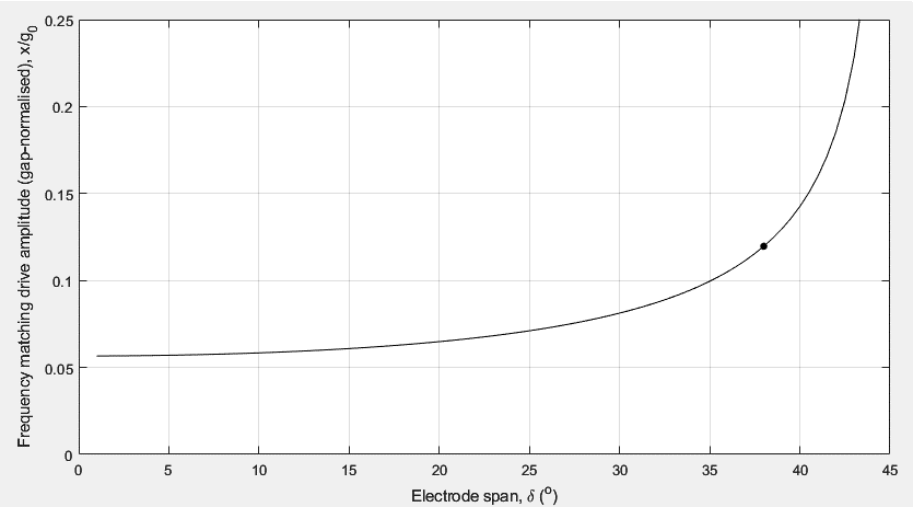

Figure 4.9: Effect of electrode span on the required drive amplitude for frequency matching when the parametric pumping voltage is tuned to nullify the net parametric excitation

Figure 4.9 shows that the drive amplitude to achieve frequency matching increases with increasing electrode span and is increasingly sensitive to electrode span when electrode continuity is approached. This is because frequency matching relies on the difference between the drive and sense mode softening rates, which is dictated by the difference between the coupled-mode stiffnesses κ_0, κ_λ and single-mode stiffnesses γ_0, γ_λ. Smaller electrode spans result in weaker nonlinear elastic coupling between the drive and sense modes, resulting in negligible coupled-mode stiffnesses which maximise the softening rate difference between the drive and sense modes and allowing frequency matching to be achieved at lower drive amplitudes. This softening rate difference diminishes as κ_0 and κ_λ approach γ_0 and γ_λ as electrode continuity is approached. In this case, using larger electrode spans is advantageous as trimmed rate output can be achieved at higher drive amplitudes where the Coriolis force amplitudes and rate sensitivities are larger.

4.3.6. Summary

For an imperfect device with a basic electrostatic configuration, frequency splitting and self-induced parametric excitation induce non-zero bias and nonlinear rate sensitivity effects. It has been shown that the self-induced parametric excitation can be nullified by applying a harmonic parametric pumping voltage to all electrodes to generate a separate parametric excitation which is in anti-phase with the self-induced parametric excitation.

When the net parametric excitation is nullified, the linearity of the rate and quadrature outputs is dictated by the frequency detuning between the drive and sense modes. It is found that the parametric pumping voltage serves to suppress the amplitude dependency of the frequency detuning by reducing the difference between the softening rates of the drive and sense modes. For the case of 8 evenly distributed electrodes, rate and quadrature output linearity is improved by using larger electrode spans because frequency tuning is amplitude-insensitive in this case. (Similar behaviour is also found in devices with discontinuous electrodes if the number of electrodes used is increased to 16 or 32.)

Frequency matching can also occur when the net parametric excitation is nullified under specific conditions. In this case, the rate output of a device which is both linear and trimmed is reproduced, while the quadrature output is linearised but not generally nullified. The parametric pumping voltage increases the drive amplitude at which frequency-matching occurs and this increase is more significant in devices with larger electrode spans. An investigation into frequency matching indicates that the drive amplitude at which matching occurs also depends on the imperfection (magnitude and orientation) and electrode span, as well as the applied parametric pumping voltages. A consequence of this is that the drive amplitude at which rate trimming occurs may be too large or too small for practical

implementation. Ideally it would be preferable to match the frequencies over a range of drive amplitudes. However, this only occurs under special conditions (e.g. continuous electrode). To ensure the quadrature output is also nullified over a range of drive amplitudes, the drive misalignment-induced linear elastic coupling must also be eliminated, in addition to the frequency matching. It is found that these can only be simultaneously achieved in perfect devices.

In what follows a general framework is presented for manipulating the electrostatic forces to nullify the self-induced parametric excitation and achieve trimming at a selected drive amplitude using discontinuous electrodes.

4.4. General framework for manipulation of electrostatic forces using electrostatic configuration selection

In Section 4.3.1, the parametric pumping voltage component in (4.11) is used to modify the electrostatic forces and nullify the net parametric excitation. The resulting rate output is linear with drive amplitude for a continuous electrode but becomes increasingly nonlinear as the electrode span decreases. In addition, the drive amplitude at which frequency matching and rate output trimming occurs is dependent on the imperfections present. In what follows the aim is to linearise and trim the rate output at a selected drive amplitude regardless of the level of imperfection and electrode span while nullifying the quadrature output, and this is achieved by applying additional modifications to the electrostatic configuration in (4.11).

This section investigates manipulating the electrostatic forces using a strategic, goal-based selection of the electrostatic configuration. The aim is to develop a general framework for selecting the voltage distribution and electrode number based on the desired form of electrostatic force. For this investigation, the form of electrostatic forces is generalised to consider a general voltage distribution and electrode number. The voltage and capacitance distributions and resulting electrostatic potential energy are modelled to take account of how these quantities vary from electrode to electrode. The interaction between the capacitance and voltage distributions is used to derive a general form for the total electrostatic potential energy in terms of the voltages. When incorporating the electrostatic potential energy into Lagrange's equation, an explicit relationship between the resulting electrostatic forces and the voltages is derived, which enables specific tailoring of the electrostatic forces based on the voltages applied and number of electrodes chosen.

4.4.1. General representation of modal electrostatic forces

The equations of motion as developed using Lagrange's equation can be represented as follows when the mechanical and electrostatic contributions are separated:

$$f_{m,X}\left(\ddot{X},\dot{X},\dot{Y},X,Y\right)+f_{U,X}(X,Y)=0 \tag{4.43a}$$

$$f_{m,Y}\left(\ddot{X},\dot{X},\dot{Y},X,Y\right)+f_{U,Y}(X,Y)=0 \tag{4.43b}$$

where

$$\begin{bmatrix}f_{m,X}\\ f_{m,Y}\end{bmatrix}=\bar{\bar{\boldsymbol{q}}}_{\mathbf{1}}+\begin{bmatrix}2\Gamma & -G_{\Omega}\Omega\\ G_{\Omega}\Omega & 2\Gamma\end{bmatrix}\bar{\boldsymbol{q}}_{\mathbf{1}}+{\omega_m}^2\bar{\bar{\Delta}}_m\bar{\boldsymbol{q}}_{\mathbf{1}} \tag{4.44}$$

$$f_{U,X}=\frac{\partial U(X,Y)}{M\partial X}=\sum_{q=1}^{4}\left[\sum_{p=0}^{q-1}\left(A^{fX}_{X^{q-p-1}Y^{p}}X^{q-p-1}Y^{p}\right)\right] \tag{4.45a}$$

$$f_{U,Y}=\frac{\partial U(X,Y)}{M\partial Y}=\sum_{q=1}^{4}\left[\sum_{p=0}^{q-1}\left(A^{fY}_{X^{q-p-1}Y^{p}}X^{q-p-1}Y^{p}\right)\right] \tag{4.45b}$$

$f_{m,X}$ and $f_{m,Y}$ are the modal-mass-normalised mechanical forces for the drive and sense equations respectively, where the contributions from the kinetic energy and bending potential energy of the ring and support structures have been combined. These forces are linear in terms of the modal displacement, velocity and acceleration. In (4.44), ${\omega_m}^2$ is the mechanical component of the linear resonant frequency, defined in (3.18) with the final term discarded, i.e. ${\omega_m}^2={\omega_0}^2|_{V_0=0}$. $\bar{\bar{\Delta}}_m$ is the scaled structural imperfection matrix given by:

$$\bar{\bar{\Delta}}_m=\begin{bmatrix}1+\Delta_m\cos 4\Theta_{\omega} & \Delta_m\sin 4\Theta_{\omega}\\ \Delta_m\sin 4\Theta_{\omega} & 1-\Delta_m\cos 4\Theta_{\omega}\end{bmatrix} \tag{4.46}$$

where Δ_m is the scaled imperfection parameter such that ${\omega_m}^2\Delta_m={\omega_0}^2\Delta_{\omega}$. $|\Delta_m|<|\Delta_{\omega}|$ because $\omega_m>\omega_0$ with the electrostatic softening effects excluded from ω_m. This form of distinction allows the imperfection effects to be represented as a mechanical effect.

$f_{U,X}$ and $f_{U,Y}$ are the modal-mass-normalised electrostatic forces, and are directly dependent on the electrostatic potential energy U. These forces can be expressed as a polynomial expansion in terms proportional to X, Y, X^2, XY, Y^2, etc. due to the Taylor series expansion of the capacitance when deriving the electrostatic potential energy, as described in (3.1) – (3.3), (3.10a) and (3.10b). q represents the order of the Taylor series expansion of the capacitance in the radial displacement. The electrostatic forces associated with each q can be interpreted as follows:

- $q \geq 3$ represents nonlinear electrostatic forces, where $q = 3$ and 4 correspond to quadratic and cubic forces respectively.
- $q = 2$ represents the linear electrostatic restoring forces responsible for the linear modal softening, causing $\omega_0 < \omega_m$.
- $q = 1$ represents the zero-order electrostatic forces, as these forces are independent of the modal coordinates. As such, these forces can be regarded as the direct, non-conservative forces when shifted to the right side of the equations of motion in (4.43a) and (4.43b). An example of the zero-order electrostatic force is the harmonic drive force $\chi \cos \omega t$ in (3.14) and (4.14).

The magnitudes of the nonlinear electrostatic forces diminish significantly as q increases. As such, q has been capped at $q = 4$ in (4.45a) and (4.45b), limiting the nonlinear electrostatic forces to cubic order, similar to the approximation used to derive the equations of motion in (3.14) and (4.14), as well as in previous studies [48, 49].

A desired form of the electrostatic forces $f_{U,X}$ and $f_{U,Y}$ can be determined to achieve specific features of the sense dynamics targeted at enhancing rate sensing performance, such as trimming and linearising the rate output while retaining nullified quadrature output, as will be investigated later in this chapter. Based on the desired form of $f_{U,X}$ and $f_{U,Y}$, the required form of the electrostatic potential energy U can be determined by integrating (4.45a) and (4.45b) with respect to the corresponding modal coordinates.

4.4.2. Electrostatic potential energy distribution

The total electrostatic potential energy U is obtained from the summation of the electrostatic potential energy of each electrode as given in (3.4), noting that $U = -W$. Using (3.1) and (3.4) while grounding the ring such that the potential difference is identical to the voltage applied to each electrode, i.e. $\Delta V^{\pm} = V^{\pm}[\theta_0(i)]$, the electrostatic potential energy for the i^{th} electrode (outer/inner) is given by the interaction between the capacitance and voltage of the electrode as governed by the following relationship:

$$U^{\pm}[\theta_0(i)] = -\frac{c^{\pm}[\theta_0(i)]V^{\pm}[\theta_0(i)]^2}{2} \tag{4.47}$$

where $\theta_0(i)$ is given by $\theta_0(i) = 2i\pi/j$. The total number of electrodes j in each of the inner/outer sets is generalised in this investigation and so is not restricted to the $j = 8$ case considered previously.

The voltage distribution $V^{\pm}[\theta_0(i)]$, the capacitance $c^{\pm}[\theta_0(i)]$ and electrostatic potential energy $U^{\pm}[\theta_0(i)]$ are expressed as functions of the central angular position $\theta_0(i)$ to facilitate

the proceeding analysis. An example of this representation for the capacitance, voltage and electrostatic potential energy of each electrode is illustrated in Figure 4.10 for an electrostatic configuration implementing inner and outer electrode sets with $j = 16$ electrodes within each set. However, the following analysis will be developed for a generic number of electrodes, unrestricted to the case of $j = 16$.

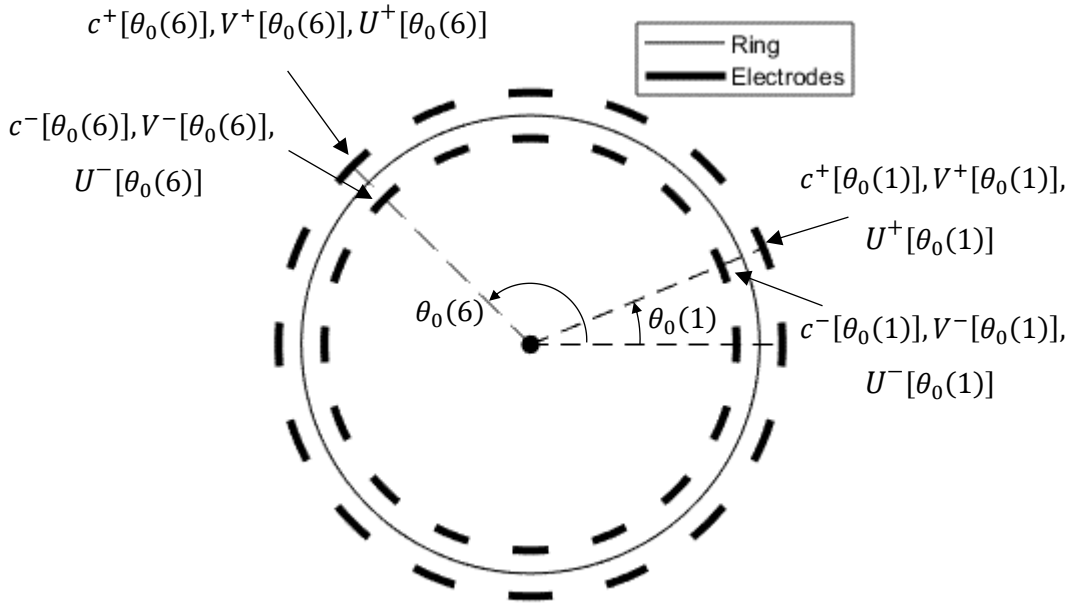

Figure 4.10: Representation of the capacitance, voltage and electrostatic potential energy for electrodes $i = 1, 6$ of the inner and outer electrode sets, and the corresponding central angular positions

With the electrostatic potential energy arising from each electrode described in (4.47), the summation of $U^{\pm}[\theta_0(i)]$ across all electrodes determines the resulting form of the total electrostatic potential energy U and the electrostatic forces $f_{U,X}$ and $f_{U,Y}$. As shown in (4.47), $U^{\pm}[\theta_0(i)]$ is determined by the voltage and capacitance distributions, and this is discussed next.

4.4.3. Capacitance distribution

To facilitate the analysis of the capacitance of each electrode in the context of its interaction with the voltage distribution in (4.47), it is convenient to express the capacitance in the same form as the voltage distribution. For this purpose, this section aims to represent the capacitance $c^{\pm}[\theta_0(i)]$ as a discrete Fourier series in terms of the central angular position $\theta_0(i)$, in a manner similar to the voltage distribution cases in (3.6) and (4.11).

Substituting (3.3) into (3.1) and implementing a Taylor's series expansion in the radial displacement u up to the 4th order gives the following expressions for the capacitance for the i^{th} electrode of the inner/outer electrode set:

$$c^{\pm}[\theta_0(i)] = \sum_{q=0}^{4} c_q^{\pm}[\theta_0(i)] \tag{4.48}$$

where $c_q^{\pm}[\theta_0(i)]$ represents the capacitance component of the i^{th} electrode with order q, given by:

$$c_q^{\pm}[\theta_0(i)] = \frac{\varepsilon_0 BR}{g_0} \int_{\theta_0(i)-\frac{\delta}{2}}^{\theta_0(i)+\frac{\delta}{2}} \left(\pm\frac{u}{g_0}\right)^q d\theta \tag{4.49}$$

The order of the Taylor series expansion of the capacitance, q here directly corresponds to the order of the electrostatic forces in (4.45a) and (4.45b). The summation in (4.48) decomposes the different-ordered terms in the capacitance, thus allowing the origins of the different ordered electrostatic forces in (4.45a) and (4.45b) to be distinguished.

Substituting the expression for the radial displacement u in (4.49) and evaluating the integral over the electrode span allows each q-ordered capacitance component to be expressed as finite, discrete Fourier series in the central angular position $\theta_0(i)$. This gives the following results for odd and even q:

$$\begin{aligned} c_q^{\pm}[\theta_0(i)] &= c_{2q_c+1}^{\pm}[\theta_0(i)] \\ &= \sum_{p_c=0}^{q_c} \Big[\alpha_{q,2(2p_c+1)}^{\pm} \cos 2(2p_c+1)\theta_0(i) \\ &\quad + \beta_{q,2(2p_c+1)}^{\pm} \sin 2(2p_c+1)\theta_0(i)\Big] \end{aligned} \tag{4.50a}$$

$$c_q^{\pm}[\theta_0(i)] = c_{2q_c}^{\pm}[\theta_0(i)] = \sum_{p_c=0}^{q_c} \left[\alpha_{q,4p_c}^{\pm} \cos 4p_c\theta_0(i) + \beta_{q,4p_c}^{\pm} \sin 4p_c\theta_0(i)\right] \tag{4.50b}$$

where q_c is a non-negative integer, capped at $q_c = 1$ and $q_c = 2$ for odd and even q respectively. The distribution components of the capacitance in (4.50a) and (4.50b) have distinct contributions to the electrostatic forces. The $\cos 0\theta_0(i)$ capacitance distribution component in (4.50b) contributes to the equal linear softening of the drive and sense modes, and is associated with the bias voltage for the basic electrostatic configuration. The $\cos 2\theta_0(i)$

and $\sin 2\theta_0(i)$ capacitance distributions component in (4.50a) contribute to direct electrostatic forces on the drive and sense modes respectively.

The coefficients $\alpha^{\pm}_{q,2(2p_c+1)}$, $\beta^{\pm}_{q,2(2p_c+1)}$, $\alpha^{\pm}_{q,4p_c}$, $\beta^{\pm}_{q,4p_c}$ are polynomials in terms of modal coordinates, where the order of the polynomial corresponds to q. For example, when $q = 3$, in (4.50a), the coefficients $\alpha^{\pm}_{3,2}$, $\beta^{\pm}_{3,2}$, $\alpha^{\pm}_{3,6}$, $\beta^{\pm}_{3,6}$ are 3rd order polynomials in the modal coordinates, containing terms proportional to X^3, X^2Y, XY^3, Y^3.

The $q = 0$ capacitance component corresponds to the capacitance of the undeflected ring. Setting $q = 0$ gives $q_c = 0$ and $p_c = 0$ in (4.50b) and the following expression for capacitance component $c_0^{\pm}$:

$$c_0^{\pm} = \alpha^{\pm}_{0,0} = \frac{\varepsilon_0 BR}{g_0} \tag{4.51}$$

This capacitance component is the $\cos 0\theta_0(i)$ variation component in (4.50b) and as such, is identical for all electrodes. Also, as expected, $c_0^{\pm}$ is a polynomial of zero-order and is independent of the modal coordinates. As such, $c_0^{\pm}$ is insignificant as it has no net effect on the resulting electrostatic forces when the derivatives in (4.45a) and (4.45b) are evaluated.

For $q \geq 1$, the capacitance expressions can be quite complicated. However, the definitions of the coefficients $\alpha^{\pm}_{q,2(2p_c+1)}$, $\beta^{\pm}_{q,2(2p_c+1)}$ can be obtained from Table 4.4 for odd orders $q = 1,3$, while the coefficients $\alpha^{\pm}_{q,4p_c}$, $\beta^{\pm}_{q,4p_c}$ can be obtained from Table 4.5 for even orders $q = 2,4$. In all cases, the entries in Table 4.4 and Table 4.5 must be multiplied by $\varepsilon_0 BR/{g_0}^{q+1}$ to obtain the definitions of these coefficients.

Table 4.4: Coefficients for capacitance components of odd orders $q = 1, 3$

		$\cos 2\theta_0(i)$	$\sin 2\theta_0(i)$	$\cos 6\theta_0(i)$	$\sin 6\theta_0(i)$
		$\alpha^{\pm}_{1,2}$	$\beta^{\pm}_{1,2}$		
$q = 1$	X	$\pm \sin\delta$	0	0	0
	Y	0	$\pm \sin\delta$	0	0
		$\alpha^{\pm}_{3,2}$	$\beta^{\pm}_{3,2}$	$\alpha^{\pm}_{3,6}$	$\beta^{\pm}_{3,6}$

$q=3$	X^3	$\pm\frac{3}{4}\sin\delta$	0	$\pm\frac{\sin 3\delta}{12}$	0
	$3X^2Y$	0	$\pm\frac{\sin\delta}{4}$	0	$\pm\frac{\sin 3\delta}{12}$
	$3XY^2$	$\pm\frac{\sin\delta}{4}$	0	$\mp\frac{\sin 3\delta}{12}$	0
	Y^3	0	$\pm\frac{3}{4}\sin\delta$	0	$\mp\frac{\sin 3\delta}{12}$

Table 4.5: Coefficients for capacitance components of even orders $q = 2, 4$

		$\cos 0\theta_0(i)$	$\cos 4\theta_0(i)$	$\sin 4\theta_0(i)$	$\cos 8\theta_0(i)$	$\sin 8\theta_0(i)$
		$\alpha_{2,0}^{\pm}$	$\alpha_{2,4}^{\pm}$	$\beta_{2,4}^{\pm}$		
$q=2$	X^2	$\frac{\delta}{2}$	$\frac{\sin 2\delta}{4}$	0	0	0
	$2XY$	0	0	$\frac{\sin 2\delta}{4}$	0	0
	Y^2	$\frac{\delta}{2}$	$-\frac{\sin 2\delta}{4}$	0	0	0
		$\alpha_{4,0}^{\pm}$	$\alpha_{4,4}^{\pm}$	$\beta_{4,4}^{\pm}$	$\alpha_{4,8}^{\pm}$	$\beta_{4,8}^{\pm}$
$q=4$	X^4	$\frac{3\delta}{8}$	$\frac{\sin 2\delta}{4}$	0	$\frac{\sin 4\delta}{32}$	0
	$4X^3Y$	0	0	$\frac{\sin 2\delta}{8}$	0	$\frac{\sin 4\delta}{32}$
	$6X^2Y^2$	$\frac{\delta}{8}$	0	0	$-\frac{\sin 4\delta}{32}$	0
	$4XY^3$	0	0	$\frac{\sin 2\delta}{8}$	0	$-\frac{\sin 4\delta}{32}$

	Y^4	$\frac{3\delta}{8}$	$-\frac{\sin 2\delta}{4}$	0	$\frac{\sin 4\delta}{32}$	0

In Table 4.4, the coefficients corresponding to the inner and outer electrode capacitance components have opposite signs (hence the '$\pm$' and '$\mp$' signs) while those in Table 4.5 have identical signs. This is because, from (4.48), $c_q^+[\theta_0(i)] = -c_q^-[\theta_0(i)]$ and $c_q^+[\theta_0(i)] = -c_q^-[\theta_0(i)]$ for odd and even q respectively.

The entries in the columns corresponding to coefficients $\alpha_{q,2(2p_c+1)}^{\pm}$, $\beta_{q,2(2p_c+1)}^{\pm}$, $\alpha_{q,4p_c}^{\pm}$, $\beta_{q,4p_c}^{\pm}$ must be multiplied by the modal coordinate terms in the second columns of Table 4.4 and Table 4.5. The result is then summed for all the modal coordinate terms involved before multiplying by $\varepsilon_0 BR/{g_0}^{q+1}$ to obtain the definitions of the coefficients $\alpha_{q,2(2p_c+1)}^{\pm}$, $\beta_{q,2(2p_c+1)}^{\pm}$, $\alpha_{q,4p_c}^{\pm}$, $\beta_{q,4p_c}^{\pm}$. For example, to identify the coefficient of $\sin 4\theta_0(i)$ in the $q = 4$ capacitance component $c_4^{\pm}[\theta_0(i)]$ in (4.50b), which is $\beta_{4,4}^{\pm}$, the column corresponding to $\sin 4\theta_0(i)$ and $\beta_{4,4}^{\pm}$ in Table 4.5 shows nonzero entries for the modal coordinate terms $4X^3Y$ and $4XY^3$, giving the following definition for $\beta_{4,4}^{\pm}$:

$$\beta_{4,4}^{\pm} = \frac{\varepsilon_0 BR}{{g_0}^5}\left(4\frac{\sin 2\delta}{8}X^3Y + 4\frac{\sin 2\delta}{8}XY^3\right)$$

All the other coefficients $\alpha_{q,2(2p_c+1)}^{\pm}$, $\beta_{q,2(2p_c+1)}^{\pm}$, $\alpha_{q,4p_c}^{\pm}$, $\beta_{q,4p_c}^{\pm}$ can be determined in this manner and substituted into (4.50a) and (4.50b) to determine the polynomial representation of the different ordered capacitance components in terms of the modal coordinates. The resulting expressions for capacitance components along with the $q = 0$ order capacitance component in (4.51) are then summed in (4.48) to obtain the capacitance of the i^{th} inner and outer electrodes, $c^{\pm}[\theta_0(i)]$. This is then substituted into (4.47) to evaluate the electrostatic potential energy for the corresponding electrode once the voltage distribution $V^{\pm}[\theta_0(i)]$ is known.

4.4.4. Voltage distribution

The voltage distribution $V^{\pm}[\theta_0(i)]$ such as those in (3.6) and (4.11) is expressed in terms of the central angular position, which is a function of the electrode number i. As such, the voltage only varies from electrode to electrode, but is constant across the angular span of each electrode. This voltage model is typical in capacitive devices where the voltages for each electrode correspond to the particular role of the electrode, such as drive, parametric pumping or bias.

To use (4.47), the distribution of the voltage squared is of interest. A discrete Fourier series representation of the voltage squared distribution is given by:

$$V^{\pm}[\theta_0(i)]^2 = \sum_{m_V=0}^{j} \left[\xi_{m_V}^{\pm} \cos m_V\theta_0(i) + \zeta_{m_V}^{\pm} \sin m_V\theta_0(i)\right] \tag{4.52}$$

where coefficients $\xi_{m_V}^{\pm}$ and $\zeta_{m_V}^{\pm}$ depend on the voltages applied to each electrode. (4.6) is a basic example of the voltage squared distribution, where only constant and $\cos 2\theta_0(i)$ variation components are present, i.e. all coefficients in (4.52) except $\xi_0^{\pm}$ and $\xi_2^{\pm}$ are zero. As (4.52) describes the square of the voltage applied to each electrode and a bias voltage is always applied in practice, then $\xi_0^{+} > 0$ and $\xi_0^{-} > 0$ for any chosen voltage distribution. Using (4.52) and recalling that the central angular position is $\theta_0(i) = 2i\pi/j$, the voltage applied to the i^{th} inner/outer electrode can be obtained by substituting the corresponding electrode index number i into (4.52).

The different variation components of the voltage squared distribution in (4.52) have distinct contributions to the net electrostatic force, in a manner similar to the capacitance distribution described in (4.50a) and (4.50b). $\xi_0^{\pm} \cos 0\theta_0(i)$ affects the modal linear electrostatic forces evenly, thus contributing to equal linear softening of the drive and sense modes. $\xi_2^{\pm} \cos 2\theta_0(i)$ and $\zeta_2^{\pm} \sin 2\theta_0(i)$ contribute to direct forces on the drive and sense modes. $\xi_4^{\pm} \cos 4\theta_0(i)$ affects the linear electrostatic forces unevenly, thus resulting in electrostatic-induced frequency splits.

In practice coefficients $\xi_{m_V}^{\pm}$ and $\zeta_{m_V}^{\pm}$ are important parameters that must be carefully chosen when designing a suitable voltage distribution to achieve specific targeted forms of electrostatic forces in (4.45a) and (4.45b).

4.4.5. Relationship between voltage and electrostatic force distributions

With the voltage squared distribution defined by (4.52) and the capacitance components defined by (4.50a) and (4.50b), electrostatic potential energy (4.47) can be represented in a similar form. To aid the selection of the voltage distribution, this section investigates the effects of spatial variation m_V in (4.52).

To achieve this, it is convenient to decompose the electrostatic potential energy in (4.47) according to order q to give:

$$U^{\pm}[\theta_0(i)] = \sum_{q=0}^{4} U_q^{\pm}[\theta_0(i)] \tag{4.53}$$

where

$$U_q^{\pm}[\theta_0(i)] = -\frac{c_q^{\pm}[\theta_0(i)]V^{\pm}[\theta_0(i)]^2}{2} \tag{4.54}$$

This form helps to identify the capacitance component $c_q^{\pm}[\theta_0(i)]$ contributing to the various ordered electrostatic forces, thus providing useful insight into how the different ordered capacitance components interact with the voltage squared distribution $V^{\pm}[\theta_0(i)]^2$. The total electrostatic force for each q is then given by:

$$f_{U,X}|_q = \frac{\partial U_q}{M\partial X} = \frac{\partial}{M\partial X}\sum_{i=1}^{j}\left[U_q^{+}[\theta_0(i)] + U_q^{-}[\theta_0(i)]\right] \tag{4.55a}$$

$$f_{U,Y}|_q = \frac{\partial U_q}{M\partial Y} = \frac{\partial}{M\partial Y}\sum_{i=1}^{j}\left[U_q^{+}[\theta_0(i)] + U_q^{-}[\theta_0(i)]\right] \tag{4.55b}$$

(4.55a) and (4.55b) are used to obtain the total electrostatic forces described in (4.45a) and (4.45b), where $f_{U,X} = \sum_{q=1}^{4} f_{U,X}|_q$ and $f_{U,Y} = \sum_{q=1}^{4} f_{U,Y}|_q$. In practice, many of the terms in $U_q^{\pm}[\theta_0(i)]$ vanish after evaluating the summation in (4.55a) and (4.55b). The nature of this summation dictates the resulting form of the electrostatic forces for each order.

Substituting the expressions for the capacitance components in (4.50a) or (4.50b) and the voltage squared components in (4.52) into (4.54) gives the following discrete Fourier series representation of $\left[U_q^{+}[\theta_0(i)] + U_q^{-}[\theta_0(i)]\right]$in (4.55a) and (4.55b) for odd ($q = 2q_c + 1$) and even ($q = 2q_c$) orders:

$$U_q^{+}[\theta_0(i)] + U_q^{-}[\theta_0(i)] = U_{2q_c+1}^{+}[\theta_0(i)] + U_{2q_c+1}^{-}[\theta_0(i)] \tag{4.56a}$$

$$= -\frac{1}{2}\sum_{p_c=0}^{q_c}\sum_{m_V=0}^{j}\left\{\frac{\alpha_{q,2(2p_c+1)}^{+}\left(\xi_{m_V}^{+} - \xi_{m_V}^{-}\right) - \beta_{q,2(2p_c+1)}^{+}\left(\zeta_{m_V}^{+} - \zeta_{m_V}^{-}\right)}{2}\cos(4p_c + 2 + m_V)\theta_0(i)\right.$$

$$+ \frac{\alpha_{q,2(2p_c+1)}^{+}\left(\zeta_{m_V}^{+} - \zeta_{m_V}^{-}\right) + \beta_{q,2(2p_c+1)}^{+}\left(\xi_{m_V}^{+} - \xi_{m_V}^{-}\right)}{2}\sin(4p_c + 2 + m_V)\theta_0(i)$$

$$+ \frac{\alpha_{q,2(2p_c+1)}^{+}\left(\xi_{m_V}^{+} - \xi_{m_V}^{-}\right) + \beta_{q,2(2p_c+1)}^{+}\left(\zeta_{m_V}^{+} - \zeta_{m_V}^{-}\right)}{2}\cos(4p_c + 2 - m_V)\theta_0(i)$$

$$\left. - \frac{\alpha_{q,2(2p_c+1)}^{+}\left(\zeta_{m_V}^{+} - \zeta_{m_V}^{-}\right) - \beta_{q,2(2p_c+1)}^{+}\left(\xi_{m_V}^{+} - \xi_{m_V}^{-}\right)}{2}\sin(4p_c + 2 - m_V)\theta_0(i)\right\}$$

$$U_q^+[\theta_0(i)] + U_q^-[\theta_0(i)] = U_{2q_c}^+[\theta_0(i)] + U_{2q_c}^-[\theta_0(i)] \tag{4.56b}$$

$$= -\frac{1}{2}\sum_{p_c=0}^{q_c}\sum_{m_V=0}^{j}\left\{\frac{\alpha_{q,4p_c}^+\left(\xi_{m_V}^+ + \xi_{m_V}^-\right) - \beta_{q,4p_c}^+\left(\zeta_{m_V}^+ + \zeta_{m_V}^-\right)}{2}\cos(4p_c\right.$$

$$+ m_V)\theta_0(i) + \frac{\alpha_{q,4p_c}^+\left(\zeta_{m_V}^+ + \zeta_{m_V}^-\right) + \beta_{q,4p_c}^+\left(\xi_{m_V}^+ + \xi_{m_V}^-\right)}{2}\sin(4p_c + m_V)\theta_0(i)$$

$$+ \frac{\alpha_{q,4p_c}^+\left(\xi_{m_V}^+ + \xi_{m_V}^-\right) + \beta_{q,4p_c}^+\left(\zeta_{m_V}^+ + \zeta_{m_V}^-\right)}{2}\cos(4p_c - m_V)\theta_0(i)$$

$$\left. - \frac{\alpha_{q,4p_c}^+\left(\zeta_{m_V}^+ + \zeta_{m_V}^-\right) - \beta_{q,4p_c}^+\left(\xi_{m_V}^+ + \xi_{m_V}^-\right)}{2}\sin(4p_c - m_V)\theta_0(i)\right\}$$

where trigonometric multiplication identities have been applied. Substituting (4.56a) or (4.56b) into (4.55a) and (4.55b) and evaluating the summation across all electrodes gives an expression of the $q-1$ ordered electrostatic force components in terms of the voltage squared components $\xi_{m_V}^{\pm}$ and $\zeta_{m_V}^{\pm}$. The resulting expression enables direct control of the form of the electrostatic force using a chosen voltage distribution, by determining specific conditions for $\xi_{m_V}^{\pm}$ and $\zeta_{m_V}^{\pm}$.

Using the summation results in (D-6a) and (D-6b), many of the terms in (4.56a) and (4.56b) vanish after evaluating the summation in (4.55a) and (4.55b). Noting that electrode numbers of $j = 8$, 16 or 32 are typical in practice, the following interpretations apply for the summation of (4.56a) and (4.56b):

i. All the sine terms vanish.

ii. Cosine terms involving $\xi_{m_V}^{\pm}$ and $\zeta_{m_V}^{\pm}$ with odd m_V always vanish, so these coefficients can be set nonzero without affecting the total electrostatic force.

iii. Cosine terms involving $\xi_{m_V}^{\pm}$ and $\zeta_{m_V}^{\pm}$ with even m_V, but not a multiple of 4, only contribute to the electrostatic force components with odd q.

iv. Cosine terms involving $\xi_{m_V}^{\pm}$ and $\zeta_{m_V}^{\pm}$ with even m_V which is also a multiple of 4 only contribute to the electrostatic force components with even q.

Conditions i and ii significantly simplify the electrostatic potential energy expression after the summations in (4.55a) and (4.55b) are evaluated, while conditions iii and iv allow the contributions of the voltage components to be distinguished. Using the voltage distribution of the basic electrostatic configuration in (3.6) as an example, the biasing electrostatic potential energy component $\overline{U}$ in (4.7) is composed of modal coordinate terms with orders $q = 0,2,4$, originating from the voltage squared coefficients $\xi_{m_V}^{\pm}$ with $m_V = 0$, corresponding to condition iv. The drive electrostatic potential energy component U_{AC} in (4.8) is composed of

modal coordinate terms with orders $q = 1,3$, originating from the voltage squared coefficients $\xi_{m_V}^{\pm}$ with $m_V = 2$, corresponding to condition iii. The roles of the bias and drive voltages are distinct because there are no cross-contributions between $\xi_0^{\pm}$ and $\xi_2^{\pm}$ towards $\overline{U}$ and U_{AC}.

Using these interpretations, constraints for $\xi_{m_V}^{\pm}$ and $\zeta_{m_V}^{\pm}$ can be determined based on targeted forms of $f_{U,X}|_q$ and $f_{U,Y}|_q$, which then allows one to select a suitable voltage distribution $V^{\pm}[\theta_0(i)]$. This goal-based selection is discussed next.

4.4.6. General procedures for voltage distribution selection

To improve rate sensing performance in the presence of imperfections while accounting for electrostatic nonlinearities, the sense dynamics must be manipulated. The electrostatic forces acting on the sense mode, $f_{U,Y}$ in (4.45b) can be manipulated for this purpose, such as to negate the performance degrading effects of the ring imperfections or generate a parametric excitation to negate the self-induced parametric excitation such as the approach outlined in Section 4.3. Based on specific sensor performance aims, the desired form of sense electrostatic force $f_{U,Y}$ can be determined. Based on this desired form, the analysis presented earlier can be used to identify a suitable voltage squared distribution, $V^{\pm}[\theta_0(i)]^2$ in (4.52), which determines the voltages that must be applied to each electrode to generate the appropriate form of $f_{U,Y}$.

The procedure to determine the voltage distribution is outlined in Table 4.6 below, where the shaded cells describe an example of the implementation at each step for the $j = 8$ case. Table 4.6 can similarly be used for any identified aims associated with the drive electrostatic force $f_{U,X}$.

Table 4.6: Goal-based selection procedure of voltage squared distribution $V^{\pm}[\theta_0(i)]^2$ with example

Steps	
1	Determine the desired or undesired terms in $f_{U,Y}$ and the nature (if applicable) in (4.45b) based on sense dynamics aims and the corresponding order, q.
A term proportional to XY must appear in $f_{U,Y}$, with a harmonic coefficient at frequency ω and phase matching the drive phase ϕ_x. This is a quadratic electrostatic force, with $q = 3$. The force coefficient of interest, $A_{X^1Y^1}^{fY}$ is proportional to $\cos(\omega t + \phi_x)$.	
2	Integrate (4.55b) with respect to Y to determine the corresponding terms in U_q.

U_3 must contain a term proportional to $A_{X^1Y^1}^{fY} XY^2$.	
3	Use Table 4.4 (odd q) or Table 4.5 (even q) to identify the capacitance coefficients $\alpha_{q,2(2p_c+1)}^{\pm}$, $\beta_{q,2(2p_c+1)}^{\pm}$ or $\alpha_{q,4p_c}^{\pm}$, $\beta_{q,4p_c}^{\pm}$ containing the desired terms.
Table 4.4 shows that capacitance coefficients $\alpha_{3,2}^{\pm}$ and $\alpha_{3,6}^{\pm}$ contain terms proportional to XY^2.	
4	Identify p_c for the capacitance coefficients of interest.
$\alpha_{3,2}^{\pm}$ and $\alpha_{3,6}^{\pm}$ correspond to $p_c = 0$ and $p_c = 1$ respectively.	
5	Check which (p_c, m_V) combinations result in integer values of $(4p_c + 2 \pm m_V)/j$ for odd q, or $(4p_c \pm m_V)/j$ for even q. This determines the m_V values of interest, i.e. the $\cos m_V\theta_0(i)$ and $\sin m_V\theta_0(i)$ variation components of the voltage squared in (4.52).
The combinations are $(p_c, m_V) = (0,2), (0,6), (1,2), (1,6)$. $m_V = 2,6$ are of interest., corresponding to $\cos 2\theta_0(i)$, $\sin 2\theta_0(i)$, $\cos 6\theta_0(i)$, $\sin 6\theta_0(i)$ variation components of the voltage squared in (4.52).	
6	Disregard all the sine terms in (4.56a) for odd q or (4.56b) for even q and retain only cosine terms associated with the (p_c, m_V) combinations identified in Step 5.
Retaining only the terms in (4.56a) involving the combinations $\left(\alpha_{q,2(2p_c+1)}^{+}, m_V\right) = \left(\alpha_{3,2}^{+}, 2\right), \left(\alpha_{3,2}^{+}, 6\right), \left(\alpha_{3,6}^{+}, 2\right), \left(\alpha_{3,6}^{+}, 6\right)$ simplifies (4.56a) to: $$-\frac{1}{2}\left\{\frac{\alpha_{3,2}^{+}(\xi_2^{+} - \xi_2^{-})}{2} + \frac{\alpha_{3,6}^{+}(\xi_6^{+} - \xi_6^{-})}{2} + \left[\frac{\alpha_{3,2}^{+}(\xi_6^{+} - \xi_6^{-} + \xi_2^{+} - \xi_2^{-})}{2} + \frac{\alpha_{3,6}^{+}(\xi_2^{+} - \xi_2^{-})}{2}\right]\cos 4\theta_0(i) + \left[\frac{\alpha_{3,2}^{+}(\xi_6^{+} - \xi_6^{-})}{2} + \frac{\alpha_{3,6}^{+}(\xi_2^{+} - \xi_2^{-})}{2}\right]\cos 8\theta_0(i) + \frac{\alpha_{3,6}^{+}(\xi_6^{+} - \xi_6^{-})}{2}\cos 12\theta_0(i)\right\}$$	

7	Substitute the simplified expression for (4.56a) or (4.56b) in Step 6 into (4.55b) and evaluate the summation from $i = 1$ to j. This evaluates the portion of the electrostatic force only from the (p_c, m_V) combinations identified.
Substituting the simplified result of (4.56a) into (4.55b) gives the following terms of interest in $f_{U,Y}\|_q$: $$-\frac{j}{4M}\frac{\partial}{\partial Y}\left[(\alpha_{3,2}^{+}+\alpha_{3,6}^{+})(\xi_2^{+}-\xi_2^{-}+\xi_6^{+}-\xi_6^{-})\right]$$	
8	Use Table 4.4 or Table 4.5 to identify the definitions of the capacitance coefficients involved and substitute these definitions into the terms of interest in $f_{U,Y}\|_q$ identified in Step 7.
From Table 4.4, $$\alpha_{3,2}^{+}=\frac{\varepsilon_0 BR}{{g_0}^4}\left[\frac{3}{4}\sin\delta\,(X^3+XY^2)\right], \alpha_{3,6}^{+}=\frac{\varepsilon_0 BR}{{g_0}^4}\left[\frac{\sin 3\delta}{12}(X^3-3XY^2)\right]$$ the resulting terms in electrostatic force $f_{U,Y}\|_3$ are: $$-\frac{2\varepsilon_0}{5\rho h\pi {g_0}^4}j(\xi_2^{+}-\xi_2^{-}+\xi_6^{+}-\xi_6^{-})\left(\frac{3}{4}\sin\delta-\frac{\sin 3\delta}{4}\right)XY$$	
9	Deduce constraint for the $\xi_{m_V}^{\pm}$ involved based on the goal for $f_{U,Y}$ in Step 1.
$\xi_2^{+}-\xi_2^{-}+\xi_6^{+}-\xi_6^{-} \propto \cos(\omega t+\phi_x)$ with a nonzero amplitude.	

The outcome of Step 9 imposes a condition on the voltage squared distribution $V^{\pm}[\theta_0(i)]^2$ in (4.52), which must be satisfied to achieve the aim in Step 1. This can then be used to identify a suitable voltage distribution $V^{\pm}[\theta_0(i)]$ for this purpose. In the case where multiple aims are established based on a desired form of the sense electrostatic force $f_{U,Y}$, the steps outlined in Table 4.6 can be performed for all of the identified aims. Each aim will result in a different condition for voltage squared coefficients $\xi_{m_V}^{\pm}$, $\zeta_{m_V}^{\pm}$. The selection criteria is then based on selecting the simplest form of voltage squared distribution $V^{\pm}[\theta_0(i)]^2$ in (4.52) satisfying all the identified conditions. (4.9) and (4.10) are examples of such conditions, where (4.9) imposes a condition on $\xi_0^{+}+\xi_0^{-}$ to enable negation of the self-induced parametric excitation, and (4.10) imposes a condition on $\xi_2^{+}-\xi_2^{-}$ to avoid multi-frequency drive excitation.

4.5. Linearising and trimming sensor output

The results in Section 4.3.4 indicated that rate output linearisation can only be achieved for a wide range of drive amplitudes for a continuous electrode configuration with the net parametric excitation nullified, and Table 4.3 showed that to achieve linearisation and trimming of the rate output, frequency matching must also be achieved. The quadrature output is also not nullified after the self-induced parametric excitation is negated, indicating that the device performance has not achieved linear, trimmed state. This section addresses these issues in detail and aims to replicate the rate and quadrature outputs of a standard linear, trimmed device when the net parametric amplification is nullified for the general case when the frequencies are not matched. This study extends the results obtained in Section 4.3 to the general case by modifying the electrostatic forces using the framework proposed in Section 4.4.

The interaction and balance of forces dictating the sense response is analysed first to identify the force conditions required to ensure a linear, trimmed rate output and nullified quadrature output. These force conditions are used to obtain a target form of the electrostatic forces to replicate the force conditions in a linear, ideal/trimmed device. To achieve the targeted form of electrostatic force, a suitable voltage distribution is developed based on the selection procedures outlined in Table 4.6. The governing equations of motion are then derived based on the selected electrostatic configuration and the drive and sense dynamics are analysed. Based on the sense dynamics, the electrostatic forces generated using the selected electrostatic configuration are then used to nullify the net parametric excitation, linearise and trim the rate output, and eliminate the quadrature output. The effectiveness of the implementation is assessed by comparing the resulting rate and quadrature outputs against that for the case of nullified net parametric excitation but without addressing the force conditions, as investigated in Section 4.3. The potential of using the chosen electrostatic configuration for closed-loop rate sensing is also investigated, and the closed-loop rate sensing performance is assessed in terms of the rate sensitivity and bias rate. Alternative methods to use the proposed electrostatic configuration to linearise and trim the rate output while nullifying the quadrature output without nullifying the net parametric excitation are also discussed. The cases with and without nonlinear frequency balancing will be considered.

4.5.1. Balance of averaged forces of sense mode

The interaction between the sense mode forces can be manipulated to achieve a linear, trimmed sense response. In the following investigation, the framework of conditions to achieve this is discussed.

When the sense response is steady-state harmonic, the sense equation of motion can be used to obtain the in/antiphase and quadrature amplitudes. Averaging the sense equation of motion in (4.1) without solving for the sense amplitude components $y\cos\phi_{yx}$ and $y\sin\phi_{yx}$, gives:

$$\begin{bmatrix} -{\omega_X}^2+{\omega_Y}^2+\lambda_{1,r} & -2\Gamma\omega_X \\ -2\Gamma\omega_X & {\omega_X}^2-{\omega_Y}^2+\lambda_{1,r} \end{bmatrix}\bar{\boldsymbol{y}}=\begin{bmatrix} f_\Delta \\ f_\Omega \end{bmatrix} \tag{4.57}$$

where $\bar{\boldsymbol{y}}$ is the sense amplitude components vector:

$$\bar{\boldsymbol{y}}=\begin{bmatrix} y\cos\phi_{yx} \\ y\sin\phi_{yx} \end{bmatrix} \tag{4.58}$$

(4.57) describes the balance between the various averaged force terms in the sense equation of motion in (4.1), and replicates two coupled force balance problems distinguished by the phase of these forces. The first row in (4.57) represents the interaction of the force components in phase/antiphase with the linear elastic coupling force, characterised by the force components exhibiting harmonic variations proportional to $\cos(\omega t+\phi_x)$, while the second row represents the interaction of the force components in phase/antiphase with the Coriolis force, where these force components are proportional to $\sin(\omega t+\phi_x)$.

Revisiting (3.41), the targeted sense response of a linear, trimmed device is:

$$\bar{\boldsymbol{y}}_{\boldsymbol{0}}^{\boldsymbol{l}}=\begin{bmatrix} y_0^l\cos\phi_{yx,0}^l \\ y_0^l\sin\phi_{yx,0}^l \end{bmatrix}=\begin{bmatrix} -\dfrac{f_\Omega}{2\Gamma\omega_X} \\ 0 \end{bmatrix} \tag{3.41}$$

Replacing $\bar{\boldsymbol{y}}$ in (4.57) with its targeted form $\bar{\boldsymbol{y}}_{\boldsymbol{0}}^{\boldsymbol{l}}$, it can be shown that force balance in (4.57) is only satisfied at this targeted sense amplitude under the following condition:

$$\left(-{\omega_X}^2+{\omega_Y}^2+\lambda_{1,r}\right)y_0^l\cos\phi_{yx,0}^l=f_\Delta \tag{4.59}$$

which is equivalent to nullifying the quadrature output for the basic electrostatic configuration using the condition in (3.68).

Recalling from Section 3.5.3 that that nonlinear frequency balancing requires $\lambda_{1,r}={\omega_X}^2-{\omega_Y}^2$, the term on the left side stems from the nonlinear frequency imbalance. The magnitudes of the forces stemming from the nonlinear frequency imbalance and the linear elastic coupling f_Δ must balance to satisfy (4.59) for the forces in (4.57) to be in balance when $\bar{\boldsymbol{y}}=\bar{\boldsymbol{y}}_{\boldsymbol{0}}^{\boldsymbol{l}}$. Otherwise, a nonzero quadrature response $y\sin\phi_{yx}$ will appear in $\bar{\boldsymbol{y}}$ to compensate for the

mismatch between $\left(-{\omega_X}^2+{\omega_Y}^2+\lambda_{1,r}\right)y_0^l\cos\phi_{yx,0}^l$ and f_Δ in (4.59) and restore the force balance in (4.57), thus deviating $\bar{\boldsymbol{y}}$ from its targeted form $\bar{\boldsymbol{y}}_{\boldsymbol{0}}^{\boldsymbol{l}}$.

To ensure that the resulting sense response satisfies $\bar{\boldsymbol{y}}=\bar{\boldsymbol{y}}_{\boldsymbol{0}}^{\boldsymbol{l}}$ in all cases, the force balance in (4.57) must be modified. This can be achieved by manipulating the net force vector on the right side of (4.57). For this purpose, replacing $\bar{\boldsymbol{y}}$ in (4.57) with $\bar{\boldsymbol{y}}_{\boldsymbol{0}}^{\boldsymbol{l}}$ and imposing an additional force vector $\bar{\boldsymbol{f}}_{\boldsymbol{0}}^{\boldsymbol{l}}$ on the right side of (4.57), (4.57) is modified to:

$$\begin{bmatrix}-{\omega_X}^2+{\omega_Y}^2+\lambda_{1,r} & -2\Gamma\omega_X\\ -2\Gamma\omega_X & {\omega_X}^2-{\omega_Y}^2+\lambda_{1,r}\end{bmatrix}\bar{\boldsymbol{y}}_{\boldsymbol{0}}^{\boldsymbol{l}}=\begin{bmatrix}f_\Delta\\ f_\Omega\end{bmatrix}+\bar{\boldsymbol{f}}_{\boldsymbol{0}}^{\boldsymbol{l}} \tag{4.60}$$

To ensure $\bar{\boldsymbol{y}}=\bar{\boldsymbol{y}}_{\boldsymbol{0}}^{\boldsymbol{l}}$, $\bar{\boldsymbol{f}}_{\boldsymbol{0}}^{\boldsymbol{l}}$ is defined as:

$$\bar{\boldsymbol{f}}_{\boldsymbol{0}}^{\boldsymbol{l}}=\begin{bmatrix}f_0^l\\ 0\end{bmatrix}=\begin{bmatrix}-f_\Delta+\dfrac{{\omega_X}^2-{\omega_Y}^2-\lambda_{1,r}}{2\Gamma\omega_X}f_\Omega\\ 0\end{bmatrix} \tag{4.61}$$

Substituting (4.61) into (4.60) and comparing the result against the original force balancing case in (4.57) shows that this implementation is simply superposing a balancing force with amplitude f_0^l, in phase/antiphase with the linear elastic coupling force. (4.61) can be obtained by adding f_0^l to the right side of (4.59) and solving for f_0^l. This additional balancing force acts to negate the residual force resulting from the mismatch between the magnitudes of the forces stemming from the nonlinear frequency imbalance and the linear elastic coupling in (4.59).

Noting that (4.57) is the averaged result of the sense equation of motion in (4.1), the modified sense equation of motion in the presence of the additional force f_0^l corresponding to the corrected force balance in (4.60) can be deduced. This gives:

$$\begin{aligned}\ddot{Y}+2\Gamma\dot{Y}+\left[{\omega_Y}^2+2\lambda_{1,r}\cos 2(\omega t+\phi_x)\right]Y\\ =f_\Omega\sin(\omega t+\phi_x)+f_\Delta\cos(\omega t+\phi_x)+f_0^l\cos(\omega t+\phi_x)\end{aligned} \tag{4.62}$$

where (4.60) is the averaged result of (4.62).

Since the drive mode is forced into resonance, $\phi_x=-90°$, so the balancing force $f_0^l\cos(\omega t+\phi_x)$ is set at a 90° phase lag relative to the drive excitation. It is worth noting that f_0^l, as shown in (4.61), is rate-dependent unless nonlinear frequency balancing applies, meaning that the force amplitude must be tuned with angular rate changes. In practice, the balancing force amplitude f_0^l must be tuned until the quadrature output nullifies to achieve the

targeted amplitude in (4.61). f_0^l is linearly related to the angular rate and if $f_\Delta = 0$, the balancing force is proportional to the angular rate in a manner similar to FTR mode operation.

4.5.2. Selection of voltage distribution

The targeted form of sense equation of motion to guarantee linear, trimmed sense response is given by (4.62) and in what follows, the analysis presented in Section 4.4 is used to generate the appropriate form of electrostatic forces to achieve this aim.

Substituting (4.44) and (4.45a) into (4.43a), and (4.44) and (4.45b) into (4.43b) general forms for the drive and sense equations of motion can be expressed as:

$$\ddot{X} + 2\Gamma\dot{X} + {\omega_m}^2(1 + \Delta_m \cos 4\Theta_\omega)X + f_{U,X}(X,Y) = f_{XY}(t) \tag{4.63a}$$

$$\ddot{Y} + 2\Gamma\dot{Y} + {\omega_m}^2(1 - \Delta_m \cos 4\Theta_\omega)Y + f_{U,Y}(X,Y) = f_{YX}(t) \tag{4.63b}$$

where

$$f_{XY}(t) = G_\Omega \Omega \dot{Y} - {\omega_m}^2 \Delta_m \sin 4\Theta_\omega \, Y \tag{4.64a}$$

$$f_{YX}(t) = -G_\Omega \Omega \dot{X} - {\omega_m}^2 \Delta_m \sin 4\Theta_\omega \, X \tag{4.64b}$$

$f_{XY}(t)$ and $f_{YX}(t)$ represent the intermodal forcing between the drive and sense modes, and can be treated as direct forces acting on the drive and sense modes respectively.

To ensure (4.63b) achieves the targeted form of sense equation of motion in (4.62) while maintaining proper operation of the drive and sense modes, the electrostatic force coefficients, $A^{fX}_{X^{q-p-1}Y^p}$ and $A^{fY}_{X^{q-p-1}Y^p}$ in (4.45a) and (4.45b) must satisfy the conditions outlined below:

i) $A^{fY}_{X^0Y^0} \propto \cos(\omega t + \phi_x)$ with tunable amplitude

ii) $\int_0^{\frac{2\pi}{\omega}} A^{fY}_{X^0Y^1} \cos n(\omega t + \phi_x)\, dt \neq 0$ only for $n = 0{,}2$

iii) $\int_0^{\frac{2\pi}{\omega}} A^{fY}_{X^0Y^1} \sin n(\omega t + \phi_x)\, dt = 0$ for all integer values of n

iv) $A^{fY}_{X^0Y^1} = A^{fX}_{X^1Y^0}$

v) $A^{fX}_{X^0Y^0} \propto \cos \omega t$ with tunable amplitude

The first condition, $A^{fY}_{X^0Y^0} \propto \cos(\omega t + \phi_x)$ is the main condition necessary to generate electrostatic force $f_0^l \cos(\omega t + \phi_x)$ in (4.62) to linearise and trim the rate output, and eliminate the quadrature output. This is a direct electrostatic force of order $q = 1$ which is independent of modal coordinates acting on the sense mode.

The second and third conditions are constraints for the nature of the net parametric excitation of the sense mode. The introduction of any voltage to achieve the first condition $A_{X^0Y^0}^{fY} \propto \cos(\omega t + \phi_x)$ must not simultaneously introduce parametric excitation to the sense mode at any frequency other than 2ω. The phase of the parametric excitation must also be twice the drive mode oscillation phase, indicated by the $\cos 2(\omega t + \phi_x)$ variation of the sense stiffness in (4.62). Coefficient $A_{X^0Y^1}^{fY}$ corresponds to a linear sense electrostatic force of order $q = 2$, proportional to the sense displacement Y, thus affecting the constant and varying components of the linear sense stiffness.

The fourth condition $A_{X^0Y^1}^{fY} = A_{X^1Y^0}^{fX}$ ensures that the linear electrostatic softening is identical for both drive and sense modes, i.e. the modal symmetry described in Section 3.3.1. When manipulating $A_{X^0Y^1}^{fY}$ to satisfy the second and third conditions, the linear modal symmetry is retained to ensure that the linear frequency split is purely attributed to the mechanical imperfections.

The fifth condition $A_{X^0Y^0}^{fX} \propto \cos \omega t$ is a constraint on the harmonic drive force. Satisfying the first condition must not shift the phase of this force away from that of the drive voltage, or introduce harmonic drive forces at other frequencies to avoid multi-frequency excitation. $A_{X^0Y^0}^{fX}$ corresponds to a direct drive force of order $q = 1$, independent of modal coordinates.

These conditions can be used to identify the corresponding conditions for the voltage squared coefficients $\xi_{m_V}^{\pm}$, $\zeta_{m_V}^{\pm}$ in (4.52) using the procedures outlined in Table 4.6. This enables a suitable voltage distribution to be identified, in addition to the default conditions $\xi_0^+ > 0$ and $\xi_0^- > 0$. The result of the analysis of the aforementioned conditions using Table 4.6 is summarised in Table 4.7 below for the case when there are 8 electrodes ($j = 8$).

Table 4.7: Constraints for the coefficients of the voltage squared distribution, $\xi_{m_V}^{\pm}$, $\zeta_{m_V}^{\pm}$ based on conditions to linearise and trim the sense response for the case of 8 inner/outer electrodes

	Electrostatic force conditions	**Voltage squared distribution constraints**
1	$A_{X^0Y^0}^{fY} \propto \cos(\omega t + \phi_x)$	$\zeta_2^+ - \zeta_2^- - \zeta_6^+ + \zeta_6^- \propto \cos(\omega t + \phi_x)$
2	$\int_0^{\frac{2\pi}{\omega}} A_{X^0Y^1}^{fY} \cos n(\omega t + \phi_x)\, dt \neq 0$ only for $n = 0,2$	$\int_0^{\frac{2\pi}{\omega}} (\xi_0^+ + \xi_0^- + \xi_4^+ + \xi_4^- + \xi_8^+ + \xi_8^-) \cos n(\omega t + \phi_x)\, dt \neq 0$ only for $n = 0,2$

3	$\int_0^{\frac{2\pi}{\omega}} A_{X^0Y^1}^{fY} \sin n(\omega t + \phi_x)\, dt = 0$ for all $n \in \mathbb{Z}$	$\int_0^{\frac{2\pi}{\omega}} (\xi_0^+ + \xi_0^- + \xi_4^+ + \xi_4^- + \xi_8^+ + \xi_8^-) \sin n(\omega t + \phi_x)\, dt = 0$ for all $n \in \mathbb{Z}$
4	$A_{X^0Y^1}^{fY} = A_{X^1Y^0}^{fX}$	$\xi_4^+ + \xi_4^- = 0$
5	$A_{X^0Y^0}^{fX} \propto \cos \omega t$	$\xi_2^+ - \xi_2^- + \xi_6^+ - \xi_6^- \propto \cos \omega t$

In general, multiple voltage distributions are compatible with the constraints listed in Table 4.7. However, it is of practical interest to select the simplest possible voltage distribution relative to that of the basic electrostatic configuration in (3.6). One example of such a voltage distribution is:

$$V^+[\theta_0(i)] = V_0 + V_\lambda \sin(\omega t + \phi_x) + V_\Delta \cos\left(\frac{\omega t + \phi_x + i_\Delta \pi}{2}\right) \cos\theta_0(i) + V_\Delta \cos\left(\frac{\omega t + \phi_x + i_\Delta \pi}{2}\right) \sin\theta_0(i) + V_{AC} \cos\omega t \cos 2\theta_0(i) \tag{4.65a}$$

$$V^-[\theta_0(i)] = V_0 - V_\lambda \sin(\omega t + \phi_x) + V_\Delta \sin\left(\frac{\omega t + \phi_x + i_\Delta \pi}{2}\right) \cos\theta_0(i) + V_\Delta \sin\left(\frac{\omega t + \phi_x + i_\Delta \pi}{2}\right) \sin\theta_0(i) - V_{AC} \cos\omega t \cos 2\theta_0(i) \tag{4.65b}$$

This voltage distribution is similar to (4.11), but with additional balancing voltage components involving amplitude V_Δ to satisfy condition 1 in Table 4.7. The balancing voltage phase index number i_Δ is an integer. As will be shown, the balancing amplitude V_Δ is tuned to eliminate the sense quadrature response to achieve the aim of the balancing force established in Section 4.5.1.

The spatial variation involved in this voltage distribution is maximised at $2\theta_0(i)$, ensuring the resulting voltage squared coefficients $\xi_{m_V}^\pm, \zeta_{m_V}^\pm = 0$ for all $m_V > 4$. Squaring (4.65a) and (4.65b) and comparing the result with (4.52), the nonzero voltage squared coefficients are given by:

$$\xi_0^{\pm} = {V_0}^2 + \frac{{V_\lambda}^2}{2} + \frac{{V_\Delta}^2}{2} + \frac{{V_{AC}}^2}{4} \pm \left[2V_0V_\lambda \sin(\omega t + \phi_x) + \frac{{V_\Delta}^2}{2}\cos(\omega t + \phi_x + i_\Delta \pi)\right] - \frac{{V_\lambda}^2}{2}\cos 2(\omega t + \phi_x) + \frac{{V_{AC}}^2}{4}\cos 2\omega t \tag{4.66a}$$

$$\xi_1^{+} = 2V_\Delta \cos\left(\frac{\omega t + \phi_x + i_\Delta \pi}{2}\right)\left[V_0 + V_\lambda \sin(\omega t + \phi_x) + \frac{V_{AC}}{2}\cos \omega t\right] \tag{4.66b}$$

$$\zeta_1^{+} = 2V_\Delta \cos\left(\frac{\omega t + \phi_x + i_\Delta \pi}{2}\right)\left[V_0 + V_\lambda \sin(\omega t + \phi_x) - \frac{V_{AC}}{2}\cos \omega t\right] \tag{4.66c}$$

$$\xi_1^{-} = 2V_\Delta \sin\left(\frac{\omega t + \phi_x + i_\Delta \pi}{2}\right)\left[V_0 - V_\lambda \sin(\omega t + \phi_x) - \frac{V_{AC}}{2}\cos \omega t\right] \tag{4.66d}$$

$$\zeta_1^{-} = 2V_\Delta \sin\left(\frac{\omega t + \phi_x + i_\Delta \pi}{2}\right)\left[V_0 - V_\lambda \sin(\omega t + \phi_x) + \frac{V_{AC}}{2}\cos \omega t\right] \tag{4.66e}$$

$$\xi_2^{\pm} = \pm 2V_0V_{AC}\cos \omega t + V_\lambda V_{AC}[\sin(2\omega t + \phi_x) + \sin \phi_x] \tag{4.66f}$$

$$\zeta_2^{\pm} = \frac{{V_\Delta}^2}{2}[1 \pm \cos(\omega t + \phi_x + i_\Delta \pi)] \tag{4.66g}$$

$$\xi_3^{+} = \zeta_3^{+} = V_\Delta V_{AC}\cos\left(\frac{\omega t + \phi_x + i_\Delta \pi}{2}\right)\cos \omega t \tag{4.66h}$$

$$\xi_3^{-} = \zeta_3^{-} = -V_\Delta V_{AC}\sin\left(\frac{\omega t + \phi_x + i_\Delta \pi}{2}\right)\cos \omega t \tag{4.66i}$$

$$\xi_4^{\pm} = \frac{{V_{AC}}^2}{4}(1 + \cos 2\omega t) \tag{4.66j}$$

The definitions in (4.66a) - (4.66j) show that the resulting voltage squared distribution is composed of constant, $1\theta_0(i)$, $2\theta_0(i)$, $3\theta_0(i)$ and $4\theta_0(i)$ variation components.

The constant component determines the linear electrostatic force, thus contributing to the linear softening of the drive and sense modes. As shown in (4.66a), when terms involving ${V_{AC}}^2$ are neglected, the sum $\xi_0^{+} + \xi_0^{-}$ is composed of a constant component and a double-frequency component. The parametric pumping voltage contributes to the double-frequency component and is responsible for generating the linear parametric excitation to counteract the self-induced parametric excitation.

The $2\theta_0(i)$ variation component generates the direct forces acting on the drive and sense modes. From (4.52), coefficients $\xi_2^{\pm}$ and $\zeta_2^{\pm}$ are associated with the $\cos 2\theta_0(i)$ and $\sin 2\theta_0(i)$ variation components respectively. As such, $\xi_2^{\pm}$ results in the direct electrostatic forcing of the drive mode while $\zeta_2^{\pm}$ acts on the sense mode. From (4.66f), $\xi_2^{+} - \xi_2^{-}$ is proportional to $V_0 V_{AC}$ and is responsible for generating the harmonic drive force to initiate the drive mode vibration. From (4.66g), $\zeta_2^{+} - \zeta_2^{-}$ is proportional to ${V_\Delta}^2$, serving to generate the sense mode balancing force $f_0^l \cos(\omega t + \phi_x)$ in (4.62) to eliminate the quadrature output.

In principle, the $4\theta_0(i)$ variation component contributes to linear frequency splits. However, since $\xi_4^{\pm}$ is proportional to ${V_{AC}}^2$, $\xi_4^{\pm}$ is negligible and this frequency split is insignificant.

The $1\theta_0(i)$ and $3\theta_0(i)$ variation components will not contribute to the total electrostatic force, as these correspond to odd m_V (see the discussion in Section 4.4.5). As such, the voltage squared coefficients $\xi_1^{\pm}$, $\zeta_1^{\pm}$, $\xi_3^{\pm}$, $\zeta_3^{\pm}$ in (4.66b), (4.66c), (4.66d), (4.66e), (4.66h) and (4.66i) can be disregarded.

Using (4.66a), (4.66f), (4.66g) and (4.66j), it can be confirmed that the conditions in Table 4.7 are all satisfied except for condition 4 requiring $\xi_4^{+} + \xi_4^{-} = 0$. However, since the drive voltage is small, this will have negligible impact on the resulting modal dynamics. Similar to previous analyses, terms involving ${V_{AC}}^2$ are neglected in the subsequent investigation. To distinguish the roles of the bias, drive, parametric pumping and balancing voltage components in (4.65a) and (4.65b), the coefficients in (4.66a) – (4.66j) will be used to define the various electrostatic force terms appearing in the equations of motion. This is discussed next.

4.5.3. Modal dynamics for linearisation and trimming conditions

In what follows equations of motions are developed based on the voltage distribution selected in (4.65a) and (4.65b). The resulting equations of motion are then analysed by applying the same techniques implemented on (3.14) and (4.14) to derive the resulting drive and sense dynamics. The conditions for linearising and trimming the sensor output will then be identified for the case of nullified net parametric excitation.

Equations of motion

Using Table 4.4 and Table 4.5 to obtain the full expressions of the capacitance components $c_q^{\pm}[\theta_0(i)]$ and substituting the result into (4.54) along with the expression for the chosen voltage distribution in (4.65a) and (4.65b), an expression for $U_q^{\pm}[\theta_0(i)]$ can be determined for $q = 1,2,3,4$. Substituting these results into (4.55a) and (4.55b) then gives the $q-1$ ordered

electrostatic forces. Using summations $f_{U,X} = \sum_{q=1}^{4} f_{U,X}|_q$ and $f_{U,Y} = \sum_{q=1}^{4} f_{U,Y}|_q$ gives the following total electrostatic forces:

$$\begin{bmatrix} f_{U,X} \\ f_{U,Y} \end{bmatrix} = \overline{\boldsymbol{A}}_{\boldsymbol{0}} + \overline{\overline{\boldsymbol{A}}}_{\boldsymbol{1}}\overline{\boldsymbol{q}}_{\boldsymbol{1}} + \overline{\overline{\boldsymbol{A}}}_{\boldsymbol{2}}\overline{\boldsymbol{q}}_{\boldsymbol{2}} + \overline{\overline{\boldsymbol{A}}}_{\boldsymbol{3}}\overline{\boldsymbol{q}}_{\boldsymbol{3}} \tag{4.67}$$

The vector $\overline{\boldsymbol{A}}_{\boldsymbol{0}}$ and the matrices $\overline{\overline{\boldsymbol{A}}}_{\boldsymbol{1}}, \overline{\overline{\boldsymbol{A}}}_{\boldsymbol{2}}, \overline{\overline{\boldsymbol{A}}}_{\boldsymbol{3}}$ are the results of the participation of the various voltage squared distribution coefficients in (4.66a) – (4.66j) and are given by:

$$\overline{\boldsymbol{A}}_{\boldsymbol{0}} = -\frac{\varepsilon_0}{5\rho\pi h {g_0}^2} j \sin\delta \begin{bmatrix} \xi_2^+ - \xi_2^- \\ \zeta_2^+ - \zeta_2^- \end{bmatrix} \tag{4.68a}$$

$$\overline{\overline{\boldsymbol{A}}}_{\boldsymbol{1}} = -\frac{2\varepsilon_0}{5\rho\pi h {g_0}^3} j\delta \begin{bmatrix} \xi_0^+ + \xi_0^- & 0 \\ 0 & \xi_0^+ + \xi_0^- \end{bmatrix} \tag{4.68b}$$

$$\begin{aligned} \overline{\overline{\boldsymbol{A}}}_{\boldsymbol{2}} = -\frac{\varepsilon_0}{20\rho\pi h {g_0}^4} j \Bigg\{ & (9\sin\delta + \sin 3\delta) \begin{bmatrix} \xi_2^+ - \xi_2^- & 0 & 0 \\ 0 & 0 & \zeta_2^+ - \zeta_2^- \end{bmatrix} \\ & + (3\sin\delta - \sin 3\delta) \begin{bmatrix} 0 & 2(\zeta_2^+ - \zeta_2^-) & \xi_2^+ - \xi_2^- \\ \zeta_2^+ - \zeta_2^- & 2(\xi_2^+ - \xi_2^-) & 0 \end{bmatrix} \Bigg\} \end{aligned} \tag{4.68c}$$

$$\begin{aligned} \overline{\overline{\boldsymbol{A}}}_{\boldsymbol{3}} = -\frac{\varepsilon_0}{20\rho\pi h {g_0}^5} j \Bigg\{ & (12\sin\delta + \sin 4\delta) \begin{bmatrix} \xi_0^+ + \xi_0^- & 0 & 0 & 0 \\ 0 & 0 & 0 & \xi_0^+ + \xi_0^- \end{bmatrix} \\ & + (12\sin\delta - 3\sin 4\delta) \begin{bmatrix} 0 & 0 & \xi_0^+ + \xi_0^- & 0 \\ 0 & \xi_0^+ + \xi_0^- & 0 & 0 \end{bmatrix} \Bigg\} \end{aligned} \tag{4.68d}$$

where the coefficients with odd m_V, i.e. $\xi_1^{\pm}$, $\zeta_1^{\pm}$, $\xi_3^{\pm}$, $\zeta_3^{\pm}$ have no contributions to the net electrostatic force after summing the electrostatic potential energy for all electrodes.

Noting that the mechanical component of the equations of motion is unaffected by the applied voltage distribution, (4.43a) and (4.43b) can be used directly to obtain the modal-mass normalised equations of motion. Substituting the electrostatic forces in (4.67) and the mechanical forces in (4.44) into (4.43a) and (4.43b) gives the following equations of motion:

$$\begin{aligned} & \ddot{\overline{\boldsymbol{q}}}_{\boldsymbol{1}} + 2\Gamma\dot{\overline{\boldsymbol{q}}}_{\boldsymbol{1}} + \overline{\overline{\boldsymbol{\eta}}}_{\boldsymbol{1}}(t)\overline{\boldsymbol{q}}_{\boldsymbol{1}} + \overline{\overline{\boldsymbol{\eta}}}_{\boldsymbol{3}}(t)\frac{\overline{\boldsymbol{q}}_{\boldsymbol{3}}}{{g_0}^2} \\ & \quad = \Omega\overline{\overline{\boldsymbol{G}}}_{\boldsymbol{\Omega}}\dot{\overline{\boldsymbol{q}}}_{\boldsymbol{1}} + \overline{\boldsymbol{\chi}}(t) \\ & \quad + \left[\chi\cos\omega t\,\overline{\overline{\boldsymbol{\eta}}}_{\boldsymbol{\chi}} + \chi_\Delta\cos(\omega t + \phi_x + i_\Delta\pi)\,\overline{\overline{\boldsymbol{\eta}}}_{\boldsymbol{\chi\Delta}}\right]\frac{\overline{\boldsymbol{q}}_{\boldsymbol{2}}}{{g_0}^2} \end{aligned} \tag{4.69}$$

Due to the presence of the balancing voltage in (4.65a) and (4.65b), (4.69) differs from (4.14) through the terms in the matrices $\overline{\overline{\boldsymbol{\eta}}}_{\boldsymbol{1}}(t)$, $\overline{\overline{\boldsymbol{\eta}}}_{\boldsymbol{3}}(t)$, and the newly introduced vector $\overline{\boldsymbol{\chi}}(t)$ and matrix $\overline{\overline{\boldsymbol{\eta}}}_{\boldsymbol{\chi\Delta}}$.

$\overline{\boldsymbol{\chi}}(t)$ and $\overline{\overline{\boldsymbol{\eta}}}_{\boldsymbol{\chi\Delta}}$ are arranged on the right side of (4.69) as they stem from the voltage components giving rise to the direct forces acting on the drive and sense modes. $\overline{\boldsymbol{\chi}}(t)$ is the direct force vector of order $q = 1$ and $\overline{\overline{\boldsymbol{\eta}}}_{\boldsymbol{\chi\Delta}}$ is a matrix characterising the quadratic correction of the harmonic force $\chi_\Delta \cos(\omega t + \phi_x + i_\Delta \pi)$. The bracketed terms on the right side of (4.69) have been arranged to show the similarities of quadratic correction roles of $\overline{\overline{\boldsymbol{\eta}}}_{\boldsymbol{\chi\Delta}}$ and $\overline{\overline{\boldsymbol{\eta}}}_{\boldsymbol{\chi}}$. $\overline{\boldsymbol{\chi}}(t)$ and $\overline{\overline{\boldsymbol{\eta}}}_{\boldsymbol{\chi\Delta}}$ are given by:

$$\overline{\boldsymbol{\chi}}(t) = -\overline{\boldsymbol{A}}_{\boldsymbol{0}} = \begin{bmatrix} \chi \cos \omega t \\ \chi_\Delta \cos(\omega t + \phi_x + i_\Delta \pi) \end{bmatrix} \tag{4.70}$$

$$\overline{\overline{\boldsymbol{\eta}}}_{\boldsymbol{\chi\Delta}} = \begin{bmatrix} 0 & 1 - \cos 2\delta & 0 \\ \dfrac{1 - \cos 2\delta}{2} & 0 & \dfrac{5 + \cos 2\delta}{2} \end{bmatrix} \tag{4.71}$$

where

$$\chi_\Delta = j \frac{\varepsilon_0 \sin \delta}{5 \rho h \pi {g_0}^2} {V_\Delta}^2 \tag{4.72}$$

χ_Δ defines the modal-mass-normalised amplitude of the force directly applied on the sense mode, in a manner similar to the harmonic drive force amplitude χ defined in (3.19). Comparing (4.70) and (4.68a), the role of the voltage squared coefficients $\zeta_2^{\pm}$ for direct forcing of the sense mode is clear. $\chi_\Delta \propto \zeta_2^+ - \zeta_2^-$, which is the result of satisfying the first condition in Table 4.7. This direct sense force is used as the balancing force $f_0^l \cos(\omega t + \phi_x)$ in the targeted sense equation of motion in (4.62).

Matrices $\overline{\overline{\boldsymbol{\eta}}}_{\boldsymbol{1}}(t)$, $\overline{\overline{\boldsymbol{\eta}}}_{\boldsymbol{3}}(t)$ are associated with the linear ($\overline{\overline{\boldsymbol{A}}}_{\boldsymbol{1}}\overline{\boldsymbol{q}}_{\boldsymbol{1}}$) and cubic ($\overline{\overline{\boldsymbol{A}}}_{\boldsymbol{3}}\overline{\boldsymbol{q}}_{\boldsymbol{3}}$) electrostatic forces in (4.67) respectively, so they only depend on the voltage squared coefficients $\xi_0^{\pm}$. $\overline{\overline{\boldsymbol{\eta}}}_{\boldsymbol{1}}(t)$ and $\overline{\overline{\boldsymbol{\eta}}}_{\boldsymbol{3}}(t)$ are given by:

$$\begin{aligned} \overline{\overline{\boldsymbol{\eta}}}_{\boldsymbol{1}}(t) = &\begin{bmatrix} {\omega_{0,\lambda,\Delta}}^2 & 0 \\ 0 & {\omega_{0,\lambda,\Delta}}^2 \end{bmatrix} + {\omega_m}^2 \begin{bmatrix} \Delta_m \cos 4\Theta_\omega & \Delta_m \sin 4\Theta_\omega \\ \Delta_m \sin 4\Theta_\omega & -\Delta_m \cos 4\Theta_\omega \end{bmatrix} \\ &+ \begin{bmatrix} {\omega_\lambda}^2 & 0 \\ 0 & {\omega_\lambda}^2 \end{bmatrix} \cos 2(\omega t + \phi_x) \end{aligned} \tag{4.73}$$

$$\overline{\overline{\boldsymbol{\eta}}}_{\boldsymbol{3}}(t) = \begin{bmatrix} \gamma_{0,\lambda,\Delta} & 0 & \kappa_{0,\lambda,\Delta} & 0 \\ 0 & \kappa_{0,\lambda,\Delta} & 0 & \gamma_{0,\lambda,\Delta} \end{bmatrix} - \begin{bmatrix} \gamma_{\lambda} & 0 & \kappa_{\lambda} & 0 \\ 0 & \kappa_{\lambda} & 0 & \gamma_{\lambda} \end{bmatrix} \cos 2(\omega t + \phi_x) \tag{4.74}$$

where

$$\omega_{0,\lambda,\Delta}{}^2 = \omega_0{}^2 - \omega_\lambda{}^2 - \omega_\Delta{}^2 \tag{4.75}$$

$$\gamma_{0,\lambda,\Delta} = \gamma_0 + \gamma_\lambda + \gamma_\Delta \tag{4.76}$$

$$\kappa_{0,\lambda,\Delta} = \kappa_0 + \kappa_\lambda + \kappa_\Delta \tag{4.77}$$

In these equations $\omega_{0,\lambda,\Delta}{}^2$, $\gamma_{0,\lambda,\Delta}$ and $\kappa_{0,\lambda,\Delta}$ represent the linear resonant frequency, single and couple-mode cubic stiffnesses (modal-mass-normalised) respectively, and the '$0, \lambda, \Delta$' subscripts indicate contributions from the bias voltage V_0, and the amplitudes of the parametric pumping voltage V_λ and the balancing voltage V_Δ to these quantities. (4.73) and (4.74) only differ from (4.15) and (4.16) through these terms. Comparing the definitions of these terms in (4.75), (4.76) and (4.77) against those of $\omega_{0,\lambda}{}^2$, $\gamma_{0,\lambda}$ and $\kappa_{0,\lambda}$ in (4.17), (4.18) and (4.19), additional terms with the subscript 'Δ' are present to highlight the contribution from the balancing voltage. $\omega_\Delta{}^2$, γ_Δ and κ_Δ are given by:

$$\omega_\Delta{}^2 = j\frac{2\varepsilon_0 V_\Delta{}^2}{5\rho h \pi {g_0}^3}\delta \tag{4.78}$$

$$\gamma_\Delta = -j\frac{3\varepsilon_0 V_\Delta{}^2}{5\rho h \pi {g_0}^3}\left(\delta + \frac{\sin 4\delta}{12}\right) \tag{4.79}$$

$$\kappa_\Delta = -j\frac{3\varepsilon_0 V_\Delta{}^2}{5\rho h \pi {g_0}^3}\left(\delta - \frac{\sin 4\delta}{4}\right) \tag{4.80}$$

Comparing $\omega_\Delta{}^2$, γ_Δ and κ_Δ against $\omega_\lambda{}^2$, γ_λ and κ_λ in (4.21), (4.22) and (4.23), clear similarities can be observed. The corresponding definitions simply involve an interchange between the voltage amplitudes V_Δ and V_λ. This similarity is because of the similarity of the contributions of these voltage components to the coefficient sum $\xi_0^+ + \xi_0^-$ defined in (4.66a). As such, $\gamma_\Delta = \kappa_\Delta$ only for the case of a continuous electrode distribution when $j = 8$ in a manner similar to the relationship between γ_λ and κ_λ, and when $j = 16$ or 32, $\gamma_\Delta = \kappa_\Delta$ for all electrode spans as the terms involving $\sin 4\delta$ in (4.79) and (4.80) vanish after the summation of the electrostatic potential energy.

The parametric pumping voltage and balancing voltage are harmonic voltages, they interact constructively to strengthen both the linear and nonlinear electrostatic softening effects, i.e. ${\omega_{0,\lambda,\Delta}}^2 < {\omega_{0,\lambda}}^2 < {\omega_0}^2, |\gamma_{0,\lambda,\Delta}| > |\gamma_{0,\lambda}| > |\gamma_0|$ and $|\kappa_{0,\lambda,\Delta}| > |\kappa_{0,\lambda}| > |\kappa_0|$. The latter, where the coupled-mode stiffness is increased indicates a stronger nonlinear elastic coupling, thus increasing the amplitude of the resulting self-induced parametric excitation.

With the definitions described, it can be shown by setting the balancing voltage amplitude V_Δ to zero equations of motion in (4.69) revert to (4.14). Also if the parametric pumping voltage amplitude V_λ is zero, (4.69) is identical to the equations of motion for the basic electrostatic configuration in (3.14).

Drive dynamics

Applying the same assumptions as those relevant to (3.24) and (4.24), the drive equation of motion in (4.69) can be simplified to:

$$\ddot{X} + 2\Gamma\dot{X} + \left[{\omega_{0,\lambda,\Delta}}^2 + {\omega_m}^2\Delta_m \cos 4\Theta_\omega + {\omega_\lambda}^2 \cos 2(\omega t + \phi_x)\right]X + \left[\gamma_{0,\lambda,\Delta} - \gamma_\lambda \cos 2(\omega t + \phi_x)\right]\frac{X^3}{{g_0}^2} = \chi \cos \omega t \left(1 + c_{XX}\frac{X^2}{{g_0}^2}\right) \tag{4.81}$$

which yields the averaged drive frequency:

$${\omega_X}^2 = {\omega_{0,\lambda,\Delta}}^2 + {\omega_m}^2\Delta_m \cos 4\Theta_\omega + \frac{{\omega_\lambda}^2}{2} + \left(\frac{3}{4}\gamma_{0,\lambda,\Delta} - \frac{1}{2}\gamma_\lambda\right)\frac{x^2}{{g_0}^2} \tag{4.82}$$

where the additional linear and nonlinear softening due to the balancing voltage is clear, as shown in the terms involving ${\omega_{0,\lambda,\Delta}}^2$ and $\gamma_{0,\lambda,\Delta}$ respectively.

Sense dynamics

The approximated sense equation of motion is similarly obtained from (4.69). This gives:

$$\begin{aligned}\ddot{Y} + 2\Gamma\dot{Y} + \Bigg\{&{\omega_{0,\lambda,\Delta}}^2 - {\omega_m}^2\Delta_m \cos 4\Theta_\omega + \left({\omega_\lambda}^2 - \kappa_\lambda\frac{X^2}{{g_0}^2}\right)\cos 2(\omega t + \phi_x) \\ &+ \kappa_{0,\lambda,\Delta}\frac{X^2}{{g_0}^2} - \frac{\chi c_{XY}}{g_0}\cos \omega t \frac{X}{g_0}\Bigg\} Y \\ &= -G_\Omega \Omega \dot{X} - {\omega_m}^2\Delta_m \sin 4\Theta_\omega\, X \\ &+ \chi_\Delta \cos(\omega t + \phi_x + i_\Delta \pi)\left(1 + c_{\Delta,XX}\frac{X^2}{{g_0}^2}\right)\end{aligned} \tag{4.83}$$

where $c_{\Delta,XX} = \sin^2\delta$ and $\omega = \omega_X$.

(4.83) yields an averaged force balance case similar to (4.60), giving the following result when $\omega = \omega_X$:

$$\begin{bmatrix} -\bar{\omega}^2 + \lambda_{1,r} & -2\Gamma\omega_X \\ -2\Gamma\omega_X & \bar{\omega}^2 + \lambda_{1,r} \end{bmatrix} \bar{\boldsymbol{y}} = \begin{bmatrix} f_\Delta + f_0^l \\ f_\Omega \end{bmatrix} \tag{4.84}$$

In this equation f_0^l is the balancing force imposed on the sense mode to nullify the quadrature output and ensure that $\bar{\boldsymbol{y}} = \bar{\boldsymbol{y}}_{\boldsymbol{0}}^{\boldsymbol{l}}$, and is given by:

$$f_0^l = \chi_\Delta \cos i_\Delta \pi \left(1 + c_{\Delta,XX} \frac{3x^2}{4{g_0}^2}\right) \tag{4.85}$$

Recalling from (4.72) that $\chi_\Delta > 0$, the phase index number i_Δ is required to allow for negative values of f_0^l. This is important because as shown in (4.61), the required f_0^l can be negative depending on the angular rate, nonlinear frequency imbalance and the linear elastic coupling force. Noting from (4.61) that the required f_0^l is linearly related to the angular rate and that $\chi_\Delta \propto {V_\Delta}^2$ from the definition in (4.72), equating (4.61) and (4.85) shows that ${V_\Delta}^2$ is linearly related to the angular rate. If there is no linear elastic coupling force ($f_\Delta = 0$), ${V_\Delta}^2$ is proportional to the angular rate, similar to FTR mode operation [26]. The potential of using the balancing voltage for rate sensing will be considered later.

In (4.84) $\bar{\omega}^2$ and $\lambda_{1,r}$ are the effective frequency detuning parameter and parametric excitation amplitude respectively and are given by:

$$\bar{\omega}^2 = {\omega_X}^2 - {\omega_Y}^2 = {\bar{\omega}^l}^2 - {\bar{\omega}^c}^2(x) \tag{4.86}$$

$$\lambda_{1,r} = \lambda_{1,0}(x) + \lambda_{1,\Delta}(x) + \lambda_{1,\lambda} \tag{4.87}$$

where the amplitude-dependent terms in (4.86) and (4.87) have been defined as functions of the drive amplitude.

The frequency detuning terms in (4.86) have been decomposed according to the order of the originating forces, linear or cubic. The frequency detuning components are given by:

$${\bar{\omega}^l}^2 = 2{\omega_m}^2 \Delta_m \cos 4\Theta_\omega + \frac{{\omega_\lambda}^2}{2} \tag{4.88}$$

$${\bar{\omega}^c}^2(x) = -\left[\frac{1}{4}(3\gamma_0 - 2\kappa_0) + \frac{1}{4}(\gamma_\lambda - \kappa_\lambda) + \frac{1}{4}(3\gamma_\Delta - 2\kappa_\Delta)\right] \frac{x^2}{{g_0}^2} \tag{4.89}$$

where the contributions from the bias, parametric pumping and balancing voltages have been decomposed.

The balancing voltage only affects the cubic force contribution towards the total frequency detuning, i.e. $\bar{\omega}^{c^2}(x)$. Noting the definitions of γ_0, κ_0, γ_λ, κ_λ, γ_Δ, κ_Δ, $\bar{\omega}^{c^2}(x) > 0$ indicating that that the cubic restoring forces exhibit greater softening effects on the drive mode than the sense mode in a manner similar to the previous cases. The balancing voltage increases the softening rate difference between the drive and sense modes. However, the parametric pumping voltage can be used to tune the corresponding frequency component ${\omega_\lambda}^2$ in (4.88) to adjust the total frequency detuning. Since $\bar{\omega}^{c^2}(x)$ is scaled by the square of the drive amplitude ratio x/g_0, ${\bar{\omega}^l}^2$ is typically orders of magnitude larger than $\bar{\omega}^{c^2}(x)$ unless the imperfection is small. As such, it is more effective to adjust the total frequency detuning by regulating its linear contribution ${\bar{\omega}^l}^2$, as using $\bar{\omega}^{c^2}(x)$ for this purpose will require larger voltages.

In (4.87) the net parametric excitation amplitude is composed of the self-induced parametric excitation $\lambda_{1,0}(x)$ defined in (4.37), the linear amplitude-independent parametric excitation $\lambda_{1,\lambda}$ also defined in (4.37) and an additional parametric excitation arising from the balancing voltage, defined as:

$$\lambda_{1,\Delta}(x) = \kappa_\Delta \frac{x^2}{4{g_0}^2} \tag{4.90}$$

$\lambda_{1,\Delta}(x)$ and the self-induced parametric excitation arise due to modulation of the sense mode stiffness by large oscillatory drive displacements, resulting in the drive amplitude dependencies of these parametric excitation components. This is in contrast to the linear parametric excitation $\lambda_{1,\lambda}$ which directly stems from pump voltage modulation. As such, one has direct control of the linear parametric excitation $\lambda_{1,\lambda}$ by tuning the parametric pumping voltage. The significance of $\lambda_{1,\lambda}$ is demonstrated in the following.

4.5.4. Linearisation and trimming of sense response with nullified net parametric excitation

In this section, the conditions to use the balancing voltage to nullify the quadrature output and replicate linear, trimmed sense response with the net parametric excitation nullified is investigated, and the potential of using the balancing voltage for rate sensing is considered. The effects of nullifying the net parametric excitation in the presence of the balancing voltage is investigated to assess the resulting rate sensing performance using the balancing voltage.

Similar to the sense displacement based open-loop rate sensing, the rate sensing performance using the balancing voltage is assessed in terms of the rate sensitivity and bias rate.

Rate sensing using balancing voltage with linearised and trimmed sense response

To linearise and trim the rate output and nullify the quadrature output, using (4.61), the balancing force amplitude in (4.85) must be adjusted such that:

$$\chi_\Delta \left(1 + c_{\Delta,xx} \frac{3x^2}{4{g_0}^2}\right) \cos i_\Delta \pi = \chi_{\Delta,\Delta} + \chi_{\Delta,\Omega}(\Omega) \tag{4.91}$$

$\chi_{\Delta,\Delta}$ and $\chi_{\Delta,\Omega}(\Omega)$ represent the rate-independent and rate-dependent components of the balancing force amplitude respectively, given by:

$$\chi_{\Delta,\Delta} = j \frac{\varepsilon_0 \sin\delta}{5\rho h \pi {g_0}^2} {V_{\Delta,\Delta}}^2 \cos i_{\Delta,\Delta}\pi = -f_\Delta \tag{4.92a}$$

$$\chi_{\Delta,\Omega}(\Omega) = j \frac{\varepsilon_0 \sin\delta}{5\rho h \pi {g_0}^2} {V_{\Delta,\Omega}}^2 \cos i_{\Delta,\Omega}\pi = \frac{\bar{\omega}^2 - \lambda_{1,r}}{2\Gamma\omega_X} f_\Omega \tag{4.92b}$$

Using the definition of χ_Δ in (4.72), the definitions in (4.92a) and (4.92b) are such that:

$${V_\Delta}'^2 \cos i_\Delta \pi = {V_{\Delta,\Delta}}^2 \cos i_{\Delta,\Delta}\pi + {V_{\Delta,\Omega}}^2 \cos i_{\Delta,\Omega}\pi \tag{4.93}$$

where $V_{\Delta,\Delta}$, $V_{\Delta,\Omega}$ are the rate-independent and rate-dependent components of the balancing voltage amplitude respectively, and $i_{\Delta,\Delta}$, $i_{\Delta,\Omega}$ are integers representing the corresponding phase index numbers. ${V_\Delta}'$ is the nonlinear-corrected balancing voltage amplitude, given by:

$$V_\Delta' = V_\Delta \sqrt{1 + c_{\Delta,xx} \frac{3x^2}{4{g_0}^2}}$$

Using (4.92a) and (4.92b) in (4.93) shows that ${V_\Delta}^2 \cos i_\Delta \pi$ is linearly related to the Coriolis force and angular rate through its rate-dependent component ${V_{\Delta,\Omega}}^2 \cos i_{\Delta,\Omega}\pi$. From (4.93), the required ${V_\Delta}^2 \cos i_\Delta \pi$ is the sum of two distinct parts:

- A rate-independent component ${V_{\Delta,\Delta}}^2 \cos i_{\Delta,\Delta}\pi$ to counteract the linear elastic coupling force f_Δ. ${V_{\Delta,\Delta}}^2$ is proportional to the drive amplitude as $f_\Delta \propto x$.
- A rate-dependent part ${V_{\Delta,\Omega}}^2 \cos i_{\Delta,\Omega}\pi$, proportional to the angular rate serving to counteract the nonlinear frequency imbalance $\bar{\omega}^2 - \lambda_{1,r}$. ${V_{\Delta,\Omega}}^2$ is generally nonlinear

in the drive amplitude unless the nonlinear frequency imbalance $\bar{\omega}^2 - \lambda_{1,r}$ is invariant with the drive amplitude.

When $f_\Delta = 0$ as in the case of drive alignment, $V_{\Delta,\Delta} = 0$ as the balancing voltage only serves to counteract the nonlinear frequency imbalance, so ${V_\Delta}^2 \cos i_\Delta \pi \propto \Omega$. This linear relationship demonstrates the potential for rate sensing using the balancing voltage amplitude. In this dissertation, the usage of the balancing voltage for rate sensing is referred as closed-loop rate sensing, owing to similarities with standard FTR operation. In this manner, the nullification of the sense quadrature response allows dual operation of the device: in open-loop using the trimmed, linearised sense amplitude, or in closed-loop using the square of the balancing voltage amplitude required for nullifying the sense quadrature response amplitude.

Nullifying net parametric excitation in the presence of balancing voltage

The potential to use the linear parametric excitation $\lambda_{1,\lambda}$ to counteract the self-induced parametric excitation $\lambda_{1,0}(x)$ was investigated in Section 4.3. Using a similar approach involving setting $\lambda_{1,r}$ in (4.87) to zero, the parametric pumping voltage amplitude V_λ is adjusted such that the linear parametric excitation $\lambda_{1,\lambda}$ counteracts the amplitude-dependent parametric excitation components $\lambda_{1,0}(x), \lambda_{1,\Delta}(x)$. This parametric pumping voltage amplitude adjustment fixes its linear resonant frequency contribution at:

$$ {\omega_\lambda}^2|_{\lambda_{1,r}=0} = -(\kappa_\Delta + \kappa_0)\frac{x^2}{2{g_0}^2} \tag{4.94} $$

The effective nonlinear elastic coupling is strengthened due to the balancing voltage. As such, the required parametric pumping voltage to achieve net parametric excitation negation is increased, as can be observed by comparing (4.94) against (4.38).

(4.94) constrains ${\omega_\lambda}^2$ and when substituted into the linear frequency detuning component in (4.88), results in the amplitude-dependency of ${\bar{\omega}^l}^2$. Substituting the resulting amplitude-dependent expression for ${\bar{\omega}^l}^2$ and (4.89) into (4.86) gives the following result for the constrained frequency detuning:

$$ \bar{\omega}^2|_{\lambda_{1,r}=0} = {\bar{\omega}^l}^2(x)|_{\lambda_{1,r}=0} + {\bar{\omega}^c}^2(x) \tag{4.95} $$

where ${\bar{\omega}^l}^2(x)|_{\lambda_{1,r}=0}$ is the result of substituting (4.94) into (4.88), given by:

$$\bar{\omega}^{l^2}(x)|_{\lambda_{1,r}=0} = 2{\omega_m}^2\Delta_m \cos 4\Theta_\omega - \kappa_0 \frac{x^2}{4{g_0}^2} - \kappa_\Delta \frac{x^2}{4{g_0}^2} \tag{4.96}$$

As discussed in Section 4.3, without implementing the balancing voltage, the amplitude dependency of the constrained frequency detuning dictates the linearity of the rate and quadrature outputs. Since the amplitude dependencies of $\bar{\omega}^{l^2}(x)|_{\lambda_{1,r}=0}$ and $\bar{\omega}^{c^2}(x)$ are both quadratic, the amplitude dependency of the constrained frequency detuning in (4.95) is given by the following derivative:

$$\frac{\partial \bar{\omega}^2|_{\lambda_{1,r}=0}}{\partial (x')^2} = \frac{1}{4}[3(\gamma_0 - \kappa_0) + (\gamma_\lambda - \kappa_\lambda) + 3(\gamma_\Delta - \kappa_\Delta)] \tag{4.97}$$

where $x' = x/g_0$. The amplitude dependency of the frequency detuning is dictated by the relative softening rates between the drive and sense modes, and the effects of the bias, parametric excitation and balancing voltages are clear in (4.97).

Comparing the amplitude dependencies of the frequency detuning in (4.86) and its constrained form in (4.95), it is clear that setting the parametric pumping voltage to negate the self-induced parametric excitation also reduces the softening rate difference between the drive and sense modes, similar to the case without the balancing voltage investigated in Section 4.3.4. However, the softening rate of the sense mode does not exceed that of the drive mode, as $\partial \bar{\omega}^2|_{\lambda_{1,r}=0}/\partial (x')^2 \leq 0$. This effect is maximised when a continuous electrode distribution is implemented ($\gamma_0 = \kappa_0, \gamma_\lambda = \kappa_\lambda, \gamma_\Delta = \kappa_\Delta$), as the nonlinear softening rates of the drive and sense modes are equalised. However, when the electrodes are discontinuous, the drive mode softens at a more significant rate than the sense mode. Similarly, the effects of the electrode discontinuities can be avoided by increasing the number of electrodes to 16 or 32. However, the investigation on the balance of the forces on the sense mode in Section 4.5.1 shows that the introduction of the balancing force stemming from the balancing voltage can be used to address the force imbalances due to the nonlinear frequency imbalance associated with electrode discontinuities in the 8 electrode design.

The role of the balancing voltage to address the nonlinear frequency imbalance is demonstrated in the following investigation by considering the influence of the frequency detuning on the balancing voltage amplitude. Systems 1 and 2 in Table 4.2 are considered for this investigation, subjected to an angular of $\Omega = 250\,°/s$. The balancing voltage amplitude V_Δ is calculated using (4.91) and the phase index i_Δ is set at 0 or 1 depending on the sign of the right side of (4.91). The required parametric pumping voltage amplitude V_λ to nullify the net parametric excitation is then calculated using (4.94). Figure 4.11(a) and (b) show

comparisons of the drive amplitude dependency of the drive and sense frequencies for the basic electrostatic configuration case with self-induced parametric excitation present ($V_\lambda = V_\Delta = 0$) against the case of nullified net parametric excitation in the presence of the balancing voltage for systems 2 and 1 respectively. Figure 4.12(a) and (b) show the corresponding variations of ${V_\Delta}^2 \cos i_\Delta \pi$ with the gap-normalised drive amplitude, along with the rate-dependent and independent components, ${V_{\Delta,\Omega}}^2 \cos i_{\Delta,\Omega}\pi$ and ${V_{\Delta,\Delta}}^2 \cos i_{\Delta,\Delta}\pi$. The rate-independent component ${V_{\Delta,\Delta}}^2 \cos i_{\Delta,\Delta}\pi$ is calculated using (4.91) in the absence of angular rate. The rate-dependent component ${V_{\Delta,\Omega}}^2 \cos i_{\Delta,\Omega}\pi$ is obtained by subtracting ${V_{\Delta,\Delta}}^2 \cos i_{\Delta,\Delta}\pi$ from ${V_\Delta}^2 \cos i_\Delta \pi$ using the relationship in (4.93).

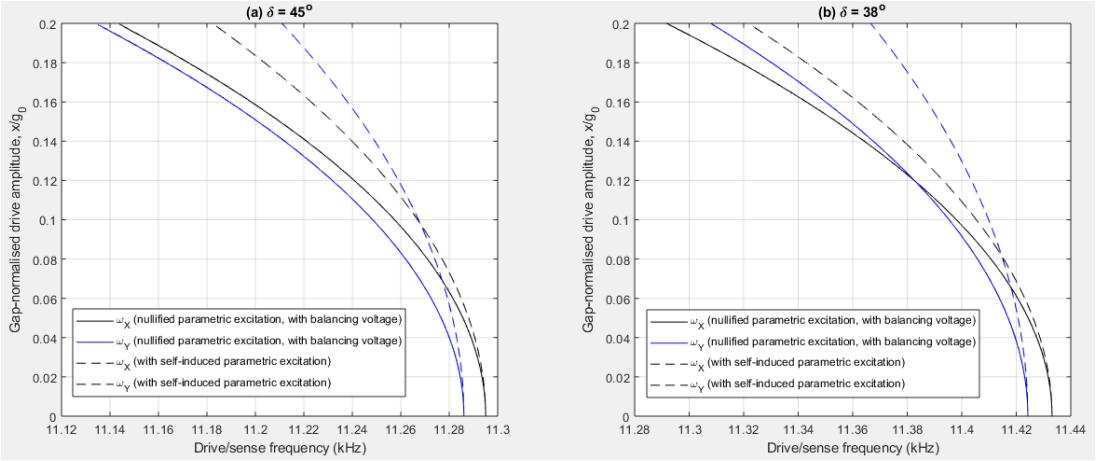

Figure 4.11: Drive and sense frequency variations with the gap-normalised drive amplitude for the cases of with the self-induced parametric excitation present and nullified net parametric excitation in the presence of balancing voltage for electrode spans of (a) 45° and (b) 38°

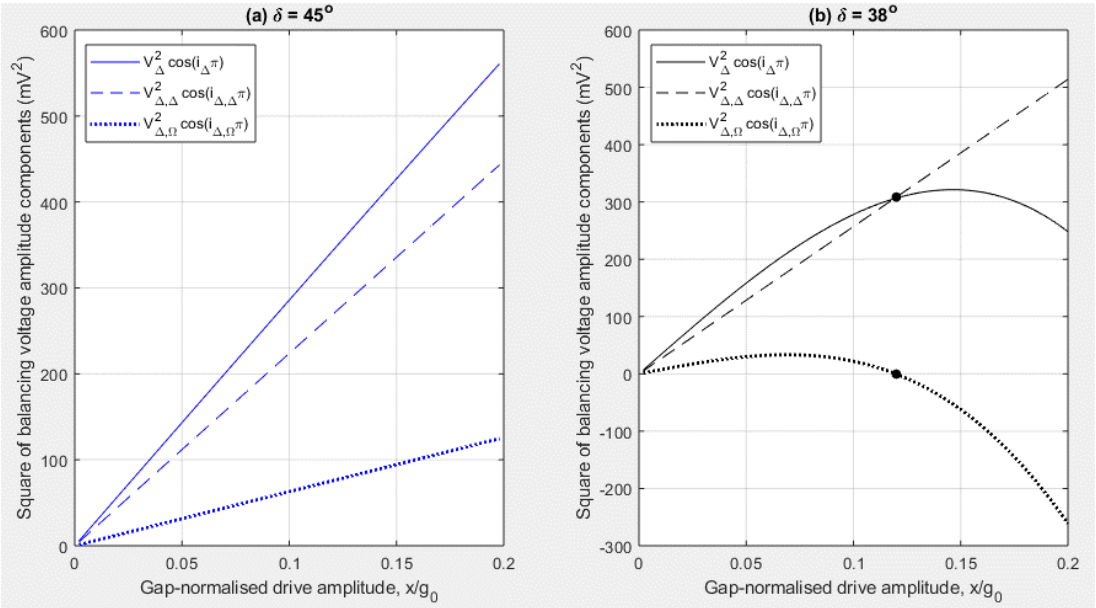

Figure 4.12: Variations of the square of the balancing voltage amplitude components with the gap-normalised drive amplitude for electrode spans of (a) 45° and (b) 38°

In Figure 4.11(a) and (b), nullifying the net parametric excitation significantly reduces the softening rate difference between the drive and sense modes compared to the case where self-induced parametric excitation is not nullified. However, as noted previously, the sense mode softens less significantly than the drive mode unless the electrodes are continuous. Comparing Figure 4.11(a) and (b) with the results without the balancing voltage in Figure 4.8(a) and (b), the drive and sense frequencies are very similar between these sets of results. This is because the calculated balancing voltage amplitude is relatively small, not exceeding $(V_\Delta/V_0)^2 = 1.4e-4$. However, in practice the required amplitude V_Δ can be orders of magnitude larger if the damping is low (see (4.92b)). From the results in Figure 4.11(a) and (b), the nullification of the net parametric excitation only results in amplitude-insensitive frequency detuning for the continuous electrode case, owing to the equal softening rates of the drive and sense modes.

In Figure 4.12(a) and (b), the rate-independent component ${V_{\Delta,\Delta}}^2 \cos i_{\Delta,\Delta}\pi$ is proportional to the drive amplitude in both cases, indicating the linearity of the linear elastic coupling force. However, ${V_{\Delta,\Omega}}^2 \cos i_{\Delta,\Omega}\pi$ is only linear with respect to the drive amplitude for the continuous electrode case. This is because, as noted previously, the linearity of ${V_{\Delta,\Omega}}^2 \cos i_{\Delta,\Omega}\pi$ depends on the frequency detuning. The nonlinear drive amplitude dependency of ${V_{\Delta,\Omega}}^2 \cos i_{\Delta,\Omega}\pi$ in Figure 4.12(b) is the direct result of the frequency detuning in Figure 4.11(b) varying with the drive amplitude. At $x/g_0 = 0.12$, Figure 4.12(b) shows that $V_{\Delta,\Omega} = 0$ and $V_\Delta = V_{\Delta,\Delta}$, indicating that the balancing voltage is purely used to negate the linear elastic coupling force. This occurs because as shown in Figure 4.11(b), frequency matching occurs at this drive amplitude. Consequently, the balancing voltage amplitude does not vary with the angular rate if this drive amplitude is chosen in operation.

Closed-loop rate sensing performance with nullified net parametric excitation

When the balancing voltage is adjusted to satisfy (4.91), the rate and quadrature output components of the sense response are linearised because the nonlinear amplitude dependence of the frequency detuning has been balanced by $\chi_{\Delta,\Omega}(\Omega)$, effectively 'transferring' the nonlinear drive amplitude dependency of the sense response to the balancing voltage as shown in Figure 4.12(b). Setting $\lambda_{1,r} = 0$ due to nullifying the net parametric excitation using the condition in (4.94), and substituting the resulting expression for the constrained frequency detuning in (4.95) into (4.91) gives the following expression for the required balancing force amplitude and phase to counteract the force mismatch between the frequency detuning and linear elastic coupling, thus linearising and trimming the rate output while nullifying the quadrature output:

$$\chi_\Delta{}' \cos i_\Delta \pi = -f_\Delta + \left(\bar{\omega}^2|_{\lambda_{1,r}=0}\right)\frac{f_\Omega}{2\Gamma\omega_X} \tag{4.98}$$

where the frequency detuning $\bar{\omega}^2|_{\lambda_{1,r}=0}$ dictates the rate-dependence of the balancing voltage and the linearity with respect to the drive amplitude.

Recalling that $\chi_\Delta{}' \propto {V_\Delta}^2$, the closed-loop rate sensing is described using the relationship ${V_\Delta}^2 \cos i_\Delta \pi = S^V(\Omega + \Omega_z^V)$, where S^V and Ω_z^V are the corresponding rate sensitivity and bias rate respectively, given by:

$$S^V = S^V|_{\lambda_{1,r}=0} = \frac{\frac{G_\Omega x}{2\Gamma}\left(\bar{\omega}^2|_{\lambda_{1,r}=0}\right)}{j\frac{\varepsilon_0}{5\rho h\pi {g_0}^2}\sin\delta\left(1 + c_{\Delta,XX}\frac{3x^2}{4{g_0}^2}\right)} \tag{4.99}$$

$$\Omega_z^V = \Omega_z^V|_{\lambda_{1,r}=0} = \frac{{\omega_m}^2\Delta_\omega \sin 4\Theta_\omega}{\frac{G_\Omega}{2\Gamma}\left(\bar{\omega}^2|_{\lambda_{1,r}=0}\right)} \tag{4.100}$$

In contrast to open-loop rate sensing, a larger frequency detuning $\bar{\omega}^2|_{\lambda_{1,r}=0}$ beneficially affects the closed-loop rate sensing, by increasing the closed-loop rate sensitivity while suppressing the corresponding bias rate. On the other hand, if $\bar{\omega}^2|_{\lambda_{1,r}=0} = 0$ due to frequency matching, $S^V = 0$ as the balancing voltage amplitude V_Δ is invariant with the angular rate, in which case the balancing voltage cannot be used for rate sensing. The closed-loop rate sensitivity S^V is drive amplitude dependent, characterised by two factors:

- a linear scaling because $f_\Omega \propto x$
- a nonlinear variation because the constrained frequency detuning $\bar{\omega}^2|_{\lambda_{1,r}=0}$ has quadratic-ordered amplitude dependency, unless $\partial\bar{\omega}^2|_{\lambda_{1,r}=0}/\partial(x')^2 = 0$ for the case of $\gamma_0 = \kappa_0, \gamma_\lambda = \kappa_\lambda, \gamma_\Delta = \kappa_\Delta$.

Effects of balancing voltage on open-loop rate sensitivity with continuous/discontinuous electrodes

The effectiveness of applying the balancing voltage to linearise and trim the rate output is investigated by assessing the open-loop rate sensitivity. For this investigation, systems 1 and 2 in Table 4.2 are considered. Balancing voltages are applied on these systems, where the balancing voltage phase index number i_Δ is set at 0 or 1 depending on the calculated values of the right side of (4.91). The balancing voltage amplitude V_Δ is tuned iteratively until the quadrature sense response nullifies. The parametric pumping voltage is applied with an amplitude V_λ as calculated in (4.94) to nullify the net parametric excitation. In practice, it is

necessary to incorporate a control system to achieve this with sufficient precision. Due to the manual adjustment of V_Δ in this investigation, the tolerance is such that the resulting relative phase is within 0.5° of the linear, ideal case of $\phi^l_{yx,0} = \pm\pi$. Figure 4.13(a) shows the variation of the normalised rate sensitivity S/S^l with the drive amplitude when the net parametric excitation has been nullified and the balancing voltage has been applied to nullify the quadrature sense response in system 2. The results in Figure 4.2(a) for the cases of without the balancing voltage, with and without negating the self-induced parametric excitation are also included for comparison. Figure 4.13(b) shows similar sets of results for system 1. The normalised linear, trimmed rate sensitivity S^l_0/S^l is also shown. FE results have also been included, where the required values of V_Δ, i_Δ and V_λ are obtained using the aforementioned methods.

Figure 4.14(a) and (b) show the corresponding results for the relative phase variation with the drive amplitude for $\Omega = 250\,°/s$. The results for the case without the balancing voltage are identical to those shown in Figure 4.3 for the corresponding electrode spans.

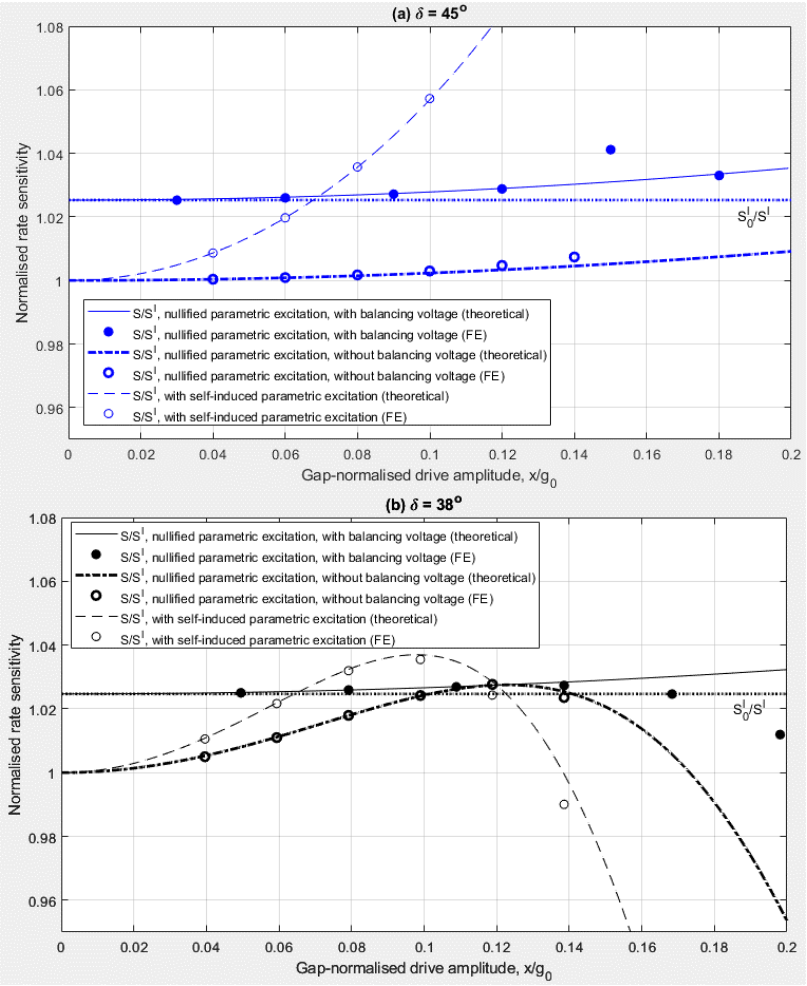

Figure 4.13: Comparison of the normalised rate sensitivities for the cases of with the self-induced parametric excitation and nullified net parametric excitation, with and without the balancing voltage applied for electrode spans of (a) 45° and (b) 38°

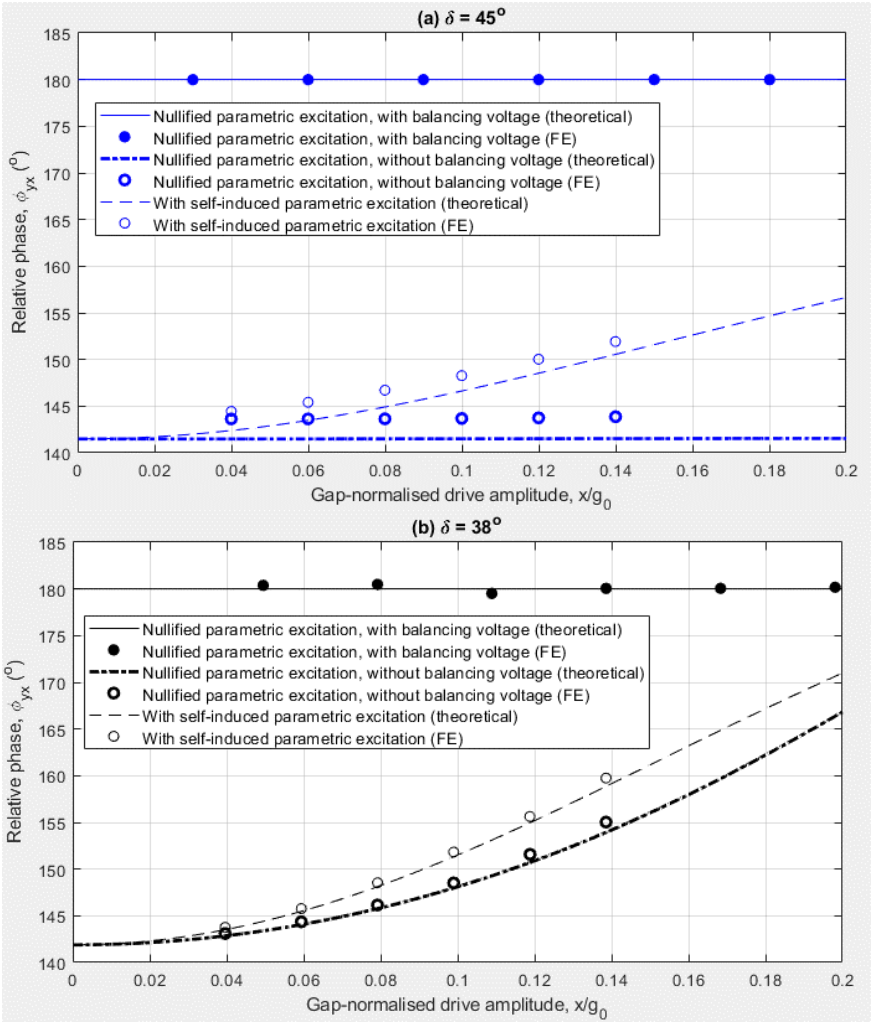

Figure 4.14: Variation of relative phase with drive amplitude for the cases of with the self-induced parametric excitation and nullified net parametric excitation, with and without the balancing voltage applied for electrode spans of (a) 45° and (b) 38°

In Figure 4.13(a), when the electrodes are continuous, the rate sensitivity approximates linear behaviour even without the balancing voltage due to the drive amplitude insensitivity of the frequency detuning (see (4.97)). The balancing voltage only acts to rectify the effects of this constant frequency detuning to achieve rate sensitivity trimming, as the rate sensitivity is increased to the perfect case S_0^l. Similar to the results in Figure 4.2(a), the slight increase of the rate sensitivity at higher drive amplitudes is attributed to residual parametric excitation due to the drive voltage as discussed in Section 3.4.2. Except for the data point at $x/g_0 \approx 0.15$, the FE results exhibit excellent agreement with the theoretical results, confirming the linearisation and trimming of the rate output.

The role of the balancing voltage is more significant when the electrodes are discontinuous. In Figure 4.13(b), comparison of the rate sensitivities with and without the balancing voltage shows that the balancing voltage exhibits both linearisation and trimming effects for rate sensitivity. Compared to the two cases without the balancing voltage, the low amplitude rate

sensitivity is increased to the perfect case S_0^I, and the nonlinear variation of the rate sensitivity is suppressed further. This shows that the elimination of the quadrature sense response is increasingly useful at larger drive amplitudes, where the increased frequency detuning magnitude must be compensated by the balancing voltage to avoid the rate sensitivity degrading at larger drive amplitudes as observed for the case without balancing voltage. The FE results with the balancing voltage included shows good agreement with the theoretical results for small drive amplitudes but shows rate sensitivity degradation at larger drive amplitudes, albeit less significantly compared to the other two cases without the balancing voltage. A possible explanation for this discrepancy is fringing effects at the electrodes, which is absent when the electrodes are continuous. Another possible explanation is the precision of the achieved nullification of the quadrature response, which can be observed from the relative phase results in Figure 4.14(a) and (b).

Figure 4.14(a) and (b) show that the relative phase in the presence of the balancing voltage is approximately $180°$ across the range of drive amplitudes considered, confirming the ability of the balancing voltage to eliminate the quadrature response. The nonlinear drive amplitude dependency of the relative phase is also significantly reduced for both electrode spans, indicating that the balancing voltage also has linearisation effects on the sense response. The FE results exhibit better agreement with the theoretical results for this case compared to the other two cases without the balancing voltage, where systematic offsets of approximately $1°$ are evident between the relative phases obtained theoretically and using FE. When comparing the results with the balancing voltage in Figure 4.14(a) and (b), the nullification of the quadrature response is less precisely achieved for the discontinuous electrode case. This is a possible explanation for the difference between the corresponding theoretical and FE results in Figure 4.13(b).

Effects of frequency detuning on closed-loop rate sensitivity

The effects of frequency detuning on the closed-loop rate sensitivity are investigated for devices implementing continuous and discontinuous electrode distributions. Similarly, systems 1 and 2 in Table 4.2 are considered for this investigation, and the following results are based on the same voltage conditions to generate the results in Figure 4.13(a) and (b) for the case involving the balancing voltage. Figure 4.15(a) shows the frequency backbone curves for the drive and sense frequencies as the drive amplitude increases when the net parametric excitation is nullified and the balancing voltage is applied to nullify the quadrature response, and is a combination of the plots in Figure 4.11(a) and (b) since these are based on the same systems. Figure 4.15(b) shows the corresponding closed-loop rate sensitivities, obtained based on the balancing voltage amplitudes used to linearise and trim the rate sensitivity shown in

Figure 4.13(a) and (b). The corresponding FE results are also included. A marker has also been shown in Figure 4.15(a) and (b) to indicate the amplitude and frequency when frequency matching occurs.

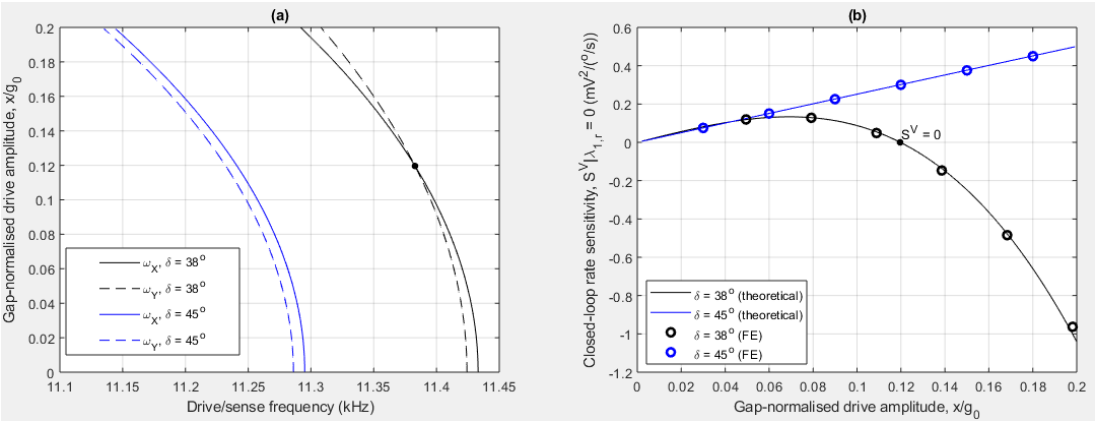

Figure 4.15: (a) Drive amplitude dependency of the resulting drive and sense frequencies when the net parametric excitation is nullified and the balancing voltage is applied to nullify the quadrature response and (b) the corresponding closed-loop rate sensitivity

Figure 4.15(b) shows that the closed-loop rate sensitivity varies nonlinearly with drive amplitude at larger drive amplitudes for the discontinuous electrode configuration. As discussed previously, the observed variation is the net effect of the interaction between linear scaling due to the Coriolis force, and the nonlinear drive amplitude dependency of the aforementioned frequency detuning. Linear scaling is dominant at smaller amplitudes, but the nonlinear frequency detuning results in a nonlinear decrease of the closed-loop rate sensitivity as drive amplitude increases. At $x/g_0 = 0.12$, the closed-loop rate sensitivity nullifies, indicating that the balancing voltage is insensitive to angular rate variations, in which case the balancing voltage cannot be used for rate sensing. At this drive amplitude, as shown in Figure 4.15(a), frequency matching occurs so the rate-dependent component of the balancing voltage is nullified (see (4.92b) with $\lambda_{1,r} = 0$), in which case the balancing voltage is purely used to counteract the linear elastic coupling force. In this manner, closed-loop rate sensing is best implemented when the frequency detuning is large at larger drive amplitudes, where the closed-loop rate sensitivity is linearly amplified by the Coriolis force, and nonlinearly amplified by the frequency detuning.

The nonlinearity drive amplitude dependency of the closed-loop rate sensitivity is absent for the case of a continuous electrode distribution because, as confirmed in Figure 4.15(a), the constrained frequency detuning is invariant with drive amplitude as the drive and sense modes soften at equal rates. As such, the corresponding closed-loop rate sensitivity in Figure 4.15(b) only exhibits linear scaling with drive amplitude due to the linear amplification of the Coriolis force. The FE results exhibit excellent agreement with the theoretical results for the range of

drive amplitudes considered, thus confirming the significance of the amplitude dependence of the frequency detuning on closed-loop rate sensitivity.

Effects of drive misalignment on closed-loop bias rate

The following investigates the effects of the drive misalignment on closed-loop bias rate when the imperfection magnitude is kept constant. System 1 in Table 4.2 is considered for this investigation, and two other systems of identical parameters except for the drive misalignment. Drive misalignments of $\Theta_\omega = 0°$ and $0.5°$ are considered, asides from the $\Theta_\omega = 1°$ case for system 1. Figure 4.16 plots the closed-loop bias rate Ω_z^V against drive amplitude for these drive misalignment cases.

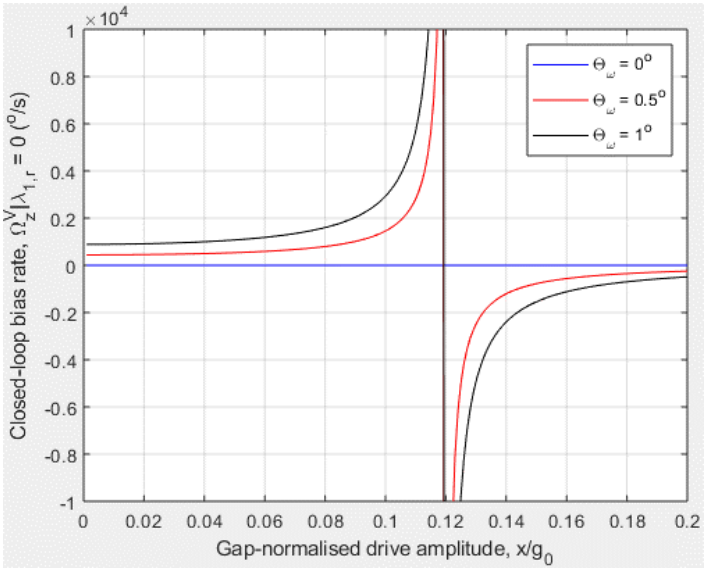

Figure 4.16: Effect of drive misalignment angle on closed-loop bias rate

Figure 4.16 shows that the closed-loop bias rate stems from the linear elastic coupling force, similar to the open-loop sense response. As such, this bias rate nullifies when the drive electrodes are aligned, i.e. $\Theta_\omega = 0°$. When drive misalignments are present, the bias rate increases with misalignment.

With small drive misalignments, large bias rates in the order of $100°/s$ are introduced at small drive amplitudes. This is because of the relatively large damping associated with the systems considered, which corresponds to a low Q factor of 120 without parametric excitation, and promotes larger bias rates (see (4.100)). However, the bias rate reduces at larger drive amplitudes, exhibiting nonlinear amplitude dependency. This nonlinearity is attributed to the drive amplitude dependency of the frequency detuning obtained from Figure 4.15(a). At drive amplitudes where the frequency detuning magnitude increases, the magnitude of the closed-loop bias rate diminishes. On the other hand, frequency matching occurs at $x/g_0 = 0.12$, significantly increasing the bias rate as the balancing voltage is invariant with angular rate.

4.5.5. Alternatives for linearisation and trimming of sense response

In this section, alternative implementations of the chosen electrostatic configuration in (4.65a) and (4.65b) are proposed and discussed to similarly linearise and trim the rate output and nullify the quadrature outputs, but without negating the self-induced parametric excitation. Only the theoretical basis of these alternative implementations will be discussed, as the targeted sense response is identical to that investigated previously for the case of nullified net parametric excitation.

As discussed in Section 4.5.3, the balancing voltage in (4.65a) and (4.65b) generates a direct electrostatic force acting on the sense mode, which as discussed in Section 4.5.1 serves to balance the mismatch between the amplitudes of the forces stemming from the imperfection-induced linear elastic coupling and the nonlinear frequency imbalance, thus reproducing the force balance in a linear, ideal/trimmed device. This implementation involves tuning the balancing voltage amplitude V_Δ until the quadrature sense amplitude nullifies, in which case (4.91) is satisfied. Revisiting (4.91) with the definitions of $\chi_{\Delta,\Delta}$ and $\chi_{\Delta,\Omega}$ in (4.92a) and (4.92b) substituted:

$$\chi_\Delta{}' \cos i_\Delta \pi = -f_\Delta + \frac{\bar{\omega}^2 - \lambda_{1,r}}{2\Gamma\omega_X} f_\Omega \tag{4.91}$$

where

$$\chi'_\Delta = \chi_\Delta \left(1 + c_{\Delta,XX} \frac{3x^2}{4{g_0}^2}\right)$$

The previous case specifically deals with the case when $\lambda_{1,r} = 0$ and as such, setting the balancing voltage to satisfy (4.91) involves counteracting the effects of the linear elastic coupling and the constrained frequency detuning $\bar{\omega}^2|_{\lambda_{1,r}=0}$. However, (4.91) shows that there are alternatives to linearise and trim the sense response without nullifying the net parametric excitation. These are discussed in what follows.

Nonlinear frequency balancing using parametric pumping voltage

Instead of tuning the parametric pumping voltage to nullify the net parametric excitation using the condition in (4.94), V_λ can be tuned to achieve nonlinear frequency balancing. As discussed in Section 3.5.3, this condition requires matching the parametric excitation amplitude and the frequency detuning, i.e. setting $\bar{\omega}^2 = \lambda_{1,r}$. This simplifies the condition in (4.91) such that $\chi_\Delta{}' \cos i_\Delta \pi = -f_\Delta$, as the balancing voltage only serves to negate the linear elastic coupling due to drive misalignment. In this case, the balancing voltage is independent

of the Coriolis force and as such, closed-loop rate sensing is not applicable. The case where the net parametric excitation is nullified $(\lambda_{1,r} = 0)$ in conjunction with frequency matching $(\bar{\omega}^2 = 0)$ as investigated in Section 4.3.5 is one way nonlinear frequency balancing is achieved. The nonlinear frequency imbalance is defined as:

$$\lambda_{1,r} - \bar{\omega}^2 = -2{\omega_m}^2 \Delta_m \cos 4\Theta_\omega - \frac{1}{4}[3(\gamma_0 - \kappa_0) + (\gamma_\lambda - \kappa_\lambda) + 3(\gamma_\Delta - \kappa_\Delta)]\frac{x^2}{{g_0}^2} \tag{4.101}$$

Comparing this against the constrained frequency detuning $\bar{\omega}^2|_{\lambda_{1,r}=0}$ in (4.95) shows that the nonlinear frequency imbalance is defined in an identical manner as $-\bar{\omega}^2|_{\lambda_{1,r}=0}$. However, without nullifying the net parametric excitation, the parametric pumping voltage amplitude V_λ is not constrained. The parametric pumping voltage can be tuned to nullify the nonlinear frequency imbalance in (4.101).

To ensure $\lambda_{1,r} - \bar{\omega}^2 = 0$, V_λ must be adjusted to tune the nonlinear stiffness coefficients γ_λ and κ_λ in (4.101) to achieve nonlinear frequency balancing at a selected drive amplitude. However, from (4.101) it is clear this implementation is subjected to several restrictions, as certain conditions can lead to drive amplitudes which are too large or small for practical implementation, similar to the case for frequency matching without involving the balancing voltage as investigation in Section 4.3.4. The conditions for practical nonlinear frequency balancing are the same as those identified in Table 4.3, which are:

- Since $\gamma_0 \leq \kappa_0, \gamma_\lambda \leq \kappa_\lambda, \gamma_\Delta \leq \kappa_\Delta$, $\lambda_{1,r} - \bar{\omega}^2 = 0$ is only possible for drive misalignments such that $\cos 4\Theta_\omega > 0$
- Δ_m or $\cos 4\Theta_\omega$ must be sufficiently small
- The electrodes are sufficiently discontinuous to allow for different drive amplitude dependencies of the frequencies ${\omega_X}^2$ and ${\omega_Y}^2 + \lambda_{1,r}$, thus enabling these frequencies to coincide and achieve nonlinear frequency balancing at a specific drive amplitude. As exception to this is when $\Delta_m \cos 4\Theta_\omega = 0$, where electrode continuity allows nonlinear frequency balancing for a wide range of drive amplitudes.

Direct application without parametric pumping voltage

The present approach can also be implemented in the absence of parametric pumping voltage, in which case the condition in (4.91) reduces to:

$$\chi'_{\Delta} \cos i_{\Delta}\pi = -f_{\Delta} - \frac{\left(\lambda_{1,r} - \bar{\omega}^2\right)|_{V_\lambda=0}}{2\Gamma\omega_X} f_{\Omega} \tag{4.102}$$

where $\left(\lambda_{1,r} - \bar{\omega}^2\right)|_{V_\lambda=0}$ is the nonlinear frequency imbalance in the absence of the parametric pumping voltage, equivalent to (4.101) when $\gamma_\lambda = \kappa_\lambda = 0$.

In contrast to the previous case where nonlinear frequency balancing is achieved, the presence of the nonlinear frequency imbalance in (4.102) ensures that the balancing voltage is rate-dependent and can be used for closed-loop rate sensing. Similar to the case with nullified parametric excitation in (4.98), the closed-loop rate sensitivity amplifies as the magnitude of the nonlinear frequency imbalance $\left(\lambda_{1,r} - \bar{\omega}^2\right)|_{V_\lambda=0}$ increases.

This implementation offers a simplified voltage distribution while avoiding the restrictions associated with using the parametric pumping voltage for nonlinear frequency balancing.

4.6. Summary and conclusions

This chapter considers an approach to enhance the rate sensing behaviour of ring based CVGs with basic electrostatic configuration as discussed in Chapter 3. The main aim is to replicate the sensor output for a linear, ideal/trimmed device and the approach used involves: i) modifying the electrostatic configuration to nullify the net parametric excitation; ii) linearising and trimming the rate output; and iii) eliminating the quadrature output.

To nullify the net parametric excitation, the voltage distribution for the basic electrostatic configuration is updated to include a harmonic parametric pumping voltage component, which generates a linear parametric excitation in antiphase with the self-induced parametric excitation. In addition to negating the self-induced parametric excitation, the parametric pumping voltage reduces the difference in the softening rates between the drive and sense modes as the drive amplitude increases. The main advantage is that the nonlinear drive amplitude dependence of the rate sensitivity and bias rate is suppressed compared to the basic electrostatic configuration. This suppression is most significant in devices implementing 8 continuous electrodes, or 16 or 32 discontinuous electrodes because the frequency detuning is insensitive to drive amplitude. To trim the rate output, frequency matching of the drive and sense modes must also be achieved. For the 8 electrode configuration, it is found that unless the electrodes are continuous, frequency matching and rate output trimming can only be achieved at specific drive amplitudes determined by the magnitude of the imperfection, drive misalignment and electrode span. Depending on the interactions between these quantities the drive amplitudes to achieve frequency matching can be too small or large for practical implementation. To ensure that the quadrature output is also nullified, the linear elastic

coupling force must be nullified, in addition to frequency matching and nullifying the net parametric excitation. These conditions cannot be simultaneously achieved for a continuous electrode distribution unless the device is perfect. To address these restrictions, the electrostatic forces are modified by updating the electrostatic configuration.

A key contribution of this chapter is the development of a general framework to tailor the form of the electrostatic forces using strategic selections of voltage distributions and electrode number. This framework is used to linearise and trim the rate output while nullifying the quadrature sense output at a selected drive amplitude, regardless of the magnitude and location of imperfections and electrode span. This framework considers the capacitance and voltage contributions from electrode to electrode and identifies expressions for the electrostatic forces in terms of the voltage components. This representation of the electrostatic forces allows the resulting form of electrostatic force to be controlled by selecting the voltages applied to each electrode. By identifying the desired form of electrostatic force to ensure trimmed rate and quadrature outputs, the framework provides useful insight into the voltage distributions that achieve this aim.

To replicate the rate and quadrature outputs of a linear, ideal/trimmed device, the balance of forces for the sense mode is analysed, with the aim of identifying electrostatic force conditions which can be applied to address any undesirable force imbalances. It is found that the forces stemming from the linear elastic coupling and the nonlinear frequency imbalance cause the sense response to deviate from that of a linear, ideal/trimmed device. To ensure the forces acting on the sense mode are balanced and the sensor output is trimmed, electrostatic forces are applied directly to the sense mode. Harmonic balancing force components are imposed on the electrostatic configuration to generate direct sense forces that are in phase or antiphase with the linear elastic coupling force, in addition to the parametric pumping voltage used to negate the self-induced parametric excitation. By adjusting the balancing voltage amplitude to counteract the linear elastic coupling and nonlinear frequency imbalance, the quadrature response is eliminated while restoring the linearity and trimmed state of the rate output. In this implementation, it is found that the square of the required balancing voltage amplitude is proportional to the angular rate, thus enabling closed-loop rate sensing. It is also found that the closed loop rate sensitivity and bias rate performances significantly improve with larger frequency detuning, in direct contrast to the open loop rate sensing without balancing voltage. The effects of the implementation of the balancing voltage were also demonstrated by comparing the open loop rate sensitivity with and without the balancing voltage when net parametric excitation is nullified. The results show that the balancing voltage trims the rate sensitivity and significantly improves the linearity of the rate sensitivity. It has also been shown that the applicability of the balancing voltage is not restricted to the case where net

parametric excitation is nullified. The balancing voltage can also be used to restore the sense response in a linear, ideal/trimmed device for cases of with and without nonlinear frequency balancing.

5. PARAMETRIC AMPLIFICATION FOR RATE SENSING PERFORMANCE ENHANCEMENT

5.1. Introduction

Chapter 3 shows the potential of parametric excitation for enhancing the rate sensitivity enhancement beyond what is expected of a linear, trimmed device. This is a purely nonlinear effect as the maximum attainable rate sensitivity enhancement depends on the self-induced parametric excitation. However, this form of rate sensitivity enhancement is accompanied by the presence of quadrature errors and bias rates. On the other hand, Chapter 4 investigates practical approaches where the sense dynamics can replicate linear, trimmed behaviour at increased drive amplitudes, but the rate sensitivity enhancement described in Chapter 3 is not attained in this case. As such, it is clear that the parametric excitation is key to rate sensitivity enhancement and it is of practical interest to identify cases and approaches where rate output enhancement can be achieved while retaining nonlinear trimming of the rate and quadrature outputs.

This chapter aims to investigate the potential of using electrostatic forces to amplify the rate sensitivity beyond that of the linear, trimmed case while avoiding the introduction of quadrature errors and bias rates using key results identified in Chapter 4. The phase generality of the parametric excitation and its effects on the rate output amplification are considered, based on which the linear and quadratic electrostatic forces are exploited to generate the phase tuneable parametric excitation.

Section 5.2 discusses the general form of the sense dynamics subjected to phase-variable parametric excitation. Accounting for the phase variability of the parametric excitation, the balance of the various sense mode forces is investigated in a manner similar to the case without this phase variability in Section 4.5.1. Force conditions are identified where the parametric excitation can give rise to rate output amplification, hence rate sensitivity enhancement, while retaining trimmed sense response. Based on the force conditions identified, Sections 5.3 and 5.4 investigate feasible electrostatic configurations to achieve the targeted form of the electrostatic forces using the general framework developed in Section 4.4. Section 5.3 is based on using linear electrostatic forces to generate the required parametric excitation in a manner similar to Chapter 4, but with a tuneable phase. The trimming approach implemented is similar to that investigated in Section 4.5, involving the use of rate-dependent balancing voltage. Section 5.4 is based on using quadratic electrostatic forces for this purpose, and an alternative trimming approach involving aligning the drive forces and nonlinear frequency balancing is investigated. For both approaches, equations of motion are developed for the corresponding

electrostatic configurations chosen, based on which the drive and sense mode dynamics are analysed to identify the voltage conditions required to trim and amplify the rate output and nullify the quadrature output. Results obtained using FE methods are also included to validate the effectiveness of the approaches. The advantages and disadvantages of these approaches are then discussed and compared.

5.2. Effects of parametric excitation phase on sense dynamics

This section investigates an extension of the mathematical formulation of the parametric excitation on the sense mode in Section 4.2 to include phase-tuneable parametric excitation. The resulting sense dynamics from this phase variation is then investigated. Based on the sense dynamics, the balance of the sense mode forces is considered to identify the required force conditions to achieve amplified rate output, while retaining nullified quadrature output.

5.2.1. General sense response with phase-tuneable parametric excitation

The general form of the sense mode subjected to parametric excitation has been shown in (4.1), revisited here:

$$\ddot{Y} + 2\Gamma\dot{Y} + \left[{\omega_Y}^2 + 2\lambda_{1,r}\cos 2(\omega t + \phi_x)\right]Y = f_\Omega \sin(\omega t + \phi_x) + f_\Delta \cos(\omega t + \phi_x) \tag{4.1}$$

Noting that $X = x\cos(\omega t + \phi_x)$, the parametric excitation phase is twice the drive mode oscillation phase. Since this form of parametric excitation is self-induced and the contributing bias voltage is constant, this phase relationship between the drive displacement and the parametric excitation is fixed.

The phase of the parametric excitation has been shown to have significant impacts on the sense response [50]. To demonstrate the applicability of phase-tuneable parametric excitation on the sense mode, the parametric excitation term in (4.1) is modified, giving the following form of the sense equation of motion:

$$\ddot{Y} + 2\Gamma\dot{Y} + \left[{\omega_Y}^2 + 2\lambda_{1,r}\cos 2(\omega t + \phi_x) + 2\lambda_{2,r}\sin 2(\omega t + \phi_x)\right]Y = f_\Omega \sin(\omega t + \phi_x) + f_\Delta \cos(\omega t + \phi_x) \tag{5.1}$$

where an additional parametric excitation component with amplitude $2\lambda_{2,r}$ has been introduced within the sense stiffness modulation. This parametric excitation component acts in quadrature relative to the self-induced parametric excitation, serving to enable phase-tuning of the net parametric excitation when the amplitude $2\lambda_{2,r}$ is adjusted.

In principle, the form of phase-tuneable parametric excitation shown in (5.1) is already imposed on the sense mode for the basic electrostatic configuration case, where (3.33) is the result for the averaged sense response of (5.1) when $\lambda_1 = \lambda_{1,r}$ and $\lambda_2 = \lambda_{2,r}$ due to resonant operation. However in this case, as is shown from (3.40), due to the proportionality of λ_2 to χ, λ_2 is associated with the drive voltage so it is negligible compared to the self-induced parametric excitation. On the other hand, setting large values of the drive voltage amplitude V_{AC} to tune $\lambda_{2,r}$ is impractical as this can result in significantly increased drive amplitudes, thus risking pull-in.

Using the averaging method on (5.1) gives the following averaged force balance:

$$\begin{bmatrix} -{\omega_X}^2 + {\omega_Y}^2 + \lambda_{1,r} & -2\Gamma\omega_X - \lambda_{2,r} \\ -2\Gamma\omega_X + \lambda_{2,r} & {\omega_X}^2 - {\omega_Y}^2 + \lambda_{1,r} \end{bmatrix} \bar{\boldsymbol{y}} = \begin{bmatrix} f_\Delta \\ f_\Omega \end{bmatrix} \tag{5.2}$$

with the averaged sense amplitude components

$$\bar{\boldsymbol{y}} = -\frac{\begin{bmatrix} {\omega_X}^2 - {\omega_Y}^2 + \lambda_{1,r} & 2\Gamma\omega_X + \lambda_{2,r} \\ 2\Gamma\omega_X - \lambda_{2,r} & -{\omega_X}^2 + {\omega_Y}^2 + \lambda_{1,r} \end{bmatrix} \begin{bmatrix} f_\Delta \\ f_\Omega \end{bmatrix}}{{P_{1,r}}^2 - P_{2,r}^+ P_{2,r}^-} \tag{5.3}$$

where $P_{2,r}^+ P_{2,r}^- < {P_{1,r}}^2$ and $P_{2,r}^\pm$ are:

$$P_{2,r}^\pm = \left({\lambda_{1,r}}^2 + {\lambda_{2,r}}^2\right)^{\frac{1}{2}} \pm \left(-{\omega_X}^2 + {\omega_Y}^2\right) \tag{5.4}$$

and $P_{1,r}$ has been defined in (3.62), given by $P_{1,r} = 2\Gamma\omega_X$.

From (5.2) and (5.3), it is clear that the parametric excitation amplitude components $\lambda_{1,r}$ and $\lambda_{2,r}$ have distinct effects. The parametric excitation component $\lambda_{1,r}$ interacts with the frequency detuning while $\lambda_{2,r}$ interacts with the linear damping. From (5.4), $\lambda_{2,r}$ also increases the product $P_{2,r}^+ P_{2,r}^-$ compared to the purely self-induced parametric excitation case, thus promoting parametric resonance. These suggest that the $\lambda_{2,r}$ parametric excitation component can be used modify the effective damping and Q factor, thus amplifying the sense amplitude.

For the case where the self-induced parametric excitation is negated, i.e. $\lambda_{1,r} = 0$ and the drive and sense frequencies are matched, (5.3) simplifies to:

$$\bar{\boldsymbol{y}}|_{\omega_X=\omega_Y,\lambda_{1,r}=0} = -\begin{bmatrix} \dfrac{f_\Omega}{2\Gamma\omega_X - \lambda_{2,r}} \\ \dfrac{f_\Delta}{2\Gamma\omega_X + \lambda_{2,r}} \end{bmatrix} \tag{5.5}$$

The contributions of the Coriolis and linear elastic coupling forces to the rate and quadrature outputs are decoupled in this case. Also, when $\lambda_{2,r} > 0$, the rate output amplifies (limited by $|\lambda_{2,r}| < 2\Gamma\omega_X$) beyond its linear, trimmed form $y_0^l \cos\phi_{yx,0}^l$ (see (3.41)), while the quadrature output attenuates. The opposite is the case when $\lambda_{2,r} < 0$ and is undesirable. Being the result of parametric excitation, these behaviours are known as parametric amplification and attenuation [51].

The parametric amplification and attenuation of the sense amplitude components are shown in Figure 5.1 for a system where $\lambda_{1,r} = 0$, $\omega_X = \omega_Y = 11.3\ kHz$, $\Gamma = 56.5\ Hz$ and $f_\Omega = 64\ mm/s$. The variations of the rate output $(y\cos\phi_{yx})$ and quadrature output $(y\sin\phi_{yx})$ against the normalised parametric excitation amplitude $\lambda_{2,r}/(2\Gamma\omega_X)$ are shown for linear elastic coupling force amplitudes of $f_\Delta/f_\Omega = 0.2, 0.5$ and 1.

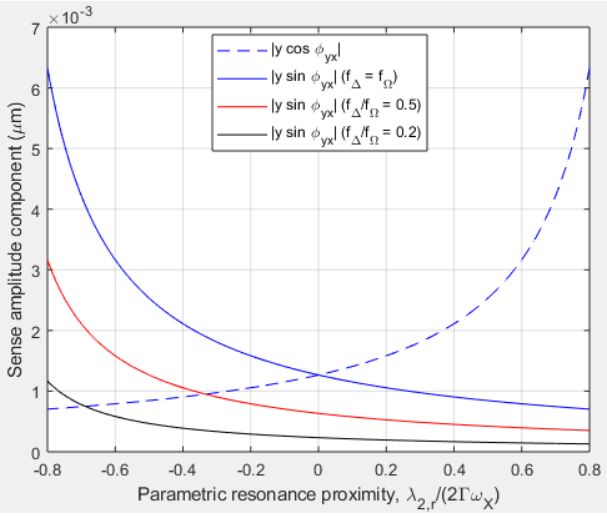

Figure 5.1: Effect of parametric excitation amplitude component $\lambda_{2,r}$ on the rate and quadrature outputs for the case of frequency matching and negated self-induced parametric excitation

The opposite effects of the parametric excitation amplitude component $\lambda_{2,r}$ on the rate and quadrature outputs in Figure 5.1 is clear, where $\lambda_{2,r} > 0$ is desirable for quadrature output suppression and rate output and rate sensitivity enhancement. When $\lambda_{2,r} < 0$, the quadrature output growth is suppressed for smaller linear elastic coupling force amplitudes, which can be achieved with improved drive electrode alignment. Based on these results, it can be concluded that a large, positive $\lambda_{2,r}$ in conjunction with a small (or nullified) linear elastic coupling force amplitude $|f_\Delta|$ is most desirable.

5.2.2. Balance of averaged forces on sense mode for parametric amplification of rate output

Based on (5.5) and the results shown in Figure 5.1, the targeted form of the sense amplitude components is:

$$\bar{\boldsymbol{y}}_{\boldsymbol{\lambda 2}} = \begin{bmatrix} -\dfrac{f_\Omega}{2\Gamma\omega_X - \lambda_{2,r}} \\ 0 \end{bmatrix} \tag{5.6}$$

yielding a rate sensitivity of:

$$S = -\frac{G_\Omega x \omega_X}{2\Gamma\omega_X - \lambda_{2,r}} \tag{5.7}$$

To ensure that the averaged force balance in (5.2) is satisfied at $\bar{\boldsymbol{y}} = \bar{\boldsymbol{y}}_{\boldsymbol{\lambda 2}}$, an additional balancing force component can be incorporated into the right side of (5.2). Including this balancing force in (5.2) and replacing $\bar{\boldsymbol{y}}$ with $\bar{\boldsymbol{y}}_{\boldsymbol{\lambda 2}}$ gives the following modified averaged force balance:

$$\begin{bmatrix} -{\omega_X}^2 + {\omega_Y}^2 + \lambda_{1,r} & -2\Gamma\omega_X - \lambda_{2,r} \\ -2\Gamma\omega_X + \lambda_{2,r} & {\omega_X}^2 - {\omega_Y}^2 + \lambda_{1,r} \end{bmatrix} \bar{\boldsymbol{y}}_{\boldsymbol{\lambda 2}} = \begin{bmatrix} f_\Delta \\ f_\Omega \end{bmatrix} + \bar{\boldsymbol{f}}_{\boldsymbol{\lambda 2}} \tag{5.8}$$

where $\bar{\boldsymbol{f}}_{\boldsymbol{\lambda 2}}$ is a force vector representing the balancing force components which must be applied to the sense mode to fix the sense amplitude components at $\bar{\boldsymbol{y}} = \bar{\boldsymbol{y}}_{\boldsymbol{\lambda 2}}$. $\bar{\boldsymbol{f}}_{\boldsymbol{\lambda 2}}$ is then solved for in (5.8), in a manner similar to $\bar{\boldsymbol{f}}_{\boldsymbol{0}}^{\boldsymbol{l}}$ in (4.60). This gives the following:

$$\bar{\boldsymbol{f}}_{\boldsymbol{\lambda 2}} = \begin{bmatrix} f_{\lambda 2} \\ 0 \end{bmatrix} = \begin{bmatrix} -f_\Delta + \dfrac{{\omega_X}^2 - {\omega_Y}^2 - \lambda_{1,r}}{2\Gamma\omega_X - \lambda_{2,r}} f_\Omega \\ 0 \end{bmatrix} \tag{5.9}$$

Substituting (5.9) into (5.8) then shows that the corrected force balance in (5.8) is the averaged result of:

$$\begin{aligned} \ddot{Y} + 2\Gamma\dot{Y} + \left[{\omega_Y}^2 + 2\lambda_{1,r}\cos 2(\omega t + \phi_x) + 2\lambda_{2,r}\sin 2(\omega t + \phi_x)\right] Y \\ = f_\Omega \sin(\omega t + \phi_x) + f_\Delta \cos(\omega t + \phi_x) + f_{\lambda 2}\cos(\omega t + \phi_x) \end{aligned} \tag{5.10}$$

This is the targeted form of the sense equation of motion for rate sensitivity enhancement while retaining nullified bias rate and quadrature error.

f_0^l in (4.61) is a specific case of $f_{\lambda 2}$ when $\lambda_{2,r} = 0$, in which case (5.10) is of similar form as the targeted form of the sense equation of motion in (4.62). These similarities show that the presence of the quadrature parametric excitation amplitude component $\lambda_{2,r}$ does not alter the phase of the balancing force required to balance the sense mode. Comparing (5.10) and (4.62), the balancing forces $f_{\lambda 2}\cos(\omega t + \phi_x)$ and $f_0^l \cos(\omega t + \phi_x)$ have identical phases, acting in phase/antiphase with the linear elastic coupling force. Through the use of control loops, the balancing force amplitude $f_{\lambda 2}$ can be similarly tuned to eliminate the quadrature output. However, the required balancing force amplitude is modified by the parametric excitation component $\lambda_{2,r}$.

Similar to f_0^l, $f_{\lambda 2}$ is also composed of two distinct parts: i) a rate-independent component to counteract the linear elastic coupling force f_Δ; and ii) a rate-dependent component to counteract the nonlinear frequency imbalance ${\omega_X}^2 - {\omega_Y}^2 - \lambda_{1,r}$. As such, the balancing force amplitude $f_{\lambda 2}$ can be similarly used for closed-loop rate sensing. An exception to this is when nonlinear frequency balancing applies $\left(\lambda_{1,r} = {\omega_X}^2 - {\omega_Y}^2\right)$, in which case the balancing force only serves to negate the linear elastic coupling force.

5.3. Linear parametric amplification

In this section, the use of the linear electrostatic forces for phase-tuneable parametric excitation is investigated. Using the general framework developed in Section 4.4, a suitable voltage distribution is identified to generate the required electrostatic forces and achieve the targeted form of the sense equation of motion identified in Section 5.2.2. Based on the chosen voltage distribution, the resulting equations of motion are developed and the modal dynamics are analysed to identify the necessary voltage conditions to enhance rate sensitivity, while retaining trimmed rate output and nullified quadrature output. The potential of using the chosen electrostatic configuration for rate sensing is investigated for the cases of dual mode rate sensing with both open-loop and closed-loop operations, and single mode rate sensing without the closed-loop operation. For the case without involving closed-loop rate sensing, the conditions to ensure only single-mode rate sensing in open loop are investigated. For the case involving closed-loop rate sensing, the closed-loop rate sensing performance is assessed in terms of the rate sensitivity and bias rate, and the effects of the phase-tuneable parametric excitation on the closed-loop and open-loop rate sensing performance are investigated. FE results are also included to validate the theoretical results and the effectiveness of the proposed approach to amplify rate output.

5.3.1. Selection of voltage distribution

Linear parametric excitation has been achieved in the equations of motion (4.69) for linearisation and trimming of the rate output. The linear parametric excitation appears in the coefficient matrix of the linear modal coordinates vector, $\bar{\bar{\boldsymbol{\eta}}}_{\mathbf{1}}(t)$. The definition of $\bar{\bar{\boldsymbol{\eta}}}_{\mathbf{1}}(t)$ in (4.73) is revisited here:

$$\bar{\bar{\boldsymbol{\eta}}}_{\mathbf{1}}(t) = \begin{bmatrix} {\omega_{0,\lambda,\Delta}}^2 & 0 \\ 0 & {\omega_{0,\lambda,\Delta}}^2 \end{bmatrix} + {\omega_m}^2 \begin{bmatrix} \Delta_m \cos 4\Theta_\omega & \Delta_m \sin 4\Theta_\omega \\ \Delta_m \sin 4\Theta_\omega & -\Delta_m \cos 4\Theta_\omega \end{bmatrix} + \begin{bmatrix} {\omega_\lambda}^2 & 0 \\ 0 & {\omega_\lambda}^2 \end{bmatrix} \cos 2(\omega t + \phi_x) \tag{4.73}$$

where the linear parametric excitation phase is locked at twice the drive mode oscillation phase. The phase of the parametric excitation can be tuned by introducing a $\sin 2(\omega t + \phi_x)$ variation component in $\bar{\bar{\boldsymbol{\eta}}}_{\mathbf{1}}(t)$. Based on this aim, it follows that a simple modification to the conditions in Table 4.7 involving the linear electrostatic force coefficient $A^{fY}_{X^0Y^1}$ in (4.45b) is required. The modified conditions for the required voltage distribution for this purpose are shown in Table 5.1. Similar to Section 4.5, the following considers the case of 8 evenly distributed electrodes.

Table 5.1: Constraints for the coefficients of the voltage squared distribution, $\xi^{\pm}_{m_V}$, $\zeta^{\pm}_{m_V}$ based on conditions to trim and amplify the rate output for the case of 8 inner/outer electrodes

	Electrostatic force conditions	**Voltage squared distribution constraints**
1	$A^{fY}_{X^0Y^0} \propto \cos(\omega t + \phi_x)$	$\zeta_2^+ - \zeta_2^- - \zeta_6^+ + \zeta_6^- \propto \cos(\omega t + \phi_x)$
2	$\int_0^{\frac{2\pi}{\omega}} A^{fY}_{X^0Y^1} \cos n(\omega t + \phi_x)\, dt \neq 0$ only for $n = 0,2$	$\int_0^{\frac{2\pi}{\omega}} (\xi_0^+ + \xi_0^- + \xi_4^+ + \xi_4^- + \xi_8^+ + \xi_8^-) \cos n(\omega t + \phi_x)\, dt \neq 0$ only for $n = 0,2$
3	$\int_0^{\frac{2\pi}{\omega}} A^{fY}_{X^0Y^1} \sin n(\omega t + \phi_x)\, dt \neq 0$ only for $n = 2$	$\int_0^{\frac{2\pi}{\omega}} (\xi_0^+ + \xi_0^- + \xi_4^+ + \xi_4^- + \xi_8^+ + \xi_8^-) \sin n(\omega t + \phi_x)\, dt \neq 0$ only for $n = 2$
4	$A^{fY}_{X^0Y^1} = A^{fX}_{X^1Y^0}$	$\xi_4^+ + \xi_4^- = 0$
5	$A^{fX}_{X^0Y^0} \propto \cos \omega t$	$\xi_2^+ - \xi_2^- + \xi_6^+ - \xi_6^- \propto \cos \omega t$

Compared to Table 4.7, only the third condition has been modified to include the aforementioned $\sin 2(\omega t + \phi_x)$ variation component in $\bar{\bar{\boldsymbol{\eta}}}_{\mathbf{1}}(t)$. As such, a simple

modification to the voltage distribution in (4.65a) and (4.65b) is sufficient to satisfy all the conditions in Table 5.1. This gives the following chosen voltage distribution:

$$V^{+}[\theta_0(i)] = V_0 + V_\lambda \cos\left(\omega t + \phi_x + \frac{\phi_\lambda}{2}\right) + V_\Delta \cos\left(\frac{\omega t + \phi_x + i_\Delta \pi}{2}\right)\cos\theta_0(i) + V_\Delta \cos\left(\frac{\omega t + \phi_x + i_\Delta \pi}{2}\right)\sin\theta_0(i) + V_{AC}\cos\omega t \cos 2\theta_0(i) \tag{5.11a}$$

$$V^{-}[\theta_0(i)] = V_0 - V_\lambda \cos\left(\omega t + \phi_x + \frac{\phi_\lambda}{2}\right) + V_\Delta \sin\left(\frac{\omega t + \phi_x + i_\Delta \pi}{2}\right)\cos\theta_0(i) + V_\Delta \sin\left(\frac{\omega t + \phi_x + i_\Delta \pi}{2}\right)\sin\theta_0(i) - V_{AC}\cos\omega t \cos 2\theta_0(i) \tag{5.11b}$$

where ϕ_λ is the linear parametric excitation phase. The voltage distribution in (4.65a) and (4.65b) is a specific case of (5.11a) and (5.11b) where $\phi_\lambda = -\pi$. Similar to the previous case, V_Δ and i_Δ are the balancing voltage amplitude and phase index which are tuned to nullify the quadrature output. However, in the present scheme, the parametric pumping voltage amplitude V_λ is not set to negate the self-induced parametric excitation. Instead, in conjunction with the phase ϕ_λ, it is tuned to adjust the parametric excitation force amplitude.

Based on (5.11a) and (5.11b), the nonzero voltage squared distribution coefficients in (4.52) are given by:

$$\xi_0^{\pm} = {V_0}^2 + \frac{{V_\lambda}^2}{2} + \frac{{V_\Delta}^2}{2} + \frac{{V_{AC}}^2}{4} \pm \left[2V_0 V_\lambda \cos\left(\omega t + \phi_x + \frac{\phi_\lambda}{2}\right) + \frac{{V_\Delta}^2}{2}\cos(\omega t + \phi_x + i_\Delta \pi)\right] + \frac{{V_\lambda}^2}{2}\cos[2(\omega t + \phi_x) + \phi_\lambda] + \frac{{V_{AC}}^2}{4}\cos 2\omega t \tag{5.12a}$$

$$\xi_1^{+} = 2V_\Delta \cos\left(\frac{\omega t + \phi_x + i_\Delta \pi}{2}\right)\left[V_0 + V_\lambda \cos\left(\omega t + \phi_x + \frac{\phi_\lambda}{2}\right) + \frac{V_{AC}}{2}\cos\omega t\right] \tag{5.12b}$$

$$\zeta_1^{+} = 2V_\Delta \cos\left(\frac{\omega t + \phi_x + i_\Delta \pi}{2}\right)\left[V_0 + V_\lambda \cos\left(\omega t + \phi_x + \frac{\phi_\lambda}{2}\right) - \frac{V_{AC}}{2}\cos\omega t\right] \tag{5.12c}$$

$$\xi_1^{-} = 2V_\Delta \sin\left(\frac{\omega t + \phi_x + i_\Delta \pi}{2}\right)\left[V_0 - V_\lambda \cos\left(\omega t + \phi_x + \frac{\phi_\lambda}{2}\right) - \frac{V_{AC}}{2}\cos\omega t\right] \tag{5.12d}$$

$$\zeta_1^{-} = 2V_\Delta \sin\left(\frac{\omega t + \phi_x + i_\Delta \pi}{2}\right)\left[V_0 - V_\lambda \cos\left(\omega t + \phi_x + \frac{\phi_\lambda}{2}\right) + \frac{V_{AC}}{2}\cos\omega t\right] \tag{5.12e}$$

$$\xi_2^{\pm} = \pm 2V_0 V_{AC} \cos\omega t + V_\lambda V_{AC}\left[\cos\left(2\omega t + \phi_x + \frac{\phi_\lambda}{2}\right) + \cos\left(\phi_x + \frac{\phi_\lambda}{2}\right)\right] \tag{5.12f}$$

$$\zeta_2^{\pm} = \frac{{V_\Delta}^2}{2}[1 \pm \cos(\omega t + \phi_x + i_\Delta \pi)] \tag{5.12g}$$

$$\xi_3^{+} = \zeta_3^{+} = V_\Delta V_{AC} \cos\left(\frac{\omega t + \phi_x + i_\Delta \pi}{2}\right)\cos\omega t \tag{5.12h}$$

$$\xi_3^{-} = \zeta_3^{-} = -V_\Delta V_{AC} \sin\left(\frac{\omega t + \phi_x + i_\Delta \pi}{2}\right)\cos\omega t \tag{5.12i}$$

$$\xi_4^{\pm} = \frac{{V_{AC}}^2}{4}(1 + \cos 2\omega t) \tag{5.12j}$$

The roles of these voltage squared distribution coefficients in the total electrostatic forces are identical to those in (4.66a) – (4.66j), except for $\xi_0^{\pm}$ in (5.12a). The phase of the 2ω variation term in $\xi_0^{+} + \xi_0^{-}$ can be tuned using ϕ_λ, and is the result of satisfying the third condition in Table 5.1. The coefficients $\xi_0^{\pm}$ are key to generate the targeted phase-tuneable parametric excitation.

5.3.2. Modal dynamics

In the following, equations of motions are developed based on the voltage distribution selected in (5.11a) and (5.11b). Using the same techniques, conditions and approximations on (3.14), (4.14) and (4.69), the resulting equations of motion are analysed to derive the resulting drive and sense dynamics.

Equations of motion

Following the same procedures outlined in Section 4.5.3, the total electrostatic forces stemming from the voltage distribution in (5.11a) and (5.11b) are given by:

$$\begin{bmatrix} f_{U,X} \\ f_{U,Y} \end{bmatrix} = \bar{\boldsymbol{A}}_{\boldsymbol{0}} + \bar{\bar{\boldsymbol{A}}}_{\boldsymbol{1}}\bar{\boldsymbol{q}}_{\boldsymbol{1}} + \bar{\bar{\boldsymbol{A}}}_{\boldsymbol{2}}\bar{\boldsymbol{q}}_{\boldsymbol{2}} + \bar{\bar{\boldsymbol{A}}}_{\boldsymbol{3}}\bar{\boldsymbol{q}}_{\boldsymbol{3}} \tag{5.13}$$

where the vector $\bar{\boldsymbol{A}}_{\boldsymbol{0}}$ and the matrices $\bar{\bar{\boldsymbol{A}}}_{\boldsymbol{1}}$, $\bar{\bar{\boldsymbol{A}}}_{\boldsymbol{2}}$, $\bar{\bar{\boldsymbol{A}}}_{\boldsymbol{3}}$ are given by:

$$\bar{\boldsymbol{A}}_{\boldsymbol{0}} = -\frac{\varepsilon_0}{5\rho\pi h {g_0}^2} j \sin\delta \begin{bmatrix} \xi_2^{+} - \xi_2^{-} \\ \zeta_2^{+} - \zeta_2^{-} \end{bmatrix} \tag{5.14a}$$

$$\overline{\overline{\boldsymbol{A}}}_{\mathbf{1}} = -\frac{2\varepsilon_0}{5\rho\pi h {g_0}^3} j\delta \begin{bmatrix} \xi_0^+ + \xi_0^- & 0 \\ 0 & \xi_0^+ + \xi_0^- \end{bmatrix} \tag{5.14b}$$

$$\begin{aligned} \overline{\overline{\boldsymbol{A}}}_{\mathbf{2}} = -\frac{\varepsilon_0}{20\rho\pi h {g_0}^4} j \Bigg\{ & (9\sin\delta + \sin 3\delta) \begin{bmatrix} \xi_2^+ - \xi_2^- & 0 & 0 \\ 0 & 0 & \zeta_2^+ - \zeta_2^- \end{bmatrix} \\ & + (3\sin\delta - \sin 3\delta) \begin{bmatrix} 0 & 2(\zeta_2^+ - \zeta_2^-) & \xi_2^+ - \xi_2^- \\ \zeta_2^+ - \zeta_2^- & 2(\xi_2^+ - \xi_2^-) & 0 \end{bmatrix} \Bigg\} \end{aligned} \tag{5.14c}$$

$$\begin{aligned} \overline{\overline{\boldsymbol{A}}}_{\mathbf{3}} = -\frac{\varepsilon_0}{20\rho\pi h {g_0}^5} j \Bigg\{ & (12\sin\delta + \sin 4\delta) \begin{bmatrix} \xi_0^+ + \xi_0^- & 0 & 0 & 0 \\ 0 & 0 & 0 & \xi_0^+ + \xi_0^- \end{bmatrix} \\ & + (12\sin\delta - 3\sin 4\delta) \begin{bmatrix} 0 & 0 & \xi_0^+ + \xi_0^- & 0 \\ 0 & \xi_0^+ + \xi_0^- & 0 & 0 \end{bmatrix} \Bigg\} \end{aligned} \tag{5.14d}$$

The coefficients $\xi_0^{\pm}$ dictate the linear electrostatic force coefficient $\overline{\overline{\boldsymbol{A}}}_{\mathbf{1}}$, confirming that the 2ω variation of the linear modal stiffness can be phase-tuned using the parametric pumping voltage phase ϕ_λ (see 5.12(a)), as required.

Incorporating the drive and sense electrostatic forces in (5.13) and the mechanical forces in (4.44) into (4.43a) and (4.43b) gives the following equations of motion:

$$\begin{aligned} & \ddot{\overline{\boldsymbol{q}}}_{\mathbf{1}} + 2\Gamma\dot{\overline{\boldsymbol{q}}}_{\mathbf{1}} + \overline{\overline{\boldsymbol{\eta}}}_{\mathbf{1}}(t)\overline{\boldsymbol{q}}_{\mathbf{1}} + \overline{\overline{\boldsymbol{\eta}}}_{\mathbf{3}}(t)\frac{\overline{\boldsymbol{q}}_{\mathbf{3}}}{{g_0}^2} \\ & \qquad = \Omega\overline{\overline{\boldsymbol{G}}}_{\boldsymbol{\Omega}}\dot{\overline{\boldsymbol{q}}}_{\mathbf{1}} + \overline{\boldsymbol{\chi}}(t) \\ & \qquad + \left[\chi\cos\omega t\,\overline{\overline{\boldsymbol{\eta}}}_{\boldsymbol{\chi}} + \chi_\Delta\cos(\omega t + \phi_x + i_\Delta\pi)\,\overline{\overline{\boldsymbol{\eta}}}_{\boldsymbol{\chi\Delta}}\right]\frac{\overline{\boldsymbol{q}}_{\mathbf{2}}}{{g_0}^2} \end{aligned} \tag{5.15}$$

(5.15) is identical to the equations of motion in (4.69), owing to the similarity of the corresponding voltage distributions. However, due to phase ϕ_λ within the parametric pumping voltage components in (5.11a) and (5.11b), the modified definition for $\xi_0^{\pm}$ affects $\overline{\overline{\boldsymbol{A}}}_{\mathbf{1}}$ in (5.14b) and $\overline{\overline{\boldsymbol{A}}}_{\mathbf{3}}$ in (5.14d), hence the linear and cubic restoring forces associated with the parametric pumping voltage are phase-modified such that $\overline{\overline{\boldsymbol{\eta}}}_{\mathbf{1}}(t)$ and $\overline{\overline{\boldsymbol{\eta}}}_{\mathbf{3}}(t)$ are modified to:

$$\begin{aligned} \overline{\overline{\boldsymbol{\eta}}}_{\mathbf{1}}(t) = & \begin{bmatrix} {\omega_{0,\lambda,\Delta}}^2 & 0 \\ 0 & {\omega_{0,\lambda,\Delta}}^2 \end{bmatrix} + {\omega_m}^2 \begin{bmatrix} \Delta_m\cos 4\Theta_\omega & \Delta_m\sin 4\Theta_\omega \\ \Delta_m\sin 4\Theta_\omega & -\Delta_m\cos 4\Theta_\omega \end{bmatrix} \\ & - \begin{bmatrix} {\omega_\lambda}^2 & 0 \\ 0 & {\omega_\lambda}^2 \end{bmatrix} \cos[2(\omega t + \phi_x) + \phi_\lambda] \end{aligned} \tag{5.16}$$

$$\overline{\overline{\boldsymbol{\eta}}}_{\boldsymbol{3}}(t) = \begin{bmatrix} \gamma_{0,\lambda,\Delta} & 0 & \kappa_{0,\lambda,\Delta} & 0 \\ 0 & \kappa_{0,\lambda,\Delta} & 0 & \gamma_{0,\lambda,\Delta} \end{bmatrix} + \begin{bmatrix} \gamma_\lambda & 0 & \kappa_\lambda & 0 \\ 0 & \kappa_\lambda & 0 & \gamma_\lambda \end{bmatrix} \cos[2(\omega t + \phi_x) + \phi_\lambda] \tag{5.17}$$

The phase ϕ_λ also affects $\overline{\overline{\boldsymbol{\eta}}}_{\boldsymbol{3}}(t)$, indicating that the nonlinear parametric excitation due to the cubic restoring forces is also affected by this phase.

The remaining terms in (5.15) have been defined in Sections 3.3.2, 4.3.2 and 4.5.3.

Drive dynamics

From (5.15), the single degree-of-freedom approximation of the drive equation of motion is given by:

$$\begin{aligned} \ddot{X} + 2\Gamma\dot{X} + \left\{{\omega_{0,\lambda,\Delta}}^2 + {\omega_m}^2\Delta_m \cos 4\Theta_\omega - {\omega_\lambda}^2 \cos[2(\omega t + \phi_x) + \phi_\lambda]\right\}X \\ + \left\{\gamma_{0,\lambda,\Delta} + \gamma_\lambda \cos[2(\omega t + \phi_x) + \phi_\lambda]\right\}\frac{X^3}{{g_0}^2} \\ = \chi \cos \omega t \left(1 + c_{XX}\frac{X^2}{{g_0}^2}\right) \end{aligned} \tag{5.18}$$

Applying the averaging method on (5.18) gives the following results for the drive resonant frequency and the corresponding drive amplitude:

$${\omega_X}^2 = {\omega_{0,\lambda,\Delta}}^2 + {\omega_m}^2\Delta_m \cos 4\Theta_\omega - \frac{{\omega_\lambda}^2}{2}\cos\phi_\lambda + \left(\frac{3}{4}\gamma_{0,\lambda,\Delta} + \frac{1}{2}\gamma_\lambda \cos\phi_\lambda\right)\frac{x^2}{{g_0}^2} \tag{5.19}$$

$$x_r = \frac{\chi\left(1 + c_{XX}\frac{{x_r}^2}{4{g_0}^2}\right)}{2\Gamma_X\omega_X} \tag{5.20}$$

where Γ_X is the effective drive damping coefficient, given by:

$$\Gamma_X = \Gamma - \frac{\frac{{\omega_\lambda}^2}{2}\sin\phi_\lambda - \gamma_\lambda \sin\phi_\lambda \frac{x^2}{4{g_0}^2}}{2\omega_X} \tag{5.21}$$

The drive frequency in (5.19) shows that the linear and nonlinear softening of the drive mode depend on the parametric pumping voltage phase ϕ_λ. When $\cos\phi_\lambda > 0$, both linear and nonlinear softening of the drive mode are strengthened as the drive frequency ω_X decreases. The opposite applies when $\cos\phi_\lambda < 0$.

The resonant drive amplitude x_r in (5.20), unlike the previous cases, is subjected to a variable effective damping Γ_X, which also varies the resulting Q factor. Γ_X can be tuned using the parametric pumping voltage, provided that $\sin\phi_\lambda \neq 0$. This damping variability does not occur for the previous electrostatic configurations because ϕ_λ is set at $-\pi$ resulting in $\sin\phi_\lambda = 0$, or $V_\lambda = 0$ for the basic electrostatic configuration. From (5.21), the following are deduced:

- when $\sin\phi_\lambda > 0$, parametric amplification of drive response occurs
- when $\sin\phi_\lambda < 0$, parametric attenuation of drive response occurs

The former case is desirable for the implementation of the AGC, as a larger drive amplitude can be attained using smaller drive voltages, where $\phi_\lambda = \pi/2$ yields maximum parametric amplification.

Sense dynamics

The approximated sense equation of motion from (5.15) is given by:

$$\begin{aligned}\ddot{Y} + 2\Gamma\dot{Y} + \Bigg\{ & {\omega_{0,\lambda,\Delta}}^2 - {\omega_m}^2\Delta_m \cos 4\Theta_\omega \\ & - \left({\omega_\lambda}^2 - \kappa_\lambda \frac{X^2}{{g_0}^2}\right)\cos[2(\omega t + \phi_x) + \phi_\lambda] + \kappa_{0,\lambda,\Delta}\frac{X^2}{{g_0}^2} \\ & - \frac{\chi c_{XY}}{g_0}\cos\omega t\,\frac{X}{g_0}\Bigg\} Y \\ & = -G_\Omega \Omega\dot{X} - {\omega_m}^2\Delta_m \sin 4\Theta_\omega\, X \\ & + \chi_\Delta \cos(\omega t + \phi_x + i_\Delta\pi)\left(1 + c_{\Delta,XX}\frac{X^2}{{g_0}^2}\right)\end{aligned} \tag{5.22}$$

where $\omega = \omega_X$. Using the averaging method on (5.22) then gives the following averaged force balance:

$$\begin{bmatrix} -\bar{\omega}^2 + \lambda_{1,r} & -2\Gamma\omega_X - \lambda_{2,r} \\ -2\Gamma\omega_X + \lambda_{2,r} & \bar{\omega}^2 + \lambda_{1,r} \end{bmatrix}\bar{\boldsymbol{y}} = \begin{bmatrix} f_\Delta + f_{\lambda 2} \\ f_\Omega \end{bmatrix} \tag{5.23}$$

As discussed in Section 5.2.2, the balancing force amplitude $f_{\lambda 2}$ is tuned to ensure the quadrature output is nullified, yielding a trimmed rate output where $\bar{\boldsymbol{y}} = \bar{\boldsymbol{y}}_{\boldsymbol{\lambda 2}}$. To achieve this, the following condition is imposed on the balancing voltage amplitude V_Δ and phase index i_Δ:

$$f_{\lambda 2} = \chi_\Delta \cos i_\Delta\pi\left(1 + c_{\Delta,XX}\frac{3x^2}{4{g_0}^2}\right) = -f_\Delta - \frac{\lambda_{1,r} - \bar{\omega}^2}{2\Gamma\omega_X - \lambda_{2,r}} f_\Omega \tag{5.24}$$

Using this condition, similar to the previous case with $\lambda_{2,r} = 0$, the balancing voltage amplitude V_Δ can also be used for closed-loop rate sensing as ${V_\Delta}^2$ is linearly related to the Coriolis force f_Ω and angular rate. The closed-loop rate sensitivity increases as the nonlinear frequency imbalance $\lambda_{1,r} - \bar{\omega}^2$ and parametric excitation amplitude component $\lambda_{2,r}$ increase. $\bar{\omega}^2$, $\lambda_{1,r}$ and $\lambda_{2,r}$ are given by:

$$\begin{aligned}\bar{\omega}^2 &= {\omega_X}^2 - {\omega_Y}^2 \\ &= 2{\omega_m}^2 \Delta_m \cos 4\Theta_\omega - \frac{{\omega_\lambda}^2}{2}\cos\phi_\lambda \\ &\quad + \left[3\gamma_{0,\lambda,\Delta} - 2\kappa_{0,\lambda,\Delta} + (2\gamma_\lambda - \kappa_\lambda)\cos\phi_\lambda\right]\frac{x^2}{4{g_0}^2}\end{aligned} \tag{5.25}$$

$$\lambda_{1,r} = -\frac{{\omega_\lambda}^2}{2}\cos\phi_\lambda + \left(\kappa_{0,\lambda,\Delta} + \kappa_\lambda \cos\phi_\lambda\right)\frac{x^2}{4{g_0}^2} \tag{5.26}$$

$$\lambda_{2,r} = \frac{\chi}{4g_0}c_{XY}\frac{x}{g_0} + \left(\frac{{\omega_\lambda}^2}{2} - \kappa_\lambda\frac{x^2}{4{g_0}^2}\right)\sin\phi_\lambda \tag{5.27}$$

$\lambda_{2,r}$ is maximised when the parametric pumping voltage phase is set at $\phi_\lambda = \pi/2$. From (5.7) and (5.24), maximising $\lambda_{2,r}$ amplifies both open and closed-loop rate sensitivities. In this manner, the parametric amplification effect is two-fold. First, the parametric pumping voltage amplifies the resonant drive amplitude by reducing the effective damping in (5.21) through the term ${\omega_\lambda}^2$. The amplified drive amplitude x_r then amplifies the Coriolis force f_Ω, which linearly amplifies the rate output. This linear amplification is further accompanied by the sense parametric amplification due to the enhanced sense Q factor stemming from the parametric excitation amplitude component $\lambda_{2,r}$ in (5.6). This combination of increased f_Ω and $\lambda_{2,r}$ can yield a total rate sensitivity amplification of orders of magnitude without requiring an increase in the drive voltage amplitude.

5.3.3. Single mode rate sensing without closed-loop operation

As discussed in Section 5.2.2 and as shown in (5.24), the nonlinear frequency balancing condition ($\lambda_{1,r} = \bar{\omega}^2$) eliminates the possibility for closed-loop rate sensing as the required balancing voltage amplitude is invariant with the angular rate, serving only to negate the linear elastic coupling force. If there is no linear elastic coupling force ($f_\Delta = 0$), the balancing voltage can be set to zero, simplifying the voltage distribution. The following investigates the conditions to achieve nonlinear frequency balancing, such that the device only operates in open loop.

From (5.25) and (5.26), the nonlinear frequency balancing condition is given by:

$$(\kappa_\lambda - \gamma_\lambda)\left(1 + \frac{2}{3}\cos\phi_\lambda\right)\frac{3x^2}{4{g_0}^2} = 2{\omega_m}^2\Delta_m\cos 4\Theta_\omega - [(\kappa_0 - \gamma_0) + (\kappa_\Delta - \gamma_\Delta)]\frac{3x^2}{4{g_0}^2} \tag{5.28}$$

where the contributions of the bias, parametric pumping and balancing voltages have been decomposed. (5.28) has been expressed in a manner to show that the parametric pumping voltage amplitude and phase can be used to achieve nonlinear frequency balancing. Any $(V_\lambda, \phi_\lambda)$ combination satisfying (5.28) can be used for this purpose, where each combination results in different $\lambda_{2,r}$. However, the combination resulting in the largest positive parametric excitation amplitude component $\lambda_{2,r}$ is most desirable for rate output parametric amplification. From (5.27), this requires maximising ${V_\lambda}^2\sin\phi_\lambda$, so the $(V_\lambda, \phi_\lambda)$ combinations involving larger V_λ and ϕ_λ closest to $\pi/2$ are desirable.

From (5.28), there are clear restrictions on the practicality of this approach. First, since $\gamma_\lambda \leq \kappa_\lambda$, the left side of (5.28) is non-negative, so this condition can only be satisfied if $\cos 4\Theta_\omega > 0$. Second, for the same reason, there is a maximum drive amplitude for satisfying (5.28), as larger drive amplitudes can result in the right side of (5.28) falling to negative values. The maximum drive amplitude is increased for larger imperfection magnitudes and smaller drive misalignments, i.e. larger $\Delta_m\cos 4\Theta_\omega$. Third, the required parametric pumping voltage amplitude V_λ to satisfy (5.28) can be too large for practical implementation. V_λ is large if one or more of the following applies:

- the electrodes are near continuous $(\kappa_\lambda \approx \gamma_\lambda)$
- the electrode span is small (κ_λ and γ_λ are small unless compensated by larger V_λ)
- the selected drive amplitude is too small (left side of (5.28) is small unless compensated by larger V_λ)
- the imperfection magnitude Δ_m is relatively large and $\cos 4\Theta_\omega \approx 1$, resulting in a large value of the right side of (5.28)

These restrictions are similar to those discussed in Section 4.5.5, indicating that the ability to tune the parametric pumping phase ϕ_λ does not improve the effectiveness of using the parametric pumping voltage for nonlinear frequency balancing.

Parametric pumping voltage amplitude requirements to restore nonlinear frequency balance

To demonstrate the role of the parametric pumping voltage to ensure nonlinear frequency balancing, the following investigates the effects of the nonlinear frequency imbalance on the required parametric pumping voltage amplitude to restore the nonlinear frequency balance. System 1 in Table 4.2 is considered for this investigation, subjected to an angular rate of $\Omega = 250\,°/s$. The balancing voltage amplitude and phase index number required to nullify the quadrature sense response are calculated using (5.24), and the required parametric pumping voltage amplitude to restore nonlinear frequency balance is calculated from (5.28). The parametric pumping voltage phase is set at $\phi_\lambda = \pi/2$. Figure 5.2(a) shows the backbone curve of the of the drive frequency ω_X, and the variation of the frequency $\sqrt{{\omega_Y}^2 + \lambda_{1,r}}$ with the drive amplitude for the default case with no parametric pumping voltage. The difference between these frequencies in Figure 5.2(a) gives the nonlinear frequency imbalance and a marker has been plot at the drive amplitude where these frequencies coincide, showing the default nonlinear frequency balancing point without requiring the parametric pumping voltage. Figure 5.2(b) shows the required parametric pumping voltage amplitude to restore nonlinear frequency balancing across the drive amplitude range considered in Figure 5.2(a). This marker is also shown in Figure 5.2(b), which shows the parametric pumping voltage amplitude V_λ required to achieve nonlinear frequency balancing beyond this default balancing point when $\phi_\lambda = \pi/2$.

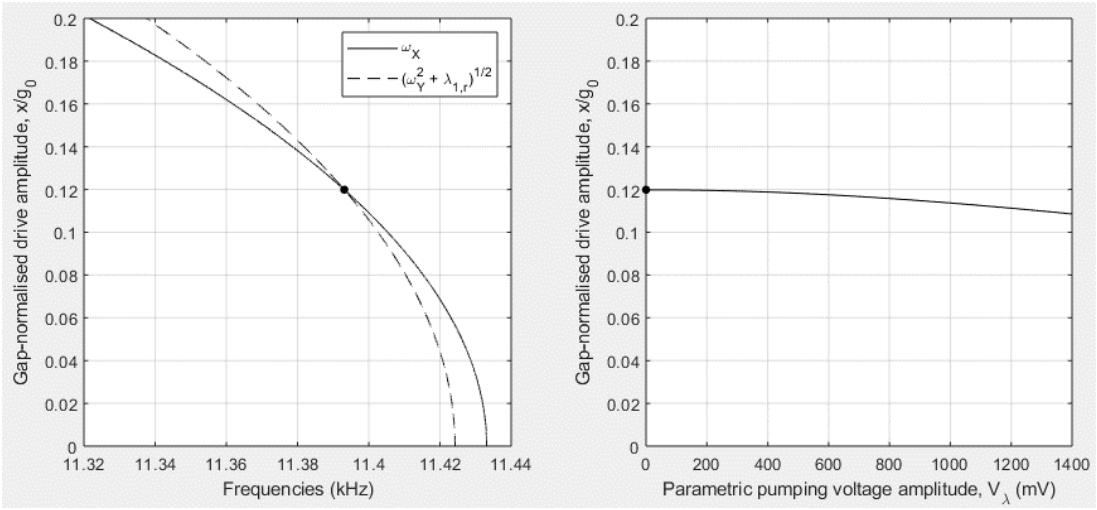

(a) (b)

Figure 5.2: (a) Variations of the frequencies ω_X and $\sqrt{{\omega_Y}^2 + \lambda_{1,r}}$ with the drive amplitude when $V_\lambda = 0$ and (b) the required parametric pumping voltage amplitudes required to match these frequencies

In Figure 5.2(a), nonlinear frequency balancing is achieved at $x/g_0 \approx 0.12$ without requiring the parametric pumping voltage and is the result of the different drive amplitude dependencies of ω_X and $\sqrt{{\omega_Y}^2 + \lambda_{1,r}}$ due to the electrode discontinuity. This corresponds to the default case where both the left and right sides of (5.28) are null. To restore nonlinear frequency balancing

at other drive amplitudes, Figure 5.2(b) shows that the required parametric pumping voltage amplitude increases significantly with small deviations from the default nonlinear frequency balancing point. When x/g_0 deviates from 12% to 10.8%, the required V_λ increases to 1.4 V, matching the order of the bias voltage shown in Table 4.2. Also, Figure 5.2(a) shows that nonlinear frequency balancing can only be restored if $\omega_X > \sqrt{{\omega_Y}^2 + \lambda_{1,r}}$ at low drive amplitudes. This is because the parametric pumping voltage reduces the drive frequency ω_X more significantly than $\sqrt{{\omega_Y}^2 + \lambda_{1,r}}$.

Conditions for parametric pumping voltage amplitude and phase to maximise parametric amplification while ensuring nonlinear frequency balance

The following investigates the multiple possible combinations of the parametric pumping voltage and phase $(V_\lambda, \phi_\lambda)$, capable of achieving nonlinear frequency imbalance and the resulting parametric amplification attained for the different combinations. System 1 in Table 4.2 is considered for this investigation. The results in Figure 5.2(a) are extended to consider a general parametric pumping voltage phase, unrestricted to $\phi_\lambda = \pi/2$. The required parametric pumping voltage amplitude V_λ to achieve nonlinear frequency balance is then calculated using (5.28) for each ϕ_λ considered. Figure 5.3(a) shows the $(V_\lambda, \phi_\lambda)$ combinations resulting in nonlinear frequency balance for drive amplitudes of $x/g_0 = 0.1175, 0.1185$ and 0.1195. The points on these plots where $V_\lambda \sin(\phi_\lambda/2) = V_\lambda \cos(\phi_\lambda/2)$, i.e. $\phi_\lambda = \pi/2$, correspond to the parametric pumping voltage amplitudes shown in Figure 5.2(b) at $x/g_0 = 0.1175, 0.1185$ and 0.1195. Figures 5.3(b), (c) and (d) show the individual plots for the various drive amplitude cases shown in Figure 5.3(a), corresponding to $x/g_0 = 0.1175, 0.1185$ and 0.1195 respectively. Contours of $\lambda_{2,r}/(2\Gamma\omega_X)$ are shown to indicate the varying parametric amplification effects of the $(V_\lambda, \phi_\lambda)$ combinations. As indicated in (5.6), larger $\lambda_{2,r}/(2\Gamma\omega_X)$ results in larger parametric amplification of the rate output.

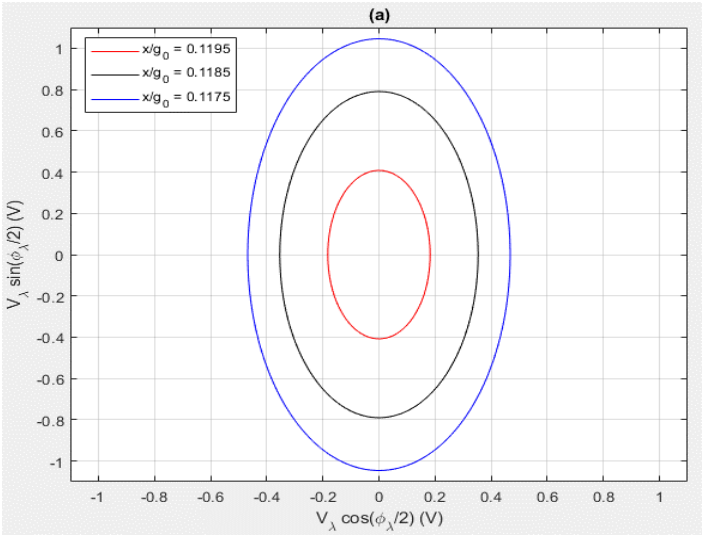

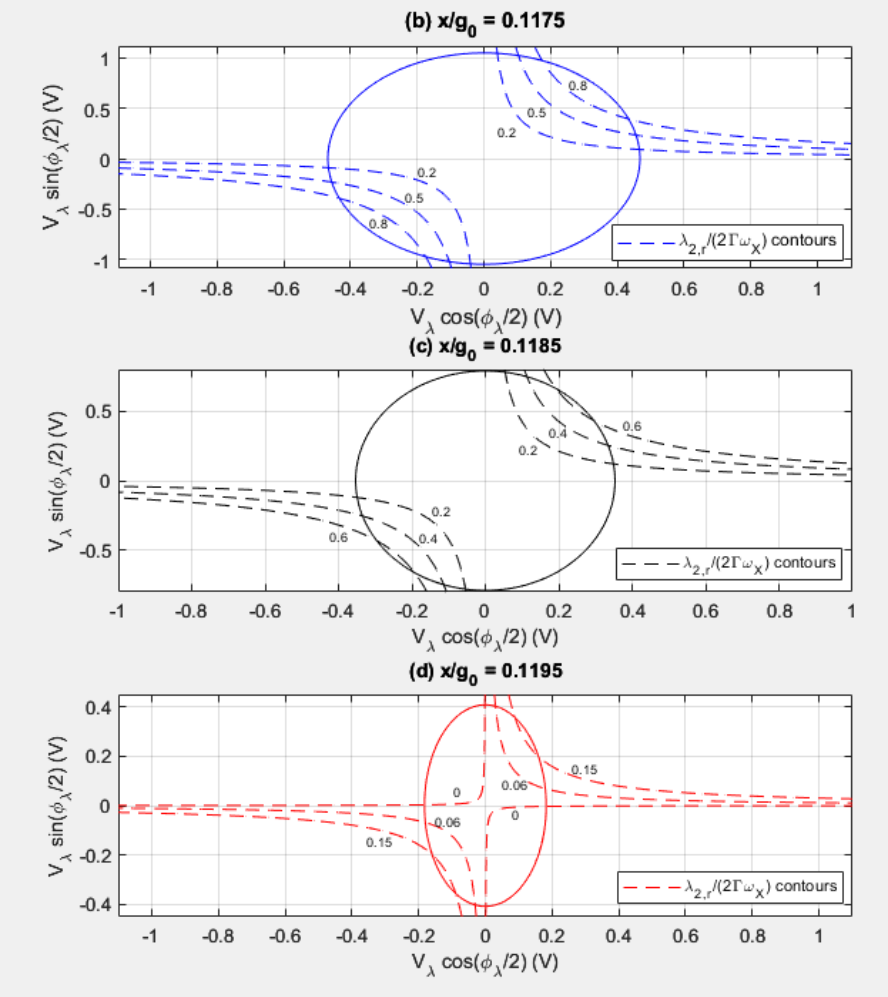

Figure 5.3: (a) Range of feasible $(V_\lambda, \phi_\lambda)$ combinations for nonlinear frequency balancing at various drive amplitudes, with $\lambda_{2,r}/(2\Gamma\omega_X)$ contours in (b) for $x/g_0 = 0.1175$, (c) for $x/g_0 = 0.1185$ and (d) for $x/g_0 = 0.1195$

In Figure 5.3(a), the ellipticity of the plots shows that nonlinear frequency balancing can be achieved at any phase ϕ_λ, and the voltage amplitude V_λ can be tuned for any chosen phase to yield nonlinear frequency balancing. Decreasing the drive amplitude from $x/g_0 = 0.1195$ to 0.1175 also increases the major and minor radii of the plots, indicating that larger parametric pumping voltage amplitudes V_λ are required to restore nonlinear frequency balancing, regardless of the chosen phase ϕ_λ. This is because decreasing the drive amplitude from $x/g_0 = 0.1195$ to 0.1175 deviates the drive amplitude further from the default nonlinear frequency balancing point shown in Figure 5.2(a) and (b), thus increasing the nonlinear frequency imbalance and the required parametric pumping voltage amplitude V_λ to restore nonlinear frequency balancing.

In Figure 5.3(b), (c) and (d), larger values of $\lambda_{2,r}/(2\Gamma\omega_X)$ occur at larger parametric pumping voltage amplitudes, i.e. points further away from the origin. Comparing Figure 5.3(b), (c) and (d), the drive amplitude case $x/g_0 = 0.1175$ in Figure 5.3(b) is subjected to the largest parametric amplification due to the larger parametric pumping voltage amplitudes involved.

This shows that larger drive amplitude deviations from the default nonlinear frequency balancing point in Figure 5.2(a) can increase the parametric amplification attained while retaining nonlinear frequency balance. However, for all drive amplitudes, the $(V_\lambda, \phi_\lambda)$ combinations intersecting with the highest-valued $\lambda_{2,r}/(2\Gamma\omega_X)$ contours lie at the points where $V_\lambda \sin(\phi_\lambda/2) = V_\lambda \cos(\phi_\lambda/2)$, i.e. $\phi_\lambda = \pm\pi/2$.

The results in Figures 5.3(b), (c) and (d) show that the attained parametric amplification is constrained by the proximity of the chosen drive amplitude to the default nonlinear frequency balancing point. This nonlinear frequency balancing restriction limits the practicality of the single-mode rate sensing approach to a narrow range of drive amplitudes below the default nonlinear frequency balancing point, as the required parametric pumping voltage amplitude can be too large for practical implementations. Nonlinear frequency balancing also cannot be achieved at larger drive amplitudes, thus limiting the rate output.

5.3.4. Dual mode rate sensing with closed-loop operation

Without nonlinear frequency balancing, the balancing voltage in (5.24) is rate-dependent, thus enabling closed-loop rate sensing. The balancing voltage must be tuned with angular rate changes to retain a nullified quadrature output.

Expressing (5.24) as ${V_\Delta}^2 \cos i_\Delta\pi = S^V(\Omega + \Omega_z^V)$, the closed-loop rate sensitivity and bias rate are:

$$S^V = \frac{-\frac{G_\Omega x\omega_X}{2\Gamma\omega_X - \lambda_{2,r}}\left(\lambda_{1,r} - \bar{\omega}^2\right)}{\alpha'} = -\frac{G_\Omega x\omega_X}{\alpha'}\left(\frac{\lambda_{1,r} - \bar{\omega}^2}{2\Gamma\omega_X - \lambda_{2,r}}\right) \tag{5.29}$$

$$\Omega_z^V = -\frac{{\omega_m}^2\Delta_\omega \sin 4\Theta_\omega}{G_\Omega\omega_X}\left(\frac{2\Gamma\omega_X - \lambda_{2,r}}{\lambda_{1,r} - \bar{\omega}^2}\right) \tag{5.30}$$

where α' is:

$$\alpha' = j\frac{\varepsilon_0}{5\rho h\pi {g_0}^2}\sin\delta\left(1 + c_{\Delta,XX}\frac{3x^2}{4{g_0}^2}\right) \tag{5.31}$$

From (5.7), (5.29) and (5.30), the presence of the parametric excitation amplitude component $\lambda_{2,r}$ amplifies both closed-loop and open-loop rate sensitivities, while suppressing the closed-loop bias rate if $\lambda_{2,r} > 0$. From (5.29) and (5.30), a larger nonlinear frequency imbalance $\lambda_{1,r} - \bar{\omega}^2$ also results in an amplified closed-loop rate sensitivity and suppressed bias rate.

This indicates that drive amplitudes further away from the default nonlinear frequency balancing point satisfying (5.28) are desirable for closed-loop rate sensing using this scheme.

Effects of phase tuneable parametric excitation on closed-loop rate sensitivity and bias rate and open-loop rate sensitivity

The following investigates the ability of the phase-tuneable parametric excitation to enhance closed-loop rate sensing performance. System 1 in Table 4.2 is considered for this investigation. The parametric pumping voltage phase is set at $\phi_\lambda = \pi/2$ and the amplitude V_λ is varied up to $0.6\,V$ to vary the parametric excitation amplitude component $\lambda_{2,r}$. The drive amplitude is fixed at $x/g_0 = 0.1$ by adjusting the drive voltage amplitude V_{AC}. As V_λ is increased, the required V_{AC} to sustain this drive amplitude decreases from $5.4\,mV$ to $1.3\,mV$ for the range of V_λ considered in these results, owing to the drive mode parametric amplification described in (5.20). The balancing voltage amplitude V_Δ is manually tuned for each angular rate measurement to achieve nullified quadrature sense amplitude, and the phase index number i_Δ is set at 0 or 1 depending on the sign of the calculated value of the right side of (5.24). Using these configurations, Figure 5.4(a) and (b) show the effects of the parametric pumping voltage amplitude V_λ on the closed-loop rate sensitivity and bias rate respectively. FE results are also shown.

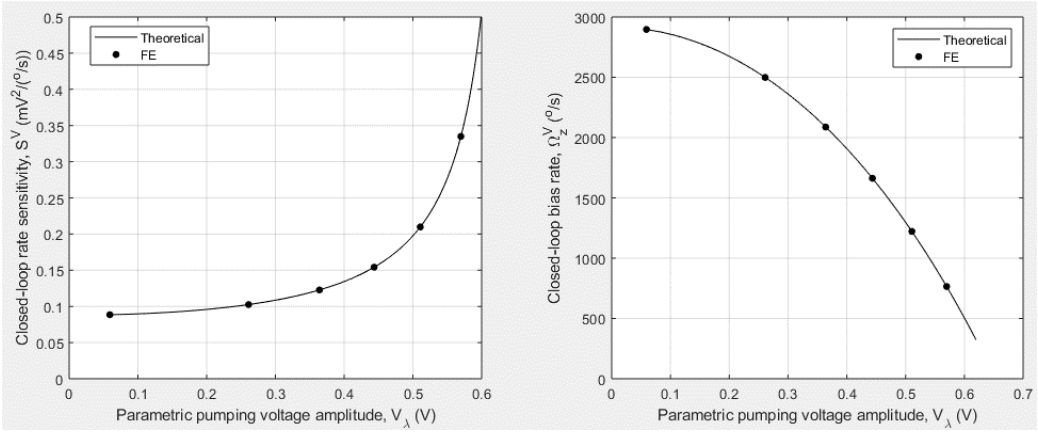

(a) (b)

Figure 5.4: Effect of parametric pumping voltage amplitude on the closed-loop (a) rate sensitivity and (b) bias rate

The FE results exhibit good agreement with the theoretical results shown in Figure 5.4(a) and (b), confirming the closed-loop rate sensing performance enhancement effects of the parametric pumping voltage. The closed-loop rate sensitivity increases significantly at larger parametric pumping voltage amplitudes as parametric resonance is approached. As such, the energy dissipation rates of both drive and sense modes decrease, thus increasing the modal Q factor without modifying the mechanical damping.

Figure 5.4(b) shows that small imperfections and drive misalignments can lead to large closed-loop bias rates. The large bias rate is due to the high linear damping of the system, corresponding to a Q factor of 120 without parametric excitation. This can also be confirmed from (5.30). However, this bias rate is significantly suppressed when parametric resonance is approached.

Figure 5.5 below shows the effects of the parametric pumping voltage amplitudes considered in Figure 5.4(a) and (b) on the corresponding open-loop rate sensitivity, shown as a gain relative to the rate sensitivity when $V_\lambda = 0$, given by $G_S = S/\left(S|_{V_\lambda=0}\right)$:

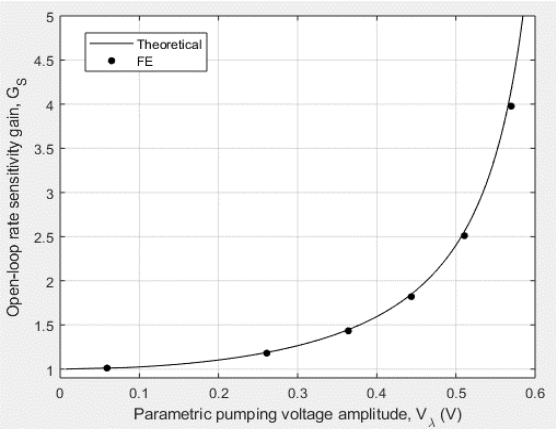

Figure 5.5: Effect of parametric pumping voltage on the open-loop rate sensitivity

In Figure 5.5, the FE results similarly exhibit good agreement with the theoretical results as Figure 5.4(a) and (b), thus confirming the effectiveness of the present scheme to amplify the open-loop rate sensitivity as aimed. One possible explanation for the slight discrepancy between the theoretical and FE results at larger parametric pumping voltage amplitudes V_λ is higher order electrostatic nonlinearities, which generally increases in significance at larger voltages.

Effects of nonlinear frequency imbalance on closed-loop bias rate amplification using the parametric pumping voltage

The following investigates the effects of the nonlinear frequency imbalance on the effectiveness of the parametric pumping voltage to enhance the closed-loop rate sensitivity. For this investigation, the nonlinear frequency imbalance is calculated from the right side of (5.28), giving the nonlinear frequency imbalance in the absence of the parametric pumping voltage. The default nonlinear frequency balancing point is identified as the drive amplitude where the right side of (5.28) is zero. The results in Figure 5.2(a) are considered for this investigation, with a default nonlinear frequency balancing point at $x/g_0 = 0.12$. The nonlinear frequency imbalance is varied by considering multiple drive amplitudes of different

proximities from $x/g_0 = 0.12$. Figure 5.6 shows a comparison of the effects of the parametric pumping voltage amplitude V_λ on the closed-loop rate sensitivity for drive amplitudes of $x/g_0 = 0.1$ and 0.1185. The result for $x/g_0 = 0.1$ is identical to the result in Figure 5.4(a).

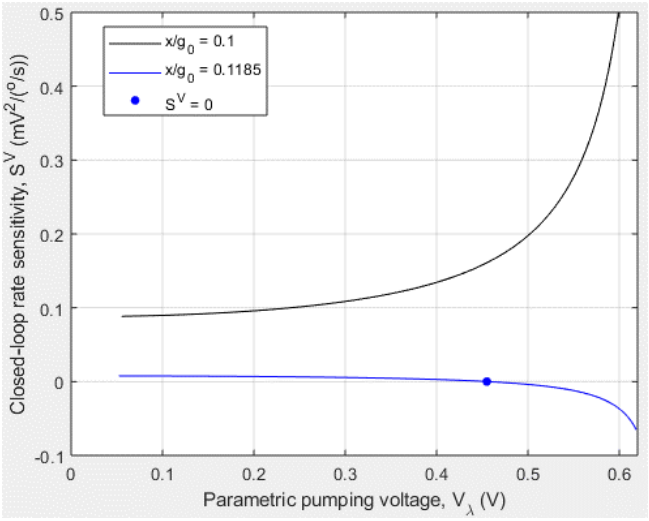

Figure 5.6: Effect of parametric pumping voltage amplitude on the closed-loop rate sensitivity at different drive amplitudes

In Figure 5.6, the drive amplitude $x/g_0 = 0.1185$ yields low closed-loop rate sensitivity. This is because, as shown in Figure 5.2(a), this drive amplitude is close to the default nonlinear frequency balancing point, result in a small nonlinear frequency imbalance. At $V_\lambda = 0.46\,V$, nonlinear frequency balancing is achieved, so $S^V = 0$. This parametric pumping voltage amplitude is also shown in Figure 5.2(b) at the point corresponding to $x/g_0 = 0.1185$. In this case, closed-loop rate sensing is not possible and the device can only operate using open-loop rate sensing. When V_λ increases beyond $0.46\,V$, the nonlinear frequency imbalance grows and closed-loop rate sensitivity increases more significantly as parametric resonance is approached.

The results in Figure 5.4(a), (b), Figure 5.5 and Figure 5.6 conclude that a combination of large nonlinear frequency imbalances and large parametric pumping voltages is ideal for closed-loop rate sensing, and the latter also promotes parametric amplification of the rate output and open-loop rate sensitivity.

5.3.5. Summary

The linear electrostatic force can be used for parametric amplification of the rate output by tuning the phase of the parametric pumping voltage. The component of the resulting parametric excitation responsible for this amplification is in quadrature with the self-induced parametric excitation. To ensure that the quadrature output is nullified and the rate output is trimmed while the rate output is amplified, an additional, rate-dependent balancing voltage component is also required, similar to the case without parametric amplification investigated

in Chapter 4. This balancing voltage serves to counteract the force imbalances stemming from the imperfection-induced linear elastic coupling and nonlinear frequency imbalance, where the latter is responsible for the rate dependency of the balancing voltage.

The rate-dependency of the balancing voltage generally enables the device to operate in open loop using the trimmed and amplified rate output, and in closed loop using the balancing voltage amplitude. An exception to this is when nonlinear frequency balancing occurs, in which case the balancing voltage only serves to negate the linear elastic coupling force and is invariant with angular rate, so closed-loop rate sensing cannot be achieved. It is found that this only occurs under special conditions where the nonlinear frequency imbalance is relatively small. The parametric pumping voltage can be used to restore nonlinear frequency balancing, but larger nonlinear frequency imbalances significantly increase the required parametric pumping voltage amplitude to restore nonlinear frequency imbalance, and can be too large for practical implementation.

When nonlinear frequency balancing is not achieved, the device is able to operate in both open and closed loops. It is shown that the parametric amplification of the rate output can be maximised by tuning the phase of the parametric pumping voltage. Increasing the parametric pumping voltage amplitude while its phase is tuned results in significant open-loop rate sensitivity enhancements, accompanied by increased closed-loop rate sensitivity and reduced closed-loop bias rate. FE results are also shown, confirming the effectiveness of the current scheme to achieve the parametric amplification of the rate output, as aimed. It is also found that the closed-loop rate sensitivity and bias rate performance can be further improved when the nonlinear frequency imbalance is increased.

5.4. Quadratic parametric amplification

In this section, the quadratic electrostatic forces are considered to generate the required phase-tuneable parametric excitation. An alternative trimming approach without involving rate-dependent balancing forces is also investigated, considering the cases of nonlinear frequency balancing and drive force alignment. As such, only open-loop rate sensing is considered in this scheme. Using the general framework developed in Section 4.4, a suitable electrostatic configuration is identified to generate the required form of electrostatic forces for these aims. For the chosen electrostatic configuration, equations of motion are developed and the modal dynamics are analysed to identify the voltage conditions for the negation of the drive misalignment, nonlinear frequency balancing and phase-tuning the resulting parametric excitation. FE results are also included to validate the effectiveness of the present approach to achieve parametric amplification the rate output.

5.4.1. Selection of voltage distribution

Trimming with drive force alignment

Revisiting the balancing force amplitude necessary for nullifying the quadrature response in (5.9):

$$\bar{\boldsymbol{f}}_{\boldsymbol{\lambda 2}} = \begin{bmatrix} f_{\lambda 2} \\ 0 \end{bmatrix} = \begin{bmatrix} -f_\Delta + \dfrac{{\omega_X}^2 - {\omega_Y}^2 - \lambda_{1,r}}{2\Gamma\omega_X - \lambda_{2,r}} f_\Omega \\ 0 \end{bmatrix} \tag{5.9}$$

The balancing force is not required to trim the rate output and nullify the quadrature output if there is no linear elastic coupling force ($f_\Delta = 0$) and nonlinear frequency balancing applies (${\omega_X}^2 - {\omega_Y}^2 = \lambda_{1,r}$), in which the balancing force $f_{\lambda 2}\cos(\omega t + \phi_x)$ in the targeted sense equation of motion in (5.10) can be set to zero. As such, drive force alignment to ensure $f_\Delta = 0$ is a key requirement to achieve this form of trimming.

Using the definition of f_Δ in (3.35) and recalling that ${\omega_m}^2\Delta_m = {\omega_0}^2\Delta_\omega$ and $X = x\cos(\omega t + \phi_x)$, the linear elastic coupling force $f_\Delta\cos(\omega t + \phi_x)$ in (5.10) expressed in terms of the modal coordinate is:

$$f_\Delta\cos(\omega t + \phi_x) = -{\omega_m}^2\Delta_m \sin 4\Theta_\omega\, X$$

This is a linear force, proportional to the drive displacement. This force can be counteracted by inducing an electrostatic force in antiphase with it, also proportional to X. This requires the appearance of a term in the sense electrostatic force in (4.45b) proportional to X. This is a linear electrostatic force of order $q = 2$, resulting in the following condition:

$$A^{fY}_{X^1Y^0} + {\omega_m}^2\Delta_m \sin 4\Theta_\omega = 0 \tag{5.32}$$

This implementation modifies the total linear elastic coupling force by introducing an electrostatic linear elastic coupling to negate the drive misalignment-induced component of the linear elastic coupling force. Using the condition in (5.32), the total linear elastic coupling force can be nullified, effectively achieving drive force alignment.

Following the steps in Table 4.6, Step 2 shows that this implementation requires the appearance of a term proportional to XY in the total electrostatic potential energy, i.e. $A^{fY}_{X^1Y^0} \neq 0$ in (4.45b), and Step 3 shows that this involves the capacitance coefficient $\beta^{\pm}_{2,4}$, corresponding to the $\sin 4\theta_0(i)$ component in the capacitance distribution $c^{\pm}[\theta_0(i)]$. From (4.50b), the component of this capacitance corresponding to $q = 2$ is given by:

$$c_2^{\pm}[\theta_0(i)] = \alpha_{2,0}^{\pm} + \alpha_{2,4}^{\pm}\cos 4\theta_0(i) + \beta_{2,4}^{\pm}\sin 4\theta_0(i) \tag{5.33}$$

where the desired term proportional to XY appears only in the coefficient $\beta_{2,4}^{\pm}$. However, noting that the electrode central angular position is defined as $\theta_0(i) = 2i\pi/j$, $\sin 4\theta_0(i) = 0$ for all i when $j = 8$, thus eliminating the last term in (5.33). This indicates that the capacitance for each electrode $c^{\pm}[\theta_0(i)]$ does not contain the term proportional to XY necessary for the electrostatic linear elastic coupling. This is because, the angular separation of each electrode is $\pi/4$ for the 8 electrode configuration, so the central angular position of each electrode coincides with the node of either the drive or sense mode. Consequently, each electrode softens only one of the modes, exhibiting no linear elastic coupling between the modes. This is shown in Figure 5.7 below, where the electrode placements relative to the modal displacements are shown for the 8 and 16 electrode configuration designs:

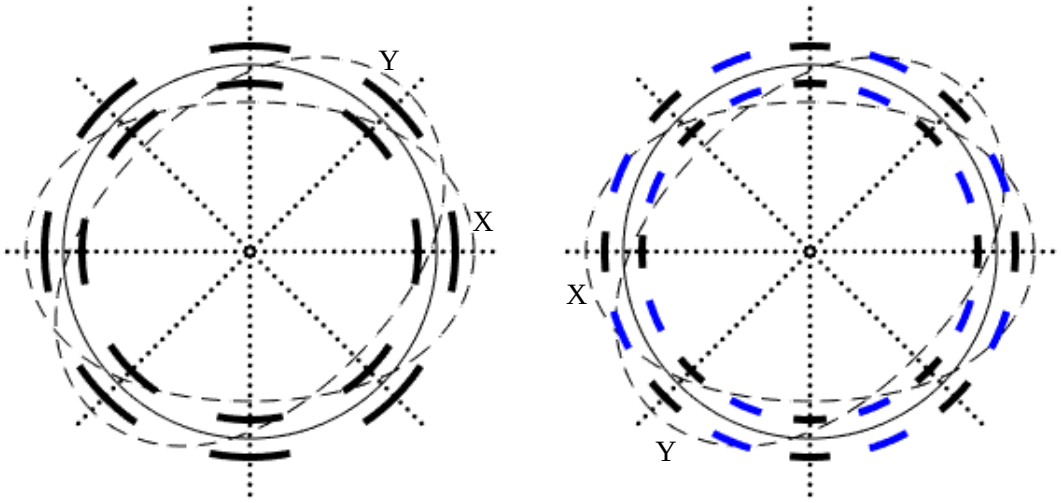

Figure 5.7: Circumferential variations of modal displacements and electrode distribution for the (a) 8 and (b) 16 electrode configurations. The blue electrodes enable electrostatic linear elastic coupling.

Consequently, when $j = 8$, $A_{X^1Y^0}^{fY} = 0$ regardless of the voltage distribution selected and the required electrostatic linear elastic coupling force for drive force alignment cannot be generated. On the other hand, for the 16 electrode configuration, the electrodes centred at $\theta_0(i)$ for odd i can be used to generate the necessary electrostatic linear elastic coupling. For this reason, the proceeding investigation on the voltage distribution selection is based on the 16 electrode configuration.

Phase-tuneable parametric excitation with quadratic electrostatic force

The parametric excitation force in (5.10) is:

$$F_\lambda = \left[2\lambda_{1,r}\cos 2(\omega t + \phi_x) + 2\lambda_{2,r}\sin 2(\omega t + \phi_x)\right]Y \tag{5.34}$$

where only the terms involving the double-frequency variation of the sense stiffness are retained.

The sense quadratic-ordered ($q = 3$) electrostatic force in (4.45b) is given by:

$$f_{U,Y}|_3 = A^{fY}_{X^2Y^0}X^2 + A^{fY}_{X^1Y^1}XY + A^{fY}_{X^0Y^2}Y^2 \tag{5.35}$$

The quadratic electrostatic force can be used to generate the required parametric excitation by ensuring that one of the terms in (5.35) equate to F_λ in (5.34). The first term is independent of the sense displacement, so it cannot be used to generate the required parametric excitation. Noting that the sense amplitude is orders of magnitude smaller than the drive amplitude, the last term in (5.35) is negligible. As such, the second term, $A^{fY}_{X^1Y^1}XY$ is best suited to generate the desired parametric excitation. Setting $A^{fY}_{X^1Y^1}XY = F_\lambda$ and noting that $X = x\cos(\omega t + \phi_x)$ gives the following conditions for the electrostatic force coefficient $A^{fY}_{X^1Y^1}$:

$$\frac{\omega}{2\pi}\int_0^{\frac{2\pi}{\omega}} \left(A^{fY}_{X^1Y^1}x\right)[\cos(\omega t + \phi_x) + \cos 3(\omega t + \phi_x)]dt = 2\lambda_{1,r} \tag{5.36a}$$

$$\frac{\omega}{2\pi}\int_0^{\frac{2\pi}{\omega}} \left(A^{fY}_{X^1Y^1}X\right)[\sin(\omega t + \phi_x) + \sin 3(\omega t + \phi_x)]dt = 2\lambda_{2,r} \tag{5.36b}$$

To ensure that the left side of (5.36a) and (5.36b) is nonzero after the integral is evaluated, the electrostatic force coefficient $A^{fY}_{X^1Y^1}$ must be harmonic with frequency ω or 3ω, thus serving to generate the double frequency parametric excitation terms in (5.34).

Conditions for selection of voltage distribution

(5.32), (5.36a) and (5.36b) establish the required form of the electrostatic forces for parametric amplification and trimming. Following the steps in Table 4.6 and recalling that $\xi_0^+ > 0$ and $\xi_0^- > 0$ due to the presence of the bias voltage, the resulting conditions for the voltage squared distribution coefficients are summarised in Table 5.3 for the case when $j = 16$.

Table 5.2: Constraints for the coefficients of the voltage squared distribution, $\xi_{m_V}^{\pm}$ to achieve quadratic parametric amplification and trimming for the case of 16 inner/outer electrodes

	Electrostatic force conditions	**Voltage squared distribution constraints**
1	$A_{X^1Y^0}^{fY} + {\omega_m}^2 \Delta_m \sin 4\Theta_\omega = 0$	$\zeta_4^+ + \zeta_4^- - \zeta_{12}^+ - \zeta_{12}^- \neq 0$ for $\sin 4\Theta_\omega \neq 0$
2	$\frac{\omega}{2\pi}\int_0^{\frac{2\pi}{\omega}} A_{X^1Y^1}^{fY} x[\cos(\omega t + \phi_x) + \cos 3(\omega t + \phi_x)]dt = 2\lambda_{1,r}$	$\int_0^{\frac{2\pi}{\omega}} (\xi_2^+ - \xi_2^- + \xi_6^+ - \xi_6^- + \xi_{10}^+ - \xi_{10}^- + \xi_{14}^+ - \xi_{14}^-)\cos(\omega t + \phi_x)\, dt \propto \lambda_{1,r}$
3	$\frac{\omega}{2\pi}\int_0^{\frac{2\pi}{\omega}} A_{X^1Y^1}^{fY} x[\sin(\omega t + \phi_x) + \sin 3(\omega t + \phi_x)]dt = 2\lambda_{2,r}$	$\int_0^{\frac{2\pi}{\omega}} (\xi_2^+ - \xi_2^- + \xi_6^+ - \xi_6^- + \xi_{10}^+ - \xi_{10}^- + \xi_{14}^+ - \xi_{14}^-)\sin(\omega t + \phi_x)\, dt \propto \lambda_{2,r}$
4	$A_{X^0Y^0}^{fX} \propto \cos \omega t$	$\xi_2^+ - \xi_2^- + \xi_{14}^+ - \xi_{14}^- \propto \cos \omega t$
5	$A_{X^0Y^0}^{fY} = 0$	$\zeta_2^+ - \zeta_2^- - \zeta_{14}^+ + \zeta_{14}^- = 0$
6	$A_{X^0Y^1}^{fY} = A_{X^1Y^0}^{fX}$	$\xi_4^+ + \xi_4^- + \xi_{12}^+ + \xi_{12}^- = 0$
7	$\frac{d}{dt}\left(A_{X^0Y^1}^{fY}\right) = 0$	$\frac{d}{dt}(\xi_0^+ + \xi_0^- + \xi_4^+ + \xi_4^- + \xi_{12}^+ + \xi_{12}^- + \xi_{16}^+ + \xi_{16}^-) = 0$

(5.32), (5.36a) and (5.36b) correspond to conditions 1, 2 and 3 in Table 5.2 respectively.

Condition 4 is similar to condition 5 in Table 5.1, representing the condition to yield a harmonic drive force at frequency ω. This condition constraints the coefficients $\xi_2^{\pm}$ and $\xi_{14}^{\pm}$, which are also involved in conditions 2 and 3. In practice, it is convenient to separate these conditions to ensure that the drive force remains only associated with the drive voltage, without interference from any other voltage components in the chosen voltage distribution. For this purpose, the remaining coefficients involved in conditions 2 and 3, $\xi_6^{\pm}$ and $\xi_{10}^{\pm}$ can be used to generate the parametric excitation, while $\xi_2^{\pm}$ and $\xi_{14}^{\pm}$ are only assigned to the drive voltage.

Condition 5 is in contrast with condition 1 in Table 5.1. Noting that the aim is to achieve trimming and parametric amplification without requiring a balancing force, direct forcing of the sense mode is avoided.

Conditions 6 and 7 define the conditions on the linear electrostatic forces, in a manner similar to conditions 2, 3 and 4 in Table 5.1. Condition 6 is identical to condition 4 in Table 5.1, while condition 7 replaces conditions 2 and 3 in Table 5.1 since the linear electrostatic force is not used to generate the targeted parametric excitation in the present scheme. Condition 7 ensures the linear electrostatic stiffness is constant.

The following voltage distribution satisfies all the conditions in Table 5.2:

$$V^{+}[\theta_0(i)] = V_0 + V_{AC}\cos\omega t\cos 2\theta_0(i) - V_\lambda \sin\left(\frac{\omega t + \phi_x + \phi_\lambda}{2}\right)\cos 3\theta_0(i) + V_4 \sin 4\theta_0(i) \tag{5.37a}$$

$$V^{-}[\theta_0(i)] = V_0 - 2V_{AC}\cos\omega t\cos 2\theta_0(i) + V_\lambda \cos\left(\frac{\omega t + \phi_x + \phi_\lambda}{2}\right)\cos 3\theta_0(i) - \frac{V_4}{2}\sin 4\theta_0(i) \tag{5.37b}$$

where the spatial variation of the voltage distribution is capped to a $4\theta_0(i)$ variation component. As such, the voltage squared distribution coefficients $\xi_{m_V}^{\pm} = \zeta_{m_V}^{\pm} = 0$ for all $m_V > 8$. The parametric pumping voltage amplitude and phase, V_λ and ϕ_λ, are used to tune the parametric excitation force amplitude. V_4 is a drive alignment voltage, which is used to negating the imperfection-induced linear elastic coupling force, i.e. condition 1 in Table 5.2. The drive alignment voltage replaces the balancing voltage in (5.11a) and (5.11b). Also, the phase of the parametric pumping voltage has been halved to satisfy conditions 2 and 3 in Table 5.2.

From (5.37a) and (5.37b), the nonzero voltage squared distribution coefficients in (4.52) are given by:

$$\begin{bmatrix}\xi_0^{+}\\ \xi_0^{-}\end{bmatrix} = \begin{bmatrix} {V_0}^2 + \frac{{V_4}^2}{2} + \frac{{V_\lambda}^2}{4}[1 - \cos(\omega t + \phi_x + \phi_\lambda)] + \frac{{V_{AC}}^2\cos^2\omega t}{2} \\ {V_0}^2 + \frac{{V_4}^2}{8} + \frac{{V_\lambda}^2}{4}[1 + \cos(\omega t + \phi_x + \phi_\lambda)] + 2{V_{AC}}^2\cos^2\omega t \end{bmatrix} \tag{5.38a}$$

$$\begin{bmatrix}\xi_1^+\\ \zeta_1^+\\ \xi_1^-\\ \zeta_1^-\end{bmatrix}=\begin{bmatrix}-V_\lambda V_{AC}\cos\omega t\sin\left(\frac{\omega t+\phi_x+\phi_\lambda}{2}\right)\\ -V_4V_\lambda\sin\left(\frac{\omega t+\phi_x+\phi_\lambda}{2}\right)\\ -2V_\lambda V_{AC}\cos\omega t\cos\left(\frac{\omega t+\phi_x+\phi_\lambda}{2}\right)\\ -\frac{V_4V_\lambda}{2}\cos\left(\frac{\omega t+\phi_x+\phi_\lambda}{2}\right)\end{bmatrix} \tag{5.38b}$$

$$\begin{bmatrix}\xi_2^+\\ \zeta_2^+\\ \xi_2^-\\ \zeta_2^-\end{bmatrix}=\begin{bmatrix}2V_0\\ V_4\\ -4V_0\\ V_4\end{bmatrix}V_{AC}\cos\omega t \tag{5.38c}$$

$$\begin{bmatrix}\xi_3^+\\ \xi_3^-\end{bmatrix}=\begin{bmatrix}-2V_0V_\lambda\sin\left(\frac{\omega t+\phi_x+\phi_\lambda}{2}\right)\\ 2V_0V_\lambda\cos\left(\frac{\omega t+\phi_x+\phi_\lambda}{2}\right)\end{bmatrix} \tag{5.38d}$$

$$\begin{bmatrix}\xi_4^+\\ \zeta_4^+\\ \xi_4^-\\ \zeta_4^-\end{bmatrix}=\begin{bmatrix}\frac{{V_{AC}}^2\cos^2\omega t}{2}\\ 2V_0V_4\\ 2{V_{AC}}^2\cos^2\omega t\\ -V_0V_4\end{bmatrix} \tag{5.38e}$$

$$\begin{bmatrix}\xi_5^+\\ \xi_5^-\end{bmatrix}=\begin{bmatrix}-V_\lambda V_{AC}\cos\omega t\sin\left(\frac{\omega t+\phi_x+\phi_\lambda}{2}\right)\\ -2V_\lambda V_{AC}\cos\omega t\cos\left(\frac{\omega t+\phi_x+\phi_\lambda}{2}\right)\end{bmatrix} \tag{5.38f}$$

$$\begin{bmatrix}\xi_6^+\\ \zeta_6^+\\ \xi_6^-\\ \zeta_6^-\end{bmatrix}=\begin{bmatrix}\frac{{V_\lambda}^2}{4}[1-\cos(\omega t+\phi_x+\phi_\lambda)]\\ V_4V_{AC}\cos\omega t\\ \frac{{V_\lambda}^2}{4}[1+\cos(\omega t+\phi_x+\phi_\lambda)]\\ V_4V_{AC}\cos\omega t\end{bmatrix} \tag{5.38g}$$

$$\begin{bmatrix}\zeta_7^+\\ \zeta_7^-\end{bmatrix}=-V_4V_\lambda\begin{bmatrix}\sin\left(\frac{\omega t+\phi_x+\phi_\lambda}{2}\right)\\ \frac{1}{2}\cos\left(\frac{\omega t+\phi_x+\phi_\lambda}{2}\right)\end{bmatrix} \tag{5.38h}$$

$$\begin{bmatrix}\xi_8^+\\ \xi_8^-\end{bmatrix}=-\frac{{V_4}^2}{8}\begin{bmatrix}4\\ 1\end{bmatrix} \tag{5.38i}$$

$\zeta_4^+ + \zeta_4^-$ in (5.38e) provides the electrostatic linear elastic coupling, contributing to the electrostatic force coefficient $A_{X^1Y^0}^{fY}$ in (5.32) and is used to negate the imperfection-induced linear elastic coupling. $\xi_6^+ - \xi_6^-$ in (5.38g) provides the phase-tuneable parametric excitation, and is harmonic at frequency ω as a result of satisfying conditions 2 and 3 in Table 5.2. $\xi_8^+ + \xi_8^-$ in (5.38i) contributes to equal linear electrostatic softening of the drive mode and sense modes, in a manner similar to $\xi_0^+ + \xi_0^-$.

The roles of the remaining coefficients are identical to those for the previous electrostatic configurations in (4.65a) and (4.65b), and (5.11a) and (5.11b). The only differences are that $\zeta_2^+ - \zeta_2^-$ in (5.38c) is zero so there is no direct forcing of the sense mode, and $\xi_0^+ + \xi_0^-$ in (5.38a) is constant (${V_{AC}}^2$ is negligible) so there is no linear parametric excitation induced with the present scheme.

5.4.2. Modal dynamics

In the following, equations of motions are developed for the chosen voltage distribution in (5.37a) and (5.37b). The drive and sense dynamics are analysed using the same techniques, assumptions and conditions on (3.14), (4.14), (4.69) and (5.15).

Equations of motion

The resulting electrostatic forces of the voltage distribution in (5.37a) and (5.37b) are given by:

$$\begin{bmatrix} f_{U,X} \\ f_{U,Y} \end{bmatrix} = \bar{\boldsymbol{A}}_{\boldsymbol{0}} + \bar{\bar{\boldsymbol{A}}}_{\boldsymbol{1}}\bar{\boldsymbol{q}}_{\boldsymbol{1}} + \bar{\bar{\boldsymbol{A}}}_{\boldsymbol{2}}\bar{\boldsymbol{q}}_{\boldsymbol{2}} + \bar{\bar{\boldsymbol{A}}}_{\boldsymbol{3}}\bar{\boldsymbol{q}}_{\boldsymbol{3}} \tag{5.39}$$

where

$$\bar{\boldsymbol{A}}_{\boldsymbol{0}} = -\frac{\varepsilon_0}{5\rho\pi h {g_0}^2} j \sin\delta \begin{bmatrix} \xi_2^+ - \xi_2^- \\ 0 \end{bmatrix} \tag{5.40a}$$

$$\bar{\bar{\boldsymbol{A}}}_{\boldsymbol{1}} = -\frac{2\varepsilon_0}{5\rho\pi h {g_0}^3} j \begin{bmatrix} \delta(\xi_0^+ + \xi_0^-) & \frac{\sin 2\delta}{4}(\zeta_4^+ + \zeta_4^-) \\ \frac{\sin 2\delta}{4}(\zeta_4^+ + \zeta_4^-) & \delta(\xi_0^+ + \xi_0^-) \end{bmatrix} \tag{5.40b}$$

$$\begin{aligned} \bar{\bar{\boldsymbol{A}}}_{\boldsymbol{2}} = -\frac{\varepsilon_0}{20\rho\pi h {g_0}^4} j \Bigg\{ & 3\sin\delta \begin{bmatrix} 3(\xi_2^+ - \xi_2^-) & 0 & \xi_2^+ - \xi_2^- \\ 0 & 2(\xi_2^+ - \xi_2^-) & 0 \end{bmatrix} \\ & + \sin 3\delta \begin{bmatrix} \xi_6^+ - \xi_6^- & 0 & -(\xi_6^+ - \xi_6^-) \\ 0 & -2(\xi_6^+ - \xi_6^-) & 0 \end{bmatrix} \Bigg\} \end{aligned} \tag{5.40c}$$

$$\bar{\bar{\boldsymbol{A}}}_{\boldsymbol{3}} = -\frac{2\varepsilon_0}{5\rho\pi h {g_0}^5} j \left\{ \frac{3\delta}{2} \begin{bmatrix} \xi_0^+ + \xi_0^- & 0 & \xi_0^+ + \xi_0^- & 0 \\ 0 & \xi_0^+ + \xi_0^- & 0 & \xi_0^+ + \xi_0^- \end{bmatrix} \right. \tag{5.40d}$$

$$+ \frac{\sin 4\delta}{8} \begin{bmatrix} \xi_8^+ + \xi_8^- & 0 & -3(\xi_8^+ + \xi_8^-) & 0 \\ 0 & -3(\xi_8^+ + \xi_8^-) & 0 & \xi_8^+ + \xi_8^- \end{bmatrix}$$

$$\left. + \frac{\sin 2\delta}{4} \begin{bmatrix} 0 & 3(\zeta_4^+ + \zeta_4^-) & 0 & \zeta_4^+ + \zeta_4^- \\ \zeta_4^+ + \zeta_4^- & 0 & 3(\zeta_4^+ + \zeta_4^-) & 0 \end{bmatrix} \right\}$$

Within $\bar{\bar{\boldsymbol{A}}}_{\boldsymbol{1}}$, the coefficients $\zeta_4^{\pm}$ contribute to the off-diagonal elements, in a manner similar to $\Delta_m \sin 4\Theta_\omega$ in the imperfection matrix $\bar{\bar{\Delta}}_m$ in (4.46). In this manner, when the mechanical and electrostatic forces are summed, $\zeta_4^{\pm}$ can be used to tune the net drive misalignment effect.

The coefficients $\xi_6^{\pm}$ appear within $\bar{\bar{\boldsymbol{A}}}_{\boldsymbol{2}}$, thus affecting the quadratic electrostatic forces as required.

Incorporating (5.40a) - (5.40d) into (5.39) and substituting the resulting drive and sense electrostatic forces and the mechanical forces in (4.44) into (4.43a) and (4.43b) gives the following equations of motion:

$$\ddot{\bar{\boldsymbol{q}}}_{\boldsymbol{1}} + 2\Gamma\dot{\bar{\boldsymbol{q}}}_{\boldsymbol{1}} + \bar{\bar{\boldsymbol{\eta}}}_{\boldsymbol{1}}\bar{\boldsymbol{q}}_{\boldsymbol{1}} + \bar{\bar{\boldsymbol{\eta}}}_{\boldsymbol{2}}(t)\frac{\bar{\boldsymbol{q}}_{\boldsymbol{2}}}{g_0} + \bar{\bar{\boldsymbol{\eta}}}_{\boldsymbol{3}}\frac{\bar{\boldsymbol{q}}_{\boldsymbol{3}}}{{g_0}^2} = \Omega\bar{\bar{\boldsymbol{G}}}_{\boldsymbol{\Omega}}\dot{\bar{\boldsymbol{q}}}_{\boldsymbol{1}} + \chi\cos\omega t\left(\begin{bmatrix}1\\0\end{bmatrix} + \bar{\bar{\boldsymbol{\eta}}}_{\boldsymbol{\chi}}\frac{\bar{\boldsymbol{q}}_{\boldsymbol{2}}}{{g_0}^2}\right) \tag{5.41}$$

The primary differences with the equations of motion corresponding to the linear parametric amplification case in (5.15) are:

- $\bar{\bar{\boldsymbol{\eta}}}_{\boldsymbol{1}}$ and $\bar{\bar{\boldsymbol{\eta}}}_{\boldsymbol{3}}$ are constant. The linear and cubic electrostatic forces are not actively used for parametric excitation, asides from self-induced mechanisms.
- the time-dependent matrix $\bar{\bar{\boldsymbol{\eta}}}_{\boldsymbol{2}}(t)$ appears, which is used to generate phase-tuneable parametric excitation using the quadratic electrostatic force.
- $\chi_\Delta = 0$, so there is no direct force acting on the sense mode.

The matrices $\bar{\bar{\boldsymbol{\eta}}}_{\boldsymbol{1}}$, $\bar{\bar{\boldsymbol{\eta}}}_{\boldsymbol{2}}(t)$ and $\bar{\bar{\boldsymbol{\eta}}}_{\boldsymbol{3}}$ are given by:

$$\bar{\bar{\boldsymbol{\eta}}}_{\boldsymbol{1}} = {\omega_{0,\lambda,4}}^2\begin{bmatrix}1 & \Delta_{0,4}\\ \Delta_{0,4} & 1\end{bmatrix} + {\omega_m}^2\begin{bmatrix}\Delta_m\cos 4\Theta_\omega & \Delta_m\sin 4\Theta_\omega\\ \Delta_m\sin 4\Theta_\omega & -\Delta_m\cos 4\Theta_\omega\end{bmatrix} \tag{5.42}$$

$$\bar{\bar{\boldsymbol{\eta}}}_{\boldsymbol{2}}(t) = -\begin{bmatrix}\nu & 0 & -\nu\\ 0 & -2\nu & 0\end{bmatrix}\cos(\omega t + \phi_x + \phi_\lambda) \tag{5.43}$$

$$\bar{\bar{\boldsymbol{\eta}}}_{\boldsymbol{3}} = \begin{bmatrix}\gamma_{0,\lambda,4} & \tilde{\kappa}_{0,4} & \kappa_{0,\lambda,4} & \tilde{\gamma}_{0,4}\\ \tilde{\gamma}_{0,4} & \kappa_{0,\lambda,4} & \tilde{\kappa}_{0,4} & \gamma_{0,\lambda,4}\end{bmatrix} \tag{5.44}$$

Compared to (5.16) and (5.17), the linear resonant frequency and cubic single and coupled-mode stiffness have been replaced with ${\omega_{0,\lambda,4}}^2$, $\gamma_{0,\lambda,4}$ and $\kappa_{0,\lambda,4}$. As the subscript indicates, these quantities contain contributions from the drive alignment voltage instead of the balancing voltage. In addition, the modal coupling is altered by the terms involving $\Delta_{0,4}$ in $\overline{\overline{\boldsymbol{\eta}}}_{\boldsymbol{1}}$ and $\tilde{\gamma}_{0,4}, \tilde{\kappa}_{0,4}$ in $\overline{\overline{\boldsymbol{\eta}}}_{\boldsymbol{3}}$. As the subscripts indicate, these terms stem from the bias and drive alignment voltage components, given by:

$$ {\omega_{0,\lambda,4}}^2 \Delta_{0,4} = -\frac{\varepsilon_0 V_0 V_4}{10\rho\pi h {g_0}^3} j \sin 2\delta \tag{5.45} $$

$$ \tilde{\gamma}_{0,4} = -\frac{\varepsilon_0 V_0 V_4}{10\rho\pi h {g_0}^3} j \sin 2\delta \tag{5.46} $$

$$ \tilde{\kappa}_{0,4} = -\frac{3\varepsilon_0 V_0 V_4}{10\rho\pi h {g_0}^3} j \sin 2\delta \tag{5.47} $$

These terms are obtained from the elements in the electrostatic force coefficient matrices $\overline{\overline{\boldsymbol{A}}}_{\boldsymbol{1}}$ and $\overline{\overline{\boldsymbol{A}}}_{\boldsymbol{3}}$ involving $\zeta_4^+ + \zeta_4^-$, and can be used to negate the imperfection-induced drive misalignment. This is shown in (5.42) when evaluating the off-diagonal elements.

In $\overline{\overline{\boldsymbol{\eta}}}_{\boldsymbol{2}}(t)$, ν is given by:

$$ \nu = -\frac{\varepsilon_0 {V_\lambda}^2}{40\rho\pi h {g_0}^3} j \sin 3\delta \tag{5.48} $$

The parametric pumping voltage amplitude V_λ scales the quadratic electrostatic force. ν and ϕ_λ are important parameters used to tune the parametric excitation amplitude and phase.

The definition of the remaining terms in (5.41) are given in Appendix E.

Drive dynamics

The single-degree-of-freedom approximation of the drive equation in (5.41) is given by:

$$ \ddot{X} + 2\Gamma\dot{X} + \left({\omega_{0,\lambda,4}}^2 + {\omega_m}^2 \Delta_m \cos 4\Theta_\omega\right) X - \nu \cos(\omega t + \phi_x + \phi_\lambda) \frac{X^2}{g_0} + \gamma_{0,\lambda,4} \frac{X^3}{{g_0}^2} = \chi \cos \omega t \left(1 + c_{XX} \frac{X^2}{{g_0}^2}\right) \tag{5.49} $$

where $c_{XX} = 9/4$.

Applying the averaging procedure on (5.49) yields the following results for the drive frequency and resonant drive amplitude:

$$\omega_X{}^2 = \omega_{0,\lambda,4}{}^2 + \omega_m{}^2\Delta_m \cos 4\Theta_\omega - \frac{3}{4}\nu \cos\phi_\lambda \frac{x}{g_0} + \frac{3}{4}\gamma_{0,\lambda,4}\frac{x^2}{g_0{}^2} \tag{5.50}$$

$$x_r = \frac{\chi\left(1 + c_{XX}\frac{x_r{}^2}{4g_0{}^2}\right)}{2\Gamma_X\omega_X} \tag{5.51}$$

where the effective drive damping coefficient Γ_X is:

$$\Gamma_X = \Gamma - \frac{\frac{\nu}{4}\sin\phi_\lambda}{2\omega_X}\left(\frac{x}{g_0}\right) \tag{5.52}$$

Similar to the linear parametric excitation case in (5.21), the parametric pumping voltage can have parametric amplification ($\sin\phi_\lambda < 0$) or attenuation ($\sin\phi_\lambda > 0$) effects on the drive amplitude. An important difference between (5.21) and (5.52) is that in (5.52), the parametric amplification/attenuation effect is scaled linearly by the drive amplitude ratio x/g_0. As such, compared to the linear parametric excitation case, a larger ν is required to yield the same amplification/attenuation effect, thus necessitating a larger parametric pumping voltage amplitude. For the same parametric pumping voltage amplitude, the parametric excitation from the quadratic electrostatic force is generally weaker than the linear electrostatic force due to this scaling.

Sense dynamics

The approximated sense equation of motion in (5.41) is given by:

$$\begin{aligned}\ddot{Y} + 2\Gamma\dot{Y} + \Bigg\{&\omega_{0,\lambda,4}{}^2 - \omega_m{}^2\Delta_m \cos 4\Theta_\omega + 2\nu\cos(\omega t + \phi_x + \phi_\lambda)\frac{X}{g_0} \\ &- \frac{\chi c_{XY}}{g_0}\cos\omega t\frac{X}{g_0} + \kappa_{0,\lambda,4}\frac{X^2}{g_0{}^2}\Bigg\}Y \\ &= -G_\Omega\Omega\dot{X} - \left(\omega_m{}^2\Delta_m \sin 4\Theta_\omega + \omega_{0,\lambda,4}{}^2\Delta_{0,4}\right)X - \tilde{\gamma}_{0,4}\frac{X^3}{g_0{}^2}\end{aligned} \tag{5.53}$$

where $\omega = \omega_X$.

The coefficient of Y is composed of terms with various orders of drive displacement dependency. The quadratic electrostatic forces contribute to the terms with a linear dependence on the drive displacement.

Applying the averaging procedure on (5.53) gives the rate and quadrature outputs identified in (5.3):

$$\overline{\boldsymbol{y}} = -\frac{\begin{bmatrix} {\omega_X}^2 - {\omega_Y}^2 + \lambda_{1,r} & 2\Gamma\omega_X + \lambda_{2,r} \\ 2\Gamma\omega_X - \lambda_{2,r} & -{\omega_X}^2 + {\omega_Y}^2 + \lambda_{1,r} \end{bmatrix} \begin{bmatrix} f_\Delta \\ f_\Omega \end{bmatrix}}{{P_{1,r}}^2 - P_{2,r}^+ P_{2,r}^-} \tag{5.3}$$

where the general expressions of the energy dissipation parameters $P_{1,r}$, $P_{2,r}^+ P_{2,r}^-$ in terms of $\overline{\omega}^2$, $\lambda_{1,r}$ and $\lambda_{2,r}$ have been obtained in (3.62) and (5.4), revisited here:

$$P_{1,r} = 2\Gamma\omega_X \tag{3.62}$$

$$P_{2,r}^{\pm} = \left({\lambda_{1,r}}^2 + {\lambda_{2,r}}^2\right)^{\frac{1}{2}} \pm \left(-{\omega_X}^2 + {\omega_Y}^2\right) \tag{5.4}$$

The sense frequency ${\omega_Y}^2$ and the phase-decomposed parametric excitation amplitude components $\lambda_{1,r}$ and $\lambda_{2,r}$ are given by:

$${\omega_Y}^2 = {\omega_{0,\lambda,4}}^2 - {\omega_m}^2 \Delta_m \cos 4\Theta_\omega + \nu \cos\phi_\lambda \frac{x}{g_0} + \kappa_{0,\lambda,4} \frac{x^2}{2{g_0}^2} \tag{5.54}$$

$$\lambda_{1,r} = \nu \cos\phi_\lambda \frac{x}{2g_0} + \kappa_{0,\lambda,4} \frac{x^2}{4{g_0}^2} \tag{5.55}$$

$$\lambda_{2,r} = -\nu \sin\phi_\lambda \frac{x}{2g_0} + \frac{\chi}{4g_0} c_{XY} \frac{x}{g_0} \tag{5.56}$$

Comparing (5.50) with (5.54) and (5.55), the contribution of the quadratic electrostatic force in the terms involving ν are of opposite signs. As such, depending on the chosen parametric pumping voltage phase ϕ_λ, the parametric pumping voltage hardens either the drive or the sense mode while softening the other. This can be used for nonlinear frequency balancing $\left(-{\omega_X}^2 + {\omega_Y}^2 + \lambda_{1,r} = 0\right)$, subjected to the following conditions:

- If $\cos 4\Theta_\omega > 0$, $\cos\phi_\lambda < 0$ is required
- If $\cos 4\Theta_\omega < 0$, $\cos\phi_\lambda > 0$ is required

This contrasts the effects of the cubic electrostatic forces for the previous electrostatic configurations considered, where the cubic nonlinearities always soften both the drive and sense modes and nonlinear frequency balancing purely relies on the difference of the corresponding softening rates. In (5.50), (5.54) and (5.55), the cubic electrostatic forces contribute to ${\omega_X}^2$, ${\omega_Y}^2$ and $\lambda_{1,r}$ through the terms with quadratic drive amplitude dependence.

Since $\kappa_{0,\lambda,4} < 0$ and $\gamma_{0,\lambda,4} < 0$, similarly, the cubic electrostatic forces soften both the drive and sense modes. Since these terms are subjected to quadratic scaling by the drive amplitude ratio x/g_0, the contributions of the cubic electrostatic forces are relatively small compared to the quadratic electrostatic forces, particularly at lower drive amplitudes.

The total linear elastic coupling force amplitude is:

$$f_\Delta = -x\left({\omega_m}^2\Delta_m \sin 4\Theta_\omega + {\omega_{0,\lambda,4}}^2\Delta_{0,4}\right) - \frac{3}{4}\tilde{\gamma}_{0,4}\frac{x^3}{{g_0}^2} \tag{5.57}$$

The presence of the forces represented by the terms involving $\Delta_{0,4}$ and $\tilde{\gamma}_{0,4}$ in (5.53) results in additional forces components acting in phase/antiphase with the imperfection-induced linear elastic coupling force. As such, these forces have the potential to align the drive force.

5.4.3. Trimming

As discussed in Section 5.4.1, to replicate the output of a trimmed device without involving a rate-dependent balancing voltage, the linear elastic coupling force must be eliminated and nonlinear frequency balancing must be achieved. The following investigates the conditions to achieve these aims.

Drive force alignment requires the elimination of the total linear elastic coupling force, that is, setting f_Δ in (5.57) to zero. This imposes the following condition for the drive alignment voltage:

$${\omega_{0,\lambda,4}}^2\Delta_{0,4} + \frac{3}{4}\tilde{\gamma}_{0,4}\frac{x^2}{{g_0}^2} = -{\omega_m}^2\Delta_m \sin 4\Theta_\omega \tag{5.58}$$

This condition involves fixing the phase of the electrostatic forces arising from the drive alignment voltage to be in antiphase with the misalignment-induced linear elastic coupling force. The required drive alignment voltage to satisfy (5.58) is drive amplitude-dependent due to the term involving the cubic stiffness coefficient $\tilde{\gamma}_{0,4}$. However, in practice this amplitude-dependency is negligible because the term involving $\tilde{\gamma}_{0,4}$ in (5.58) is diminished by the quadratic-ordered scaling by the drive amplitude ratio, being the result of cubic electrostatic forces. This term is orders of magnitude smaller than ${\omega_{0,\lambda,4}}^2\Delta_{0,4}$, noting from (5.45) and (5.46) that ${\omega_{0,\lambda,4}}^2\Delta_{0,4} = \tilde{\gamma}_{0,4}$. Unlike the balancing voltage used in the previous electrostatic configurations, the drive alignment voltage remains unchanged with angular rate variations.

Nonlinear frequency balancing requires satisfying the condition $\lambda_{1,r} = {\omega_X}^2 - {\omega_Y}^2$. The parametric pumping voltage can be used to achieve this. From (5.50), (5.54) and (5.55), the condition for nonlinear frequency balancing is:

$$\nu \cos \phi_\lambda = \frac{2{\omega_m}^2 \Delta_m \cos 4\Theta_\omega + (\gamma_4 - \kappa_4)\frac{3x^2}{4{g_0}^2}}{\frac{9}{4}\left(\frac{x}{g_0}\right)} \tag{5.59}$$

where γ_4, κ_4 are identical to $\gamma_{0,\lambda,4}, \kappa_{0,\lambda,4}$ in (E-2) and (E-3), but with V_0 and V_λ set to zero, so the difference $\gamma_4 - \kappa_4$ is proportional to ${V_4}^2$.

The nonlinear frequency balancing condition in (5.59) has been arranged to show the explicit role of the parametric pumping voltage amplitude and phase to restore nonlinear frequency balance when the right side of (5.59) is nonzero. Any combination of the parametric pumping voltage amplitude (dictating ν) and phase ϕ_λ can be used to satisfy (5.59).

For an ideal/trimmed device, $\Delta_m = 0$ and no drive alignment voltage is required, so $\gamma_4 = \kappa_4 = 0$. In this case, the right side of (5.59) nullifies and nonlinear frequency balancing is achieved without requiring the parametric pumping voltage, i.e. $\nu = 0$. This is identical to the perfect, nonlinear case for the basic electrostatic configuration investigated in Section 3.5.2 when the electrodes are continuous. On the other hand, in the presence of imperfections, the right side of (5.59) is generally nonzero, so a parametric pumping voltage must be applied to restore the nonlinear frequency imbalance. When the right side of (5.59) is kept constant such as the case of a fixed drive amplitude and a given imperfection magnitude, the required parametric pumping voltage phase ϕ_λ approaches $\pm\pi/2$ when $|\nu|$ increases.

The default nonlinear frequency balancing point occurs at the drive amplitude where the right side of (5.59) is nullified. Since $\kappa_4 < \gamma_4$, this requires $\cos 4\Theta_\omega < 0$. At other drive amplitudes, V_λ and ϕ_λ can be tuned to restore the nonlinear frequency balance at a chosen drive amplitude. However, this form of nonlinear frequency balancing cannot be achieved at low drive amplitudes as this requires a large ν to satisfy (5.59). This is because the quadratic nonlinearities associated with the parametric pumping voltage diminish at low drive amplitudes, unless compensated by larger parametric pumping voltage amplitudes.

Parametric pumping voltage amplitude and phase conditions for nonlinear frequency balancing

The following investigates the effects of the imperfection magnitude on the required parametric pumping voltage amplitude and phase combinations for nonlinear frequency balancing. In this investigation and throughout the remainder of this chapter, a system with

parameters as listed in Table 5.3 is used as the control, in addition to the parameters listed Table C.1.

Table 5.3: Parameters of control set of system

Parameter	Value
δ (°)	15
V_0 (V)	1
j	16
δE	5.9e-4
Θ_ω (°)	1
Γ (Hz)	56.5

In Table 5.3, the elastic modulus variation magnitude $\delta E = 5.9e-4$ corresponds to a linear frequency split of 4 Hz. For this investigation, two other systems with identical parameters to those in Table 5.3, but with $\delta E = 0$ and $1.5e-3$ are also considered, corresponding to the perfect device and a linear frequency split of 10 Hz respectively. The drive alignment voltage is calculated using (5.58). The parametric pumping voltage and phase combinations required for nonlinear frequency balancing are calculated based on (5.59). The phase ϕ_λ is varied from 0 to 2π and for each phase considered, the required amplitude V_λ is calculated. The drive voltage is regulated to fix the drive amplitude at $x/g_0 = 0.1$.

Figure 5.8 below plots the combinations of $V_\lambda \cos\phi_\lambda/2$ and $V_\lambda \sin\phi_\lambda/2$ required for nonlinear frequency balancing. Contours of constant parametric pumping voltage amplitudes

are also shown, represented as circles with radii matching the parametric pumping voltage amplitude.

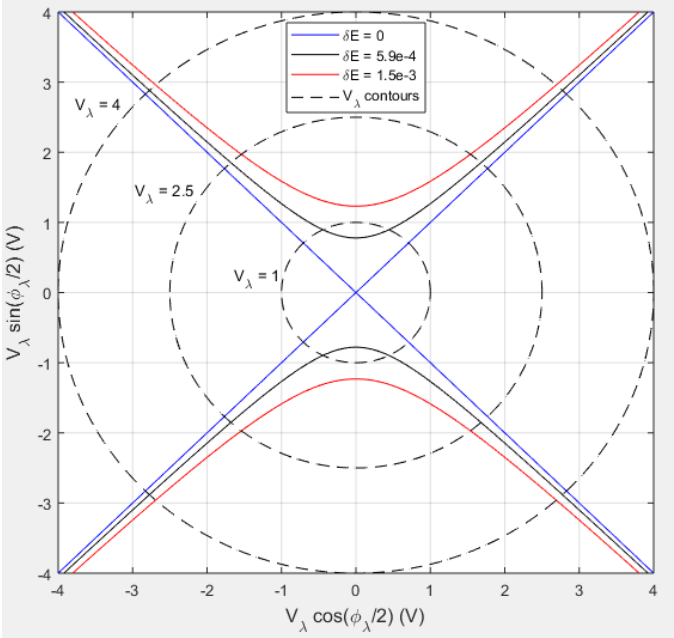

Figure 5.8: $(V_\lambda \cos \phi_\lambda/2, V_\lambda \sin \phi_\lambda/2)$ combinations required for nonlinear frequency balancing at multiple imperfection magnitudes with constant parametric pumping voltage amplitude contours

In Figure 5.8, for all imperfection magnitude cases, the parametric pumping voltage amplitude required to achieve nonlinear frequency balancing is minimised when $\cos \phi_\lambda/2 = 0$, i.e. $\phi_\lambda = \pm\pi$, indicating that selecting this parametric pumping voltage phase is most effective for nonlinear frequency balancing. However, at this phase, the required parametric pumping voltage amplitude to restore nonlinear frequency balance increases as the imperfection magnitude increases. When $\phi_\lambda = \pm\pi$, no parametric pumping voltage is required to achieve nonlinear frequency balancing for the perfect ring, i.e. the origin in Figure 5.8, but the required V_λ increases to $0.78\,V$ and $1.23\,V$ for $\delta E = 5.9e-4$ and $1.5e-3$ respectively. This is due to the increased nonlinear frequency imbalance when larger imperfections are present, thus requiring larger V_λ to counteract the larger nonlinear frequency imbalance.

For the perfect device, Figure 5.8 shows that the nonlinear frequency balance is retained at larger parametric pumping voltage amplitudes when $V_\lambda \cos \phi_\lambda/2 = \pm V_\lambda \sin \phi_\lambda/2$, i.e. $\phi_\lambda = \pm \pi/2$. In the presence of imperfections, Figure 5.8 shows that the corresponding plots for the cases of $\delta E = 5.9e-4$ and $1.5e-3$ approach the plot for the perfect device at larger V_λ. This indicates that nonlinear frequency balancing can still be approximately achieved by setting $\phi_\lambda = \pm \pi/2$ in the presence of imperfections, provided that the amplitude V_λ is sufficiently large. As such, this parametric pumping voltage phase condition is key to retaining the nonlinear frequency imbalance when the parametric pumping voltage amplitude is increased.

Using parametric pumping voltage to achieve nonlinear frequency balance

The following investigates the nonlinear frequency balancing effects of the parametric pumping voltage. The system in Table 5.3 is considered for this investigation. For the imperfections considered in this system, a drive alignment voltage of $V_4 = 1.7\ mV$ is required to nullify the linear elastic coupling as calculated using (5.58). A range of drive amplitudes up to 20% of the nominal capacitive gap is considered, and is attained by incrementally varying the drive voltage amplitude up to $V_{AC} = 21\ mV$. Figure 5.9(a) shows the frequency backbone curve of the drive frequency and the drive amplitude dependency of the frequency $\sqrt{\omega_Y{}^2 + \lambda_{1.r}}$ for the case without the parametric pumping voltage, shown as a difference relative to the linear drive frequency. Figure 5.9(b) shows the same set of results, but with the parametric pumping voltage amplitude and phase selected to achieve nonlinear frequency balancing at 10% of the nominal capacitive gap. The parametric pumping voltage amplitude and phase in this case are $V_\lambda = 779mV$ and $\phi_\lambda = 180°$, which is a nonlinear frequency balancing point at $(V_\lambda \cos\phi_\lambda/2\,, V_\lambda \sin\phi_\lambda/2) = (0{,}0.78)$ on the plot corresponding to $\delta E = 5.9e-4$ in Figure 5.8.

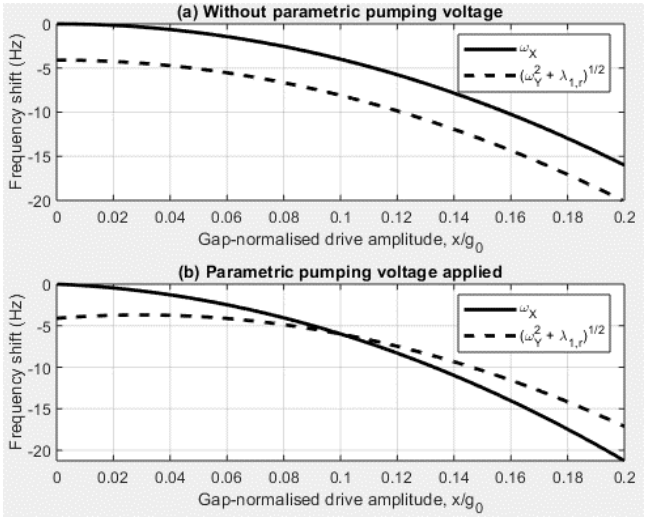

Figure 5.9: Variations of the frequencies ω_X and $\sqrt{\omega_Y{}^2 + \lambda_{1,r}}$ with the drive amplitude for the cases of (a) $V_\lambda = 0$ and (b) $V_\lambda \neq 0$ aimed at achieving nonlinear frequency balancing at $x/g_0 = 0.1$

In Figure 5.9(a), the frequencies do not coincide. Nonlinear frequency balancing point is not achieved as the frequency curves are approximately parallel. Without the parametric pumping voltage, the primary factor dictating the difference of the drive amplitude dependencies of these frequencies is the drive alignment voltage V_4 (compare the definitions of $\gamma_{0,\lambda,4}$ and $\kappa_{0,\lambda,4}$ in (E-2) and (E-3)), which is set to small values in this system due to the small imperfections.

In Figure 5.9(b), at the drive amplitude $x/g_0 = 0.2$, the reduction of the drive frequency ω_X from its linear value is increased to $21Hz$, compared to a decrease of $16Hz$ in Figure 5.9(a).

On the other hand, the frequency $\sqrt{{\omega_Y}^2 + \lambda_{1.r}}$ reduces less significantly in the presence of the parametric pumping voltage. These opposite effects are attributed to the quadratic electrostatic forces generated using the present scheme, as has been previously noted. The effects of the quadratic electrostatic forces are most significant at lower drive amplitudes, where the quadratic electrostatic forces dominate the nonlinear behaviour compared to the cubic electrostatic forces. The quadratic electrostatic forces result in a slight increase of the frequency $\sqrt{{\omega_Y}^2 + \lambda_{1.r}}$ up to $x/g_0 = 0.03$ before decreasing at higher drive amplitudes when the cubic electrostatic forces gain dominance. This result shows that the quadratic electrostatic forces promote nonlinear frequency balancing.

Effects of chosen drive amplitude on the required parametric pumping voltage amplitude for nonlinear frequency balancing

Figure 5.9(b) shows that nonlinear frequency balancing is achieved at $x/g_0 = 0.1$ when the parametric pumping voltage amplitude V_λ is set at a particular value. To ensure that nonlinear frequency balancing is achieved at other chosen drive amplitudes, V_λ must adjusted accordingly. The following investigates the effects of the drive amplitude on the required parametric pumping voltage amplitude for nonlinear frequency balancing when the parametric pumping voltage phase is fixed. The system in Table 5.3 is considered for this investigation, and another system with identical parameters except that $\delta E = 1.5e^{-3}$. Similar to the previous examples, the drive alignment voltage is calculated using (5.58), resulting in $V_4 = 1.7mV$ and $4.2mV$ for the cases of $\delta E = 5.9e^{-4}$ and $1.5e^{-3}$ respectively. The parametric pumping voltage phase is fixed at $\phi_\lambda = 180°$, and the required parametric pumping voltage amplitude V_λ for nonlinear frequency balancing is calculated using (5.59) as the drive amplitude is varied. Figure 5.10 shows the variation of the required parametric pumping voltage amplitude for nonlinear frequency balancing with the gap-normalised drive amplitude for both imperfection magnitude cases considered.

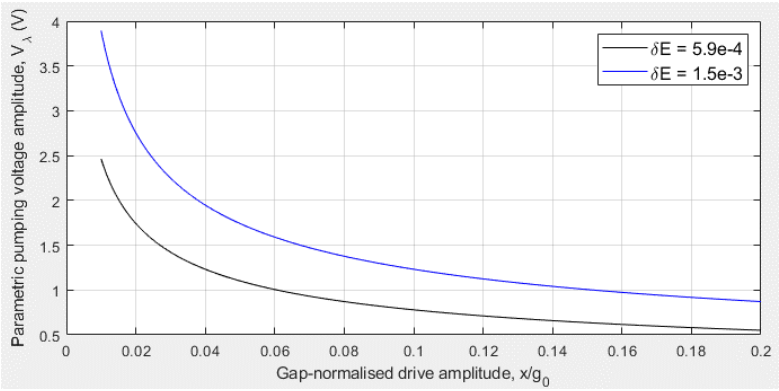

Figure 5.10: Effects of drive amplitude on the parametric pumping voltage amplitude required for nonlinear frequency balancing at different imperfection magnitudes

In Figure 5.10, the required parametric pumping voltage amplitude to achieve nonlinear frequency balancing is significantly increased at lower drive amplitudes. This is because while the imperfection magnitude is fixed, the quadratic electrostatic forces diminish significantly when the drive amplitude reduces, thus necessitating larger parametric pumping voltage amplitudes to compensate for this reduction and negate the imperfection-induced nonlinear frequency imbalance. A larger imperfection magnitude also results in an increase of the required parametric pumping voltage amplitude as this increases the magnitude of the nonlinear frequency imbalance.

In contrast to the case of nonlinear frequency balancing investigated in Section 5.3.3, the results in Figure 5.10 show that the present scheme enables nonlinear frequency balancing at larger drive amplitudes. This highlights an advantage of using the quadratic electrostatic forces.

5.4.4. Parametric amplification

When trimming is achieved with nonlinear frequency balancing and the negation of the linear elastic coupling force, $\overline{\boldsymbol{y}} = \overline{\boldsymbol{y}}_{\boldsymbol{\lambda 2}}$ and rate output amplification is achieved through the modified energy dissipation rate. From (5.6), the effective damping on the sense mode is $2\Gamma_Y\omega_X = 2\Gamma\omega_X - \lambda_{2,r}$ where the parametric excitation amplitude component $\lambda_{2,r}$ can have effective damping reducing effects, and is key to achieving parametric amplification of the rate output. Using the definition of $\lambda_{2,r}$ in (5.56), the effective sense damping coefficient Γ_Y is:

$$\Gamma_Y = \Gamma + \frac{\frac{\nu}{2}\sin\phi_\lambda - \frac{\chi}{4g_0}c_{XY}}{2\omega_X}\left(\frac{x}{g_0}\right) \tag{5.60}$$

Compared to the effective drive damping coefficient in (5.52), the terms involving ν have opposite signs, in a manner similar to the effect of ν on the frequencies ω_X and $\sqrt{{\omega_Y}^2 + \lambda_{1.r}}$. This indicates that the parametric pumping voltage results in asymmetric effects on the modal energy dissipation rates. This contrasts the linear parametric excitation where both modes are amplified/attenuated by the parametric pumping voltage (see discussion in Section 5.3.2). Consequently, parametric amplification of the rate output results in attenuation of the drive amplitude, hence the Coriolis force. However, in practice, this can be prevented by the AGC, which fixes the drive amplitude to compensate for the parametric attenuation of the drive mode. Secondly, the potential parametric attenuation of the drive amplitude is limited. Comparing the terms involving ν in (5.52) and (5.60), when ν is sufficiently large to approach parametric resonance of the sense mode such that $\Gamma_Y \approx 0$, the effective drive damping in (5.52) is such

that $\Gamma_X \approx 3\Gamma/2$ so the parametric attenuation is limited to a $1/3$ reduction of the drive amplitude.

From (5.59), it has been established that the nonlinear frequency balancing condition imposes a condition on the value of $\nu \cos\phi_\lambda$ and that any feasible $(V_\lambda, \phi_\lambda)$ combination can be used to achieve this. However, when parametric amplification is considered, each $(V_\lambda, \phi_\lambda)$ combination results in a different value of $\nu \sin\phi_\lambda$ in (5.60), hence varying the magnitude of parametric amplification attained. Based on (5.60) and noting that $\nu < 0$, the chosen phase ϕ_λ has the following effects:

- when $\sin\phi_\lambda > 0$, $\Gamma_Y < \Gamma$. Effective damping decreases and rate output amplification occurs.
- when $\sin\phi_\lambda < 0$, $\Gamma_Y > \Gamma$. Effective damping increases and rate output attenuation occurs.

where the former phase condition is desirable. As such, the specific $(V_\lambda, \phi_\lambda)$ combinations satisfying (5.59) while yielding large, negative values of $\nu \sin\phi_\lambda$ in (5.60) are most desirable for maximising the rate output amplification while retaining nonlinear frequency balance. This corresponds to a large V_λ and a phase at $\phi_\lambda \approx \pi/2$.

Effects of parametric pumping voltage and phase on parametric amplification/attenuation

The following investigates the magnitudes of the parametric amplification or attenuation attained when selecting various combinations of parametric pumping voltage amplitude and phase achieving nonlinear frequency balance. For this investigation, the systems for the results in Figure 5.8 corresponding to the perfect device and $\delta E = 5.9e-4$ are considered. The drive alignment voltage V_4 for both imperfection magnitudes are calculated in a similar manner and the drive voltage amplitude V_{AC} is tuned to fix a drive amplitude of $x/g_0 = 0.1$. Figure 5.11 re-plots the combinations of $V_\lambda \cos\phi_\lambda/2$ and $V_\lambda \sin\phi_\lambda/2$ in Figure 5.8 required for nonlinear frequency balancing for both imperfection magnitudes. Contours of the calculated values of $\lambda_{2,r}/(2\Gamma\omega_X)$ at various $(V_\lambda \cos\phi_\lambda/2\,, V_\lambda \sin\phi_\lambda/2)$ combinations are also shown, which are determined using (5.56) and the definition of the drive frequency in (5.50). $\lambda_{2,r}/(2\Gamma\omega_X) > 0$ and $\lambda_{2,r}/(2\Gamma\omega_X) < 0$ correspond to parametric amplification and attenuation respectively (see (5.6)). Points A and C have also been shown to indicate the $(V_\lambda, \phi_\lambda)$ combinations corresponding to $\lambda_{2,r}/(2\Gamma\omega_X) \approx 0$ for $\delta E = 0$ and $5.9e^{-4}$ respectively, while points B and D yield $\lambda_{2,r}/(2\Gamma\omega_X) \approx 0.75$. The $(V_\lambda, \phi_\lambda)$ combination at point C is used to achieve the nonlinear frequency balancing shown in Figure 5.9(b)

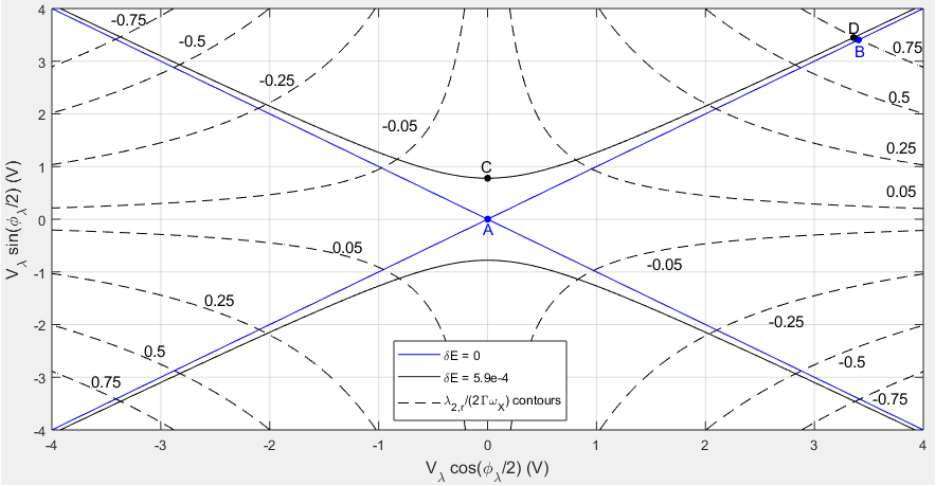

Figure 5.11: $(V_\lambda \cos \phi_\lambda/2\,, V_\lambda \sin \phi_\lambda/2)$ combinations required for nonlinear frequency balancing at multiple imperfection magnitudes and the parametric amplification/attenuation contours

Figure 5.11 shows that parametric amplification is attained when $V_\lambda \cos(\phi_\lambda/2)$ and $V_\lambda \sin(\phi_\lambda/2)$ are of the same signs, i.e. $0 < \phi_\lambda < \pi$ or $-2\pi < \phi_\lambda < -\pi$, and that increased parametric amplification is attained further away from the origin, i.e. at larger parametric pumping voltage amplitudes. On the other hand, larger parametric pumping voltage amplitudes increase the parametric attenuation when $V_\lambda \cos(\phi_\lambda/2)$ and $V_\lambda \sin(\phi_\lambda/2)$ are of opposite signs, i.e. $-\pi < \phi_\lambda < 0$ or $\pi < \phi_\lambda < 2\pi$. As such, parametric pumping voltage phase within these ranges should be avoided.

Modifying the parametric pumping voltage amplitude and phase by following along the points on the plots in Figure 5.11 allows the magnitude of parametric amplification/attenuation to be adjusted while retaining nonlinear frequency balance. Figure 5.12(a) and (b) below show the rate sensitivity gain G_S achieved for the cases of $\delta E = 0$ and $5.9e-4$ respectively when the parametric pumping voltage amplitude V_λ is varied by following along the points on the plots in Figure 5.11 where $V_\lambda \cos(\phi_\lambda/2) \geq 0$ and $V_\lambda \sin(\phi_\lambda/2) \geq 0$. In these results, the rate sensitivity gain G_S is calculated relative to the rate sensitivity at points A and C, S_A and S_C, for the corresponding perfect/imperfect ring cases, given by:

$$G_S|_{\delta E=0} = \frac{S}{S_A} \text{ or } G_S|_{\delta E=5.9e-4} = \frac{S}{S_C}$$

FE results are also shown using $(V_\lambda, \phi_\lambda)$ combinations from point A to B in Figure 5.11 for the perfect ring case and from point C to D for the $\delta E = 5.9e-4$ case. The range of V_λ considered is limited for the FE results because higher levels of parametric amplification result in increased durations of the transient study to achieve steady state, due to the reduced sense mode energy dissipation rate.

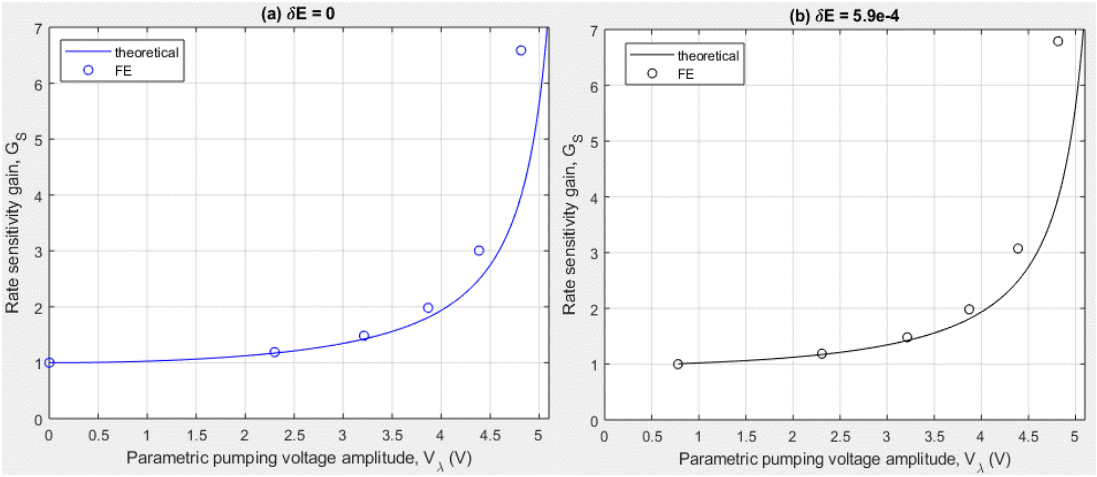

Figure 5.12: Effect of parametric pumping voltage amplitude on the rate sensitivity gain for (a) ideal/trimmed and (b) imperfect rings

Comparing Figure 5.12(a) and (b), for lower rate sensitivity gains, the presence of imperfections significantly increases the required parametric pumping voltage amplitude. This is due to the pre-existing nonlinear frequency imbalance in imperfect devices. On the other hand, the presence of imperfections has minimal impact on the gain attained at larger parametric pumping voltage amplitudes. The theoretical results show that a rate sensitivity gain of 7 is attained when $V_\lambda \approx 5V$ with or without imperfections. This demonstrates the ability of large parametric pumping voltage amplitudes to desensitise the rate sensitivity gain to the effects of imperfection.

The FE results are in good agreement with the theoretical results at lower rate sensitivity gains, but the theoretical results underestimate the rate sensitivity gain attained at larger V_λ. One possible explanation is the electrostatic fringing effects at larger V_λ. Also, the present analysis is based on neglecting sense-to-drive back coupling. As the sense amplitude amplifies while the drive amplitude is fixed, the accuracy of this assumption decreases. Larger V_λ can also result in non-resonant, hard excitation of higher order modes. A Fourier transform of the ring radial displacements in (C-1) from the FE results shows the presence of a response from the $n = 3$ mode pair of the same order of magnitude as the sense amplitude.

Comparing Figure 5.12(a) and (b) against that using the linear electrostatic force in Figure 5.5 shows that the required parametric pumping voltage amplitude is an order of magnitude higher while yielding the same rate sensitivity gain. This is because the quadratic electrostatic force is generally diminished by the drive amplitude ratio x/g_0, thus requiring a larger V_λ to compensate for this and match the net parametric excitation force amplitude of the corresponding linear electrostatic force. This is clear when comparing (5.27) and (5.56). When $\lambda_{2,r}$ is equal between both cases, $|\nu| > |{\omega_\lambda}^2|$. The need for a larger parametric pumping voltage amplitude V_λ to generate the same level of parametric amplification is a disadvantage

of using the quadratic electrostatic force for this purpose compared to using the linear electrostatic force.

5.4.5. Summary

The quadratic-ordered electrostatic forces can be used to generate the required phase-tuneable parametric excitation for rate output amplification. In the present scheme, this is achieved in conjunction with drive force alignment and nonlinear frequency balancing to retain a trimmed sensor output.

The trimming approach involving a combination of drive force alignment and nonlinear frequency balancing eliminates the requirement for a rate-dependent balancing force, so the device only operates in open-loop in the present scheme. These are achieved through the introduction of a drive alignment voltage component serving to negate the imperfection-induced linear elastic coupling between the modes, and a parametric pumping voltage with tuneable amplitude and phase for nonlinear frequency balancing. The quadratic electrostatic forces result in opposite effects on the drive and sense frequencies, thus promoting nonlinear frequency balancing. In contrast to the use of linear electrostatic forces, the quadratic electrostatic forces enable nonlinear frequency balancing to be achieved at larger drive amplitudes, which is advantageous for Coriolis force amplification. It is found that for a given imperfection magnitude and drive amplitude, multiple combinations of parametric pumping voltage amplitude and phase are well-suited for nonlinear frequency balancing. However, the amplitude and phase combinations yielding the greatest rate output parametric amplification effects are the most desirable.

The quadratic electrostatic force, being nonlinear, is weaker than the linear electrostatic force due to the drive amplitude dependency. This results in smaller magnitudes of the generated parametric excitation. As such, larger parametric pumping voltage amplitudes are generally required to yield the same parametric amplification effect as the corresponding linear parametric excitation. However, larger parametric pumping voltage amplitudes have demonstrated the ability to desensitise the attained rate sensitivity gain to the effects of imperfection. FE results have also been shown, confirming the potential of the present scheme to enhance the rate sensitivity.

5.5. Summary and conclusions

In this chapter, the exploitation of the electrostatic forces to enhance rate sensitivity while ensuring trimmed rate output and nullified quadrature output has been investigated. Approaches involving the use of linear and quadratic electrostatic forces have been considered. The key feature of these schemes is a phase-tuneable parametric excitation, and the component

of the parametric excitation responsible for rate output amplification is in quadrature with the self-induced parametric excitation.

The approach involving the linear electrostatic force involves introducing a phase-tuneable parametric pumping voltage component, and is a direct extension of the electrostatic configuration used in Chapter 4 to negate the self-induced parametric excitation. Due to the similarity of the electrostatic configuration used, trimming is similarly achieved using rate-dependent balancing voltage components, and the potential of using the balancing voltage component for closed-loop rate sensing is similarly considered. The special case of nonlinear frequency balancing is first investigated, as this condition desensitises the balancing voltage to angular rate changes, in which case the device only operates in open-loop. Multiple restrictions involving the chosen drive amplitude, imperfection and electrode span apply for the conditions to achieve nonlinear frequency balancing through the use of linear electrostatic forces for parametric excitation. Most notably, nonlinear frequency balancing cannot be achieved beyond a limiting drive amplitude, thus limiting the Coriolis force magnitude. Without nonlinear frequency balancing, the device can operate in both open and closed-loop. It is found that the nonlinear frequency imbalance improves closed-loop rate sensing performance by minimising the closed-loop bias rate and increasing the closed-loop rate sensitivity. These performance enhancements are reinforced further by increasing the parametric pumping voltage amplitude, which also amplifies the sense amplitude and open-loop rate sensitivity. FE results have also been included, confirming the ability of the linear electrostatic forces to enhance the open-loop rate sensitivity.

The use of the quadratic electrostatic forces for phase-tuneable parametric excitation is similarly achieved using a phase-tuneable parametric pumping voltage component. However, an alternative trimming approach without involving rate-dependent balancing voltage components has been considered. This form of trimming is achieved through a combination of nonlinear frequency balancing and drive force alignment. A drive alignment voltage component is introduced to negate the imperfection-induced linear elastic coupling, and the parametric pumping voltage is able to achieve nonlinear frequency balancing. It is found that the quadratic electrostatic forces stemming from the parametric pumping voltage result in opposite effects on the drive and sense frequencies, thus promoting nonlinear frequency balancing. This avoids the restrictions to achieving nonlinear frequency balancing when linear electrostatic forces are used for parametric excitation. Multiple combinations of parametric pumping voltage amplitude and phase can be used to achieve nonlinear frequency balance, with each combination resulting in different magnitudes of parametric amplification or attenuation of the rate output. The combinations yielding maximised parametric amplification have been identified and the ability of the parametric pumping voltage to enhance the rate

sensitivity has been validated using FE results. Compared to the use of linear electrostatic forces, the parametric excitation magnitude when using quadratic electrostatic forces is generally smaller. As such, larger parametric pumping voltage amplitudes are required to attain the same parametric amplification effect as the case when linear electrostatic forces are used.

The investigations in this chapter demonstrate the ability of using electrostatic forces to replicate the performance of higher Q factor devices without reducing the mechanical damping. Specifically, the use of quadratic electrostatic forces to amplify the rate output is an example where, through strategic implementations, electrostatic nonlinearities can enhance rate sensing performance. The proposed schemes can be implemented at larger drive amplitudes. The combination of amplified Coriolis force at larger drive amplitude operations and enhanced Q factor due to the phase-tuneable parametric excitation has the potential to enhance rate sensitivity significantly.

6. CONCLUSIONS AND FURTHER WORK

6.1. Introduction

This research has investigated electrostatic nonlinearities for capacitive ring-based CVG's in the context of rate measurement performance. The review of electrostatic nonlinearities in Chapter 1 concludes that electrostatic nonlinearities are often regarded as an undesirable feature causing rate sensing output to differ to that expected of a linear device. This research has focused on mitigating against the undesirable effects of electrostatic nonlinearity and focused on developing strategies to leverage electrostatic nonlinearities to enhance sensor performance. The main contributions of this research relate to modelling the dynamic behaviour of the ring under different electrostatic configurations and validating theoretical predictions against numerical results obtained using a commercial finite element package.

In this final chapter, the key findings of the research are summarised in relation to meeting the aims and objectives stated in Section 1.5. Scope for future research is also proposed.

6.2. Research summary and contributions

This research aims to investigate the use of electrostatic nonlinearities to improve rate sensing performance in capacitive ring-based CVG's. The following summarises the key investigations and main outcomes of the preceding chapters.

1) In Chapter 2, the linear dynamics of a forced vibrating ring is considered in the presence of structural and damping imperfections where the imperfections are modelled as circumferentially varying density, elastic modulus and damping to represent typical material defects in practice. The linear equations of motion for the drive and sense modes of the imperfect ring are derived, and it is found that the imperfection parameters depend on the orientation of the drive force relative to the principal axes of imperfection. The resulting modal frequency response varies with drive force orientation and these variations influence the modal amplitude, phase, bandwidth and resonant frequency. These quantities are used to identify the imperfection parameters, as special conditions apply for the resonant frequency and phase, and bandwidth when the drive force orientation aligns with the principal axes. The effect of angular rate on the linear forced modal response of the ring is then considered to establish the main effects of imperfections on rate sensing performance. Structural imperfections are found to degrade rate sensing performance by: i) reducing rate sensitivity; ii) introducing a non-zero rate offset bias; and iii) inducing a quadrature output. Damping imperfections are found to mainly contribute to the bias rate. In the presence of imperfection, the effect of neglecting sense-to-drive back coupling was investigated in detail because this assumption is made throughout the thesis. It is found

that neglecting back coupling is only valid when the modal bandwidth is sufficiently large compared to the gyroscopic and elastic back coupling. The back coupling amplifies the effects of structural imperfections, thus degrading rate sensing performance as well.

2) In Chapter 3, the influence of electrostatic nonlinearity on the performance of a standard capacitive ring based CVG was investigated for a device with evenly spaced electrodes inside and outside the ring. The electrodes were modelled as parallel-plate capacitors paired with a grounded ring, and the resulting electrostatic forces were incorporated into the equations of motion for the case when only bias and drive voltage components are applied. Modelling the nonlinear electrostatic force as a power series to cubic-order it is found that the bias voltage dominates the electrostatic nonlinearities, resulting in self-induced parametric excitation and amplitude-dependent drive and sense frequencies. The primary mechanisms influencing sensor output compared to that of a linear, trimmed device are caused by linear elastic coupling force and nonlinear frequency imbalance. These effects negatively impact sensor performance by reducing rate sensitivity, and introducing bias and quadrature errors. The nonlinear frequency imbalance stems from a mismatch between the drive-sense frequency split and the self-induced parametric excitation amplitude. Nonlinear frequency balancing is achieved naturally by using 16 or 32 electrodes, but for the 8 electrode design nonlinear frequency balancing is only achieved for the continuous electrode case.

3) Forces stemming from linear elastic coupling and nonlinear frequency imbalance must be counteracted to restore linear, trimmed sensor output. In Chapter 4, this is achieved by generating specific nonlinear electrostatic forces with the purpose of negating these forces. A general framework is proposed and developed to determine the necessary electrostatic forces through a strategic, goal-based manipulation of the voltage applied to each electrode. An approach that negates the self-induced parametric excitation is developed that requires two additional voltage components to be applied, in addition to the bias and drive voltages. These are: i) a parametric pumping voltage to generate a linear parametric excitation in antiphase with the self-induced parametric excitation, and ii) a balancing voltage serving to nullify the quadrature output by replicating the sense mode force balance of the linear, ideal/trimmed case. The approach developed was applied and it was found that the self-induced parametric excitation can be negated. It is found that negating the self-induced parametric excitation suppresses the nonlinear drive amplitude dependency of the rate sensitivity and bias rate. The extent of this effect depends on the magnitude of imperfection, drive misalignment and electrode span. However, the quadrature output is not generally nullified. The balancing voltage complements negation of the self-induced parametric excitation by enabling the sense response to approach linear and trimmed behaviour at increased drive amplitudes regardless of the imperfections. The

balancing voltage is rate-dependent and can be used for closed-loop rate sensing unless frequency matching occurs.

4) To further enhance rate sensitivity a phase tuneable parametric excitation was considered in Chapter 5, in addition to negating the effects of the linear elastic coupling force and nonlinear frequency imbalance. Linear and quadratic electrostatic forces can be used to achieve this purpose and both schemes were investigated. The use of linear electrostatic forces is an extension of the implementation used to linearise sensor output in Chapter 4, but with a variable-phase parametric pumping voltage. In both schemes, the resulting parametric excitation reduces the energy dissipation rate, effectively increasing the Q factor of the sense mode and achieving parametric amplification of the rate output. Both approaches were investigated and both showed significantly improved rate sensitivity. To maintain trimmed sensor output together with amplified response, the quadratic parametric amplification scheme is advantageous compared to the linear parametric amplification scheme because the quadratic nonlinearities cause the drive and sense frequencies to change in opposition, and so is well suited to reducing or eliminating the nonlinear frequency imbalance. However, the magnitude of the parametric excitation from quadratic electrostatic forces is smaller. As such, larger parametric pumping voltages are generally required to attain the same magnitude of rate output amplification as that when using linear electrostatic forces.

The analysis to understand the effects of electrostatic nonlinearities in capacitive CVG's is quite complex because the nature of the electrostatic nonlinearities vary depending on the chosen electrostatic configuration of the device. The present research has shown that through careful implementation, electrostatic nonlinearities do not necessarily degrade rate sensing performance and have potential to enhance sensing performance instead. The research conducted provides a proof of principle that electrostatic nonlinearities can be used to enhance rate sensing performance, beyond that expected of standard ideal devices. The applicability of the proposed general framework for the manipulation of the electrostatic nonlinearities extends beyond the investigations presented so far. The next section discusses scope for future research on the exploitation of electrostatic nonlinearities to develop high performance devices.

6.3. Future research

The present research could be extended in the following areas.

6.3.1. Imperfection characterisation in the presence of electrostatic nonlinearities

In Chapter 2, the linear modal frequency responses have been used to characterise the imperfections, where the principal axes orientations are of particular interest. However, in practice, perfect linearity of the modal response is typically not achievable. The later chapters have shown that electrostatic nonlinearities are present even at low drive amplitudes, albeit having a less significant effect. Even for the case of low drive amplitudes, the strength of the electrostatic nonlinearities can be amplified with larger bias voltages. Although the present research on electrostatic nonlinearities only focuses on resonant operation, it is anticipated that the modal response across a range of drive frequencies is susceptible to electrostatic nonlinearity, potentially complicating the process of identifying the mechanical imperfection present in the ring.

For the case of perfect rings, studies on the nonlinear modal frequency response have been reported for both uncoupled and coupled mode cases [49], and the results clearly show how the frequency response varies depending on the form of the nonlinear electrostatic forces considered. The study in [49] shows the Duffing nonlinearity, when sufficiently strong, results in amplitude frequency responses not admitting one-to-one relationships between the amplitude and frequency. This is further complicated by the possibility of unstable operating points at some chosen amplitudes. When the mode-coupling electrostatic restoring forces are considered, the present research has shown that the drive and sense frequencies are non-coincident even for perfect rings. For the drive mode, the study in [49] has also shown that the nonlinear elastic coupling between the modes results in an additional peak in the amplitude frequency response, which is indicative of a nonlinear elastic back coupling from the sense mode. When imperfections are included, it is anticipated that these amplitude frequency response complexities will affect the respective variations when the drive force orientation is varied, in which case the measurement methods proposed in Chapter 2 must account for the electrostatic nonlinearities to obtain an accurate identification of the imperfection parameters.

The present research has only considered the case where the electrostatic configurations are perfect, involving evenly distributed electrodes and identical electrode spans. However, manufacturing tolerances of the device can result in slight mispositioning of the electrodes and geometric variations from electrode to electrode. Since previous research has shown that the electrostatic forces can be used to introduce artificial imperfections [45], it is of practical interest to investigate the aforementioned effects for potential electrostatic-induced imperfections such as frequency splits, and the effects on the resulting electrostatic nonlinearities.

6.3.2. Parametric amplification for bandwidth improvement

In Chapter 5, parametric amplification has been used to amplify the sense amplitude for the specific case when the drive frequency is fixed. This could be extended to off-resonance amplification of the sense response to sustain enhanced rate sensitivities in these cases. It is anticipated that this implementation is most beneficial when the imposed parametric excitation approaches parametric resonance and the quality factor is significantly enhanced, and could be used to suppress the accompanying bandwidth reduction for high quality factor operations in typical linear devices.

While the present research has shown that the form of electrostatic forces varies depending on the chosen electrostatic configuration, one study on comb drive actuated gyroscopes has demonstrated bandwidth improvements using electrostatic forces composed of only linear and cubic uncoupled restoring forces [55], achieved using a square rooted form of sinusoidal voltage. In this study, comparisons of the drive and sense amplitude frequency responses show that the parametric amplification compensates for off-resonant reductions of drive amplitudes by increasing the sensitivity of the sense mode to the Coriolis force, thus achieving a 'flattened' region on the sense amplitude frequency response. However, increasing the amplitude of this voltage decreases the maximum sense amplitude. In ring-based CVG's, it is of practical interest to consider how the electrostatic configuration can be manipulated to achieve this bandwidth improvement without reducing the peak sense amplitude.

In Chapter 2, it has been shown that the gyroscopic back coupling can result in splitting the peaks within the modal amplitude frequency responses and that the threshold of peak splitting similarly 'flattens' the peak region within the amplitude frequency responses. In this case, it is of practical interest to investigate the effects of the gyroscopic back coupling in the presence of electrostatic nonlinearities and the use of parametric amplification to replicate this effect. To achieve this, an investigation into the interaction between the fully coupled gyroscopic forces and the nonlinear electrostatic forces is required.

REFERENCES

[1] L. Foucault, "Sur les phénomènes d'orientation des corps tournants entraînés par un axe fixe à la surface de la Terre," in "CR Acad. Sci," 1852, vol. 35.

[2] C. Acar and A. Shkel, *MEMS Vibratory Gyroscopes-Structural Approaches to Improve Robustness*, 1 ed. Springer US, 2009.

[3] J. Sommeria, "Foucault and the rotation of the Earth," *Comptes Rendus Physique*, vol. 18, no. 9, pp. 520-525, 2017/11/01/ 2017.

[4] A. Lawrence, *Modern Inertial Technology : Navigation, Guidance, and Control*. New York, NY, UNITED STATES: Springer New York, 2001.

[5] Y. Pan *et al.*, "Observation and analysis of the quality factor variation behavior in a monolithic fused silica cylindrical resonator," *Sensors & Actuators: A. Physical*, vol. 260, pp. 81-89, 2017.

[6] F. Ayazi and K. Najafi, "A HARPSS polysilicon vibrating ring gyroscope," *Journal of Microelectromechanical Systems*, vol. 10, no. 2, pp. 169-179, 2001.

[7] J. T. Anders, "START vibrating gyroscope," in *IEE Colloquium on Measurement Using Resonant Sensing*, 1993, pp. 4/1-4/8.

[8] Koning and G. Menno, "Vibrating cylinder gyroscope and method," United States, 1988.

[9] D. D. Lynch, "Inertial Technology for the Future," *IEEE transactions on aerospace and electronic systems*, vol. AES-20, no. 4, X, p. 432, 1984.

[10] M. W. Putty, "A micromachined vibrating ring gyroscope," PhD, Electrical Engineering, The University of Michigan, 1995.

[11] S. Fujishima, T. Nakamura, and K. Fujimoto, "Piezoelectric vibratory gyroscope using flexural vibration of a triangular bar," in *45th Annual Symposium on Frequency Control 1991*, Los Angeles, CA, USA, 1991: IEEE, pp. 261-265.

[12] M. S. Weinberg and A. Kourepenis, "Error sources in in-plane silicon tuning-fork MEMS gyroscopes," *Journal of microelectromechanical systems*, vol. 15, no. 3, pp. 479-491, 2006.

[13] J. Bernstein, S. Cho, A. T. King, A. Kourepenis, P. Maciel, and M. Weinberg, "A micromachined comb-drive tuning fork rate gyroscope," in *IEEE Micro Electro Mechanical Systems*, Fort Lauderdale, FL, 1993: IEEE, pp. 143-148.

[14] J. Sun, H. Tang, Y. Wu, X. Xi, Y. Zhang, and X. Wu, "Research on cylindrical resonators' damping asymmetry trimming method utilizing damping characteristic of piezoelectric electrodes," *AIP Advances*, vol. 8, no. 3, 2018.

[15] G. Sérandour, "Non-linear dynamics of vibratory rate sensors," PhD, University of Nottingham, 2005.

[16] D. Sparks *et al.*, "Chip-scale packaging of a gyroscope using wafer bonding," *Sensors and Materials*, vol. 11, pp. 197-207, 1999.

[17] S. W. Yoon, S. Lee, and K. Najafi, "Vibration sensitivity analysis of MEMS vibratory ring gyroscopes," *Sensors and Actuators A: Physical*, vol. 171, no. 2, pp. 163-177, 2011/11/01/ 2011.

[18] K. M. Harish, B. J. Gallacher, J. S. Burdess, and J. A. Neasham, "Experimental investigation of parametric and externally forced motion in resonant MEMS sensors," *Journal of Micromechanics and Microengineering*, vol. 19, no. 1, p. 015021, 2008/12/10 2008.

[19] Z. Hu, B. J. Gallacher, J. S. Burdess, C. P. Fell, and K. Townsend, "A digital signal processing-based control system for a micro-electromechanical systems vibrating gyroscope with parametric amplification and force rebalance control," *Proceedings of the Institution of Mechanical Engineers, Part I: Journal of Systems and Control Engineering*, vol. 227, no. 3, pp. 347-362, 2013/03/01 2013.

[20] N. Yazdi, F. Ayazi, and K. Najafi, "Micromachined inertial sensors," *Proceedings of the IEEE*, vol. 86, no. 8, pp. 1640-1659, 1998.

[21] S. D. Senturia, *Microsystem design*. Boston, London: Kluwer Academic Publishers, Norwell, 2001.

[22] G. G. Coriolis, "Mémoire sur les équations du mouvement relatif des systèmes de corps," *Journal de l'École polytechnique,* vol. 15, pp. 142-154, 1835.

[23] W. Soedel, *Vibrations of shells and plates* 3ed. New York: New York : Marcel Dekker, 2004.

[24] S. Timoshenko, *Vibration problems in engineering*, 5 ed. New York: Wiley, 1990.

[25] G. H. Bryan, "On the beats in the vibrations of a revolving cylinder or bell," in *Proceedings of the Cambridge Philosophical Society*, 1890, vol. 7, no. 24, pp. 101-111.

[26] J. Qingan, L. Yun, W. Wenqi, F. Zhen, L. Bing, and W. Xu, "Force to Rebalance Control of HRG and Suppression of Its Errors on the Basis of FPGA," *Sensors,* vol. 11, no. 12, pp. 11761-11773, 2011.

[27] *IEEE Standard Specification Format Guide and Test Procedure for Coriolis Vibratory Gyros*, 2004.

[28] B. J. Gallacher, Z. Hu, K. M. Harish, S. Bowles, and H. Grigg, "The Application of Parametric Excitation in MEMS Gyroscopes," in *ASME 2013 International Design Engineering Technical Conferences and Computers and Information in Engineering Conference*, Portland, Oregon, USA, 2013, vol. 7B, no. 55973, Volume 7B: 9th International Conference on Multibody Systems, Nonlinear Dynamics, and Control.

[29] R. Abdolvand, B. Bahreyni, J. E. Y. Lee, and F. Nabki, "Micromachined Resonators: A Review," *Micromachines,* vol. 7, no. 9, 2016.

[30] T. Veijola, H. Kuisma, J. Lahdenperä, and T. Ryhänen, "Equivalent-circuit model of the squeezed gas film in a silicon accelerometer," *Sensors and Actuators A: Physical,* vol. 48, no. 3, pp. 239-248, 1995/05/30/ 1995.

[31] C. Benvenuti *et al.*, "Vacuum properties of TiZrV non-evaporable getter films," *Vacuum,* vol. 60, no. 1, pp. 57-65, 2001/01/01/ 2001.

[32] C. Zener, "Internal Friction in Solids II. General Theory of Thermoelastic Internal Friction," *Physical Review,* vol. 53, no. 1, pp. 90-99, 01/01/ 1938.

[33] C. Zener, "Internal friction in solids," *Proceedings of the Physical Society,* vol. 52, no. 1, pp. 152-166, 1940/01/01 1940.

[34] S. T. Hossain, S. McWilliam, and A. A. Popov, "An investigation on thermoelastic damping of high-Q ring resonators," *International Journal of Mechanical Sciences,* vol. 106, pp. 209-219, 2016/02/01/ 2016.

[35] M. S. Andrei, "Micromachined gyroscopes: challenges, design solutions, and opportunities," in *SPIE's 8th Annual International Symposium on Smart Structures and Materials*, Newport Beach, CA, United States, 2001, vol. 4334, pp. 74-85.

[36] R. Eley, C. H. J. Fox, and S. McWilliam, "Anisotropy effects on the vibration of circular rings made from crystalline silicon," *Journal of Sound and Vibration,* vol. 228, no. 1, pp. 11-35, 1999/11/18/ 1999.

[37] S. McWilliam, J. Ong, and C. H. J. Fox, "On the statistics of natural frequency splitting for rings with random mass imperfections," *Journal of Sound and Vibration,* vol. 279, no. 1, pp. 453-470, 2005/01/06/ 2005.

[38] X. Xi, Y. Wu, X. Wu, Y. Tao, and X. Wu, "Investigation on standing wave vibration of the imperfect resonant shell for cylindrical gyro," *Sensors and Actuators A: Physical,* vol. 179, pp. 70-77, 2012/06/01/ 2012.

[39] P. Bisegna and G. Caruso, "Frequency split and vibration localization in imperfect rings," *Journal of Sound and Vibration,* vol. 306, no. 3, pp. 691-711, 2007/10/09/ 2007.

[40] S. A. Tobias, "Vibrations of elastic bodies of revolution containing imperfections: a theory of imperfection," PhD, University of Edinburgh, 1950.

[41] C. H. J. Fox, "A simple theory for the analysis and correction of frequency splitting in slightly imperfect rings," *Journal of Sound and Vibration,* vol. 142, no. 2, pp. 227-243, 1990/10/22/ 1990.

[42] Y. Zhang, X. Wu, Y. Wu, X. Xi, and Y. Tao, "Nodal vibration and pattern angle error analysis of the imperfect resonators for vibratory cylinder gyroscopes," *International Journal of Precision Engineering and Manufacturing,* vol. 17, no. 4, pp. 419-426, 2016/04/01 2016.

[43] J. Sun, Y. Wu, X. Xi, Y. Zhang, Y. Xin, and X. Wu, "Investigation of cylindrical resonators' damping asymmetry via analyzing Q factor circumferential distribution," *Sensors and Actuators A: Physical,* vol. 269, pp. 535-544, 2018/01/01/ 2018.

[44] B. J. Gallacher, J. Hedley, J. S. Burdess, A. J. Harris, A. Rickard, and D. O. King, "Electrostatic correction of structural imperfections present in a microring gyroscope," *Journal of Microelectromechanical Systems,* vol. 14, no. 2, pp. 221-234, 2005.

[45] B. Gallacher, J. Hedley, J. S Burdess, A. J Harris, A. Rickard, and D. King, *Electrostatic tuning of a micro-ring gyroscope*. 2004.

[46] A. K. Rourke, S. McWilliam, and C. H. J. Fox, "Multi-mode trimming of imperfect rings," *Journal of Sound and Vibration,* vol. 248, no. 4, pp. 695-724, 2001.

[47] A. K. Rourke, S. McWilliam, and C. H. J. Fox, "Multi-mode trimming of imperfect thin rings using masses at pre-selected locations," *Journal of Sound and Vibration,* vol. 256, no. 2, pp. 319-345, 2002/09/12/ 2002.

[48] D. Arifin and S. McWilliam, "Effects of electrostatic nonlinearity on the rate measuring performance of ring based Coriolis Vibrating Gyroscopes (CVGs)," *Sensors and Actuators A: Physical,* vol. 340, p. 113539, 2022/06/16/ 2022.

[49] P. M. Polunin and S. W. Shaw, "Self-induced parametric amplification in ring resonating gyroscopes," *International Journal of Non-Linear Mechanics,* vol. 94, pp. 300-308, 2017/09/01/ 2017.

[50] S. H. Nitzan *et al.*, "Self-induced parametric amplification arising from nonlinear elastic coupling in a micromechanical resonating disk gyroscope," (in eng), *Scientific reports,* vol. 5, p. 9036, Mar 12 2015.

[51] X. Zheng, H. Wu, Y. Lin, Z. Ma, and Z. Jin, "Linear parametric amplification/attenuation for MEMS vibratory gyroscopes based on triangular area-varying capacitors," *Journal of micromechanics and microengineering,* vol. 30, no. 4, p. 45010, 2020.

[52] Z. X. Hu, B. J. Gallacher, J. S. Burdess, C. P. Fell, and K. Townsend, "A parametrically amplified MEMS rate gyroscope," *Sensors and Actuators A: Physical,* vol. 167, no. 2, pp. 249-260, 2011/06/01/ 2011.

[53] Z. Hu, B. J. Gallacher, K. M. Harish, and J. S. Burdess, "An experimental study of high gain parametric amplification in MEMS," *Sensors and Actuators A: Physical,* vol. 162, no. 2, pp. 145-154, 2010/08/01/ 2010.

[54] C. H. Ahn *et al.*, "Encapsulated high frequency (235 kHz), high-Q (100 k) disk resonator gyroscope with electrostatic parametric pump," *Applied Physics Letters,* vol. 105, no. 24, 2014.

[55] L. A. Oropeza-Ramos and K. L. Turner, "Parametric resonance amplification in a MEMGyroscope," 2005. [Online]. Available: https://ieeexplore.ieee.org/document/1597785/.

[56] J. F. Rhoads and S. W. Shaw, "The Effects of Nonlinearity on Parametric Amplifiers," presented at the ASME 2008 International Design Engineering Technical Conferences and Computers and Information in Engineering Conference, 2008.

[57] H. Goldstein, *Classical mechanics*, Third edition, Pearson new international edition. ed. Harlow : Pearson, 2014.

[58] P. M. Polunin, "Nonlinearities and noise in micromechanical resonators : from understanding to characterization and design tools," PhD, Michigan State University.

[59] X. Zhou *et al.*, "Dynamic modulation of modal coupling in microelectromechanical gyroscopic ring resonators," *Nature Communications,* vol. 10, no. 1, 2019.

[60] S. G. Krantz, *Episodic History of Mathematics*. Washington, UNITED STATES: American Mathematical Society, 2010.

[61] A. Fargas-Marques, J. Casals-Terre, and A. M. Shkel, "Resonant Pull-In Condition in Parallel-Plate Electrostatic Actuators," *Journal of Microelectromechanical Systems,* vol. 16, no. 5, pp. 1044-1053, 2007.

[62] A. H. Nayfeh, M. I. Younis, and E. M. Abdel-Rahman, "Dynamic pull-in phenomenon in MEMS resonators," *Nonlinear Dynamics,* vol. 48, no. 1, pp. 153-163, 2007/04/01 2007.

[63] B. Chouvion, S. McWilliam, and A. A. Popov, "Effect of nonlinear electrostatic forces on the dynamic behaviour of a capacitive ring-based Coriolis Vibrating Gyroscope under severe shock," *Mechanical Systems and Signal Processing,* vol. 106, pp. 395-412, 2018/06/01/ 2018.

[64] B. J. Gallacher and J. S. Burdess, "Dynamic analysis of a microelectromechanical systems resonant gyroscope excited using combination parametric resonance," *Proceedings of the Institution of Mechanical Engineers. Part C, Journal of mechanical engineering science,* vol. 220, no. 9, pp. 1463-1479, 2006.

[65] A. H. Nayfeh, Mook, Dean T., *Nonlinear oscillations*. New York: John Wiley & Sons, 1979.

[66] N. W. McLachlan, *Ordinary non-linear differential equations in engineering and physical sciences / by N.W. McLachlan*. Oxford: Oxford : Clarendon Press, 1950.

[67] J. C. Butcher, *Numerical methods for ordinary differential equations*, Third edition. ed. Chichester, West Sussex, England : John Wiley & Sons, Ltd, 2016.

Appendix A: Integrals for Calculations of the Ring Energies

Kinetic energy

Removing the integral in (2.3) yields an expression for the cross sectional kinetic energy of the ring $\Delta E_k(\theta)$.

$$\Delta E_k(\theta) = \frac{BhRd\theta}{2}\sum_{p=0}^{\infty}\left(\mathrm{A}_p\cos p\theta + \mathrm{B}_p\sin p\theta\right) \tag{A-1}$$

where the coefficients A_p and B_p are given by:

$$\sum_{p=0}^{\infty}\left(\mathrm{A}_p\cos p\theta + \mathrm{B}_p\sin p\theta\right) \tag{A-2}$$

$$= \rho\left[1+\sum_{\sigma=1}^{\infty}\left(\delta\rho_\sigma\cos\sigma\Theta_{\rho,\sigma}\cos\sigma\theta + \delta\rho_\sigma\sin m\Theta_{\rho,\sigma}\sin\sigma\theta\right)\right]\sum_{i=0}^{2}\left(\xi_{E_k}^{i}\cos in\theta + \zeta_{E_k}^{i}\sin in\theta\right)$$

where $\xi_{E_k}^{i}$ and $\zeta_{E_k}^{i}$ are the coefficients describing the circumferential variation of $\left|d\underline{\boldsymbol{r}}/dt\right|^2$, given by:

$$\xi_{E_k}^{0} = R^2\Omega^2 + \frac{n^2+1}{2n^2}(X^2+Y^2)\Omega^2 - \frac{2}{n}\Omega\left(\dot{X}Y - X\dot{Y}\right) + \frac{n^2+1}{2n^2}\left(\dot{X}^2+\dot{Y}^2\right) \tag{A-3a}$$

$$\xi_{E_k}^{1} = 2RX\Omega^2 + \frac{2}{n}R\dot{Y}\Omega \tag{A-3b}$$

$$\zeta_{E_k}^{1} = 2RY\Omega^2 - \frac{2}{n}R\dot{X}\Omega \tag{A-3c}$$

$$\xi_{E_k}^{2} = \frac{n^2-1}{2n^2}\left[\dot{X}^2 - \dot{Y}^2 + (X^2-Y^2)\Omega^2\right] \tag{A-3d}$$

$$\zeta_{E_k}^{2} = \frac{n^2-1}{n^2}\left(\dot{X}\dot{Y} + XY\Omega^2\right) \tag{A-3e}$$

Integrating $\Delta E_k(\theta)$ along the circumference of the ring gives the total kinetic energy of the ring. The following observations simplify the resulting integral:

$$\int_0^{2\pi} \cos p\theta \, d\theta = \begin{cases} 2\pi, & p = 0 \\ 0, & p \neq 0 \end{cases}$$

$$\int_0^{2\pi} \sin p\theta \, d\theta = 0$$

Applying this observation and integrating the cross-sectional kinetic energy in (A-1) from $\theta = 0$ to 2π gives the following expression for the total ring kinetic energy:

$$E_k = \mathrm{A}_0 \pi B h R \tag{A-4}$$

From (A-1), A_0 is the mean cross sectional kinetic energy and is the only component that contributes to the total kinetic energy.

From (A-2), by multiplying the two trigonometric series, (A-2) can be rearranged as:

$$\sum_{p=0}^{\infty} \left(\mathrm{A}_p \cos p\theta + \mathrm{B}_p \sin p\theta\right) \tag{A-5}$$

$$= \rho \sum_{i=0}^{2} \left(\xi_{E_k}^i \cos in\theta + \zeta_{E_k}^i \sin in\theta\right)$$

$$+ \frac{\rho}{2} \sum_{i=0}^{2} \sum_{\sigma=1}^{\infty} \begin{bmatrix} \left(\xi_{E_k}^i \delta\rho_\sigma \cos\sigma\Theta_{\rho,\sigma} - \zeta_{E_k}^i \delta\rho_\sigma \sin\sigma\Theta_{\rho,\sigma}\right)\cos(\sigma + in)\theta \\ +\left(\zeta_{E_k}^i \delta\rho_\sigma \cos\sigma\Theta_{\rho,\sigma} + \xi_{E_k}^i \delta\rho_\sigma \sin\sigma\Theta_{\rho,\sigma}\right)\sin(\sigma + in)\theta \end{bmatrix}$$

$$+ \frac{\rho}{2} \sum_{i=0}^{2} \sum_{\sigma=1}^{\infty} \begin{bmatrix} \left(\xi_{E_k}^i \delta\rho_\sigma \cos\sigma\Theta_{\rho,\sigma} + \zeta_{E_k}^i \delta\rho_\sigma \sin\sigma\Theta_{\rho,\sigma}\right)\cos(\sigma - in)\theta \\ -\left(\zeta_{E_k}^i \delta\rho_\sigma \cos\sigma\Theta_{\rho,\sigma} - \xi_{E_k}^i \delta\rho_\sigma \sin\sigma\Theta_{\rho,\sigma}\right)\sin(\sigma - in)\theta \end{bmatrix}$$

To identify A_0, the left and right sides of (A-5) are compared. As such, the (i, σ, n) combinations of interest are such that $in = 0$, $\sigma + in = 0$ or $\sigma - in = 0$. From (A-2), $i \geq 0$ and $\sigma > 0$ so $\sigma + in \neq 0$ in all cases. As such, the second group of summation in (A-5) does not contribute to A_0. In the third summation group, the $\cos(\sigma - in)\theta$ component contributes to A_0 for the density variation components $\sigma = n$ and $\sigma = 2n$. Using these results, A_0 is:

$$\mathrm{A}_0 = \rho\xi_{E_k}^0 + \frac{\rho}{2}\left(\xi_{E_k}^1 \delta\rho_n \cos n\Theta_{\rho,n} + \zeta_{E_k}^1 \delta\rho_n \sin n\Theta_{\rho,n}\right) \tag{A-6}$$

$$+ \frac{\rho}{2}\left(\xi_{E_k}^2 \delta\rho_{2n} \cos 2n\Theta_{\rho.2n} + \zeta_{E_k}^2 \delta\rho_{2n} \sin 2n\Theta_{\rho,2n}\right)$$

Substituting (A-6) into (A-4) gives the total kinetic energy expression in (2.6) and (2.7a) - (2.7c).

The $n\theta$ variation component of the density in (2.5) has negligible contributions to the equations of motion. To demonstrate this, the portion of the kinetic energy associated with the $n\theta$ density variation coefficient, $\delta\rho_n$ is given by:

$$E_k|_{m=n} = \rho\pi BhR^2\left[\left(\delta\rho_n \cos n\Theta_{\rho,n} X + \delta\rho_n \sin n\Theta_{\rho,n} Y\right)\Omega^2 + \frac{\left(\delta\rho_n \cos n\Theta_{\rho,n} \dot{Y} - \delta\rho_n \sin n\Theta_{\rho,n} \dot{X}\right)}{n}\Omega\right] \tag{A-7}$$

Using Lagrange's equations in (2.15a) and (2.15b), the resulting modal forces from this portion of the kinetic energy are:

$$\frac{\partial}{\partial t}\left(\frac{\partial E_k|_{m=n}}{\partial \dot{X}}\right) - \frac{\partial E_k|_{m=n}}{\partial X} = -\rho\pi BhR^2\Omega^2\delta\rho_n \cos n\Theta_{\rho,n} \tag{A-8a}$$

$$\frac{\partial}{\partial t}\left(\frac{\partial E_k|_{m=n}}{\partial \dot{Y}}\right) - \frac{\partial E_k|_{m=n}}{\partial Y} = -\rho\pi BhR^2\Omega^2\delta\rho_n \sin n\Theta_{\rho,n} \tag{A-8b}$$

(A-8a) and (A-8b) show that the $n\theta$ variation component in the density only contributes to the equations of motion through centripetal effects, which have been neglected in the equations motion used throughout this dissertation due to the applicability of the $\Omega \ll \omega_0$ condition. The other term in (A-7) which is linearly proportional to Ω has no net contribution to the equations of motion when $E_k|_{m=n}$ is incorporated into Lagrange's equations.

Bending potential energy

In a similar manner to the kinetic energy, the cross sectional bending potential energy of the ring can be expressed as:

$$\Delta E_{b,R}(\theta) = \frac{I}{2}E(\theta)\left(\frac{\partial^2 u}{R^2\partial\theta^2} + \frac{u}{R^2}\right)^2 Rd\theta \tag{A-9}$$

where $E(\theta)$ is given in (2.9). Substituting (2.1) and (2.9) into (A-9) gives the following expression for the cross sectional bending potential energy of the ring:

$$\Delta E_{b,R}(\theta) = \frac{EI(n^2-1)^2 d\theta}{2R^3}\sum_{p=0}^{\infty}\left(\mathrm{A}_p \cos p\theta + \mathrm{B}_p \sin p\theta\right) \tag{A-10}$$

where

$$\sum_{p=0}^{\infty}\left(\mathrm{A}_p\cos p\theta+\mathrm{B}_p\sin p\theta\right) \tag{A-11}$$
$$=\left(\frac{X^2+Y^2}{2}+\frac{X^2-Y^2}{2}\cos 2n\theta+XY\sin 2n\theta\right)$$
$$+\sum_{\sigma=1}^{\infty}\frac{X^2+Y^2}{2}\left(\delta E_\sigma\cos\sigma\Theta_{E,\sigma}\cos\sigma\theta+\delta E_\sigma\sin\sigma\Theta_{E,\sigma}\sin\sigma\theta\right)$$
$$+\sum_{\sigma=1}^{\infty}\left[\begin{array}{l}\left(\frac{X^2-Y^2}{4}\delta E_\sigma\cos\sigma\Theta_{E,\sigma}-\frac{XY}{2}\delta E_\sigma\sin\sigma\Theta_{E,\sigma}\right)\cos(\sigma+2n)\theta\\+\left(\frac{XY}{2}\delta E_\sigma\cos\sigma\Theta_{E,\sigma}+\frac{X^2-Y^2}{4}\delta E_\sigma\sin\sigma\Theta_{E,\sigma}\right)\sin(\sigma+2n)\theta\end{array}\right]$$
$$+\sum_{\sigma=1}^{\infty}\left[\begin{array}{l}\left(\frac{X^2-Y^2}{4}\delta E_\sigma\cos\sigma\Theta_{E,\sigma}+\frac{XY}{2}\delta E_\sigma\sin\sigma\Theta_{E,\sigma}\right)\cos(\sigma-2n)\theta\\-\left(\frac{XY}{2}\delta E_\sigma\cos\sigma\Theta_{E,\sigma}-\frac{X^2-Y^2}{4}\delta E_\sigma\sin\sigma\Theta_{E,\sigma}\right)\sin(\sigma-2n)\theta\end{array}\right]$$

To obtain the total bending potential energy, the cross-sectional bending potential energy $\Delta E_{b,R}(\theta)$ is integrated around the ring circumference. Consequently, in a similar manner to the kinetic energy, only A_0 is of significance in (A-10), yielding a total ring bending potential energy of:

$$E_{b,R}=\frac{EI\pi(n^2-1)^2}{R^3}\mathrm{A}_0 \tag{A-12}$$

A_0 can be obtained by equating the terms independent of θ on the left and right sides of (A-11). From (2.9), $\sigma\geq 1$ so the first and second summation groups do not contribute to A_0. The third summation group contributes to A_0 when $\sigma-2n=0$. A_0 is given by:

$$\mathrm{A}_0=\frac{X^2+Y^2}{2}+\frac{X^2-Y^2}{4}\delta E_{2n}\cos 2n\Theta_{E,2n}+\frac{XY}{2}\delta E_{2n}\sin 2n\Theta_{E,2n} \tag{A-13}$$

Substituting (A-13) into (A-12) gives the expression of the ring bending potential energy as shown in (2.10).

Appendix B: Derivation of Bending Potential Energy of Support Beams

As discussed in Section 3.3.2, the support beams considered for the equations of motion derived in (3.14) are of the semi-circular type, shown below.

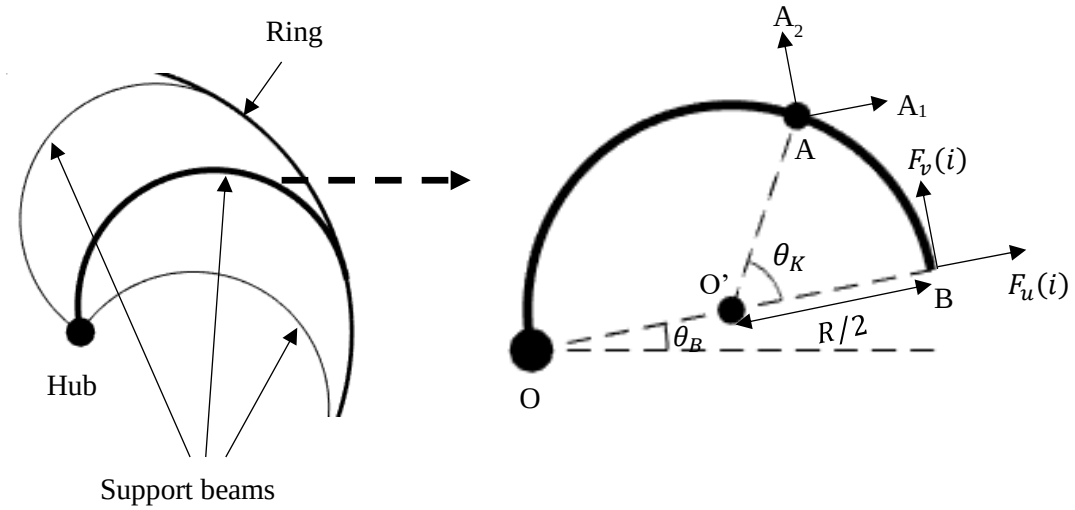

The semi-circular beam is fixed at the hub (point O) and constrained to displace with the ring at the supporting point B, subjected to the radial and tangential displacements described in (2.1) and (2.2) for n = 2. The supporting point of the i^{th} beam is selected at angular position $\theta_B + 2i\pi/8$ $(i = 1,2,\cdots,8)$ such that the support beams are unobstructed by the inner electrodes. θ_K is a general coordinate ranging from 0 to π describing an arbitrary point A on the support beam. Using the described representation of one supporting semi-circular beam, in what follows, Castigliano's theorem is employed to derive the total bending potential energy contribution from the 8 support beams.

When the ring deflects, point B displaces, applying radial and tangential forces $F_u(i)$ and $F_v(i)$ on the i^{th} semi-circular beam. These forces depend on the displacements at the supporting points of each beam, hence varying with the index i. These forces elicit a bending moment in the semi-circular beam. The bending moment at point A, $M_A(i)$ can be obtained from the cross product between the position vector of B relative to A, $\underline{\boldsymbol{r}}_{\boldsymbol{BA}}$, and the vector representation of $F_u(i)$ and $F_v(i)$, $\underline{\boldsymbol{F}}(i)$. For this purpose, the coordinate system $AA_1A_2A_3$ is implemented, where A is the origin and the A-A_3 axis is perpendicular to the AA_1A_2 plane. The moment vector $\underline{\boldsymbol{M}}_{\boldsymbol{A}}(i)$ is given by:

$$\underline{\boldsymbol{M_A}}(i) = \underline{\boldsymbol{r_{BA}}} \times \underline{\boldsymbol{F}}(i) \tag{B-1}$$

where

$$\underline{\boldsymbol{r_{BA}}} = \begin{pmatrix} \frac{R}{2}(1-\cos\theta_K) \\ -\frac{R}{2}\sin\theta_K \\ 0 \end{pmatrix} \tag{B-2}$$

$$\underline{\boldsymbol{F}}(i) = \begin{pmatrix} F_u(i) \\ F_v(i) \\ 0 \end{pmatrix} \tag{B-3}$$

$M_A(i)$ is derived from the A-A_3 component of the cross product in (B-1), giving:

$$M_A(i) = \frac{R}{2}[F_u(i)\sin\theta_K + F_v(i)(1-\cos\theta_K)] \tag{B-4}$$

This expression can also be directly derived from a geometric inspection of the diagram above.

The total bending potential energy from the i^{th} support beam, $E^i_{b,K}$, is given by the following integral:

$$E^i_{b,K} = \int_0^{\pi} \frac{M_A(i)^2}{2E_K I_K}\left(\frac{R}{2}d\theta_k\right) = \frac{R^3}{32E_K I_K}[\pi F_u(i)^2 + 8F_u(i)F_v(i) + 3\pi F_v(i)^2] \tag{B-5}$$

where the evaluated result of the integral has also been shown with $M_A(i)$ being substituted for its derived expression in (B-4). $E_K I_K$ is the flexural rigidity of the support beam.

From Castigliano's theorem, the partial derivatives of (B-5) give the radial and tangential displacements at the i^{th} supporting point, where $u_i = \partial E^i_{b,K}/\partial F_u(i)$ and $v_i = \partial E^i_{b,K}/\partial F_v(i)$. Performing these differentiation operations on (B-5) derives a linear relationship between the displacement components u_i, v_i and the force components $F_u(i), F_v(i)$, given by:

$$\begin{bmatrix} F_u(i) \\ F_v(i) \end{bmatrix} = \begin{bmatrix} k_{uu} & k_{uv} \\ k_{uv} & k_{vv} \end{bmatrix} \begin{bmatrix} u_i \\ v_i \end{bmatrix} \tag{B-6}$$

where

$$\begin{bmatrix} k_{uu} \\ k_{uv} \\ k_{vv} \end{bmatrix} = \frac{32E_K I_K}{R^3(3\pi^2 - 16)} \begin{bmatrix} \frac{3\pi}{2} \\ -2 \\ \frac{\pi}{2} \end{bmatrix} \tag{B-7}$$

The linearity of the force-displacement relationship in (B-6) shows that $F_u(i)$ and $F_v(i)$ are restoring forces defined by the stiffness coefficients k_{uu}, k_{uv} and k_{vv}. k_{uu} and k_{vv} are unidirectional stiffnesses in the radial and tangential directions respectively, while k_{uv} is the coupled-direction stiffness. These stiffness values are not arbitrary, constrained to the ratio shown in (B-7) due to the geometry of the support beam. (B-7) shows that the stiffening effects of the semi-circular supporting beams are predominantly in the radial direction.

Substituting (B-6) into (B-5) allows the potential energy $E_{b,K}^i$ to be expressed in terms of the radial and tangential displacements, giving:

$$E_{b,K}^i = \frac{1}{2}k_{uu}{u_i}^2 + k_{uv}u_i v_i + \frac{1}{2}k_{vv}{v_i}^2 \tag{B-8}$$

which takes on the expected form of the summed potential energy of linear springs in the radial, tangential and coupled directions.

Noting that the supporting points lie on the ring at angular positions $\theta = \theta_B + 2i\pi/8$ (see above diagram), the displacement components u_i, v_i can be expressed in terms of the drive and sense mode displacements using (2.1) and (2.2). This gives:

$$u_i = X\cos 2(\theta_B + 2i\pi/8) + Y\sin 2(\theta_B + 2i\pi/8) \tag{B-9}$$

$$v_i = -\frac{X}{2}\sin 2(\theta_B + 2i\pi/8) + \frac{Y}{2}\cos 2(\theta_B + 2i\pi/8) \tag{B-10}$$

Substituting (B-9) and (B-10) into (B-8), followed by summing the bending potential energy across all 8 supporting beams gives the following result for the total bending potential energy arising from the supporting beams:

$$E_{b,K} = \sum_{i=1}^{8} E_{b,K}^i = \frac{K}{2}(X^2 + Y^2) \tag{B-11}$$

where $K = 4k_{uu} + k_{vv}$, representing the effective total modal stiffness of the supporting beams. The contribution from the coupled-direction stiffness k_{uv} nullifies after the summation.

Recalling that the total bending potential energy in the equations of motion (3.5a) and (3.5b) is given by the sum $E_b = E_{b,R} + E_{b,K}$. Substituting (B-11) into this summation and substituting the resulting expression of E_b into (3.5a) and (3.5b) gives the net contribution of the support beams to the equations of motion. Since (B-11) only contains uncoupled quadratic terms in the drive and sense mode displacements, the derivatives $\partial E_b/\partial X$ and $\partial E_b/\partial Y$ in (3.5a) and (3.5b) ensure that the supporting beams only yield restoring force effects, contributing to the linear resonant frequency ω_0 defined in (3.18) through its second term.

Appendix C: Procedures for FE model setup

In Chapters 3-5, FE results have been included to validate the mathematical models resulting from the various electrostatic configurations implemented, such as (3.6), (4.65a) and (4.65b). In the following, the details of how the FE model is developed are discussed.

Default parameters and operating conditions

The system considered for all the theoretical and FE results in Chapters 3-5 possesses the default properties and operating conditions shown in Table C.1. A range of angular rates is necessary to determine the rate sensitivity and bias rate such as those shown in Figure 3.9(a), Figure 3.9(b) and Figure 3.11 using a linear fitting of the rate output against the angular rate described by the expression in (3.59).

Table C.1: Default parameters and operating conditions

Parameter/operating condition	Value
R (μm)	550
B (μm)	80
h (μm)	4
ρ (kg/m^3)	2320
E (GPa)	160
K (N/m)	0.03
g_0 (μm)	1.4
ε_0 (F/m)	8.85e-12
Ω (°/s)	230 - 250

A range of angular rates are considered to enable the linear interpolation of the rate output using the relationship in (3.59) to obtain results for the rate sensitivity and bias rate.

The dimensions of the ring correspond to the device reported in [6]. The remaining parameters and operating conditions are varied depending on the results investigated.

Numerical solutions of equations of motion

The Simulink toolbox is an integrated feature of the MATLAB software package, enabling direct solving of nonlinear equations of motion such as (3.14). Simulink uses iterative time-stepping methods such as Runge-Kutta [67], which are used to solve these equations of motion. To incorporate the equations of motion in Simulink, the equations of motion are first arranged in the form of $\ddot{X} = h_X(X, Y, \dot{X}, \dot{Y}, t)$ and $\ddot{Y} = h_Y(X, Y, \dot{X}, \dot{Y}, t)$ before solving the equations of motion.

To calculate the evolution of the modal coordinates (X, Y) with time, the main calculation parameters required are:

- Initial conditions for the modal displacements and velocities $(X, Y, \dot{X}, \dot{Y})$.
- Sampling frequency $f_s = n_\omega f$, where $f = \omega/(2\pi)$ is the drive force frequency in Hz.
- Total number of time steps N_t, usually specified as an integer multiple of the number of drive forcing cycles N_χ such that $N_t/n_\omega = N_\chi$.

where n_ω (or f_s) and N_χ (or N_t) are the solver parameters which must be determined before setting up the FE model. In this work, the initial conditions are set at the default configuration corresponding to the undeflected, stationary ring, i.e. $X = \dot{X} = Y = \dot{Y} = 0$.

Choosing a higher sampling frequency f_s ensures better accuracy of the solution for the modal displacements, but at the expense of a longer computation duration. However, the solution exhibits convergence as f_s increases. This is demonstrated in Figure C.1 for the steady-state sense amplitude when solving for Y in (5.15).

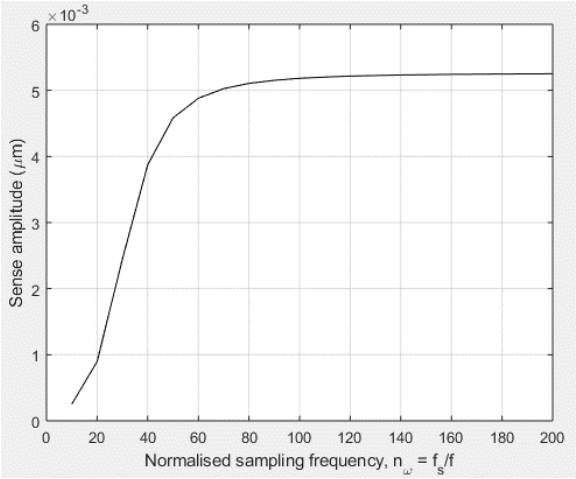

Figure C.1: Effect of n_ω on the converge of the steady-state sense amplitude

In Figure C.1, the solution exhibits minimal variations for $n_\omega > 100$ and variations of less than 1% is achieved.

The total number of time steps is determined by the time taken to achieve steady-state response, thus depending on the linear damping and parametric amplification. Figure C.2 shows the effects of the parametric amplification on the required forcing cycles for the sense response to achieve steady-state by solving (5.15). For clarity of the steady-state behaviour, the oscillatory behaviour has been discarded and only the sense displacement at the first quarter of each forcing cycle is shown in Figure C.2, i.e. at $\omega t = 2\pi N_\chi + \pi/2$. When the drive mode is phase-locked at resonance, this corresponds to the instance in each cycle where the sense displacement is at extreme. As such, the theoretical results for the steady-state rate output obtained using the averaging method are also shown for comparisons with the time-stepped results using Runge-Kutta (RK).

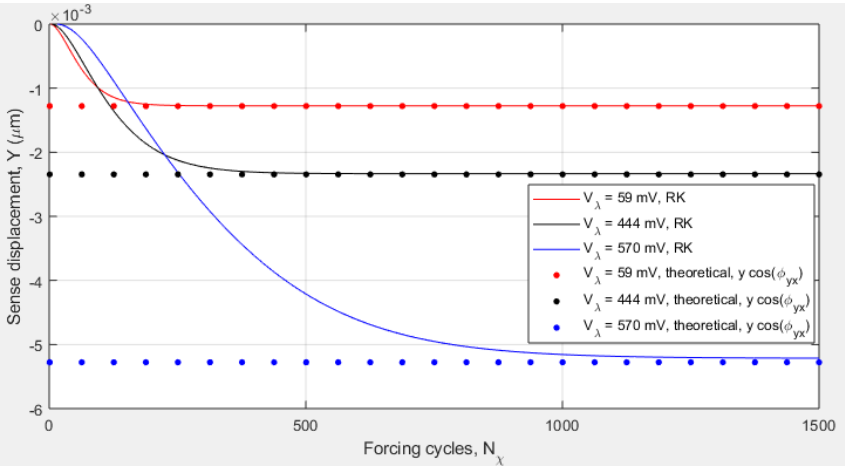

Figure C.2: Sense displacements at times $\omega t = 2\pi N_\chi + \pi/2$ for various levels of parametric amplification and the corresponding theoretical averaged rate outputs at steady-state

In a manner similar to the sampling frequency, the number of forcing cycles required to reach steady-state can be determined when the cycle-to-cycle variations of the modal displacements reduce to negligible magnitudes. For example, the results for $V_\lambda = 570\,mV$ in Figure C.2 exhibit variations of less than 1% at approximately $N_\chi \geq 800$. Figure C.2 also shows that the theoretical averaged results of the steady-state rate output exhibit good agreement with the numerical results when the Runge-Kutta method is directly applied on the equations of motion. As such, these numerical results also serve as an additional validation of the theoretical averaged results.

Careful selections of n_ω (or f_s) and N_χ (or N_t) are required in the FE model to obtain results of sufficient accuracy. The aforementioned calculations in Simulink are repeatedly performed for the various device parameters considered to obtain appropriate selections n_ω and N_χ for each parameter before being incorporated into the FE model.

FE model

Setup

The FE model is developed using the software COMSOL. The ring is modelled as a 2 - dimensional structure, surrounded by electrodes on the inner and outer sides of the circumference. Figure C.3 shows the FE model of the vibrating ring, and the electrodes are modelled as continuous circular lines. The solid corresponding to the ring is bisected into two regions separated by the mid-surface.

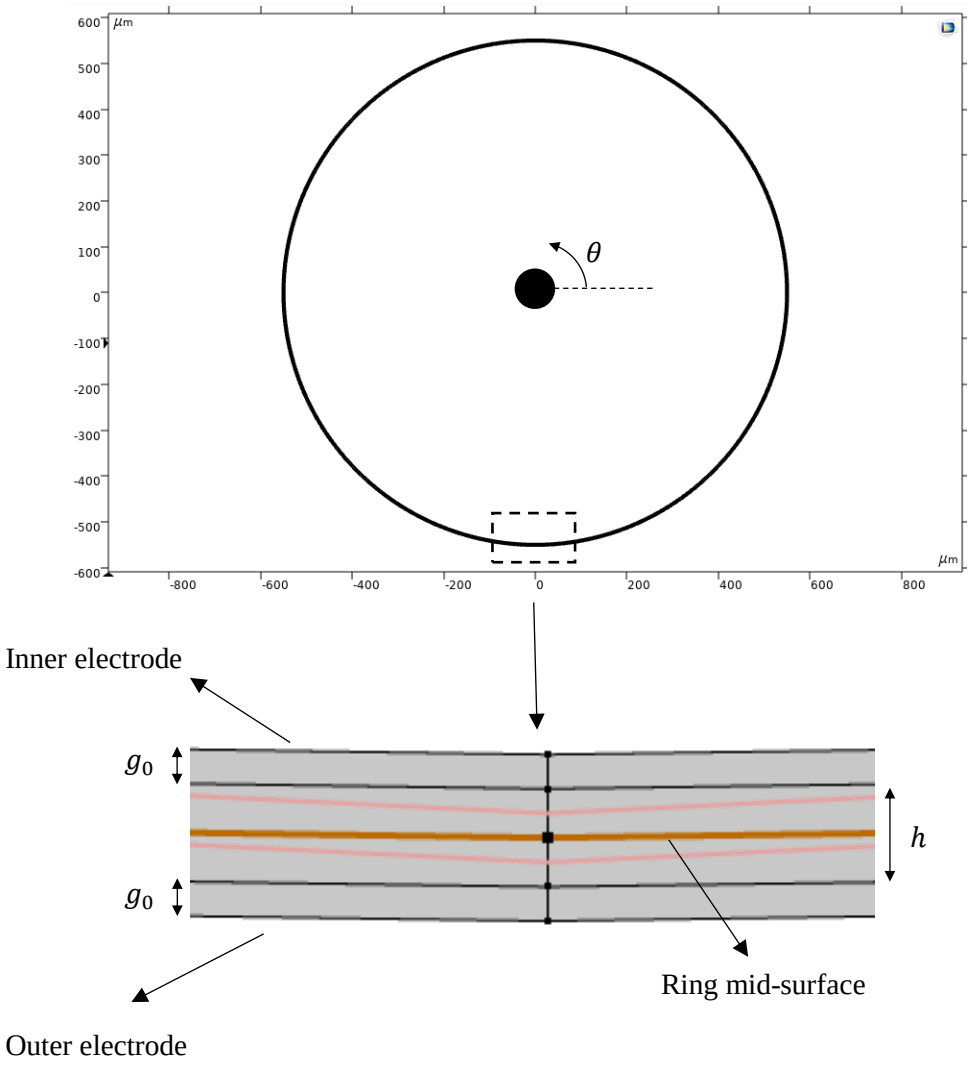

Figure C.3: FE model for the vibrating ring and electrodes

The support beams are modelled as point forces in the radial and tangential directions, acting at 8 evenly distributed points on the mid-surface. These forces depend linearly on the in-plane ring displacements, thus serving as restoring forces using the force-displacement relationship in (B-6).

Voltages are applied on the circular lines corresponding to the inner and outer electrodes, while the ring is grounded. The voltage distributions are modelled as piecewise functions of the angular position θ, characterised by zero voltages at the values of θ which are not within the electrode span and time-varying voltages at the remaining angular positions. Figure C.4 shows an example of these piecewise functions for the voltage distribution for the inner electrode set in (4.11) for the case where $a_{V,0}^{-} = 1$, $a_{V,\lambda}^{-} = a_{V,AC}^{-} = -1$ and $V_0 = 2115\,mV$, $V_\lambda = 329\,mV$, $V_{AC} = 7.6\,mV$ with 8 evenly distributed electrodes with span of $\delta = 38°$, at the instance $t = 0$.

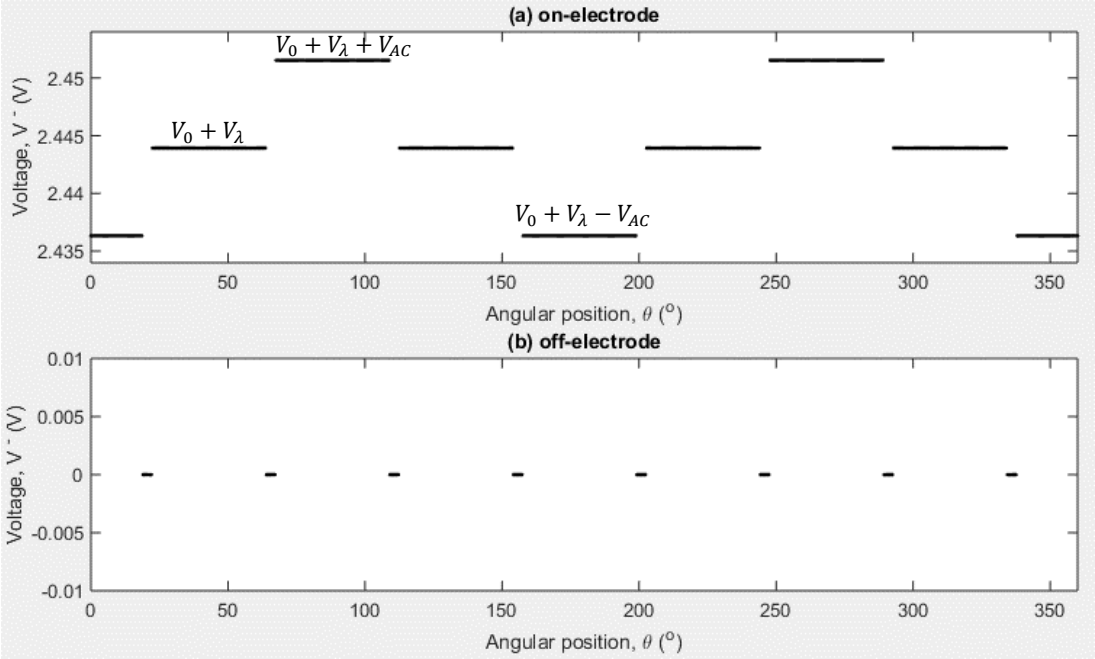

Figure C.4: Voltage distribution implementing bias, drive and parametric pumping voltage components in inner electrode set as a piecewise function of the angular position θ

The representation of the voltages as piecewise functions simplifies the geometry of the FE model significantly, as this avoids the need to split the circular electrode lines into multiple arcs when discontinuous electrodes are modelled.

Mesh convergence

Due to the nonlinearity of the model, transient analyses are required to obtain the steady-state sense response. The time required to complete the transient analyses of the FE model in COMSOL is substantial, so it is necessary to select the lowest possible mesh resolution giving steady-state results of sufficient accuracy. As such, prior to performing the transient analyses, a mesh convergence analysis is performed on the FE model. Since only the circumferential variations of the radial and tangential displacement fields are of interest in the present research, the geometry of the FE model is only meshed along the circumferential direction. The mesh convergence analysis is performed based on the built-in eigenfrequency analysis tool to obtain

the $n = 2$ natural frequencies while varying the number of mesh elements along the ring circumference. Figure C.5 below shows the variations of these frequencies with the number of mesh elements for a non-rotating ring with parameters described in Table C-1, with an electrostatic configuration composed of only a bias voltage component at $V_0 = 2V$ applied to 8 continuous inner and outer electrodes.

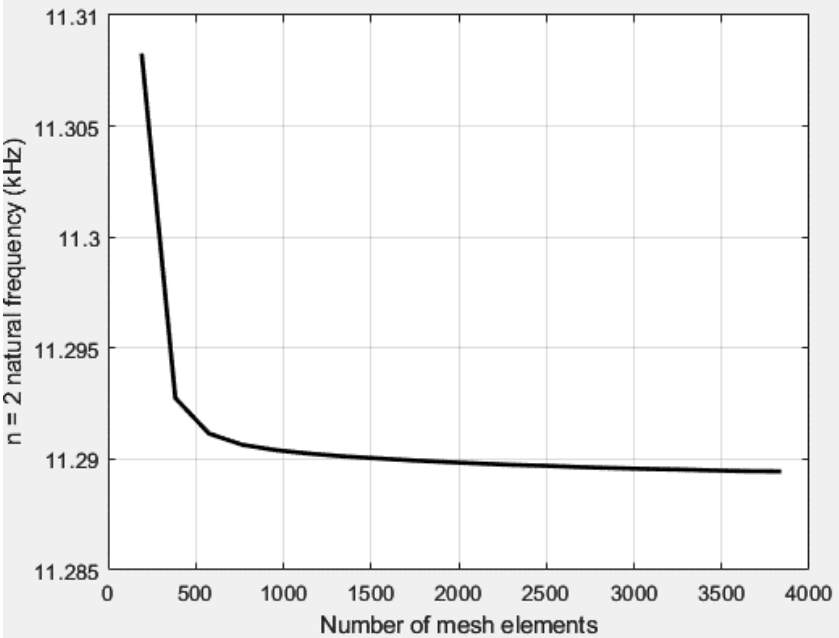

Figure C.5: Variation of calculated $n = 2$ natural frequency with number of mesh elements along ring circumference

The results in Figure C.5 show that the calculated natural frequency converges as the number of mesh elements is increased. Based on these results, the subsequent transient studies are performed using 576 mesh elements, which corresponds to a 0.015% deviation of the calculated natural frequency from the converged value.

Post-processing of transient study results

After defining the mesh resolution, the sampling frequency f_s and the number of drive cycles N_χ, the transient studies are performed to obtain the variation of the radial displacements with time. The radial displacement results are obtained at evenly-spaced positions on the ring mid-surface for each time-step, giving the following expression for the radial displacement, represented as a discrete Fourier series:

$$u(\theta_{i_\theta}, t_{i_t}) = \sum_{n=0}^{\infty} [Z_n(t_{i_t}) \cos(n\theta_i - \phi_n)] \quad \text{(C-1)}$$

where θ_{i_θ} is the angular position of the i_θ-th measurement location on the ring mid-surface, given by $\theta_i = 2i_\theta\pi/j_\theta$. j_θ is the number of points on the mid-surface where the radial displacements are obtained, and i_θ is an integer ranging from 1 to j_θ, defining the i_θ-th measurement point. In this procedure, $j_\theta = 120$ is used. t_{i_t} is the i_t-th sampling time and depends on the chosen sampling frequency f_s, given by $t_{i_t} = i_t/f_s$.

The drive and sense responses can be derived from the radial displacements in (C-1) by implementing a Fourier transform of (C-1) in θ_i, which gives $Z_n(t_{i_t})$ and ϕ_n for the various circumferential wave numbers involved. The drive and sense responses correspond to $n = 2$ and are given by:

$$X(t_{i_t}) = Z_2(t_{i_t})\cos\phi_2 \tag{C-2a}$$

$$Y(t_{i_t}) = Z_2(t_{i_t})\sin\phi_2 \tag{C-2b}$$

Once the drive and sense responses are obtained, the corresponding amplitudes and phases can be obtained. To achieve this, $X(t_{i_t})$ and $Y(t_{i_t})$ are first represented as Fourier series:

$$X(t_{i_t}) = \sum_{m=0}^{\infty}\left[x_m\cos(m\omega t_{i_t} + \phi_{x,m})\right] \tag{C-3a}$$

$$Y(t_{i_t}) = \sum_{m=0}^{\infty}\left[y_m\cos(m\omega t_{i_t} + \phi_{x,m} + \phi_{yx,m})\right] \tag{C-3b}$$

Similar to the procedure from (C-1) to (C-2a) and (C-2b), Fourier transformations of (C-3a) and (C-3b) in ωt_{i_t} are performed to obtain the amplitudes x_m, y_m and the phases $\phi_{x,m}$, $\phi_{yx,m}$ for the various harmonics m. Since the modal responses at the frequency of the drive force are of interest, the drive and sense amplitudes and phases for $m = 1$ are required, given by:

$$x = x_1 \tag{C-4a}$$

$$\phi_x = \phi_{x,1} \tag{C-4b}$$

$$y\cos\phi_{yx} = y_1\cos\phi_{yx,1} \tag{C-4c}$$

$$y\sin\phi_{yx} = y_1\sin\phi_{yx,1} \tag{C-4d}$$

The results in (C-4a) – (C-4d) correspond to averaged results from the theoretical analysis presented throughout Chapters 3-5. (C-4c) and (C-4d) give the rate and quadrature outputs respectively, which are directly compared to the theoretical averaged results presented throughout Chapters 3-5. (C-4c) and (C-4d) are obtained at multiple angular rates within the range specified in Table C.1 to obtain the rate sensitivity and bias rate using the relationship in (3.59).

Appendix D: Effects of Number of Electrodes on the Biasing Electrostatic Potential Energy Component with the Implementation of Fundamental Voltage Distribution

The square of the basic voltage distribution in (3.6) can be expanded into the following form:

$$V^{\pm}[\theta_0(i)]^2 = {V_0}^2 + \frac{{V_{AC}}^2 \cos^2 \omega t}{2} \pm 2V_0 V_{AC} \cos \omega t \cos 2\theta_0(i) + \frac{{V_{AC}}^2 \cos^2 \omega t}{2} \cos 4\theta_0(i) \tag{D-1}$$

The biasing component of the electrostatic potential energy, $\overline{U}$ in (3.8) stems from the interaction between the capacitance summation $c^{++-}(i)$ and the invariant component of the voltage squared distribution in (3.6), which are the first two terms in (D-1). However, in practice, $V_{AC} \ll V_0$ so the terms involving ${V_{AC}}^2$ can be neglected and only the bias voltage squared term, ${V_0}^2$ is shown in (3.8). Since the voltage squared component ${V_0}^2$ is identical for all electrodes, it is independent of the electrode number i and as such, the form that the summation in (3.8) takes is only dictated by the capacitance summation $c^{++-}(i)$. The analysis presented in Sections 3.3 - 3.5 is strictly focused on the case of j = 8. In what follows, the total number of electrodes j is kept general to identify its effects on $\overline{U}$ and subsequently, the equations of motion.

Substituting the radial displacement expression in (2.1) with n = 2 into (3.10a) and performing the integration enables the capacitance summation $c^{++-}[\theta_0(i)]$ to be expressed as a trigonometric series in the central angular position $\theta_0(i)$ in a manner similar to the voltage distribution in (3.6), thus identifying the capacitance of each of the i^{th} electrode. This gives:

$$c^{++-}[\theta_0(i)] = \alpha_0^{++-} + \alpha_4^{++-} \cos 4\theta_0(i) + \beta_4^{++-} \sin 4\theta_0(i) + \alpha_8^{++-} \cos 8\theta_0(i) + \beta_8^{++-} \sin 8\theta_0(i) \tag{D-2}$$

where the central angular position of the i^{th} electrode is defined as:

$$\theta_0(i) = 2i\pi/j \tag{D-3}$$

This generalises the central angular position for the total number of evenly distributed electrodes j. In Section 3.3.1, $\theta_0(i) = i\pi/4$ for the specific case for j = 8.

In (D-2), the coefficients α_0^{++-}, α_4^{++-}, β_4^{++-}, α_8^{++-}, β_8^{++-} are the result of the integration of the various ordered terms in u in (3.10a). These coefficients are given by:

$$\alpha_0^{++-} = \frac{2\varepsilon_0 BR}{g_0}\delta\left[1 + \frac{1}{2}\left(\frac{X^2+Y^2}{{g_0}^2}\right) + \frac{3}{8}\left(\frac{X^2+Y^2}{{g_0}^2}\right)^2\right] \tag{D-4a}$$

$$\alpha_4^{++-} = \frac{\varepsilon_0 BR}{2g_0}\sin 2\delta\left(\frac{X^2-Y^2}{{g_0}^2} + \frac{X^4-Y^4}{{g_0}^4}\right) \tag{D-4b}$$

$$\beta_4^{++-} = \frac{\varepsilon_0 BR}{g_0}\sin 2\delta\left(\frac{XY}{{g_0}^2} + \frac{X^3Y+XY^3}{{g_0}^4}\right) \tag{D-4c}$$

$$\alpha_8^{++-} = \frac{\varepsilon_0 BR}{16g_0}\sin 4\delta\left(\frac{X^4-6X^2Y^2+Y^4}{{g_0}^4}\right) \tag{D-4d}$$

$$\beta_8^{++-} = \frac{\varepsilon_0 BR}{4g_0}\sin 4\delta\left(\frac{X^3Y-XY^3}{{g_0}^4}\right) \tag{D-4e}$$

These expressions have been arranged in ascending powers of the modal coordinates to distinguish the contributions of the various ordered terms, i.e. u^0, u^2, u^4 in (3.10a). Specifically, α_8^{++-} and β_8^{++-} are purely composed of 4th order terms in the modal coordinates, indicating that they arise purely from the electrostatic nonlinearities. They are the direct result of the integration of the quartic term, u^4 in (3.10a). Capping the Taylor series expansion up to the 4th order in (3.10a) limits the resulting trigonometric series to an $8\theta_0(i)$ variation in (D-2).

Substituting (D-2) into (3.8) determines which of the coefficients α_0^{++-}, α_4^{++-}, β_4^{++-}, α_8^{++-}, β_8^{++-} have net contributions to $\overline{U}$ after the summation operation in (3.8) is evaluated. As such, it follows that the result of the summation of $c^{++-}[\theta_0(i)]$ dictates the resulting terms that appear in $\overline{U}$ and subsequently, the equations of motion. This gives:

$$\begin{aligned}\overline{U} = -\frac{{V_0}^2}{2}\sum_{i=1}^{j}[&\alpha_0^{++-} + \alpha_4^{++-}\cos 4\theta_0(i) + \beta_4^{++-}\sin 4\theta_0(i) + \alpha_8^{++-}\cos 8\theta_0(i) \\ &+ \beta_8^{++-}\sin 8\theta_0(i)]\end{aligned} \tag{D-5}$$

To evaluate the summation of $c^{++-}[\theta_0(i)]$ and the result of (D-6), the following conditions apply:

$$\sum_{i=1}^{j} \cos m\theta_0(i) = \sum_{i=1}^{j} \cos\frac{m}{j}(2i\pi) = \begin{cases} j, & \frac{m}{j} \in \mathbb{Z} \\ 0, & \text{else} \end{cases} \tag{D-6a}$$

$$\sum_{i=1}^{j} \sin m\theta_0(i) = \sum_{i=1}^{j} \sin\frac{m}{j}(2i\pi) = 0 \text{ for all } (m,j) \text{ combinations} \tag{D-6b}$$

where $m = 0,4,8$, representing the $\theta_0(i)$ variation components in (D-5).

The summation in (D-6b) indicates that the coefficients of the sine variations in (D-2), β_4^{++-} and β_8^{++-} have zero net contributions in $\overline{U}$ as the corresponding terms nullify after the summation across all electrodes. Also, for m = 0, m/j is always an integer regardless of the number of electrodes j. As such, the summation in (D-6a) for the case of $m/j \in \mathbb{Z}$ always applies when m = 0, indicating that α_0^{++-} in (D-2) never nullifies after the summation in (3.8). Applying these observations on (D-5) and substituting α_0^{++-}, α_4^{++-}, α_8^{++-} for the corresponding definitions in (D-4a), (D-4b) and (D-4d) gives the following results for the summation in (D-5):

Table D.1: Effect of the number of electrodes on the effective form of the biasing electrostatic potential energy component

j	$\overline{U}$
$j = 1,2,4$	$\overline{U} = -j\frac{{V_0}^2}{2}(\alpha_0^{++-} + \alpha_4^{++-} + \alpha_8^{++-})$ $= -j\frac{\varepsilon_0 BR{V_0}^2}{2g_0}\left\{2\delta + \left(\delta + \frac{\sin 2\delta}{2}\right)\frac{X^2}{{g_0}^2} + \left(\delta - \frac{\sin 2\delta}{2}\right)\frac{Y^2}{{g_0}^2} + \left(\frac{3}{4}\delta + \frac{\sin 2\delta}{2} + \frac{\sin 4\delta}{16}\right)\frac{X^4}{{g_0}^4} + \left(\frac{3}{4}\delta - \frac{3\sin 4\delta}{16}\right)\frac{2X^2Y^2}{{g_0}^4} + \left(\frac{3}{4}\delta - \frac{\sin 2\delta}{2} + \frac{\sin 4\delta}{16}\right)\frac{Y^4}{{g_0}^4}\right\}$
$j = 8$	$\overline{U} = -j\frac{{V_0}^2}{2}(\alpha_0^{++-} + \alpha_8^{++-})$ $= -j\frac{\varepsilon_0 BR{V_0}^2}{2g_0}\left[2\delta + \delta\frac{X^2+Y^2}{{g_0}^2} + \left(\frac{3}{4}\delta + \frac{\sin 4\delta}{16}\right)\frac{X^4+Y^4}{{g_0}^4} + \left(\frac{3}{4}\delta - \frac{3\sin 4\delta}{16}\right)\frac{2X^2Y^2}{{g_0}^4}\right]$

All other j	$\bar{U} = -j\frac{{V_0}^2}{2}\alpha_0^{++-} = -j\frac{\varepsilon_0 B R {V_0}^2}{2g_0}\delta\left[2 + \frac{X^2+Y^2}{{g_0}^2} + \frac{3}{4}\frac{(X^2+Y^2)^2}{{g_0}^4}\right]$

The terms involving δ, $\sin 2\delta$ and $\sin 4\delta$ arise from the coefficients α_0^{++-}, α_4^{++-} and α_8^{++-} respectively, all of which contribute to $\bar{U}$ when j = 1, 2 or 4. The terms in $\bar{U}$ contribute to the resulting drive and sense equations of motion in (3.5a) and (3.5b) with modal forces described by the derivatives $\partial\bar{U}/\partial X$ and $\partial\bar{U}/\partial Y$ respectively.

The expression for $\bar{U}$ in Table D.1 for the case of j = 1, 2 or 4 shows that α_4^{++-} results in a difference between the coefficients of the uncoupled terms, i.e. X^2 and Y^2 as well as X^4 and Y^4. This shows that using 1, 2 or 4 evenly distributed electrodes breaks the modal symmetry described in Section 3.3.1. When $\bar{U}$ is incorporated into Lagrange's equations in (3.5a) and (3.5b), this electrostatically-induced modal asymmetry elicits a splitting of the linear resonant frequency in a manner similar to the ring imperfections, as well as the splitting between the Duffing coefficients of the drive and sense modes. This is because the use of 1, 2 or 4 electrodes results in unequal spring effects on the drive and sense modes.

α_8^{++-} only affects the 4th-order terms in $\bar{U}$ and is nullified unless j = 1, 2, 4 or 8. The expression for $\bar{U}$ for the case of j = 8 in Table D.1 has been derived in (3.11). The condition $\gamma_0 = \kappa_0$ requires the 4th-order terms in $\bar{U}$ to be proportional to $(X^2+Y^2)^2$, thus the use of 1, 2, 4 or 8 electrodes must be avoided to satisfy this condition. As such, while the use of 8 electrodes is sufficient for the linear device as the linear frequency splitting effect due to α_4^{++-} can be avoided, a nonlinear frequency imbalance still exists in an otherwise ideal/trimmed ring when $\sin 4\delta \neq 0$ with electrostatic nonlinearities considered.

Appendix E: Definitions of terms in the equations of motion for quadratic parametric amplification

The equations of motion where the quadratic electrostatic forces are used for parametric excitation are given by (5.41), where $\overline{\overline{\boldsymbol{\eta}}}_{\mathbf{1}}$ and $\overline{\overline{\boldsymbol{\eta}}}_{\mathbf{3}}$ are given in (5.42) and (5.44):

$$\overline{\overline{\boldsymbol{\eta}}}_{\mathbf{1}} = {\omega_{0,\lambda,4}}^2 \begin{bmatrix} 1 & \Delta_{0,4} \\ \Delta_{0,4} & 1 \end{bmatrix} + {\omega_m}^2 \begin{bmatrix} \Delta_m \cos 4\Theta_\omega & \Delta_m \sin 4\Theta_\omega \\ \Delta_m \sin 4\Theta_\omega & -\Delta_m \cos 4\Theta_\omega \end{bmatrix} \tag{5.42}$$

$$\overline{\overline{\boldsymbol{\eta}}}_{\mathbf{3}} = \begin{bmatrix} \gamma_{0,\lambda,4} & \tilde{\kappa}_{0,4} & \kappa_{0,\lambda,4} & \tilde{\gamma}_{0,4} \\ \tilde{\gamma}_{0,4} & \kappa_{0,\lambda,4} & \tilde{\kappa}_{0,4} & \gamma_{0,\lambda,4} \end{bmatrix} \tag{5.44}$$

The linear resonant frequency ${\omega_{0,\lambda,4}}^2$ and the cubic modal stiffness coefficients $\gamma_{0,\lambda,4}, \kappa_{0,\lambda,4}$ are given by:

$${\omega_{0,\lambda,4}}^2 = {\omega_m}^2 - \frac{2\varepsilon_0}{5\rho\pi h {g_0}^3} j\delta \left(2{V_0}^2 + \frac{5{V_4}^2}{8} + \frac{{V_\lambda}^2}{2} \right) \tag{E-1}$$

$$\gamma_{0,\lambda,4} = -\frac{\varepsilon_0}{5\rho\pi h {g_0}^3} j \left[3\delta \left(2{V_0}^2 + \frac{5{V_4}^2}{8} + \frac{{V_\lambda}^2}{2} \right) - \frac{5\sin 4\delta}{32} {V_4}^2 \right] \tag{E-2}$$

$$\kappa_{0,\lambda,4} = -\frac{\varepsilon_0}{5\rho\pi h {g_0}^3} j \left[3\delta \left(2{V_0}^2 + \frac{5{V_4}^2}{8} + \frac{{V_\lambda}^2}{2} \right) + \frac{15\sin 4\delta}{32} {V_4}^2 \right] \tag{E-3}$$

$\gamma_{0,\lambda,4} = \kappa_{0,\lambda,4}$ when $V_4 = 0$, regardless of the electrode span. This coincidence occurs naturally because $j = 16$.

The harmonic drive force amplitude χ and its correction factor matrix $\overline{\overline{\boldsymbol{\eta}}}_{\boldsymbol{\chi}}$ are given by:

$$\chi = \frac{6\varepsilon_0 V_0 V_{AC}}{5\rho\pi h {g_0}^2} j \sin\delta \tag{E-4}$$

$$\overline{\overline{\boldsymbol{\eta}}}_{\boldsymbol{\chi}} = \begin{bmatrix} \frac{9}{4} & 0 & \frac{3}{4} \\ 0 & \frac{3}{2} & 0 \end{bmatrix} \tag{E-5}$$

These differ from those of the other electrostatic configurations considered due to the unequal amplitudes of the drive voltage components of the inner and outer electrode sets in (5.37a) and (5.37b).